

The Response Of Gas Giant
Ionospheres To Space
Environment Forcing



James O'Donoghue

Radio and Space Plasma Physics Group

University of Leicester

A thesis submitted for the degree of

Doctor of Philosophy

July 16th 2014

Abstract

James O'Donoghue

The Response Of Gas Giant Ionospheres To Space Environment Forcing

At high spatial and spectral resolution, the 10-metre Keck and 3-metre NASA IRTF ground-based telescopes were used to observe Saturn and Jupiter, respectively. Pole-to-pole profiles of H_3^+ emission were recorded along the planets' respective noon meridians. The low latitude ionospheric H_3^+ emission of these planets was thought to be broadly uniformly decreasing towards the equator, with the transition from bright emission at the poles produced by particle precipitation, to the weaker background glow elsewhere produced by sunlight. Instead, however, a pattern of intensity variability was detected at both Jupiter and Saturn. This pattern was found to be symmetric about the magnetic equator at Saturn, with peaks in H_3^+ intensity magnetically mapping to gaps in Saturn's rings. The transport of water ions from the gaps in Saturn's rings to the planetary ionosphere, delivered via magnetic field lines, was used to explain this, as water ions cause an increased H_3^+ density and therefore emission. In the same dataset, the temperature of Saturn's H_3^+ aurorae remained effectively constant, whilst the H_3^+ column density and total emission varied greatly. The southern auroral oval was found to be significantly warmer than its northern counterpart, having average temperatures of 583 and 527 K, respectively. This asymmetry was attributed to an inverse relationship between ionospheric Joule and ion drag heating with magnetic field strength. Jupiter's low latitude ionosphere also appears to vary significantly in H_3^+ emission, but this time in longitude. This may be due to

an inversely proportional relationship between magnetic field strength and particle precipitation. In summary, the planetary ionospheres of Saturn and Jupiter have been found to be globally subjected to space environment forcing. Whilst such forcing was well established for the auroral regions, we have here discovered that particle precipitation can dominate the low latitude ionospheres of the gas giants.

Declarations

The research undertaken during the course of this doctoral programme has led to the submission and publication of the following scientific papers:

- **O'Donoghue, J.**, T. S. Stallard, H. Melin, G. H. Jones, S. W. H. Cowley, S. Miller, K. H. Baines, and J. S. D. Blake, The domination of Saturn's low-latitude ionosphere by ring "rain", *Nature*, **496(7444)**, 193-5, doi:10.1038/nature12049, 2013.
- **O'Donoghue, J.**, Tom S. Stallard, Henrik Melin, Stan W.H. Cowley, Sarah V. Badman, Luke Moore, Steve Miller, Chihiro Tao, Kevin H. Baines, James S.D. Blake, Conjugate observations of Saturn's northern and southern aurorae, *Icarus*, **229**, 214-220, doi:10.1016/j.icarus.2013.11.009, 2013.

For Wendy

*Two roads diverged in a wood, and I took the one less travelled by,
and that has made all the difference.*

Robert Frost

Acknowledgements

I am eternally grateful to everyone that has tolerated me over the last 3 and a bit years. At this stage I am permitted to be honest and say that I literally applied to study the gas giants in a PhD so that I could go to Hawaii and observe, and I did - four times! However, I quickly caught 'the bug' and began to enjoy the research immensely. I am extremely grateful to my supervisor, Tom Stallard, for giving me the opportunity to do world-class research in the RSPP group at Leicester. Tom has been my conscience throughout the course of the PhD, chiselling down my wacky ideas into actual scientific results, and it is training that I will not soon forget! I would like to extend my gratitude to my office buddy Henrik Melin, for his unrelenting assistance in answering countless questions over the years; the answers of which were like fuel - such that - conceptually novel science could be performed.

The most science I've learnt is by getting things wrong; I get a lot of things wrong. The people that have dealt with these many wrongs, either by pointing them out or fixing them, have been the co-authors on the published works I have produced. I am thus extremely grateful for their coaching; in particular - I'd like to thank Stan Cowley for devoting a great deal of his time, which was particularly information rich! I would also like to thank the STFC and the UK tax-payer for funding this research, and my thesis committee for their support of the PhD's continuation.

The willingness to celebrate achievement in RSPP has made me try

harder throughout my time here. The RSPP group at Leicester have struck an excellent balance between productivity and sociability, without their friendliness and willing to go to the pub, I'd probably have cracked in the first year.

Last but not least, I'd like to thank my mother, Wendy - to whom I dedicate this thesis - and my little sisters, Victoria and Charlotte, for their constant encouragement throughout my academic career.

Pub?

Contents

List of Figures	xii
List of Tables	xvi
1 Introduction	1
1.1 Aims	1
1.2 Plasma physics	2
1.2.1 Single particles	2
1.2.2 Auroral ionospheric currents	6
1.3 Light and spectroscopy	11
1.3.1 Atomic spectra	11
1.3.2 Molecular spectroscopy	13
1.4 The H_3^+ molecule	19
1.4.1 Properties, formation and destruction	19
1.4.2 Local thermodynamic equilibrium	21
1.4.3 Spectroscopy	21
1.5 Saturn and Jupiter	27
1.6 Saturn	27
1.6.1 Ionosphere, thermosphere and motivations	29
1.6.2 Aurorae	31
1.6.3 Saturn's ring system and motivation	35
1.7 Jupiter	40
1.7.1 Ionosphere, thermosphere and motivation	41

1.7.2	The Jovian magnetosphere and aurorae	42
2	Data reduction and H_3^+ fitting	45
2.1	Telescope and instrument overview	45
2.1.1	The NASA IRTF and SpeX instrument	46
2.1.2	The W.M. Keck telescopes and NIRSPEC instrument	47
2.2	Instrumental considerations	49
2.2.1	CCD calibration	49
2.2.2	Echelle diffraction gratings	50
2.2.3	Single-order spectroscopy	52
2.2.4	Multiple-order spectroscopy	53
2.3	Terrestrial considerations	54
2.3.1	Terrestrial emission: Sky subtraction	55
2.3.2	Terrestrial absorption: Flux calibration	56
2.4	Pixel registration	61
2.5	Extracting properties from H_3^+	64
2.5.1	H_3^+ transition line intensities	64
2.5.2	The partition function of H_3^+	65
2.5.3	H_3^+ temperature calculation	67
2.5.4	H_3^+ column density calculation	69
2.5.5	H_3^+ total emission calculation	71
3	Ring ‘rain’ on Saturn’s ionosphere	73
3.1	Introduction to low-latitude H_3^+ at Saturn	74
3.2	Saturn-specific data acquisition	77
3.2.1	Observational setup	78
3.2.2	Data selection	80
3.3	Low-latitude H_3^+ emission	84
3.3.1	Magnetic field model: Bunce et al., 2008	84
3.3.2	Observational result	85

3.3.3	Temporal investigation	87
3.3.4	Alternative magnetic model: Connerney et al., 1982	91
3.4	Saturn’s ring ‘rain’ interpretations	92
3.4.1	The ring water source	93
3.4.2	Rain effects on ionospheric chemistry	95
3.4.3	Interpretation 1 (main): Water influx enhancing H_3^+	100
3.4.4	Interpretation 2: Water influx quenching H_3^+	101
3.4.5	Interpretation 3: Ring-ionosphere coupling currents	103
3.5	Future work	104
3.5.1	Future investigation	105
3.5.2	Future observations	105
4	 Conjugate observations of Saturn’s aurorae	108
4.1	Introduction	109
4.1.1	Previous work	109
4.1.2	Context	109
4.2	Data acquisition	110
4.3	Results	114
4.4	General discussion	117
4.4.1	Seasonal temperature differences	117
4.4.2	Correlations between parameters	118
4.5	Saturn’s conjugate aurorae	119
4.5.1	Interhemispheric energy asymmetry	119
4.5.2	Comparison to previous studies	123
4.5.3	Modelled versus observed H_3^+ density	125
4.5.4	Particle precipitation	128
4.6	Conclusions	129
5	 Jupiter: comparative aeronomy	131
5.1	Jupiter-specific data acquisition	131

5.1.1	Observations	131
5.1.2	Spectral map construction	134
5.1.3	Uncertainty limited spectral fitting	137
5.2	Comparison with previous studies	139
5.2.1	Observational differences	139
5.2.2	H_3^+ temperature comparison to Lam et al	142
5.2.3	H_3^+ column density comparison to Lam et al	144
5.2.4	H_3^+ total emission comparison to Lam et al	146
5.2.5	Validation of dataset	148
5.3	Comparison to Saturn	148
5.3.1	Mid-to-low latitudes	151
5.3.2	Auroral/polar regions	156
5.4	Conclusion	158
6	Conclusion	161
	References	164

List of Figures

1.1	Gyrofrequency to collision frequency ratio	9
1.2	Molecular behaviour of ionospheric currents	10
1.3	Bohr model for hydrogen	12
1.4	Energy level diagram	13
1.5	Vibrational energy level diagram	15
1.6	Rotational energy level diagram	16
1.7	Black-body radiation curve	18
1.8	The H_3^+ molecule	20
1.9	Vibrational modes of H_3^+	22
1.10	Modelled spectrum of H_3^+	23
1.11	Modelled spectrum of H_3^+ zoomed in between 3 - 5 micrometres	24
1.12	Modelled spectrum of H_3^+ and observed Earth's atmosphere	26
1.13	Solar system planets comparison	27
1.14	Saturn from Cassini	29
1.15	A model profile of Saturn's ionosphere	30
1.16	Saturn's magnetosphere-ionosphere coupling currents	34
1.17	Saturn's rings	37
1.18	Saturn in high contrast (green)	38
1.19	Transmission of light through the rings	39
1.20	Jupiter from Cassini	40
1.21	Model profile of Jupiter's ionosphere	42
1.22	Jovian magnetosphere-ionosphere coupling	44

LIST OF FIGURES

2.1	The NASA IRTF telescope	46
2.2	The SpeX instrument	47
2.3	The Keck telescopes	48
2.4	The NIRSPEC instrument	48
2.5	A typical flat-field spectral image	50
2.6	An Echelle diffraction grating	51
2.7	A two-slit diffraction pattern	52
2.8	A typical single-order mode spectral image	53
2.9	A typical (raw) multiple order spectrum	54
2.10	Target minus sky, (A - B) subtraction	55
2.11	A black-body spectrum in the L' Window	56
2.12	A spectral profile of Saturn	57
2.13	The spectrum of HR6035	58
2.14	A typical flux calibration spectrum	60
2.15	A flux calibrated profile of Saturn	61
2.16	Q(T) as a function temperature	66
2.17	Line ratio example	68
3.1	First low-latitude observations of H ₃ ⁺	75
3.2	Recent low-latitude H ₃ ⁺ observations	76
3.3	Simple Jupiter profile	77
3.4	Observational set-up	79
3.5	Saturn's rings smeared by seeing	81
3.6	Latitudinal error as a function of latitude	81
3.7	Background subtraction regions	82
3.8	Background subtraction effect	83
3.9	Saturn's pole-to-pole H ₃ ⁺ IR emission	86
3.10	Intensity of H ₃ ⁺ IR emission along Saturn's noon meridian	88
3.11	Saturn's ring smearing distributed by temporal bins	89
3.12	Temporal bin 1	90

LIST OF FIGURES

3.13	Temporal bin 2	90
3.14	Temporal bin 3	91
3.15	Figure 3.10 cast in the Z3 field model mapping	92
3.16	Saturn's ring rain	93
3.17	Modelled O^+ and O_2^+	94
3.18	Seasonal effects on the ionodisk	95
3.19	Saturn modelled ionosphere by STIM	100
3.20	Low-latitude current system	103
3.21	Spatial smearing of pixels	106
4.1	Observational set-up	111
4.2	A hydrocarbon subtracted spectrum of Saturn	113
4.3	Model fit to data	114
4.4	Saturn's auroral parameters as a function of time	117
4.5	Saturn's magnetic field strength versus co-latitude	120
4.6	Modelled EUV modulated H_3^+ density for nominal q	126
4.7	Modelled EUV modulated H_3^+ density for multiple values of q	127
5.1	IR image of Jupiter	133
5.2	Jovian longitudes observed	134
5.3	Latitudinal broadening of pixels	135
5.4	Longitudinal broadening of data	136
5.5	Bin allocation visualisation	138
5.6	Lam et al Jovian spectra	141
5.7	Jovian spectra; this work	141
5.8	Map of Jovian H_3^+ column density by Lam et al. (1997)	143
5.9	Comparative map of Jovian H_3^+ temperatures	143
5.10	Map of Jovian H_3^+ column density by Lam et al. (1997)	145
5.11	Comparative map of Jovian H_3^+ column density	145
5.12	Map of Jovian H_3^+ total emission	147

LIST OF FIGURES

5.13	Comparative map of Jovian H_3^+ total emission	147
5.14	Map of Jovian H_3^+ temperatures	149
5.15	Map of Jovian H_3^+ column densities	150
5.16	Map of Jovian H_3^+ total emission	150
5.17	Thresholded map of Jovian H_3^+ total emission	152
5.18	Jovian rings and small moons	155
5.19	Surface magnetic field strength of Jupiter	157

List of Tables

1.1	Comparison of the basic parameters of Earth, Saturn and Jupiter.	28
3.1	Ion-electron reactions	96
3.2	Water ion reactions with H ₂	97
3.3	Water ion reactions with H ₂	98
4.1	Saturn's main auroral oval properties as a function of time	116
5.1	Summary of Jupiter observation times and conditions	132
5.2	Observational differences between Lam et al and this work	139

Chapter 1

Introduction

1.1 Aims

One of the major motivating factors for studying the ionospheres of the gas giants is that the upper atmospheres of Saturn and Jupiter are globally observed to be hundreds of Kelvin hotter than solar heating models are able to predict; this has been colloquially termed the ‘energy crisis’ (e.g. Miller et al., 2005). Although the high temperatures can be explained by electrical (Joule) heating for the auroral/polar regions (Cowley et al., 2004, 2005b), no known heating mechanism has been able to replicate the observed temperatures at low latitude (Rego et al., 2000; Hickey et al., 2000; Smith et al., 2007; Mueller-Wodarg et al., 2012). The principle aim of this work is thus to study the interactions between the gas giants - Saturn and Jupiter - and their local space environments. We define this as ‘space environment forcing’, as the upper atmospheres are forced into a non-steady state. It is important to note here that because both Saturn and Jupiter have an energy crisis, the solution is likely to be common to each planet’s ionosphere.

Ground-based telescope data will be used to examine the emissions emanating from the respective planetary upper atmospheres. Such emissions come from the molecular ion, H_3^+ , which is located in the charged component of the atmosphere,

the ionosphere. This is a particularly useful region to study because it is here that electrical and magnetic forces are able to interact with the planet's neutral atmosphere, via collisions between charged and neutral species.

1.2 Plasma physics

A core component to understanding gas giant ionospheres and their interaction with their surrounding space environments is to understand the underlying physical processes of plasmas. A plasma is a rarefied gas composed of equal numbers of positive ions and negative electrons such that there is no net charge within a given volume (Kivelson and Russell, 1995). To remain in this state of quasi-neutrality, the particles within the plasma must have large enough kinetic energy (on the order of electronvolts) to overcome the electrostatic attractive force which tries to bind them together to form a neutral gas (Baumjohann and Treumann, 1996). The motion of charged particles within a plasma, unlike in a neutral gas, can be organised in response to the external influences of electric and magnetic fields. Here we shall discuss the general theory applicable to all planets for individual particle interactions that lead to the production of weak diffuse auroral emission, and large scale current systems responsible for ionospheric heating. Discrete auroral emission is significantly brighter and more spatially concentrated than the diffuse emission, and is driven differently for each planet we study herein. Hence, the individual driving mechanisms for Saturn and Jupiter will be discussed separately in the appropriate sections.

1.2.1 Single particles

A particle with a charge q exposed to an electric field \mathbf{E} and magnetic field \mathbf{B} will feel a force, the Lorentz force, given by

$$\mathbf{F} = q(\mathbf{E} + \mathbf{v} \times \mathbf{B}), \quad (1.1)$$

where \mathbf{v} is the velocity of the particle. In the absence of the electric field component, \mathbf{E} , and substituting $\mathbf{F} = m\mathbf{a}$, this equation reduces to

$$m \frac{d\mathbf{v}}{dt} = q(\mathbf{v} \times \mathbf{B}), \quad (1.2)$$

where m is the mass of the charged particle, which for a proton is $m_p = 1.67 \times 10^{-27}$ kg and for an electron, $m_e = 9.11 \times 10^{-31}$ kg. Taking the dot product of Equation 1.2 with velocity \mathbf{v} (and given that $\mathbf{v} \cdot (\mathbf{v} \times \mathbf{B}) = 0$), we find that

$$m \frac{d\mathbf{v}}{dt} \cdot \mathbf{v} = \frac{d}{dt} \left(\frac{m\mathbf{v}^2}{2} \right) = 0, \quad (1.3)$$

showing that for a static magnetic field, the speed and the kinetic energy are constant (Baumjohann and Treumann, 1996). Assuming a Cartesian coordinate system in which the velocity components are $v \hat{x}$, $v \hat{y}$ and $v \hat{z}$, and assuming that the magnetic field is in the z-direction, we follow a simple matrix operation to obtain

$$\begin{aligned} m \frac{dv_x}{dt} &= q\mathbf{B}v \hat{y}, \\ m \frac{dv_y}{dt} &= -q\mathbf{B}v \hat{x}, \\ m \frac{dv_z}{dt} &= 0, \end{aligned} \quad (1.4)$$

finding that the acceleration parallel to the magnetic field is zero. Charged entities such as electrons and ions thus move in a circular motion around a magnetic field line of strength B . To find the acceleration we take the second derivative of the remaining components as follows

$$\begin{aligned} \frac{d^2v_x}{dt^2} &= -\omega_g^2 v \hat{x}, \\ \frac{d^2v_y}{dt^2} &= -\omega_g^2 v \hat{y}, \end{aligned} \quad (1.5)$$

where we define the gyrofrequency in radians per second as

$$\omega_g = \frac{q\mathbf{B}}{m}. \quad (1.6)$$

A charged particle will orbit the guiding center at a radius of gyration given by

$$r_g = \frac{\mathbf{v}_\perp}{|\omega_g|} = \frac{m\mathbf{v}_\perp}{|q|\mathbf{B}}, \quad (1.7)$$

where $\mathbf{v}_\perp = \sqrt{(\mathbf{v}_x^2 + \mathbf{v}_y^2)}$ represents a constant velocity perpendicular to the magnetic field (Baumjohann and Treumann, 1996). Increasing the mass or velocity of the particle will lead to a larger gyroradius, whilst an increase in magnetic field strength will act to confine the particle to a smaller radius. For a magnetic field upwards through this page an electron will orbit counter-clockwise, whilst a proton will orbit clockwise. If a charged particle has an initial velocity parallel to the magnetic field then its path will appear helical. The angle of this trajectory is given by the pitch angle

$$\alpha = \tan^{-1} \left(\frac{\mathbf{v}_\perp}{\mathbf{v}_\parallel} \right), \quad (1.8)$$

which is a useful unit for illustrating the ratio between perpendicular and parallel velocities. The first adiabatic invariant, or magnetic moment, is given by

$$\mu = \frac{m\mathbf{v}_\perp^2}{2\mathbf{B}}, \quad (1.9)$$

and is related to the pitch angle by

$$\mu = \frac{m\mathbf{v}^2 \sin^2 \alpha}{2\mathbf{B}}. \quad (1.10)$$

A consequence of the fact that the magnetic moment is invariant is that only the pitch angle may change (Baumjohann and Treumann, 1996), this was also clear earlier when we stated that a magnetic field alone cannot cause a change in a particle's speed, only its direction. The pitch angle will increase as magnetic

field strength increases. In the context of a magnetic field around a planet, a particle bound to a field line will experience a higher magnetic field strength as it approaches the planet, and as such the perpendicular component of velocity will increase - hence the pitch angle will also increase. If the field strength becomes sufficiently strong, the particle will attain a pitch angle of 90° and be reflected back down the field line. This can then happen on the other side of the field line leading to a back-and-forth motion which renders the particle trapped in the system; this phenomenon is known as magnetic mirroring. The field strength required to mirror a particle is

$$\mathbf{B}_m = \frac{\mathbf{B}}{\sin^2 \alpha}. \quad (1.11)$$

where the right hand terms describe the field strength \mathbf{B} , and pitch angle α of the particle at a given point along a field line. If a particle has a high parallel to perpendicular velocity ratio then the pitch angle will be small and so the field strength, \mathbf{B}_m , required to mirror the particle has to be larger. In the planetary case, particles with sufficiently low pitch angles are able to escape the magnetic mirror and the range of pitch angles that result in this escape is referred to as the loss cone. Collisions between the atmospheric atoms and molecules and these incident charged particles result in auroral emissions (Kivelson and Russell, 1995). In a steady state with no other external forcing, the loss cone would quickly empty, so in order to maintain a continual escape of particles, the first adiabatic invariant must be violated. Pitch angle scattering is the process by which a particle gyrating along a field line is disturbed enough that its trajectory changes in a random way, this can result in the pitch angle becoming small enough so that it may enter the loss cone (Roberts, 1969). Although the process by which scattering occurs is not fully understood, these so-called ‘random walks’ in trajectory are generally thought to be the result of Coulomb- and wave-particle-interactions. Such interactions must act to change the kinetic energy of particles, thus violating the first

adiabatic invariant (Kivelson and Russell, 1995; Roberts, 1969; MacDonald and Walt, 1961).

1.2.2 Auroral ionospheric currents

The upper atmospheres of Saturn and Jupiter are weakly ionized media dominated by neutrals. The plasma component is formed through the photoionization of this neutral atmosphere (primarily hydrogen) by solar extreme ultraviolet (EUV) radiation and is known as the ionosphere (Baumjohann and Treumann, 1996). A secondary ionization mechanism is the precipitation of charged particles along magnetic field lines, which is far larger at auroral latitudes and leads to electron-impact ionization. If we add a collisional term to Equation 1.2 we obtain

$$m \frac{d\mathbf{v}}{dt} = q(\mathbf{E} + \mathbf{v} \times \mathbf{B}) - m\nu_c(\mathbf{v} - \mathbf{u}) \quad (1.12)$$

where ν_c is the ion-neutral collision frequency, \mathbf{v} is particle velocity and \mathbf{u} is the velocity of the impacted particle, and we see that collisions act to change the momentum in the system. The following equations will detail the behaviour of the plasma in the absence of a magnetic field ($\mathbf{B} = 0$). Simplifying further, we let m be the electron mass m_e and \mathbf{v} the electron velocity \mathbf{v}_e , and make the impacted particles stationary ($\mathbf{u} = 0$), as follows:

$$\mathbf{E} = -\frac{m_e\nu_c}{e}\mathbf{v}_e. \quad (1.13)$$

The current density is given by

$$\mathbf{j} = -en_e\mathbf{v}_e, \quad (1.14)$$

so we obtain

$$\mathbf{E} = -\frac{m\nu_c}{e}\mathbf{v}_e\left(-\frac{j}{en_e}\right), \quad (1.15)$$

such that

$$\mathbf{E} = \frac{m\nu_c}{e^2n_e}j. \quad (1.16)$$

We can substitute \mathbf{E} given the relation $\mathbf{J} = \sigma\mathbf{E}$ to find the plasma resistivity

$$\eta = \frac{m_e\nu_c}{n_e e^2} \quad (1.17)$$

and knowing that resistivity is simply the inverse of conductivity we arrive at the plasma conductivity

$$\sigma_0 = \frac{n_e e^2}{m_e \nu_c} \quad (1.18)$$

By manipulating the equations further we find the following conductivities that result in three electrical currents which flow in the polar ionosphere:

- Parallel conductivity, σ_{\parallel} , controls the magnetic field-aligned current which itself is the result of a field-aligned electric field, \mathbf{E}_{\parallel} .

$$\sigma_{\parallel} = \frac{n_e e^2}{m_e \nu_c} = \sigma_0, \quad (1.19)$$

- Pedersen conductivity, σ_P , is the conductivity pertaining to the perpendicular electric field \mathbf{E}_{\perp} . This governs the Pedersen current.

$$\sigma_P = \frac{\nu_c^2}{\nu_c^2 + \omega_g^2} \sigma_0, \quad (1.20)$$

- Hall conductivity, σ_H , is perpendicular to the electric and magnetic field in

the $-\mathbf{E} \times \mathbf{B}$ direction (Baumjohann and Treumann, 1996).

$$\sigma_H = -\frac{\omega_g \nu_c}{\nu_c^2 + \omega_g^2} \sigma_0, \quad (1.21)$$

On combining these contributions we obtain the current density

$$\mathbf{j} = \sigma_{\parallel} \mathbf{E}_{\parallel} + \sigma_P \mathbf{E}_{\perp} - \frac{\sigma_H (\mathbf{E}_{\perp} \times \mathbf{B})}{B}. \quad (1.22)$$

The charged particles within an ionosphere feel the electrical and magnetic forces that permeate it, thus this is where the local space environment interacts with the planet most fervently. At the heart of this interaction are collisions driven by magnetospheric forces (in the planetary rest frame); the ratio between the gyrofrequency, ω_g and collision frequency, ν_c dictates the relative strengths of the Pedersen and Hall ionospheric conductivities, hence the respective currents. In Figure 1.1 we show the gyro- to collision-frequency ratio ω_g/ν_c , which can be thought of as how many ‘orbits’ a particle can have about the guiding center before a collision is likely to take place. We find that where $\omega_g \approx \nu_c$ the Pedersen conductivity is at a maximum. This maximum is shared with the Hall conductivity. In a denser environment the Hall conductivity dominates whilst the Pedersen element drops to zero. The parallel conductivity is dependant on collisions in the z-plane in which the field-aligned current exists.

We now consider the Hall versus Pedersen conductivity on a molecular level within the ionosphere, as shown in Figure 1.2. The $\omega_g \approx \nu_c$ case illustrates that the electrons travel in the $-\mathbf{E}$ direction whilst also attempting to orbit a magnetic field line. However, the electron can barely perform a single gyration about the magnetic field before colliding with (mostly) neutral particles (neutrals not shown), and the resultant particle trajectory becomes Brownian, i.e. a random-walk in the direction indicated. This Pedersen current is not a straight vertical

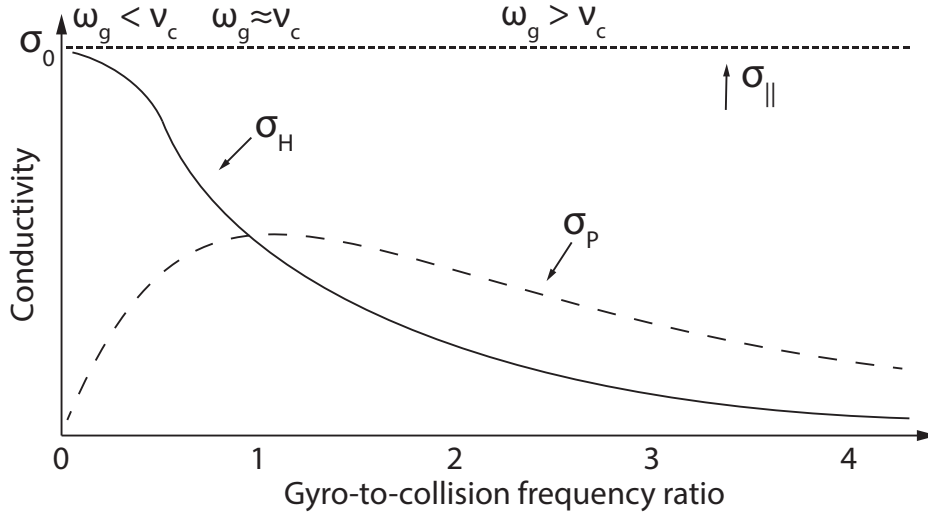


Figure 1.1: Gyrofrequency to collision frequency ratio - Here we show the behaviour of the three dominant ionospheric currents in terms of their conductivity described in the main text. This is a modified version of Figure 4.4 from Baumjohann and Treumann (1996).

line because of the contribution by the Hall current perpendicular to it, and the ions, p , are shown to be stationary relative to the electrons because of their ~ 2000 times higher mass. In the $\omega_g < \nu_c$ case the collisions become so frequent that electrons are moving primarily in the $-\mathbf{E} \times \mathbf{B}$ direction. Here the Hall current dominates whilst the Pedersen current falls to zero (see also Figure 1.1). If we assume ω_g is constant, the Pedersen current therefore acts at higher altitudes where collisions are less frequent, whilst the Hall current becomes dominant at lower altitudes. The case not pictured is that of $\omega_g > \nu_c$, at this point the plasma becomes increasingly collisionless. Recalling Equation 1.14 we find that \mathbf{E} is proportional to the collision frequency ν_c . Taking the extreme of a collisionless plasma one finds that the Lorentz forces on charged particles confines them to the field lines in circular orbits; this is the case for particles at very high altitudes that are effectively outside of the planet in a vacuum.

As we shall see in Chapter 4, the Pedersen conductivity and current is very important in determining the Joule heating rate in the ionosphere. Here, however,

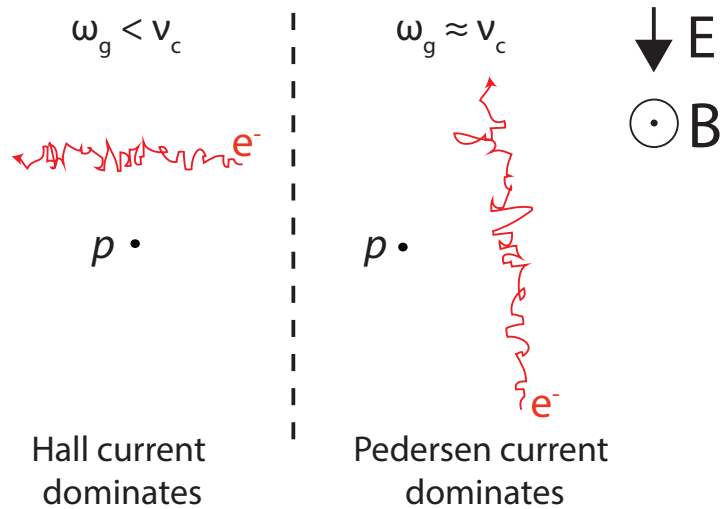


Figure 1.2: Molecular behaviour of ionospheric currents - Here we show the motion of electrons (e^-) and ions (p) in a collisional plasma environment. The plasma is permeated by a magnetic field, \mathbf{B} , coming out of the page and an electric field \mathbf{E} in the direction indicated by the black arrow. The two cases described in the main text are shown for differing ratios of ω_g and ν_c and these also correspond to the leftmost two cases in Figure 1.1.

we simply show that the power P dissipated to heat is in general

$$P = I^2 R. \quad (1.23)$$

where I is the current and R is the resistance: so the stronger the Pedersen current the more heat is released.

1.3 Light and spectroscopy

The conclusions of this thesis are drawn from the direct measurement of electromagnetic radiation (light). It is thus useful now to define the source of this light on an atomic and molecular level.

1.3.1 Atomic spectra

Atomic spectroscopy is the branch of physics concerned with the study of light emanating from, or being absorbed by, atoms. Although we do not directly study atomic spectra in this thesis, the following provides a framework for understanding molecular spectroscopy and many other topics. In the Bohr model of an atom, a nucleus containing protons (and often neutrons) is surrounded by ‘shells’ of electrons which orbit it. In the simplest case, in the hydrogen atom, a single electron is permitted to exist in a variety of quantised energy levels corresponding its electronic potential energy. The greater the potential energy, the farther away from the nucleus the electron is. An electron can receive energy by absorbing a photon, elevating it to a higher energy state, or lose energy by emitting a photon, as shown in Figure 1.3.

The potential energy in each energy level for hydrogen is given by

$$E_n = -\frac{13.6}{n^2} \text{ eV} \quad (1.24)$$

where n is the principle quantum number, -13.6 eV is the potential energy of the ground state ($n = 1$), n has quantised values of $n = 1, 2, 3, \dots, \infty$. We can also equate the energy of a photon to the energy within an atom by the Planck relation below

$$E = h\nu = \frac{hc}{\lambda} \quad (1.25)$$

where ν is the frequency in units of Hertz (Hz), c is the speed of light ($3 \times 10^8 \text{ ms}^{-1}$), λ is the wavelength of light and h is Planck’s constant (6.626×10^{-34}

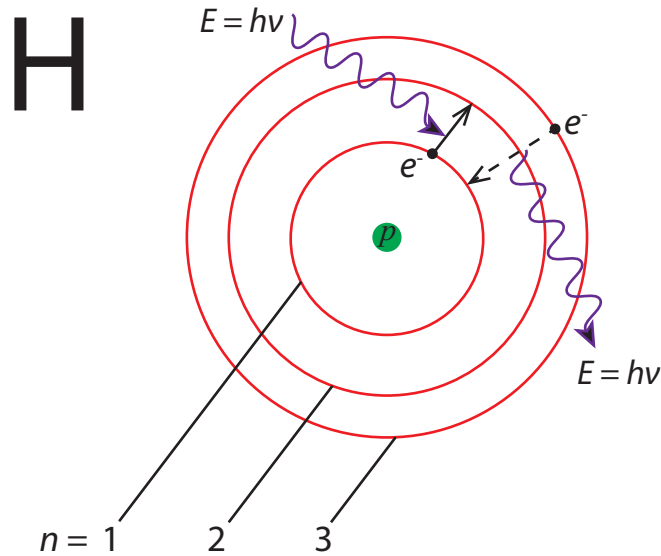


Figure 1.3: Bohr model for hydrogen - This simple schematic shows the basic structure of the atom with a proton p orbited by an electron e . The solid and dashed arrows indicate two of the many possible scenarios in which energy may be transmitted to and from the atom. The principal quantum number explained in the main text.

Js).

The above equations tell us that absorption can only occur for certain discrete quanta of energy, and as such depends on the frequency (wavelength) of light absorbed. In Figure 1.4 a number of energy levels are shown in a diagram for hydrogen. By calculating the difference in energy between two states, we can find the frequency and wavelength of the emitted light. The difference between energy levels is given by

$$\Delta E = E_f - E_i = h\nu \quad (1.26)$$

where E_i and E_f are the initial and final energy states. For example, in an absorption that leads to an increase in energy level from the $n = 1$ (ground state) to $n = \infty$, the difference between energy levels is 13.6 eV - this is the ionisation energy of hydrogen and is the energy required to remove an electron from a hydrogen atom entirely.

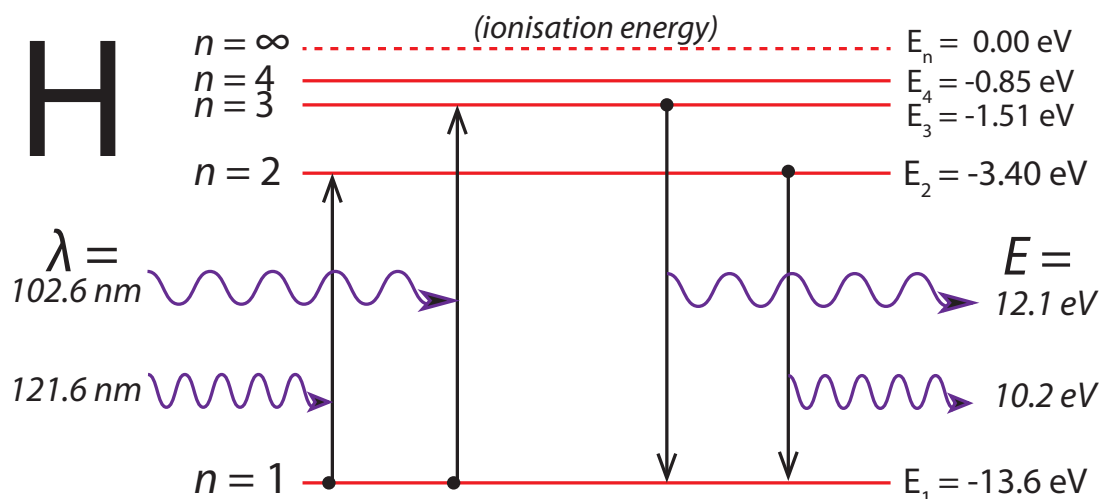


Figure 1.4: Energy level diagram - An energy level diagram for hydrogen showing the relationships discussed in the main text. Energy level $n = 1$ is the lowest state an electron can be in, the ground state; all subsequent levels or excited states are associated with values $n > 1$.

1.3.2 Molecular spectroscopy

Typically, atomic electronic transitions are highly energetic and are associated with UV or optical wavelengths. Molecules also have electronic transitions, but in addition they have quantised ‘vibrational’ and ‘rotational’ energies and these correspond to infrared (IR) and microwave wavelengths, respectively, which we will now explain in detail.

A positively charged nucleus of one atom is attracted to the negatively charged electron(s) of another atom, whilst simultaneously the nuclei of both repel. A molecule is formed when these two competing electrostatic forces remain balanced between two or more atoms. The atoms in the molecule will remain at a fixed distance apart in this equilibrium state, at some mean equilibrium distance. Molecular vibrations are essentially the periodic increase and decrease of the inter-nuclear distance (the bond length) between the individual atoms from an equilibrium state (Banwell, 1994). This periodicity is akin to standing waves on a string and therefore has a series of quantised modes or vibrational energy

levels. It is also analogous to the restoring force in Hooke's law given by

$$\mathbf{F} = -kx \quad (1.27)$$

where k is the stiffness constant of a spring and x is the distance between ends of the spring; in this case the restoring force is the electrostatic attraction between the positive and negative elements within the atoms. If there is an asymmetry in the distribution of charge within a molecule, it is said to have a dipole moment and can interact with electromagnetic waves. The amplitude of vibration in the molecule will increase if a photon of the same frequency hits it. Similarly, a molecule can emit a photon of light at its own frequency of vibration. A molecule undergoing symmetric stretching has no change in dipole moment, therefore there is no interaction with light; this type of vibration is termed IR-inactive. If there is a dipole moment in the molecule as a result of asymmetric stretches, then the molecule is said to be IR-active, and can interact with photons (of IR wavelengths); in the following section we will use H_3^+ as an example of these stretches.

Figure 1.5 shows schematically how vibrational emissions of a molecule arise in the context of the electron transitions previously described, indicating the relevant spectroscopic notations. The fundamental vibrational transition is defined as one involving the ground state '0' and the first vibrational level ' $\nu = 1$ ', denoted $\nu \leftarrow 0$ for a transition resulting in a decrease in potential energy. As the transition energies become larger and larger, an energy called the dissociation energy (DE) is attained, at this point the molecule dissociates - i.e. the molecular bond is broken. Overtones are transitions between all other vibrational energy levels to the ground state i.e. $n\nu \leftarrow 0$, where $n = 1, 2, 3 \dots \text{DE}$. Finally, hot bands are changes in vibrational levels not involving the ground state 0, e.g. $n\nu \leftarrow m\nu$ where $m = 0, n-1, n-2 \dots \text{DE}$. Each transition from one state to a lower one results in the release of a photon of energy exactly that of the energy difference between states.

The energy required to split the molecule is called the disassociation energy; in the reference frame of the center of mass of the two atoms in Figure 1.5, if the outwards force on each atom exceeds the electrostatic restoring force then the bond will break.

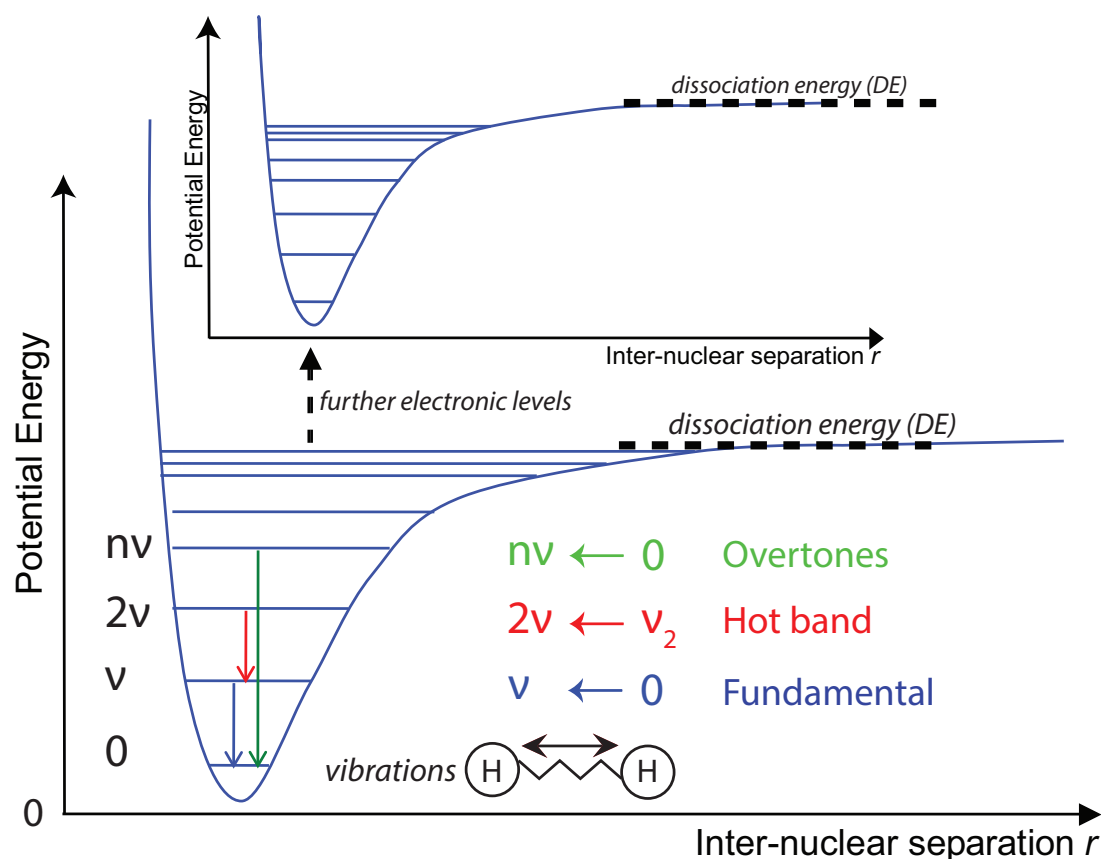


Figure 1.5: Vibrational energy level diagram - This figure shows transitions from higher to lower vibrational levels including the notation that goes with each transition. The x- and y-axes arbitrarily show the inter-nuclear distances between molecules and the potential energy at each level. As we increase the potential energy we see that the molecule enters new stable (quantised) states in which the molecule has a large inter-nuclear distance. This diagram represents the ground electronic state of a molecule, with a dashed arrow to show the first excited electronic state above. A simple line drawing containing two hydrogen (H) atoms shows the spring-like behaviour of a vibrating molecule.

The electric field component of light exerts a force on the charges of atoms within a molecule. If there is an uneven charge distribution, this results in a torque, and the molecule will rotate - a molecule like this is said to be polar (or dipolar) and will have a rotational spectrum (typically in the microwave region). Molecules which exhibit symmetry have no allowed rotational spectrum, although

there are exceptions in which rotation and vibration couple to allow ro-vibrational transitions to take place, for example in H_3^+ (Tennyson and Miller, 2001). A rotational manifold of allowed energy states exists within each vibrational level as shown in Figure 1.6, and changes in both are said to be ro-vibrational transitions.

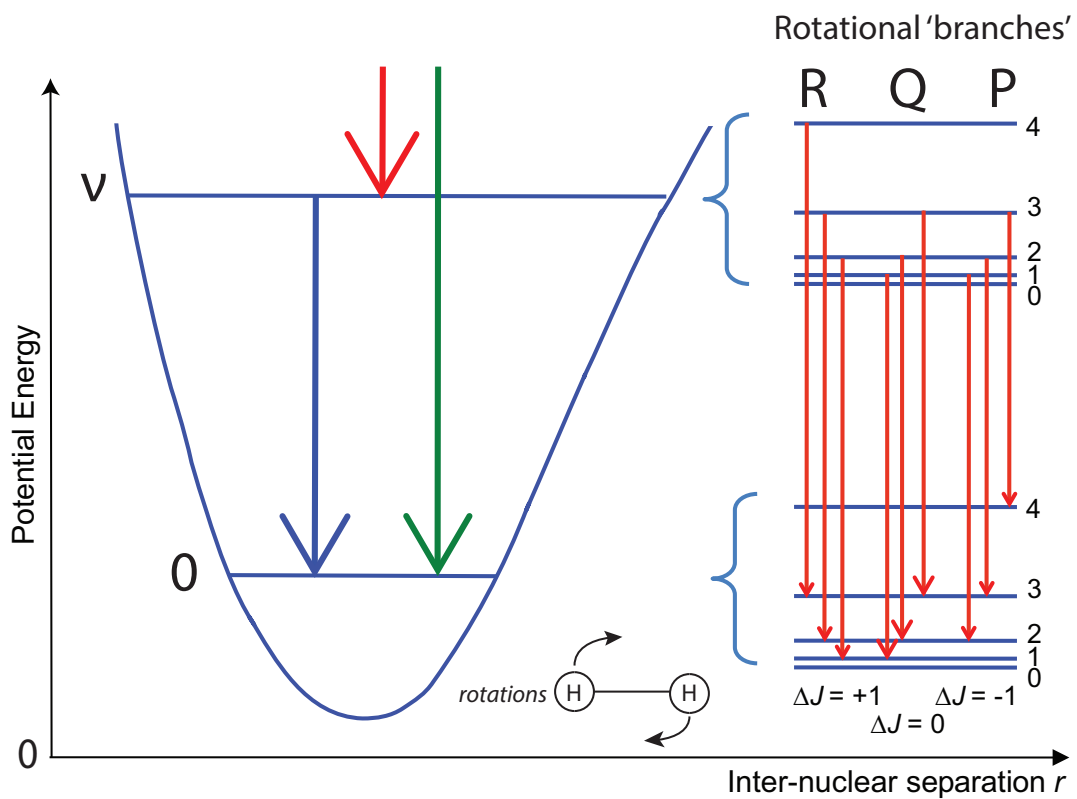


Figure 1.6: Rotational energy level diagram - This schematic shows a zoomed-in view of Figure 1.5, the axes are the same. The rotational manifolds are shown to the right by each vibrational level. The allowed rotational transitions are $\Delta J = -1, 0, +1$ and are known as the R-branch, Q-branch and P-branch, respectively - this is also the order of the amount of energy released in by each transition from lower to higher energies. A simple picture of two hydrogen atoms which have no rotational spectrum is shown for simplicity to show rotational motion; see Figure 1.9 for the ro-vibrational case for H_3^+ .

All electronic, vibrational or rotational transition systems from higher to lower energy levels result in photon emission. The photon is emitted at a particular wavelength and we call this a discrete spectral emission line. This differs from

broad continuum emission which is associated with emission across a range of wavelengths. The probability of a particle having a particular energy E is given by the Maxwell-Boltzmann distribution

$$f(E) = Ae^{-\frac{E}{kT}} \quad (1.28)$$

where A is a normalisation constant, k is Boltzmann's constant and T is the temperature of the particle. According to this formula, molecules are more likely to occupy lower energies, but with increasing temperature it is more probable for a particle to be in a more energetic state. Therefore the spectral transitions in all of the above will predominantly occur between the ground and first excited state involving fundamental transition lines. Increasing the temperature however, yields an increase in the emission via overtone and hot band transitions relative to the fundamental (Banwell, 1994).

Thermal radiation is the emission of electromagnetic radiation from a hot body. This radiation is produced in an environment in which individual atoms and molecules collide into each other frequently. These collisions add and remove energy from the discrete electronic, vibrational and rotational spectral lines, causing them to emit over a wide range of wavelengths simultaneously, and leading to a broad, continuous spectrum. Thermal radiation is organised in the form of a 'black-body' radiation curve - with the term black-body referring to an object which absorbs all incident radiation. This curve obeys Planck's radiation law

$$I_{\lambda}(T) = \frac{2hc^2}{\lambda^5} \frac{1}{e^{\frac{hc}{\lambda kT}} - 1} \quad (1.29)$$

where intensity I as a function of wavelength depends upon the absolute temperature T , λ is wavelength in nanometres, h is Planck's constant, c is the speed of light and k is Boltzmann's constant. This equation tells us that the wavelength of peak intensity corresponds directly to a specific temperature and black-body profile as shown in Figure 1.7.

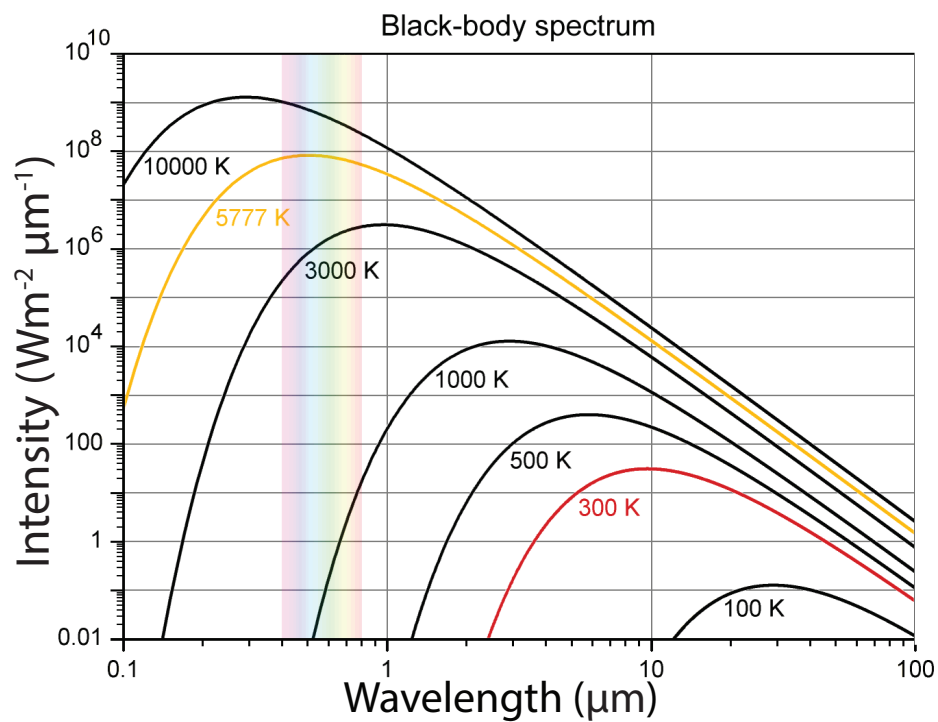


Figure 1.7: Black-body radiation curve - Here we show intensity as a function of wavelength in microns for perfectly emitting (ideal) black-body emitting object. Multiple curves are shown for different temperatures. The visible spectrum is superimposed on the diagram. The region of interest in the work herein is largely 3 - 5 microns.

For simplicity, in place of producing an entire curve using Planck's law, we may also use Wien's law. Wien's law states that the wavelength at which the peak intensity occurs corresponds to a temperature of

$$T = \frac{b}{\lambda_{peak}} \quad (1.30)$$

where b is a constant equal to 2,897,768.5 nmK. For example, $\lambda = 600$ nm corresponds to a temperature $T = 4830$ K.

1.4 The H_3^+ molecule

The infrared spectrum of the simplest polyatomic molecule, H_3^+ , was first seen in a laboratory by Oka (1980). It was subsequently detected in Jupiter's ionosphere in 1989 (Drossart et al., 1989a), the Uranian ionosphere in 1992 (Trafton et al., 1992) and Saturn's in 1993 (Geballe et al., 1993). Since then, it has been profoundly useful as an in-situ probe of the conditions in those ionospheres, particularly in the auroral regions. The following subsections describe the properties of H_3^+ on a molecular level, discussing its life cycle and corresponding information-rich emissions.

1.4.1 Properties, formation and destruction

H_3^+ is composed of three protons arranged in an equilateral triangle configuration, as shown in Figure 1.8, surrounded by two electrons in a molecular orbital. The molecule is thus a three-centre, two-electron (covalent) bond which is electron deficient.

H_3^+ is created by the extremely efficient ion-neutral reaction



which has an exothermicity (or, energy product) of 1.7 eV (Oka, 2006) which

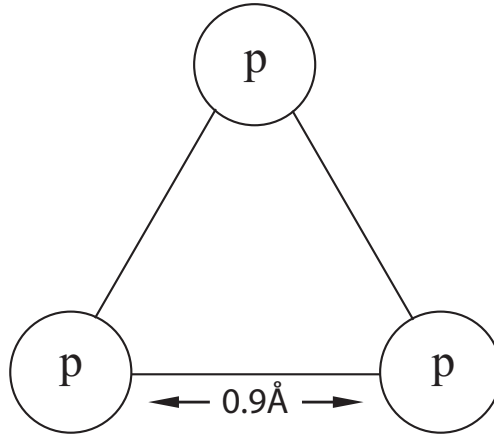


Figure 1.8: The H_3^+ molecule - A simple representation of H_3^+ , with three protons (p) arranged in an equilateral triangle. The bond lengths are 0.9 Å (0.09 nm).

may be distributed to the total energy of the molecule (rotation/vibration). After production, H_3^+ is a meta-stable ion; in the Saturnian ionosphere, for example, it has a lifetime of ~ 500 seconds at 1100 km altitude (Melin et al., 2011), giving it time to become thermalized to the other constituents therein. The proton affinity of H_2 is 4.4 eV, lower than almost all atoms and molecules, only helium (He) (e.g. 1.85 eV (Jolly, 1991)), nitrogen (N) and molecular oxygen (O_2) are lower; this is exacerbated with the addition of a further proton in the H_3^+ molecule. It is, therefore, an efficient universal proton donor (a strong acid) to most molecules with mass number above He (Oka, 2006, 2012). So, although stable, H_3^+ is highly reactive when in contact with other species; in particular, it is easily destroyed by the ion-neutral charge-exchange reaction



where X is an atom or molecule with proton affinity greater than 4.4 eV, such as methane (CH_4) which has a proton affinity of 5.72 eV (Jolly, 1991). We expand greatly on the various other pathways of H_3^+ creation and destruction in Subsection 3.4.2.

1.4.2 Local thermodynamic equilibrium

H_3^+ is generally considered to be in local thermodynamic equilibrium (LTE) or at least quasi-LTE (Miller et al., 1990a; Moore et al., 2008). A volume of molecules is said to be in LTE if it has sufficient collisional frequency, such that the temperature distribution of the particles approaches a Maxwellian distribution (Melin, 2006). In other words, the temperature of individual molecules is communicated throughout the volume by collisions; this is what we mean when we say the molecule is thermalized to the environment in which it is situated. A departure from this assumption occurs then if the collisions are adequately reduced; thus LTE breaks down increasingly with decreasing density, and this has been shown to happen in the Jovian ionosphere by Melin et al. (2005). The work herein observes column densities integrated over all altitudes as we shall see, hence includes LTE, q-LTE and non-LTE regimes. Intuitively however, the majority of the emitting material must be associated with the more densely populated lower altitudes; indeed modelling work on Saturn by Mueller-Wodarg et al. (2012) confirms that the H_3^+ temperature is within ~ 50 K of that of the surrounding ionosphere.

1.4.3 Spectroscopy

Here we provide an overview of the main spectral lines used in this thesis, in terms of how they arise and how we are able to observe them using ground-based telescopes on Earth. We will discuss in detail how we use these lines to derive temperatures in Section 2.5. H_3^+ is a non-linear molecule and in the Cartesian coordinate system it can perform translational motions in the x, y and z directions yielding 3 degrees of freedom. It is also able to rotate along each bond giving it a further 3 rotational degrees of freedom. Finally, the protons can individually move towards and away from each other in three ways, i.e. 'vibrate', yielding a further 3 possible motions. In total a polyatomic ($N > 2$, where N is the number of molecules) molecule like H_3^+ thus has $3N$ degrees of freedom (Banwell, 1994).

In Figure 1.9 we see the 3 vibrational degrees as the IR-inactive symmetric ν_1 and IR-active anti-symmetric ν_2 vibrational modes. The latter modes are responsible for the emission lines we observe, since they result in a net change in the dipole moment of the molecule.

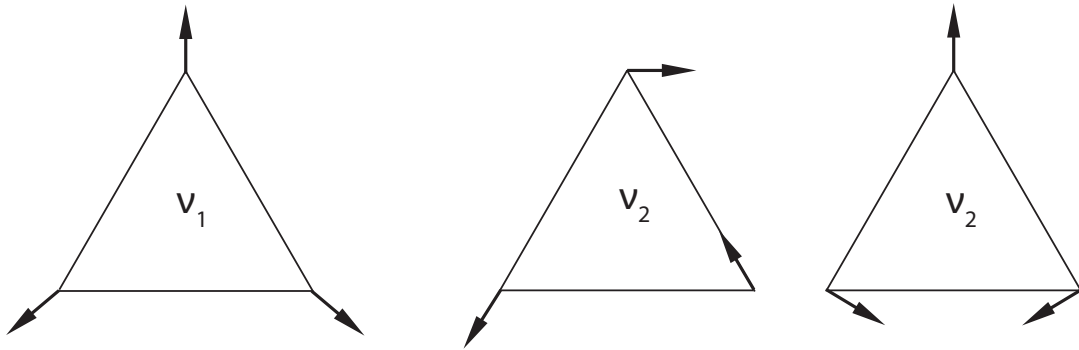


Figure 1.9: Vibrational modes of H_3^+ - The normal modes of H_3^+ : left is the symmetric ‘breathing mode’ ν_1 and the middle and right are the anti-symmetric modes, ν_2 .

The spectrum of H_3^+ is well modelled (Neale et al., 1996b), with discrete spectral emission lines ranging in wavelength from the mid-IR at $16 \mu\text{m}$ up until the visible at $\sim 0.6 \mu\text{m}$ (600 nm) (Oka, 2012) - we show most of this range in Figure 1.10 along with the associated vibrational transitions noted beside them.

Remembering the description of ro-vibrational transitions in Section 1.3, the resulting spectrum of H_3^+ is shown in Figure 1.11 as a ‘stick diagram’. In this plot are the R-branch, Q-branch and P-branches which correspond to rotational transitions of $\Delta J = -1$, $\Delta J = 0$, $\Delta J = +1$, respectively. Note that these rotational transitions are coupled to vibrational transitions, mostly the fundamental $\nu_2 \leftarrow 0$ in this wavelength range. These lines are shown as a function of wavelength, and so energy is decreasing from left to right; this is intuitive if we consider that for a given vibrational transition such as $\nu_2 \leftarrow 0$, a change in rotational energy of $\Delta J = +1$ represents a larger change in energy than $\Delta J = -1$ (this can be graphically seen in Figure 1.6).

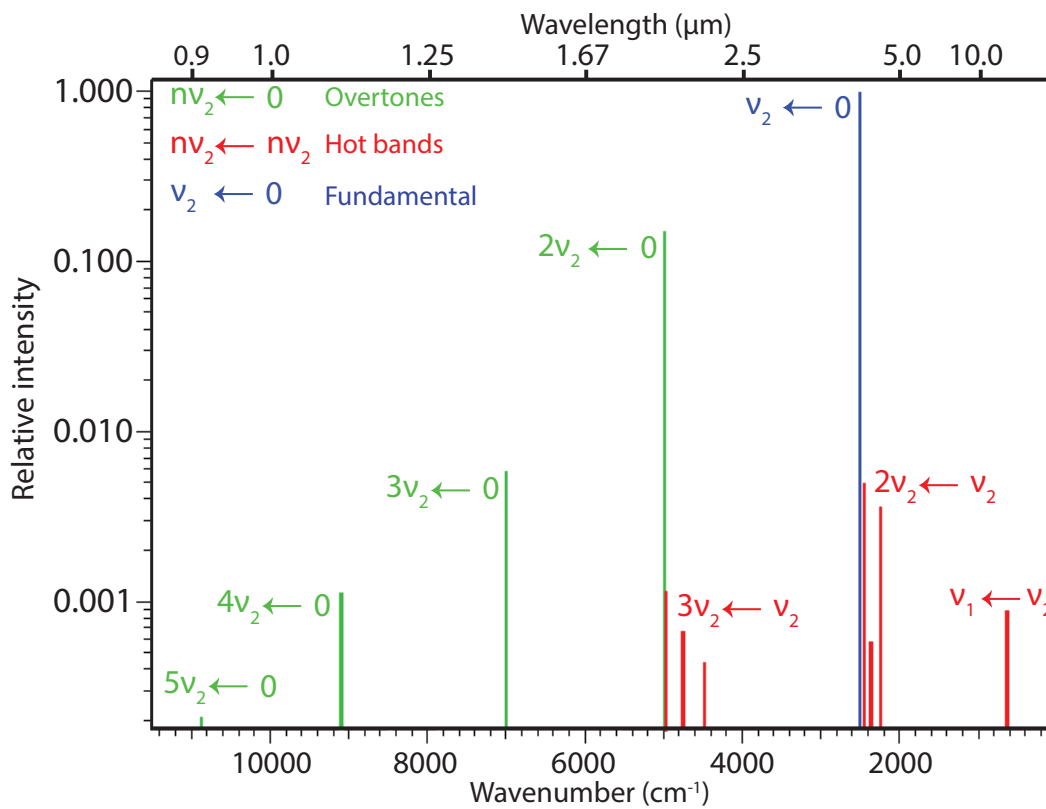


Figure 1.10: Modelled spectrum of H_3^+ - This stick diagram shows the intensity of discrete spectral lines of H_3^+ emission as a function of wavelength. Spectral lines are shown as the red vertical 'sticks' and a number of these have the corresponding spectroscopic notation written to their left.

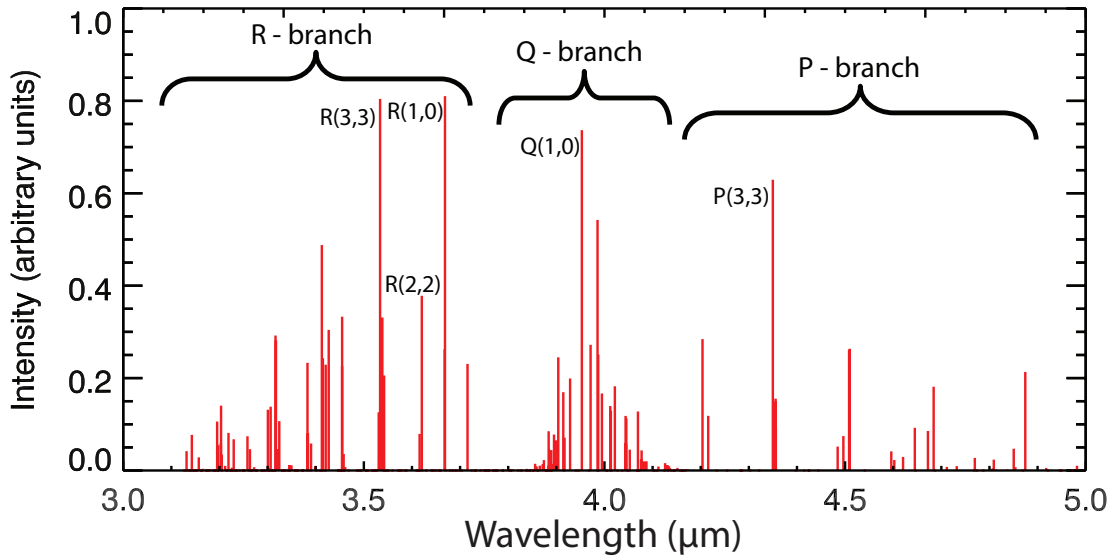


Figure 1.11: Modelled spectrum of H_3^+ zoomed in between 3 - 5 micrometres - This stick diagram shows the intensity of discrete spectral lines of H_3^+ emission as a function of wavelength. Spectral lines are shown as the red vertical ‘sticks’ and a number of these have the corresponding spectroscopic notation written to their left. The Q, R and P branches of H_3^+ are labelled, the numbers in brackets such as Q(1,0) correspond to Q(J,K), where J is the rotational angular momentum and K is the rotational angular momentum along the spin axis. The lines depicted here result from different transitions, for example the Q(1,0) line is the $\nu_2 \leftarrow 0$ transition. A temperature of 550 K was used to generate this model H_3^+ spectrum.

With the H_3^+ molecule modelled, we now consider the wavelength ranges in which we can observe it using ground-based telescopes. A number of molecules within the atmosphere are responsible for absorbing the light we would otherwise receive on Earth, water and carbon dioxide are particularly effective at this in wavelengths we are interested in (e.g. those in Figure 1.11). However, a number of so-called ‘atmospheric windows’ exist in which molecules in the Earth’s atmosphere allow certain wavelength ranges of light through with less absorption. The transmission of light through the Earth’s atmosphere as a function of wavelength is shown in Figure 1.12. In this figure the L-band window conveniently lies directly over the highest intensity H_3^+ spectral lines of the Q- and R-branches. The ‘L prime’ band (denoted L’-band) is within the L window and is a wavelength range associated with the least attenuation by the atmosphere, making it the ideal

range in which to observe H_3^+ at a high signal to noise (S/N) ratio; in addition, the CH_4 content in gas giant thermospheres acts primarily to absorb sunlight in the L' band rather than reflect it as we shall see (e.g. Subsection 3.2.1), and so it is this band we observe in this thesis. Note that ‘noise’ is defined as emission not produced by H_3^+ transitions, which can be of either Earth, object (e.g. Saturn) or instrumental origin. The majority of the P-branch is heavily attenuated by CO_2 in the Earth’s atmosphere, for instance the strongest P-branch line, P(3,3) (labelled in Figure 1.11), is invisible to a typical ground-based observatory. The M-band is degraded slightly at Earth, but more significantly at Jupiter and Saturn. This is because their thermospheres range in temperature between ~ 500 - 1000 K, and so their black-body spectrum peaks in intensity in the M-band (e.g. Figure 1.7). Also, given that the spectral lines of H_3^+ are about one-third as intense here compared with those in the L' -band, we choose not to include this wavelength range in the studies in this thesis.

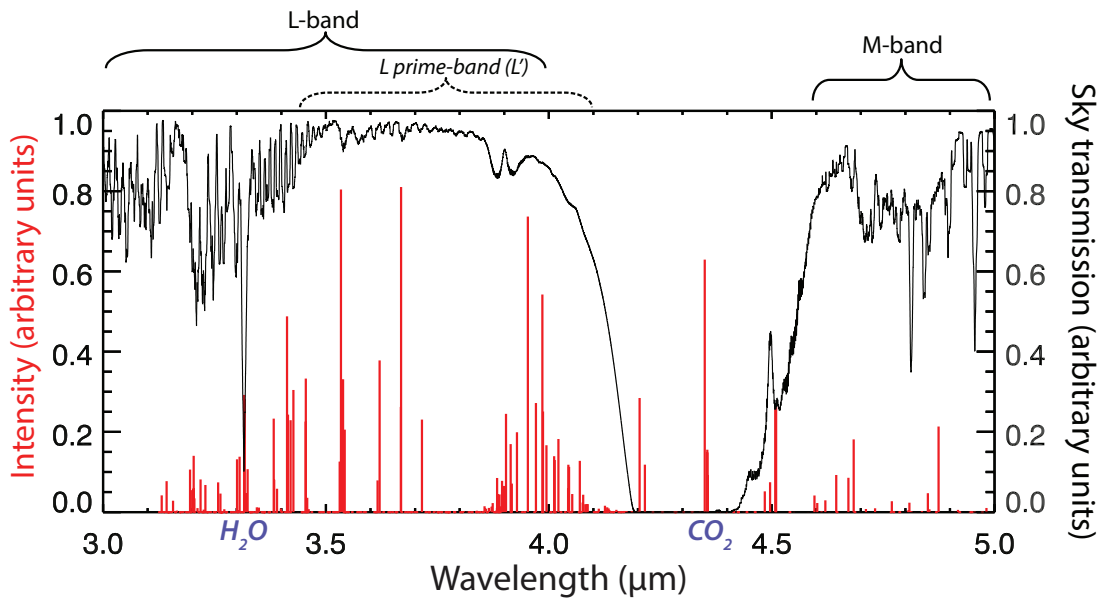


Figure 1.12: Modelled spectrum of H_3^+ and observed Earth's atmosphere - Here we show the same plot as in Figure 1.11 but this time with the normalised sky transmission overplotted. The black line shows the amount of light able to enter the Earth from space as a function of wavelength (normalised). The L-, L' and M-bands are spectral windows, notice that L' is the band associated with the least Earth-sky absorption. Water and carbon dioxide are labelled in lilac, and these are the molecules responsible for preventing sky transmission. The Earth transmission profile was obtained by the Gemini telescope based on Mauna Kea, Hawaii and is available on their website at <http://www.gemini.edu/sciops/telescopes-and-sites/observing-condition-constraints/ir-transmission-spectra>.

1.5 Saturn and Jupiter

It is useful to briefly compare the gas giants Saturn and Jupiter to other solar system planets for context, allowing us to appreciate in a broad way the planets we study herein. All the planets of our solar system are shown to scale in Figure 1.13. There have also been 1810 planets detected orbiting other stars as of July 16th, 2014 (see the exoplanet catalogue at <http://exoplanet.eu/catalog/>).

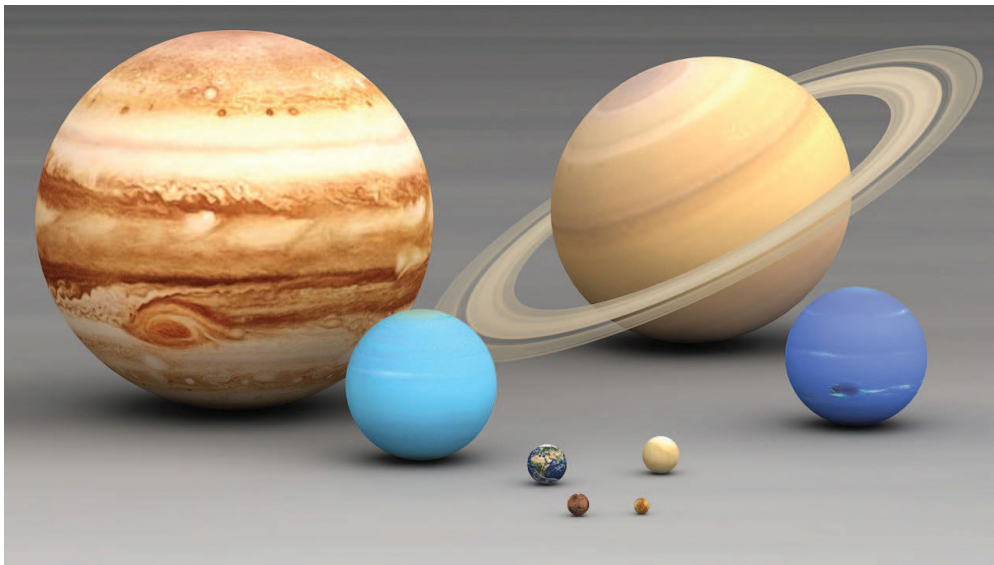


Figure 1.13: Solar system planets comparison - A 3D comparison of the 8 planets of the solar system. From top left to bottom right the planets Jupiter, Saturn, Uranus, Neptune, Earth, Venus, Mars and Mercury are shown to scale. Image credit to user Lsmppascal on Wikipedia at [commons.wikimedia.org/wiki](https://commons.wikimedia.org/wiki/File:Solar_System_Planets_Scaled).

The specific differences in bulk parameters and orbital characteristics between Earth, Saturn and Jupiter are shown in Table 1.1. Earth is also represented in the table to serve as a familiar comparison for the reader.

1.6 Saturn

Galileo Galilei, in 1609, was the first person to view Saturn in significant detail; he saw that it had rings on either side, although these were interpreted as moons at the time. Today, in addition to ground-based observations, we are afforded views such as that in Figure 1.14 by the Cassini spacecraft, which has been in-

Parameter	Earth	Saturn	Jupiter	S/E	J/E	J/S
Mass ($\times 10^{24}$ kg)	5.97	568.36	1898.3	95.20	317.97	3.34
Volume ^a ($\times 10^{12}$ km ³)	1.08	827.13	1431.3	765.86	1325.3	1.73
Radius ^a (Eqw., km)	6378	60268	71492	9.45	11.21	1.19
Radius ^a (Polar, km)	6357	54364	66854	8.55	10.52	1.23
Density ^a (kg m ⁻³)	5514	687	1326	0.12	0.24	1.93
Gravity ^a (ms ⁻²)	9.8	10.44	24.8	1.07	2.53	2.38
Black-body temp.(K)	254	81	110	0.32	0.43	1.36
Orbital period (days)	365	10759	4332	29.48	11.87	0.40
Semi-major axis (AU)	1	9.58	5.2	-	-	-
Day length (hours)	24	10.66	9.93	0.44	0.41	0.93
Axial tilt (deg)	23.44	26.73	3.13	1.14	0.13	0.12
Dipole tilt ^b (deg)	11	0.1	-9.6	-	-	-
Field strength ^c (μ T)	40	21.1	426.4	0.5	11	20
Mag. moment ($\times 10^{18}$ Tm ³)	0.0079	4.6	156	582	19770	34
Scale height (km)	8.5	62.6	25.5	-	-	-

a. These values are for the 1 bar pressure surface where 1 bar is 1×10^5 Pa.

b. The dipole tilt of the planets magnetosphere relative to the rotational axis.

c. Field strengths for Saturn and Jupiter are for 1-bar pressure surfaces at the equator.

Table 1.1: Comparison of the basic parameters of Earth, Saturn and Jupiter. Credit: NASA factsheets for Saturn and Jupiter, with magnetic field data from Burton et al. (2010) and Bagenal et al., Chapter 24. Pressure scale heights are from Table 9.4 of Bagenal et al., Chapter 9.

situ since 2004. In this thesis we hope to continue the legacy of observations of Saturn from the ground, specifically by focussing on the interactions with its local space environment via the H_3^+ molecular ion. H_3^+ was detected on Saturn for the first time in late 1992 (Geballe et al., 1993), and has since been a useful probe for examining the conditions in Saturn's upper atmosphere.

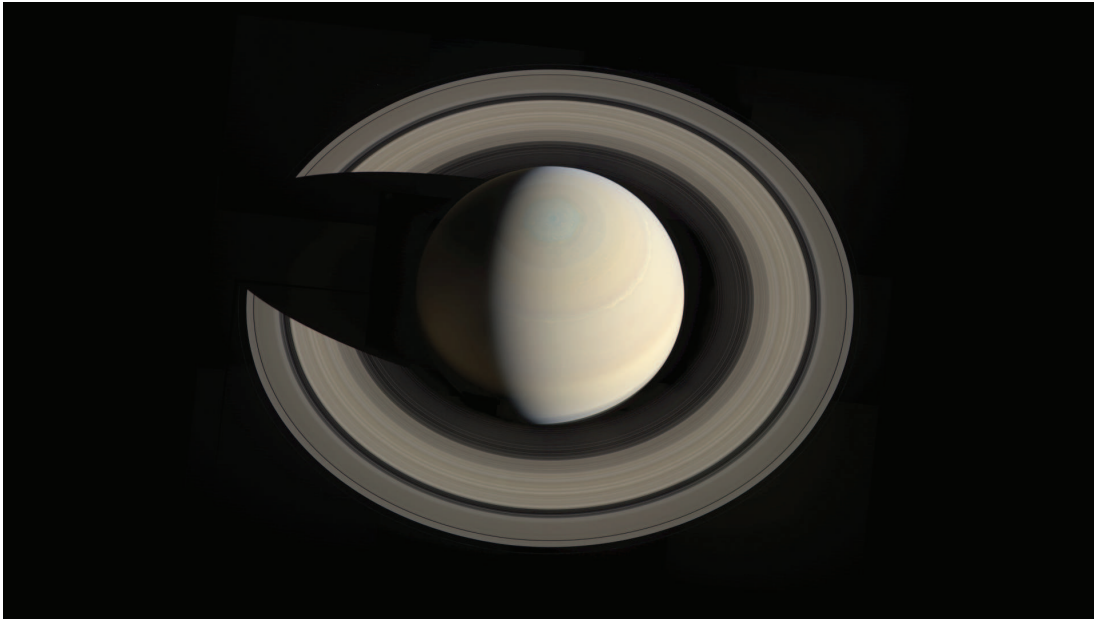


Figure 1.14: Saturn from Cassini - A rare top-down mosaic of 10 co-added images taken by the Cassini spacecraft on October 10th, 2013. Credit: NASA/JPL-Caltech/Space Science Institute/G. Ugarkovic

1.6.1 Ionosphere, thermosphere and motivations

The surface of Saturn is arbitrarily defined as the 1 bar level by analogy to Earth, with material above this pressure surface described as the Saturnian atmosphere. In terms of composition, Saturn's atmosphere is 96.3% molecular hydrogen (H_2) by volume and 3.25% helium (He). The remainder is mostly hydrogen, methane and ammonia (NH_3). Saturn's ionosphere is approximately located between 500 - 3000 km above the 1 bar level, and co-located with this is the thermosphere; the neutral component of the upper atmosphere (Moore et al., 2008; Mueller-Wodarg et al., 2012). As shown in the left panel of Figure 1.15, the dominant ions above

1000 km are H^+ and H_3^+ , whilst below this the hydrocarbon ions dominate in density. Along with their companion electrons, these ions maintain the ionosphere's quasi-neutrality. Recently, the peak altitude of H_3^+ density has been observed to occur at $1155(\pm 25)$ km altitude (Stallard et al., 2012a), therefore the ion's emission and temperature is considered to be representative of the ionosphere and thermosphere (assuming LTE, see Subsection 1.4.2) at this and adjacent altitudes (Melin et al., 2007). The modelled profile in the right panel of Figure 1.15 also illustrates this point, as the ionospheric temperature is almost constant at and above the altitudes H_3^+ occupies. Finally, the peak altitude of Pedersen conductivity - or Pedersen layer - is located at ~ 1000 km (Moore et al., 2009), and so clearly the H^+ , H_3^+ and hydrocarbon ions (with their companion electrons) in this region are responsible for the majority of the Pedersen current (outlined in Subsection 1.2.2).

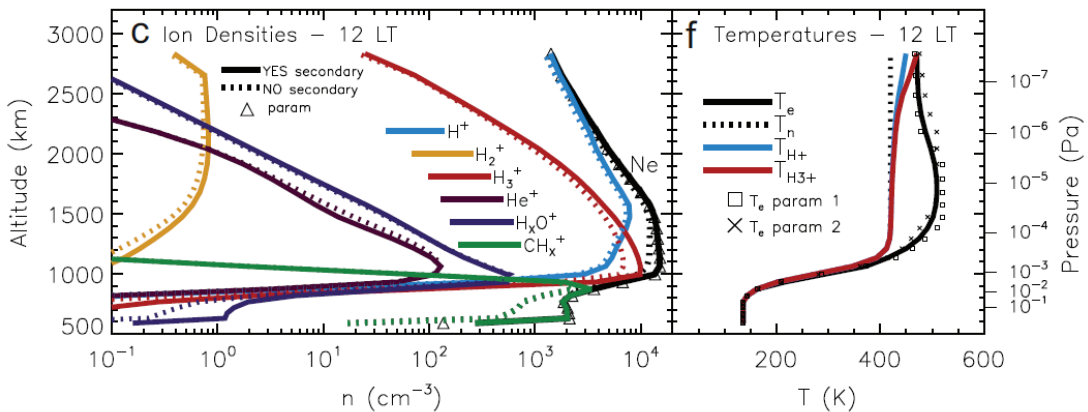


Figure 1.15: A model profile of Saturn's ionosphere - In the left panel, Saturn's plasma densities are simulated for local noon at 30°N latitude. The black line shows the electron density and therefore the total ion density. The blue and red lines show the density of the major ions, H^+ and H_3^+ , respectively. The variable 'x' represents an integer as there are so many combinations of hydrocarbon and water ions to represent (see Moses and Bass, 2000, for full tabulated lists). The right panel shows the major ions in terms of temperature. This plot is from Figure 1 of Moore et al. (2009).

One of the major motivations for studying Saturn's atmosphere is that the global thermospheric temperatures at Saturn are far from constrained. Using the Visual and Infrared Mapping Spectrometer (VIMS) (Brown et al., 2004) on

board Cassini, the polar-auroral regions of Saturn were found (prior to this work) to have temperatures in the range 570 - 620 K (Stallard et al., 2012b). Only two temperature estimates are currently available from three total analyses of stellar occultations to date by the Cassini spacecraft, and these are 300 K at mid-latitudes and 600 K at the equator (Shemansky and Liu, 2012) (at ~ 1400 km altitude). These occultations measure the absorption of starlight as a star is occulted by Saturn's atmosphere. In particular, the attenuated UV light from the star is used to find the spectrum of atmospheric H_2 and then the molecule's rotational temperature. Saturn's equatorial thermosphere is modelled to be ~ 180 K (Bagenal et al., Chapter 9) based on solar inputs, which is hundreds of Kelvins cooler than observed, and this is termed the 'energy crisis' (e.g. Miller et al., 2005). The hot auroral temperatures can at least be explained at Saturn via Joule heating and ion drag for the most part, because the total heating from these two mechanisms generates ~ 5 TW of power per hemisphere, whilst auroral particle precipitation provides an additional energy input of ~ 0.1 TW (Cowley et al., 2004). It was thought that these hot auroral regions would transfer heat equatorward, however, modelling by Smith et al. (2007) demonstrated that energy in the polar regions would be trapped due to ion drag effects, and Saturn's low latitudes would actually be cooled by circulation associated with auroral energy inputs and planetary rotation. Therefore, some unknown source of heating is currently required to heat Saturn's low latitude regions and it is estimated to be ~ 2.5 times larger than the solar EUV heating source (Mueller-Wodarg et al., 2012).

1.6.2 Aurorae

The first hints of Saturn auroral emission were first seen in the UV by the pioneer spacecraft when it flew by in 1979 (Judge et al., 1980), and was subsequently confirmed later by both Voyager spacecraft, again in UV, in 1981 and 1982 (e.g.

Shemansky and Ajello, 1983). In recent years the aurorae have been studied in greater depth, for example: in UV using the Hubble Space Telescope (HST) (Nichols et al., 2009; Meredith et al., 2013) and in radio, visible and IR wavelengths using the Cassini spacecraft (Gurnett et al., 2005; Dyudina et al., 2009; Badman et al., 2012b). Here, we focus on the aurorae in mid-IR through the discrete emission lines of the H_3^+ ion; however, it is often useful to compare our data to UV wavelengths where possible due to the differences in what each wavelength represents (see, e.g. Melin et al., 2011). The UV emission is a prompt ‘pump and dump’ mechanism emission because the timescale between collisional excitation and radiative de-excitation is small compared to other auroral processes; the temperatures associated with this emission are ~ 25000 K and so UV emissions are not representative of thermospheric temperatures (Stallard, 2001). H_3^+ on the other hand is quasi-thermalised and its emission intensity is greatly dependant on temperature. For example, an increase in H_3^+ temperature from 400 to 600 K results in the H_3^+ Q(1,0) line intensity rising by an order of magnitude (Miller et al., 2006; Melin et al., 2014).

The auroral ‘main oval’ at Saturn is a ‘discrete’ aurora, as opposed to diffuse aurora associated with pitch angle scattering, and is almost circular in nature. Statistical studies show that the main oval was located just equatorward of the open-closed magnetic field line boundary near $\sim 13.5^\circ$ (planetocentric) co-latitude in the north and $\sim 15^\circ$ co-latitude in the south (Badman et al., 2006; Cowley et al., 2004). Near equinoctial conditions the mean location of the ovals were found in UV by HST to exist at $\sim 16.3^\circ \pm 0.6^\circ$ and $\sim 17.8^\circ \pm 0.4^\circ$ for the north and south, respectively. These auroral emissions map via magnetic field lines to $\sim 15 - 20 R_S$ (Saturn radii) in Saturn’s equatorial plane.

Saturn’s equatorial plane is continuously mass-loaded by protons, oxygen and electrons (plasma) that are derived from Saturn’s rings and moons (Cowley and

Bunce, 2003). Magnetic field lines sweep through the equatorial plane causing this plasma to accelerate in the direction of planetary rotation. The rotating plasma flow and the magnetic field produce a radially outward electric field given by $\mathbf{E} = -\mathbf{v} \times \mathbf{B}$. The divergence of the radial current ($\text{div } \mathbf{J} = 0$) implies that a magnetic field-aligned current is set up between the equatorial plane and the ionosphere. Such coupling results in a frictional torque between the closed field lines and the planetary atmosphere, which in turn transfers angular momentum out of the planet and into the equatorial plasma (Cowley et al., 2008). In the reference frame of the thermosphere this motion causes the ionosphere to be accelerated in the opposite direction to the planetary rotation (Cowley and Bunce, 2003). Similarly, the open field lines in the polar caps are able to connect to the solar wind, also causing acceleration. The open and closed field line regions have different effects on the plasma angular velocity in the atmosphere: the polar cap between $0 - 12^\circ$ corotates slower with the planet than the plasma on closed field lines. The main oval emission is now generally thought to be produced by electron acceleration associated with closed field lines, as required by the shear in rotational flow at the open-closed field line boundary (Cowley et al., 2004, 2008).

Figure 1.16 illustrates the current systems on the planet due to external forcing in a view looking down onto the north pole of the planet. The central region contains the aforementioned open field lines, which corotate at just $\sim 30\%$ of the angular velocity of Saturn and are driven chiefly by reconnection at the magnetopause and/or in the magnetotail - i.e. the Dungey-cycle (Dungey, 1961; Cowley et al., 2004). It is the reconnection between open flux and the solar wind at the magnetopause and the solar wind carrying the field lines over the pole that result in the anti-sunward plasma flow over the polar cap. The Vasyliunas-cycle was originally associated with reconnection of the magnetotail of Jupiter and is theorized to be present at Saturn (Vasyliunas, 1983; Cowley et al., 2004). This process leads to bubbles of planetary plasma (plasmoids) snapping away from

the magnetosphere and heading anti-sunward. The Pedersen current in this figure flows equatorward whilst the Hall current flows anticlockwise (see Subsection 1.2.2), and the divergence of these complete the system of upward and downward field-aligned currents. The study of the emissions from the quasi-thermalized H_3^+ within the ionosphere is useful as it is sensitive to auroral processes, e.g. Pedersen-led Joule heating.

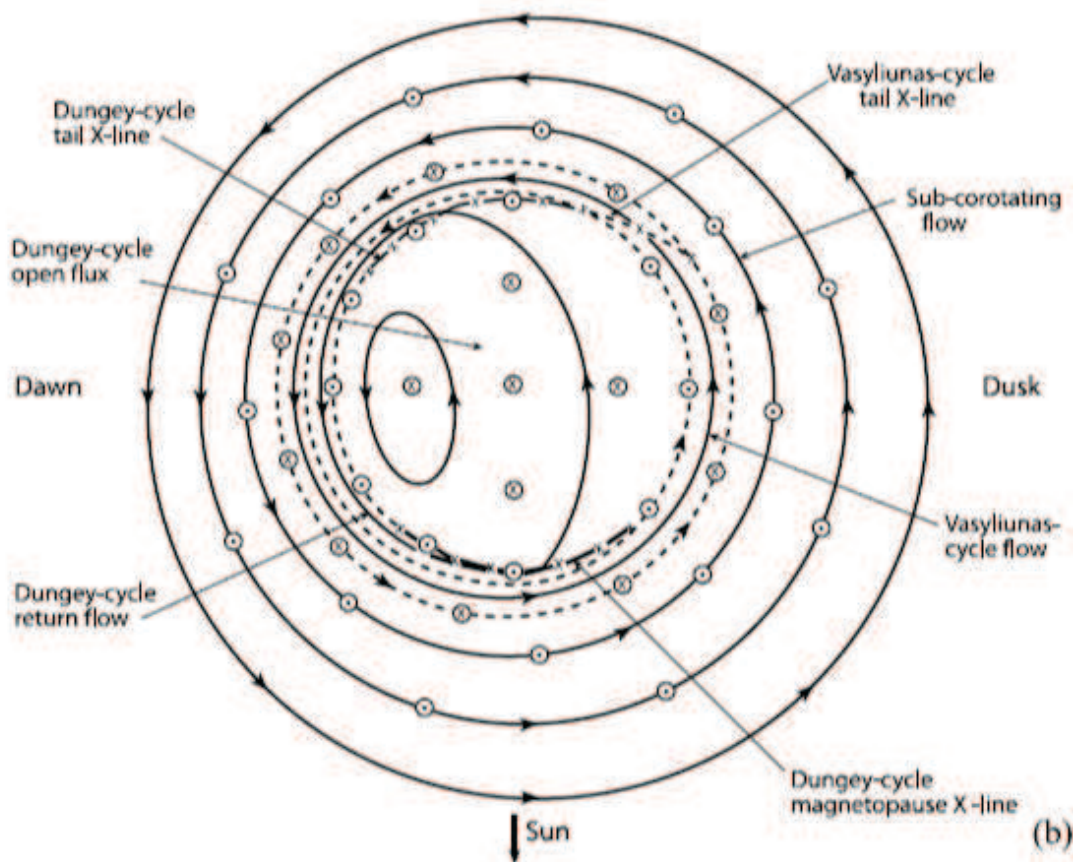


Figure 1.16: Saturn's magnetosphere-ionosphere coupling currents - A view of Saturn's northern hemisphere from above, with the outer perimeter being at 30° colatitude. The sun is to the bottom and the dawn and dusk sectors are labelled. The solid and dashed curved lines represent plasma streamlines and the boundaries between the flow regimes, respectively, with the X's showing reconnection sites associated with the Dungey- and Vasyliunas-cycles. The circled dots and crossed are upward and downward magnetic field-aligned currents, respectively. The remainder of the features are described in the main text. This sketch is from Figure 1. b) in Cowley et al. (2004).

1.6.3 Saturn's ring system and motivation

Saturn's rings are composed of between 90 and 95% water ice and are believed to be the dramatic remainder of the tidal or collisional destruction of a moon of similar mass to Enceladus (Canup, 2010). Contemporary estimates of the ring lifetime range from 4.4 million (Northrop and Connerney, 1987) to 100 million (Salmon et al., 2010) to 4.5 billion years (Canup, 2010); these wildly varying estimates highlight our lack of knowledge in ring system science. The main subdivisions and gaps of the rings are shown in high spatial resolution in Figure 1.17.

A magnetic link between Saturn's rings and its atmosphere was invoked in the early 1980s in order to explain the lower-than-expected electron densities and their latitudinal variations in the planetary ionosphere, through the influx of ring-derived water (Connerney and Waite, 1984; Connerney, 1986). This interpretation was supported by Voyager 2 fly-by observations that showed three discrete dark bands in the methane-dominated lower atmosphere (beneath the ionosphere), which Connerney (1986) interpreted to be magnetically mapped sequentially to the inner edge of the B ring, the instability radius and the orbital path of Enceladus as shown in Figure 1.18.

The water influx inferred from the ionospheric model of Connerney and Waite (1984) was 2×10^9 molecules $\text{cm}^{-2} \text{sec}^{-1}$ at B-ring associated latitudes, whilst being $\sim 4 \times 10^7$ molecules $\text{cm}^{-2} \text{sec}^{-1}$ planet-wide. Little has been published on the subject of a ring-ionosphere coupling following this modelling and discovery. Column integrated emissions from H_2O however, were observed to be emanating from Saturn by the Infrared Space Observatory (ISO) over a decade later (Feuchtgruber et al., 1997). These were combined with a photochemical model soon after to derive a globally averaged H_2O influx of $\sim 1.5 \times 10^6$ $\text{cm}^{-2} \text{sec}^{-1}$ (Moses and Bass, 2000).

Cassini spacecraft observations over Saturn's rings during its orbit insertion manoeuvre in 2004, unique in the mission to date, indicated the presence of a water-product atmosphere surrounding the rings deriving from the icy grains, that is partly ionised by solar UV analogous to the planetary ionosphere (Luhmann et al., 2006; Coates et al., 2005). This is commonly referred to as the 'ring ionosphere', but we hereafter refer to it as an 'ionodisk' to both differentiate it from Saturn's ionosphere and to make it a geometrically logical definition. Water products include anything derived from H_2O , for example O^+ , O_2^+ and H_3O^+ . According to the evidence above, these charged water products must find their way into the Saturnian atmosphere.

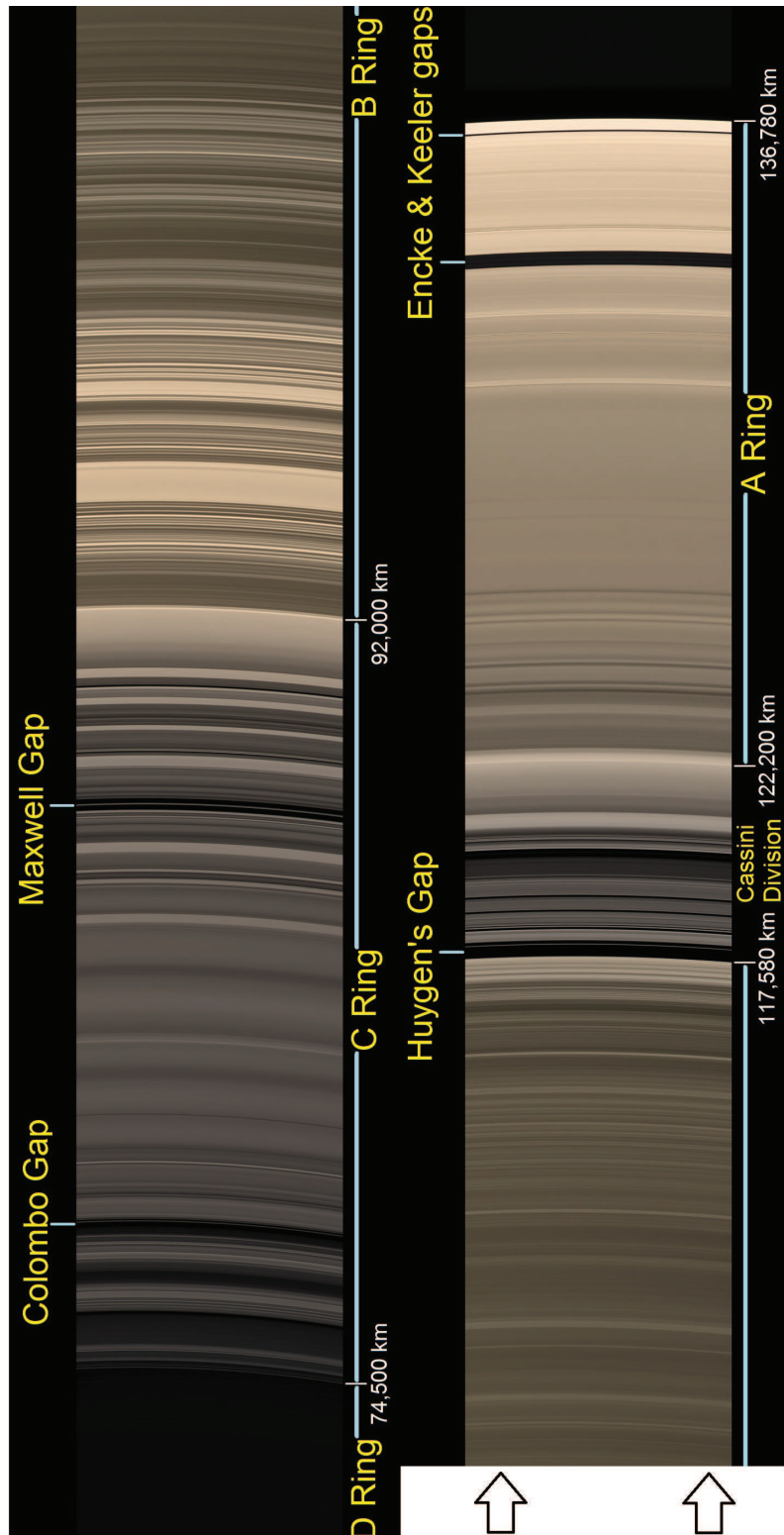


Figure 1.17: Saturn's rings - This (edited) colour image of Saturn's rings was taken by Cassini using the narrow angle camera (natural colour) on the 9th of May, 2007. Annotations of principle ring gaps and major sub-divisions are shown in yellow text. Credit: NASA/JPL.

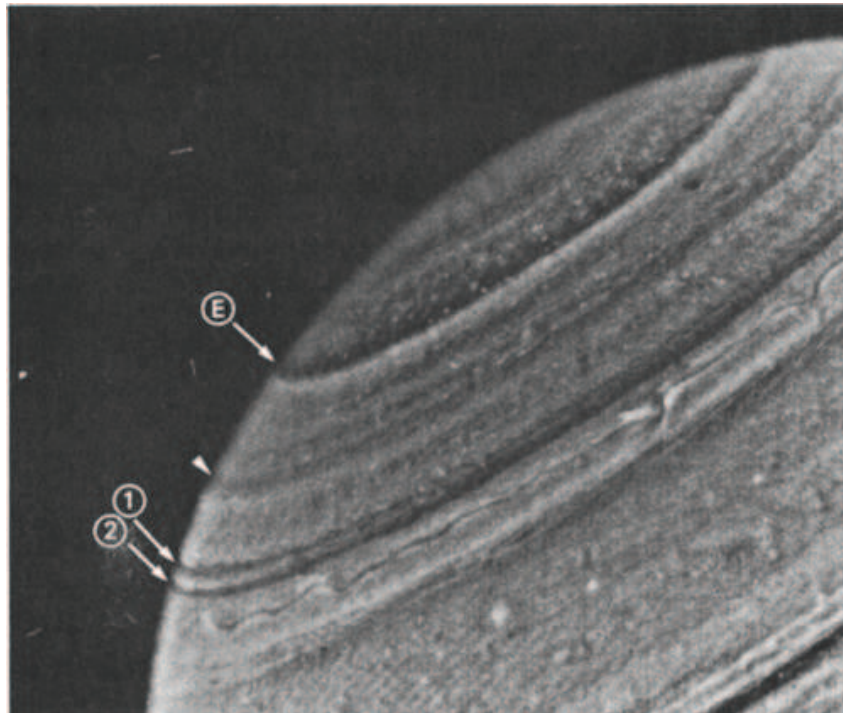


Figure 1.18: Saturn in high contrast (green) - Here, Saturn's northern hemisphere is shown in green wavelength light, the image was taken by the Voyager 2 spacecraft. Labels 1, 2 and E indicate dark circumferential bands, these are located at 44.2° , 46.3° and 65.5° planetocentric latitude north, respectively; these also map via magnetic field lines to 1.52, 1.62 and 3.95 Saturn radii in the equatorial plane, respectively. This image is Figure 2 in Connerney (1986)

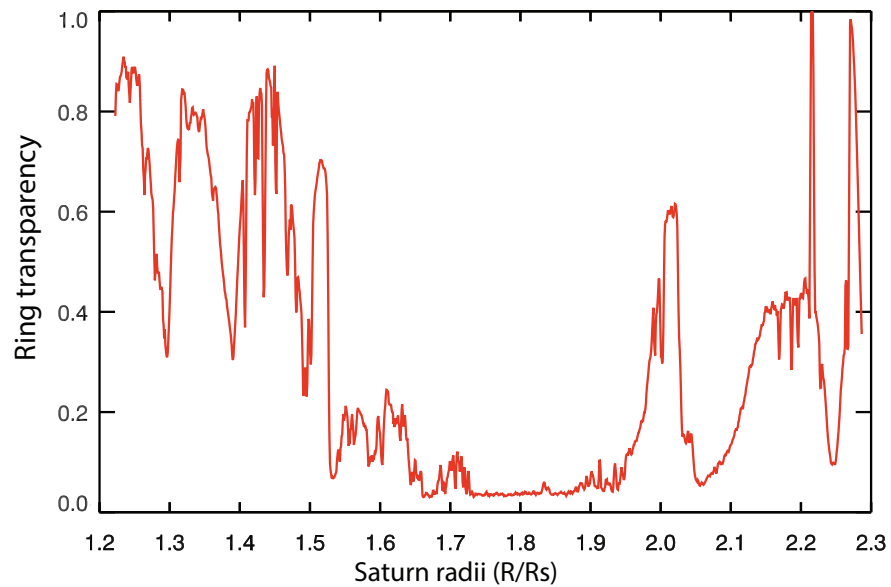


Figure 1.19: Transmission of light through the rings - A profile of UV transmittance through Saturn's rings taken by the Voyager 2 spacecraft. The x-axis shows radial distance from Saturn's center where $R_S = 60,268$ km. The y-axis shows the normalized number of photons passing through the rings; dense portions of the rings are then intuitively near to a value of zero and *vice versa* for the ring gaps (Lillie et al., 1977; Lane et al., 1982)

1.7 Jupiter

As well as observing Saturn's rings in 1610, Galileo also trained his telescope on Jupiter, allowing him to discover the planet's four largest moons, Io, Ganymede, Calisto and Europa, which are now known as the Galilean moons. Jupiter is the largest planet in our solar system and also has the shortest day, at 9 hours 55 minutes (Bagenal et al.). A modern image of Jupiter taken by the Cassini spacecraft as it flew by is shown in Figure 1.20, within which one can see distinctive dark 'belts' and light 'zones' as well as the largest continuous storm in the solar system, the Great Red Spot. For the purposes of this thesis we will focus on the ionosphere and its interactions with space as we did previously for Saturn, using the molecular ion H_3^+ as a probe which, in the case for Jupiter, was first detected in 1989 (Drossart et al., 1989b) (indeed, this was the first ever detection outside of a lab).

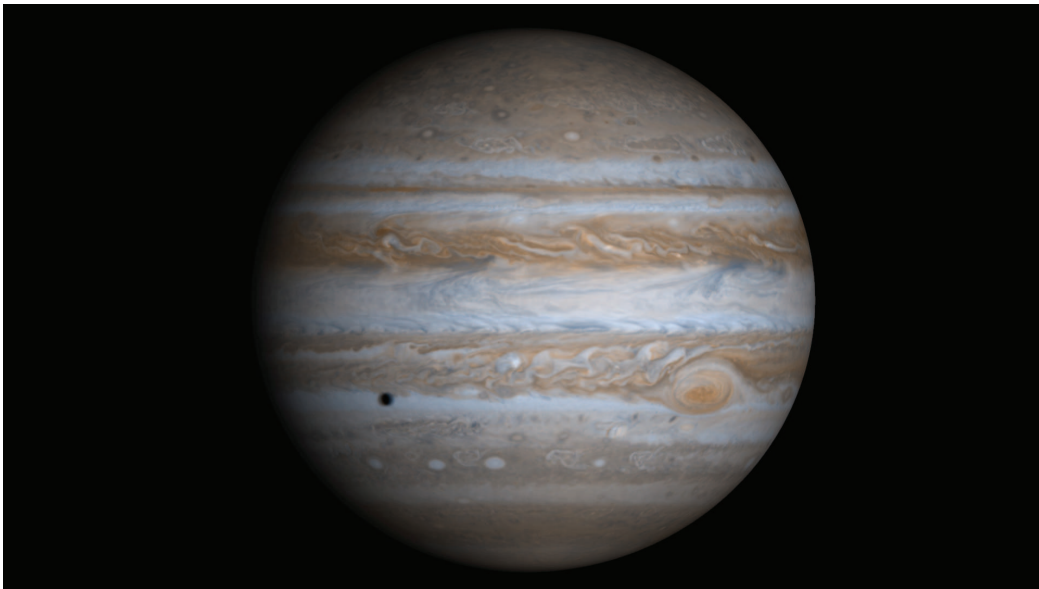


Figure 1.20: Jupiter from Cassini - A composite of four images taken by Cassini on its way to Saturn on December 7th, 2000

1.7.1 Ionosphere, thermosphere and motivation

The Jovian ionosphere and thermosphere is generally very similar to Saturn's in both composition and stratification of the various constituents. The 1 bar pressure altitude again represents the surface of Jupiter as it does with Saturn. The neutral atmosphere comprises 90% molecular hydrogen and 10% helium with the remainder being mostly methane and ammonia, again similar to Saturn. Jupiter's ionospheric constituents, which begin to form at around 240 km above the surface due to solar EUV ionisation and particle precipitation, are lower in altitude than at Saturn due to Jupiter's stronger gravitational pull which leads to a smaller scale height as shown in Figure 1.21. In this figure, which is taken from Tao et al. (2011b), one can also see the effects of adjusting the electron precipitation energy on the production rate of H_3^+ and H_2^+ . The energy range of electron precipitation is expected to be 30 - 200 keV in Jupiter's auroral region and is discussed in the next section, but we simply note here that H_3^+ density is expected to peak at ~ 600 km on Jupiter as opposed to ~ 1100 km at Saturn. The Pedersen layer at Jupiter (where most of the Pedersen current flows, see Subsection 1.2.2) is located at ~ 400 km (Moore et al., 2009).

The study of Jupiter in this thesis stems from the same major motivator as for Saturn: the energy crisis. On Jupiter, the discrepancy between models is larger, with models based on solar input alone predicting temperatures of ~ 200 K (Bagenal et al., Chapter 9) whilst observations yield between 700 K at low latitudes and upwards of 1000 K in the auroral region (Lam et al., 1997). Again, this is at least in part explainable at the polar/auroral regions, given that Joule heating there is expected to contribute some 300 TW per hemisphere, with the additional contribution by particle precipitation being 2 - 4 TW (Cowley et al., 2005b); note that these are two orders of magnitude greater than the same heating mechanisms on Saturn. The lower latitudes could be heated by particle precipitation, but this has been calculated to be of the same order of magnitude as solar EUV (Rego et al., 2000), and is not sufficient to explain the observed temperatures

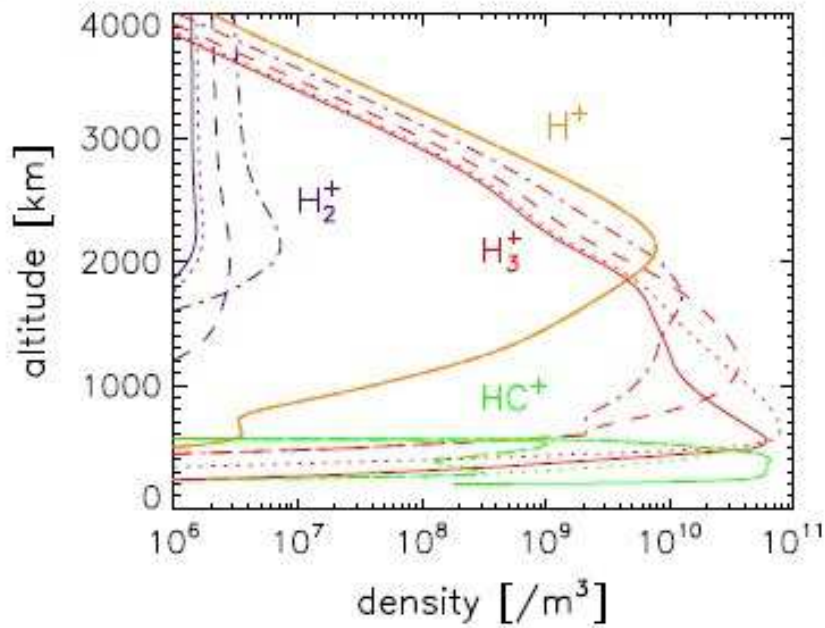


Figure 1.21: Model profile of Jupiter's ionosphere - Altitudinal model profiles of Jupiter's major ions as a function of their density for differing precipitation energies: 100 keV (solid), 10 keV (dotted), 1 keV (dashed) and 0.1 keV (dot-dashed). This is Figure 6 from Tao et al. (2011b).

there (Bagenal et al., Chapter 9). Breaking gravity waves may supply additional heat, but models indicate this can cause temperature increases of only $\sim 15 - 20$ K and can in fact cool the atmosphere under certain conditions (Hickey et al., 2000). Redistribution of auroral energy may too play a role, but by analogy with Saturn we might expect the energy to remain trapped at the poles (Smith et al., 2007): it is important to note here that because Jupiter, Saturn, Uranus and Neptune all have an 'energy crisis', the solution is likely to be common to each planet (Bagenal et al., Chapter 9). Nevertheless, in Chapter 5 we investigate global maps of temperatures in the Jovian ionosphere, comparing them to most recent maps taken in 1993 by Lam et al. (1997) as well as the conditions on Saturn described in Chapters 3 and 4.

1.7.2 The Jovian magnetosphere and aurorae

The Jovian magnetosphere is an extraordinarily large cavity in the solar wind; with a sub-solar magnetopause distance of between $45 - 100 R_J$ and a magnetotail

length of up to $7000 R_J$ (Bagenal et al., Chapter 24), it would be large enough in angular size to encompass the moon as viewed from Earth. Jupiter's magnetic field results from the motion of metallic hydrogen that surrounds Jupiter's core which comprises a highly hot, pressurised fluid of electrons and protons acting as an electrical conductor.

Jupiter's equatorial plasma is predominantly oxygen and sulphur ions (matched in equal measure by electrons) originating from the volcanic moon Io. This material forms a torus in the inner magnetosphere between 5 and $10 R_J$ that, when ionized, becomes sensitive to the magnetic field and is then accelerated up to partial corotation with the magnetosphere. The plasma is then thought to be driven radially away from the planet via centrifugally-driven flux tube interchange (Southwood and Kivelson, 1989; Nichols and Cowley, 2004; Cowley et al., 2005b). In the absence of this material the sub-solar magnetopause would occur at $\sim 42 R_J$ (Bagenal et al., Chapter 24). A sketch of the system is shown in Figure 1.22. The angular velocity of the equatorial plasma falls inversely as the square of the distance when no external torques are acting on it, and when it falls below that of Jupiter's ionospheric Pedersen layer (Ω_J^*) the ion-neutral collisions there provide a torque to the equatorial plasma which acts to spin it back up to near-rigid corotation. It is this torque that is responsible for the bending of the field lines out of the meridian plane. The current system in the figure is completed by field-aligned currents which link the equatorward-directed Pedersen currents in each hemisphere to the outward flowing radial current in the equatorial plane in a similar manner to at Saturn (Hill, 1979; Cowley and Bunce, 2001; Nichols and Cowley, 2004).

Jupiter's 'main oval' is located at around 15° magnetic colatitude and is produced by particle precipitation accelerated down onto the planet along field-aligned associated with upward-directed currents (Nichols and Cowley, 2004; Cowley et al., 2005b). The electron energy range for precipitating particles associated with the upward currents was determined from far UV observations to be

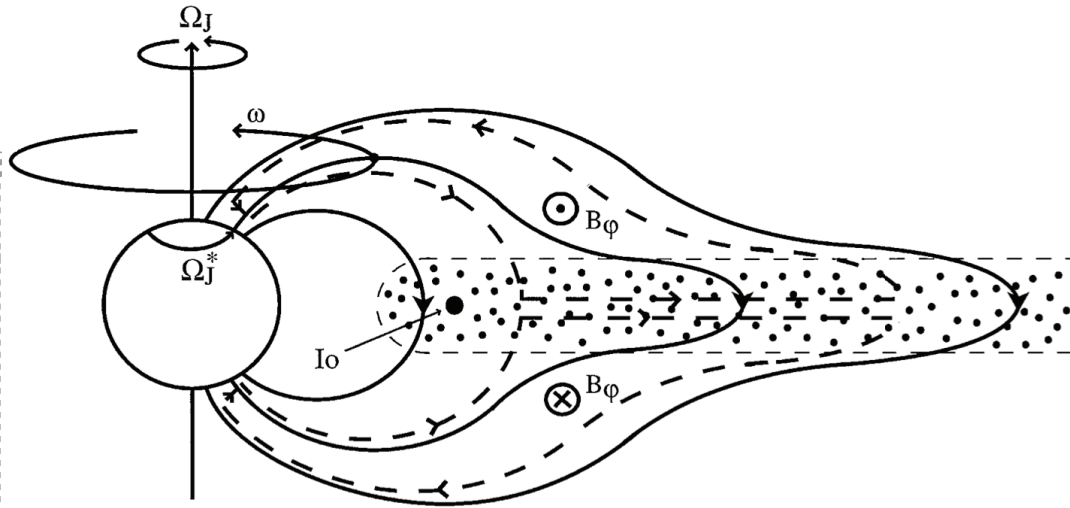


Figure 1.22: Jovian magnetosphere-ionosphere coupling - A meridian cross-section of Jupiter's inner and middle magnetosphere. The arrowed solid lines are magnetic field lines, the arrowed dashed lines are the magnetosphere-ionosphere coupling current system. The dotted area indicates the continuously replenished plasma torus which is accelerated in the direction of the planetary magnetic field. Ω_J , Ω_J^* and ω are the solid-body, ionospheric Pedersen layer and equatorial plasma angular velocities, respectively. Figure 1 from Cowley and Bunce (2001).

30 - 200 keV by Gustin et al. (2004).

Chapter 2

Data reduction and H_3^+ fitting

This chapter outlines the methodology employed in this study for obtaining, reducing and analysing data from the upper atmospheres of the giant planets Jupiter and Saturn.

2.1 Telescope and instrument overview

The observations herein were all performed at observatories built atop the dormant volcano Mauna Kea (White Mountain, in English), which is on Big Island, the largest island in the Hawaiian island chain. These observatories are ~ 4200 m above sea level, serving to keep it above the inversion layer where water condenses to form clouds. This altitude also reduces the column of atmosphere through which light must pass to enter the telescopes from space (by $\sim 35\%$), thus reducing both IR emission and absorption from the constituents of the Earth's atmosphere such as water. Following the acquisition of data, data reduction is performed. Reduction, or cleaning, is the name for the removal of non- H_3^+ emission and the processing techniques used to transform raw data into a usable scientific form from which physical parameters (e.g. temperature) can be extracted. There are 3 main considerations to astronomical data reduction: instrumental effects, telluric (Earth) effects and target (Jupiter and Saturn) effects.

2.1.1 The NASA IRTF and SpeX instrument

The NASA InfraRed Telescope Facility (IRTF) is a 3-metre reflector telescope built in 1979. It is situated near the summit of Mauna Kea, pictured in Figure 2.1. The instrument used in this work was the SpeX near/mid-IR spectrograph and imager (Rayner et al., 2003) and is illustrated in Figure 2.2. This spectrometer, when used in medium-resolution single-order mode, has a spectral resolution of $R = \lambda/\Delta\lambda \sim 2500$, this gives a minimum resolvable wavelength resolution at $3.5 \mu\text{m}$ of $\delta\lambda \sim 1.4 \text{ nm}$. The accessible wavelength range is $0.8 - 5.4 \mu\text{m}$, and the wavelength range used herein was $3.13 - 3.5 \mu\text{m}$, thus only the R branch regions of the IR spectrum are included. The slit on the spectrometer was orientated in a north-south position on Jupiter and the field of view is $0.3''$ (seconds of arc, width) by $60''$ (height) on the sky. The IRTF was used to observe Jupiter for 4 nights between the 4th and 8th of December (UT) in 2012; an extended discussion of the observations is presented in Chapter 5.



Figure 2.1: The NASA IRTF telescope - located 4200 metres above sea level atop Mauna Kea, Hawaii. The facility website contains additional images.

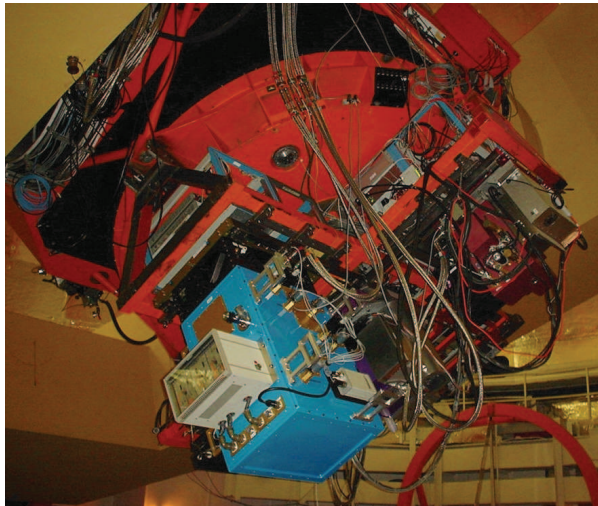


Figure 2.2: The SpeX instrument - this is a medium resolution IR (0.8-5.4 μm) spectrograph and imager. Image courtesy of the IRTF website

2.1.2 The W.M. Keck telescopes and NIRSPEC instrument

The W.M. Keck telescopes are twin telescopes, the primary mirrors are composed of 36 hexagonal segments which work together to form a single mirror. The Keck I and Keck II telescopes were built in 1993 and 1996 respectively, and the latter was used in this study to observe Saturn on the 17th of April, 2011. In terms of the usable area for light collection, these telescopes are currently the largest optical/IR telescopes in the world (as of February 2014). The spectrometer NIRSPEC (McLean et al., 1998) was used in conjunction with Keck II and is shown in Figure 2.4. This is a high resolution spectrometer used in cross-dispersed mode, the spectral resolution is $R = \lambda/\Delta\lambda \sim 25,000$, giving a minimum resolvable resolution of $\delta\lambda \approx 0.16 \text{ nm}$ (at $3.975 \mu\text{m}$). The total wavelength range of this instrument is $0.8 - 5.5 \mu\text{m}$, and the data in this thesis uses the R and Q branch regions between $3.5-4.1 \mu\text{m}$. The spectrometer slit was orientated in a north-south position on Saturn; the planet then rotates beneath the slit allowing for the acquisition of spectral data. The slit itself subtends $0.432''$ in width by $24''$ (height) on the sky.

2.1 Telescope and instrument overview



Figure 2.3: The Keck telescopes - located 4200 metres above sea level atop Mauna Kea, Hawaii. The facility website contains additional images.

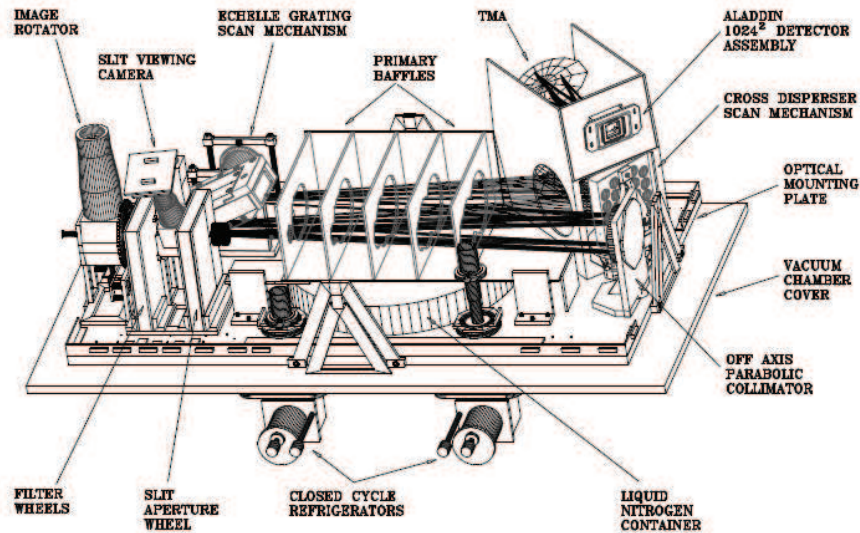


Figure 2.4: The NIRSPEC instrument - A schematic showing the design of the NIRSPEC instrument, a high resolution IR spectrometer with a wavelength range of 0.8 - 5.5 μm . Image courtesy of the Keck observatory website

2.2 Instrumental considerations

The light that these telescopes gather is reflected through the instrumentation before landing on the charged coupled device (CCD) surface. This CCD detector counts the number of incident photons and converts them into digital information which is suitable for analysis by computers. Prior to being recorded on the CCD, the light has been reflected by an echelle (ladder, in English) diffraction grating, splitting light into multiple beams of different wavelengths. On the CCD these beams of light are displayed in sequence along one axis (x) whilst spatial information is shown vertically along another (y); this results in a plot of intensity as a function of wavelength and position along the axis of the slit. There are two modes in which this is reflected, single-order and multi-order (see Subsections 2.2.3 and 2.2.4 respectively).

2.2.1 CCD calibration

The surface of a CCD can contain contaminants such as dust particles and design imperfections, leading to a varying efficiency in the detection of light across the array. This variable output is corrected for by dividing images with a flat-field images (flats), these flats are also dark-current (dark) subtracted to account for thermal noise at the detector. A flat-field image is an image taken where the CCD is exposed to a uniformly illuminated light source, thus any relative differences in sensitivity can be seen - an example is shown in Figure 2.5. Dividing an image by a median-normalised flat-field will raise areas in brightness that are darkened by such effects, thus accounting for inaccurate photon counts. Flat fielded images are normalised to a median value of 1 so that when dividing through, all negative values are taken out - this operation does not affect the relative intensities of the data. The CCDs of both instruments are cooled to ~ 30 K (Rayner et al., 2003; McLean et al., 1998), at this temperature the wavelength of peak blackbody emission is $\sim 96 \mu\text{m}$, such that the CCD is not contaminated. However, dark

2.2 Instrumental considerations

current is produced by a relatively small electric current passing through the CCD - which can be detected as photons. To remove this, a dark image is created by taking a long exposure with the shutter on the instrument closed, and then subsequently dividing it by the exposure time to obtain the dark current per second at each pixel. Flats and darks are taken at the start and end of an observation run so that the raw data is always within a few hours of calibration images. Flats by their nature are unlikely to vary in time, whereas darks may exhibit some variability: it is assumed that both phenomena do not vary on temporal scales small enough to affect this work, given the close proximity (in time) of the calibration images.

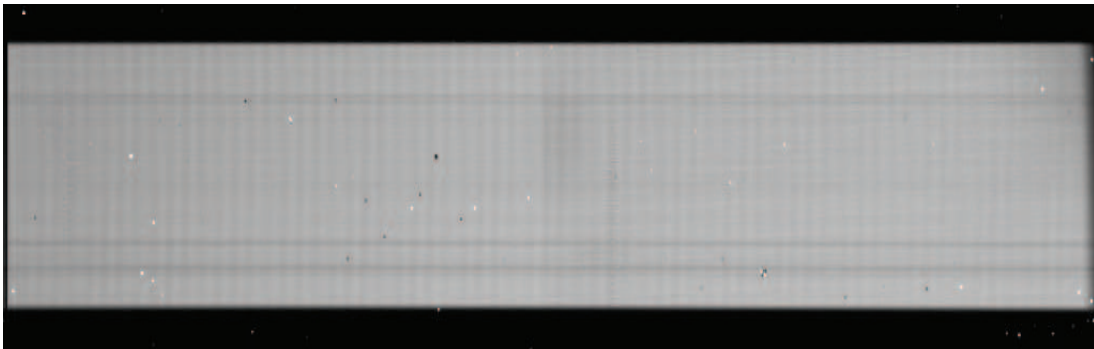


Figure 2.5: A typical flat-field spectral image - This flat-field image is from the Keck telescope and NIRSPEC instrument. Recorded on the 17th of April, 2011. Deficiencies in sensitivity are black spots/streaks whilst areas that are overly sensitive are brighter.

2.2.2 Echelle diffraction gratings

An Echelle diffraction grating is a reflective surface with grooves cut into it which reflects light at different angles depending on the wavelength, in other words it produces a spectrum. An schematic of how an Echelle reflective diffraction grating works is shown in Figure 2.6. The principle of superposition states that when two or more wave fronts (e.g. light waves) meet at a point in space, there is a net disturbance at that point which is equal to the sum of disturbances in both waves individually. For this type of diffraction grating, constructive interference between two wave fronts is relied upon - i.e. the interference of two wave fronts

that are completely in phase.

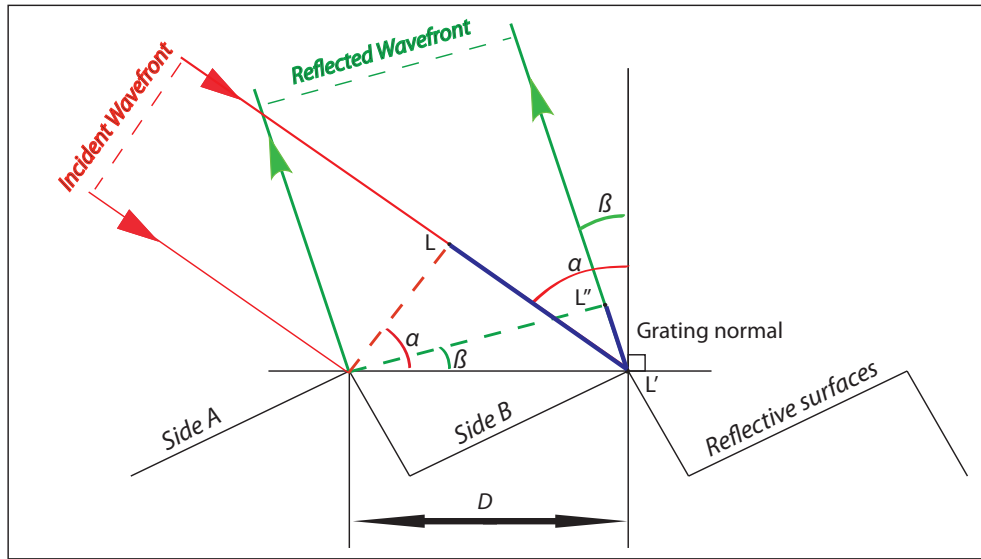


Figure 2.6: An Echelle diffraction grating - The wave front of light entering the system (shown in red) has an angle of incidence α to the normal, the light emerging has an angle β . Light from side A and B will constructively interfere with each other if the difference in length of the blue line, LL'L'', is an integer number of wavelengths. The difference in path length from L' to L'' is $D(\sin(\alpha) + \sin(\beta))$.

In Figure 2.6, it can be seen that the reflected wave front is in phase only if the spacing between them is an integral number of wavelengths apart. To find the distance between wavelengths we must find the length of the blue coloured line in this Figure, which is of length LL'L'', to do this we use trigonometry; $D\sin(\alpha) + D\sin(\beta)$. The conditions for constructive interference are thus met when

$$D(\sin(\alpha) + \sin(\beta)) = n\lambda \quad (2.1)$$

where α and β are the angles of incidence and reflection respectively, D is the length between grating sides, n is the spectral order number (integers, 1,2... n) and λ is the wavelength of the incident light. This is known as the grating equation (Palmer and Loewen, 2005). The same wavelength of light is reflected into multiple directions, the spectral order number, when adjusted, gives the angle each reflection occurs at. Holding all variables the same, apart from spectral

order (1,2...n), shows that light reflects onto different portions of the CCD surface simultaneously - taking advantage of the principle of superposition. On the scale of the entire grating, each reflection isn't truly a 'ray' of light and each groove (side) can be considered a point source. Point sources of light are emitted spherically and thus interfere constructively and destructively as shown in Figure 2.7.

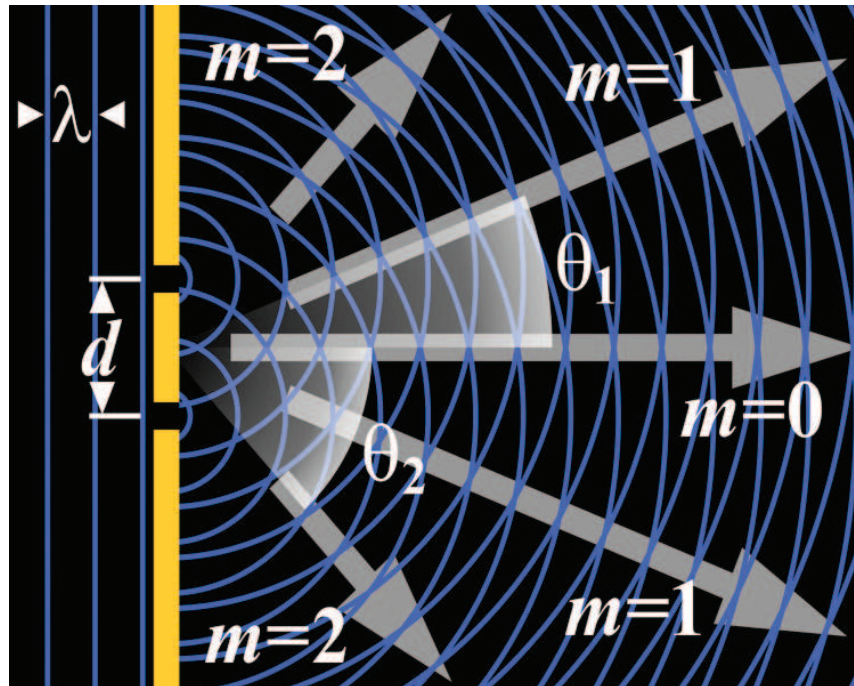


Figure 2.7: A two-slit diffraction pattern - showing how waves can constructively interfere when they are in phase. This is taken from user Epzcaw on Wikipedia at en.wikipedia.org/wiki/.

2.2.3 Single-order spectroscopy

Standard spectroscopy is in single-order mode, we use single-order here to differentiate it from multi-order. The aim of spectroscopy for the purposes of the work in this thesis is to obtain the intensity of light as a function of wavelength and position on the planetary body under study. The relative intensities of H_3^+ are of interest since they can be used to obtain physical properties of the region in which it is observed, as discussed in section 2.5. The intention of this work was to record a large amount of spatial information from pole to pole at local noon

on Jupiter. Data obtained with the NASA IRTF and SpeX instrument used a long slit (of 60'' height) to encompass the large angular size of Jupiter in the sky ($\sim 44''$). An example sky-subtracted spectral image is shown in Figure 2.8.

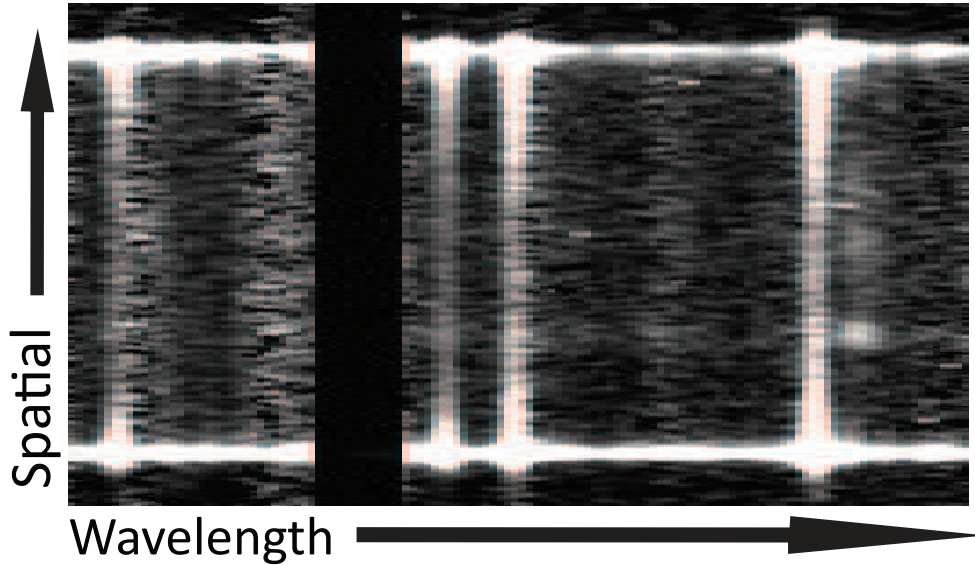


Figure 2.8: A typical single-order mode spectral image - This spectral image of Jupiter was taken using the NASA IRTF and SpeX instrument on the 4th of December, 2012. The x- and y-axes show wavelength and spatial components, respectively, of light incident on the CCD's surface.

2.2.4 Multiple-order spectroscopy

Multiple-order spectroscopy is obtained using a cross-dispersion technique whereby multiple ranges (orders) of wavelengths are simultaneously written on a CCD as described in section 2.2.2. This often results in a better use of space on a CCD surface - i.e. a higher percentage of pixels are used to obtain data. Due to Saturn's distance, it subtends $\sim 19''$ in the Earth's sky at opposition; although this is a disadvantage when compared to Jupiter in terms of the light available to collect, it is outweighed somewhat by the Keck telescopes 10-metre diameter mirror. For Saturn, using the Keck II telescope and NIRSPEC, a 24'' slit was used, encompassing the entire planet. Since the emission line intensities are less well known for H_3^+ on Saturn and to make best use of the available space on the CCD, the light is cross-dispersed into multiple orders. As shown in Figure 2.9,

this method can lead to a greater wavelength coverage when compared with the single order mode.

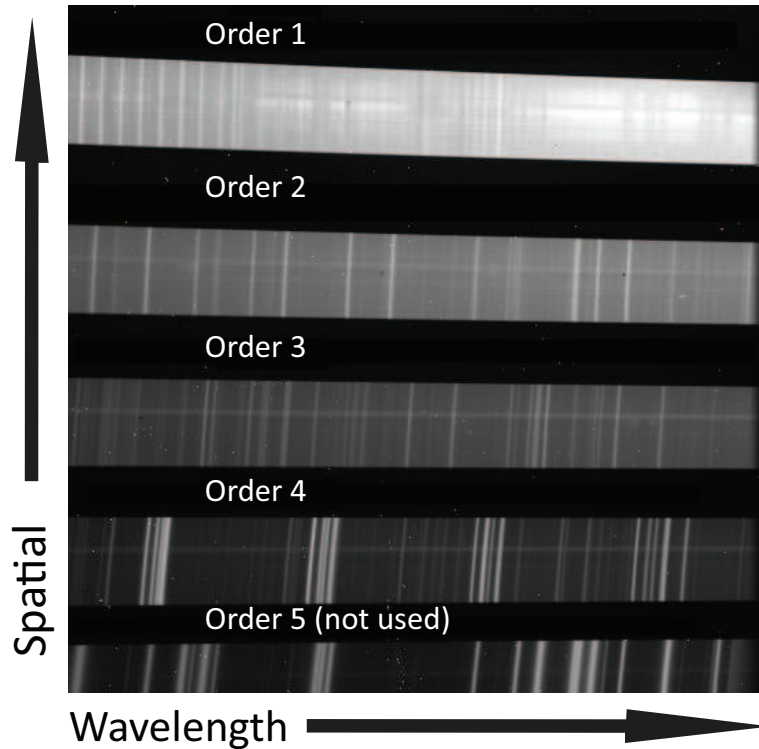


Figure 2.9: A typical (raw) multiple order spectrum - This is from the W.M. Keck and NIRSPEC instrument data recorded on the 17th of April, 2011. The x and y axes show wavelength and spatial components of each order, respectively, of light incident on the CCD's surface. This figure shows the entire chip surface and that spectral resolution is higher using this method.

2.3 Terrestrial considerations

The atmosphere of the Earth contains a myriad of chemical constituents. In the wavelength region we are interested in (2 - 5 μm) it is mainly H_2O that absorbs radiation, with CH_4 absorbing a significant amount, followed by CO_2 and N_2O to a lesser extent (Gates and Harrop, 1963). As well as absorbing radiation, the Earth's atmosphere also emits it; IR radiation is emitted mostly by CO_2 . The following sections describe how these terrestrial effects are accounted for.

2.3.1 Terrestrial emission: Sky subtraction

When observing a target such as Jupiter and Saturn in the IR region of the spectrum, emission from the Earth's atmosphere presents a problem. The Earth emits varying intensities of IR radiation as a function of wavelength, i.e. certain wavelengths are emitted more or less intensely than others. This emission from the sky can be almost completely removed however, in a process known as 'sky subtraction'. Sky subtraction starts with recording an image of a target 'A' (e.g. Saturn) and then subsequently an image (of the same exposure time) is recorded of the sky 'B' in an area in which no significant astronomical bodies reside. This process is called 'nodding' as the telescope must 'nod' between the target and the sky. With these two images we can simply subtract the intensity of the sky from the intensity of the target ($A - B$), leaving a clear image of the object ($A - B$) as illustrated in Figure 2.10, which illustrates the extent to which the sky IR emission interferes with a clean spectrum of Saturn.

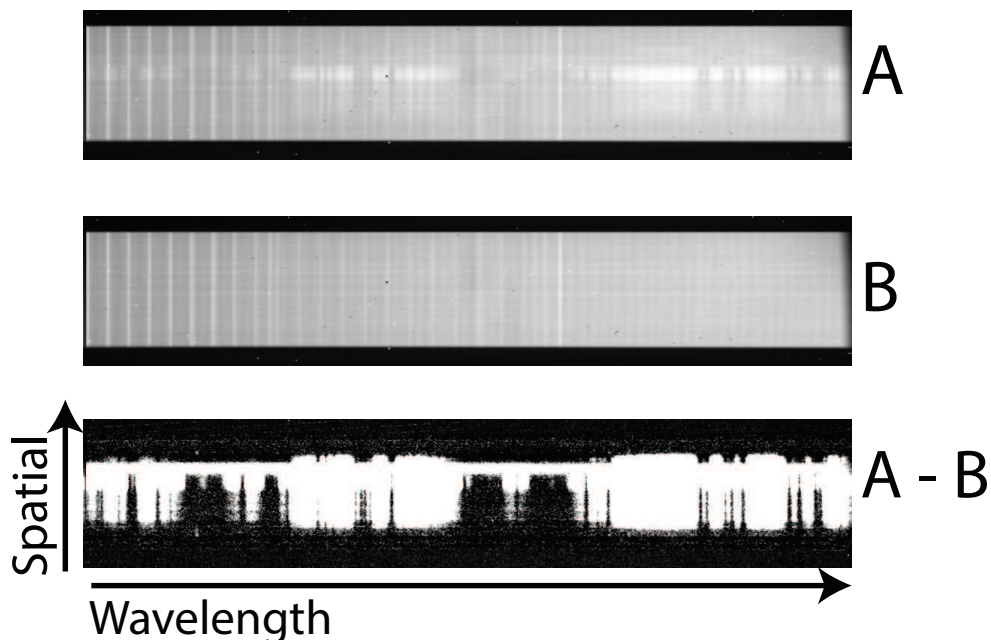


Figure 2.10: Target minus sky, ($A - B$) subtraction - This Figure depicts the sky (B) subtraction from Saturn (A). Low to high intensity corresponds to black to white in the shading.

Fortunately, the Earth's atmosphere does not vary significantly on timescales of the exposure lengths in the observations in this thesis (typically ~ 60 seconds) so

this approach is assumed to account for atmospheric IR emission fully, although any uncertainty introduced is given within the H_3^+ fitting routine. The data obtained in this thesis uses a nodding pattern of ABBA for both Jupiter and Saturn, meaning that the telescope moves from object to sky and then back to object again.

2.3.2 Terrestrial absorption: Flux calibration

Accounting for terrestrial emission is relatively simple, but more difficult is accounting for radiation that has been absorbed. A black-body curve for the Q-branch region within the L' window (see again Subsection 1.4.3) is shown in Figure 2.11.

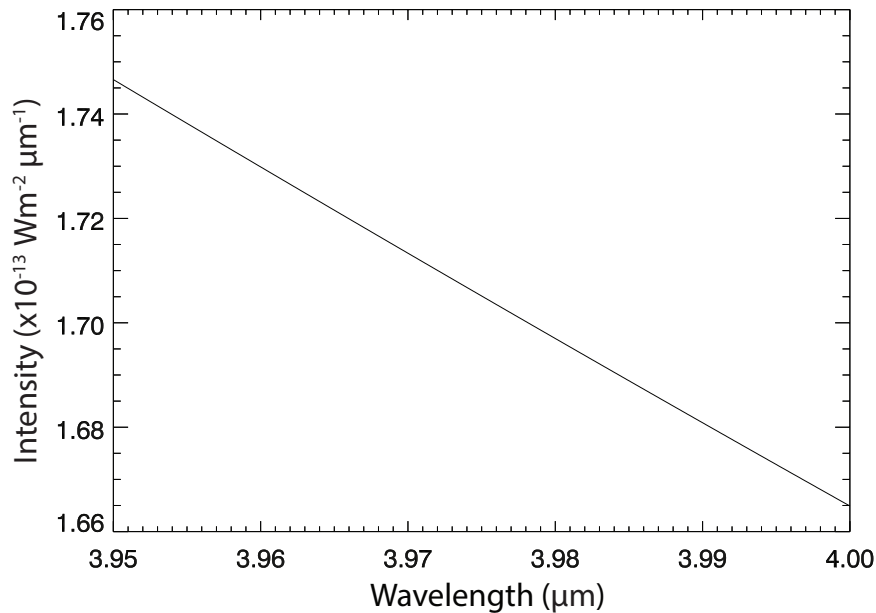


Figure 2.11: A black-body spectrum in the L' Window - This plot shows the intensity of black-body radiation as a function of wavelength at a temperature of 10,000 K. This star has a magnitude $m = 6.02$ in this L' window which extends from $\sim 3.4 - 4.1 \mu\text{m}$. Note the large variability due to atmospheric extinction in the Earth's atmosphere

The apparent magnitude of a star is a measure of the flux it produces at a given wavelength. The star α Lyr (Vega) is considered to be the reference from which all other star magnitudes are calibrated and thus holds an apparent visual magnitude of $m = 0$. In measuring the known continuum emission from a

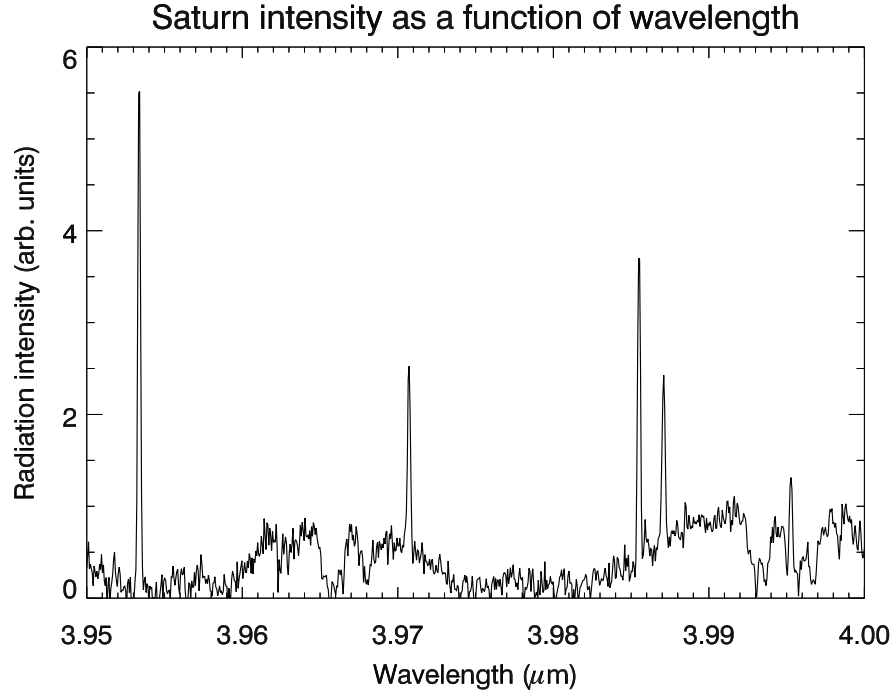


Figure 2.12: A spectral profile of Saturn - showing intensity as a function of wavelength from Saturn taken by W.M. Keck and NIRSPEC on the 17th of April, 2011. This has been sky subtracted but not yet flux calibrated or corrected for Saturnian hydrocarbon reflection.

star that emits as a black-body in IR, such as a standard main-sequence star of spectral classification ‘A0’, we can find how much intensity is lost as a function of wavelength through absorption by the Earth’s atmosphere. An example of a 10,000 K standard star spectrum is shown in Figure 2.13.

The aim of flux calibration is to adjust extraterrestrial flux in wavelengths at which the Earth’s atmosphere affects it. This is usually achieved by enhancing those spectral regions that are weakened by atmospheric absorption. The flux from α Lyr varies as a function of wavelength and therefore varies as a function of atmospheric window. α Lyr’s flux is found by observation to be $7.3 \times 10^{-11} \text{ Wm}^{-2}\mu\text{m}^{-1}$ in the L window and $5.24 \times 10^{-11} \text{ Wm}^{-2}\mu\text{m}^{-1}$ in the L’ window (Blackwell et al., 1983). The calculation for the flux of a star of magnitude m_λ is given below

$$F_{star}(\lambda) = F_\lambda \times 10^{-0.4 \times m_\lambda}, \quad (2.2)$$

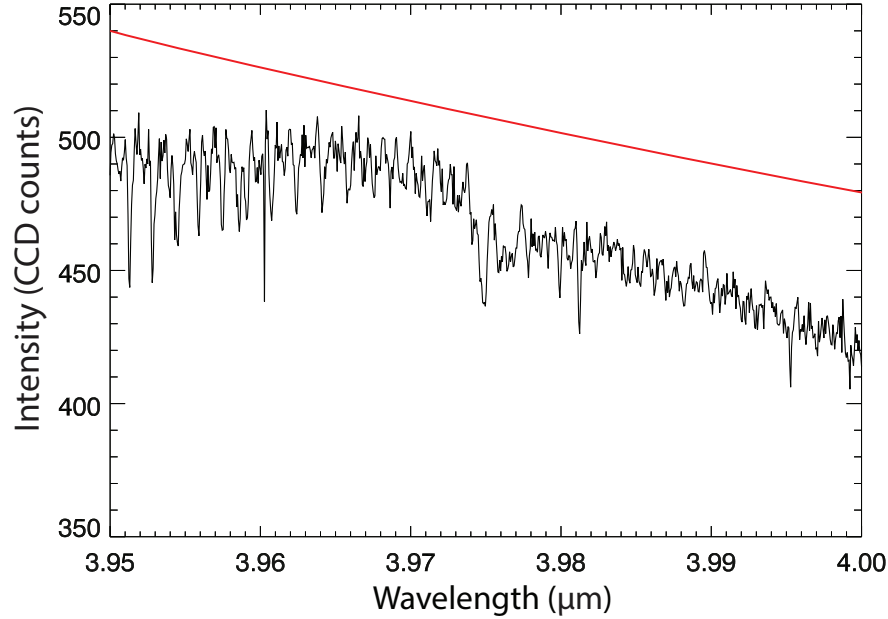


Figure 2.13: The spectrum of HR6035 - The black line shows the intensity of the standard A0 star HR6035 as a function of wavelength. This was taken by W.M. Keck and NIRSPEC on the 17th of April, 2011. Overplotted in red is the black body spectrum of an A0 star at $T = 10,000$ K. Note the irregularity due to the atmosphere of the Earth absorbing different quantities of radiation at different wavelengths.

where $F_{star}(\lambda)$ is the flux as a function of wavelength for a star, F_{λ} is the flux of the star at the detector as a function of wavelength, and where m_{λ} is the magnitude of the star at wavelength λ . For HR6035 for example, the equation reads

$$F_{star}(\lambda) = 5.24 \times 10^{-11} \times 10^{-(0.4m_{\lambda})}, \quad (2.3)$$

where $F_{star}(\lambda)$ is the flux of HR6035 at $3.8 \mu\text{m}$ wavelength, $5.24 \times 10^{-11} \text{ Wm}^{-2}\mu\text{m}^{-1}$ is the flux of α Lyr at $3.8 \mu\text{m}$, -0.4 is a constant and m_{λ} is the magnitude of HR6035 at wavelength $3.8 \mu\text{m}$, which is 6.02 in this case. This flux expresses the amount of energy per unit time that is incident on a given area at a particular wavelength. The corresponding black-body flux as a function of wavelength can

2.3 Terrestrial considerations

then be expressed as (Melin, 2006):

$$F_{bb}(\lambda) = F_{3.8} \left(\frac{3.8}{\lambda} \right)^5 \frac{\exp \frac{14388}{3.8T} - 1}{\exp \frac{14388}{\lambda T} - 1}, \quad (2.4)$$

where $F_{bb}(\lambda)$ is the black-body flux at wavelength λ which in this case is 3.8 μm , $F_{3.8}$ is as shown in equation 2.3 and T is the temperature of the star. The expression $3.8 \mu\text{m}/\lambda$ has the effect of reducing the flux at higher wavelengths of λ or increasing the flux at lower wavelengths. By dividing the theoretical flux from a perfect black-body emitter by the flux from a standard star like HR6035, a calibration spectrum is produced that is given by

$$F_{\lambda} = \frac{F_{bb}(\lambda)}{F_{star}(\lambda)}, \quad (2.5)$$

where F_{λ} is the calibration spectrum in units of ($\text{Wm}^{-2}\mu\text{m}^{-1}\text{count}^{-1}$) and where $F_{bb}(\lambda)$ and $F_{star}(\lambda)$ are from equations 2.4 and 2.2 respectively. In Figure 2.14 a flux calibrated spectrum has been produced for the star HR6035 using the above equation. This corrects for atmospheric attenuation and converts the observed counts on the array for the star into physical quantities.

The spectrum derived from Saturn emission is multiplied by this calibration spectrum to both convert it into units of ($\text{Wm}^{-2} \mu\text{m}^{-1}$) and to correct it for atmospheric attenuation. The flux calibrated spectrum is also converted from square arcseconds to units of per steradian (sr^{-1}), the standard units in the literature. This is performed as follows

$$I[\text{Wm}^{-2}\mu\text{m}^{-1}\text{sr}^{-1}] = I[\text{Wm}^{-2}\mu\text{m}^{-1}] \times \left[\frac{4.2545 \times 10^{10}}{0.43 \times 0.143} \right]. \quad (2.6)$$

where $I[\text{Wm}^{-2}\mu\text{m}^{-1}\text{sr}^{-1}]$ is the final flux calibrated intensity per steradian, $I[\text{Wm}^{-2}\mu\text{m}^{-1}]$ is the flux calibrated intensity, 4.2545×10^{10} is 1 steradian of solid angle squared

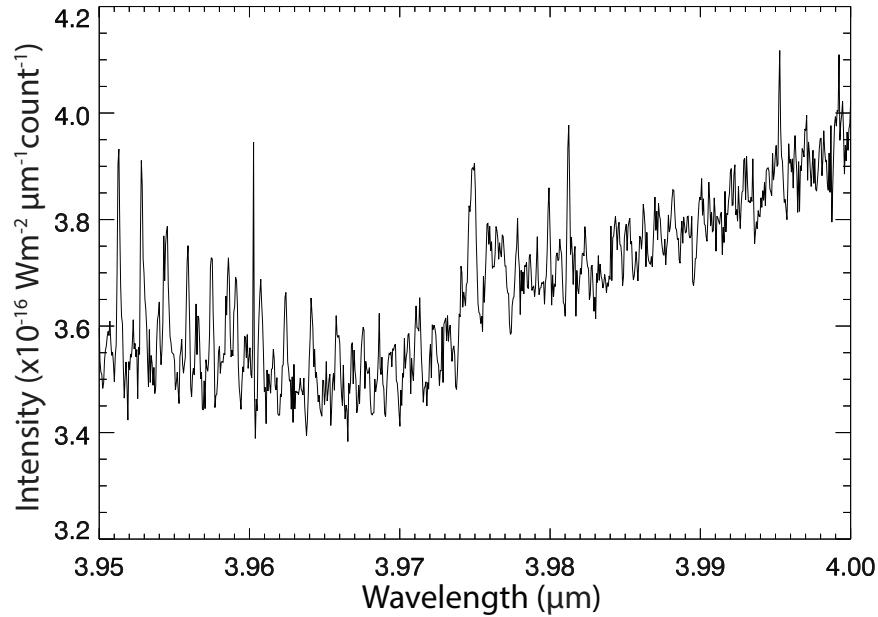


Figure 2.14: A typical flux calibration spectrum - This is from order 1 of the W.M. Keck and NIRSPEC instrument on the 17th of April, 2011. The x- and y-axes show wavelength and intensity, respectively, of light incident on the CCD's surface. Note the large variability due to atmospheric extinction in the Earth's atmosphere.

converted into seconds of arc squared and $0.42''$ and $0.143''$ are the pixel width and height in seconds of arc. A flux calibrated spectrum of Saturn is shown in Figure 2.15 in units of flux per steradian.

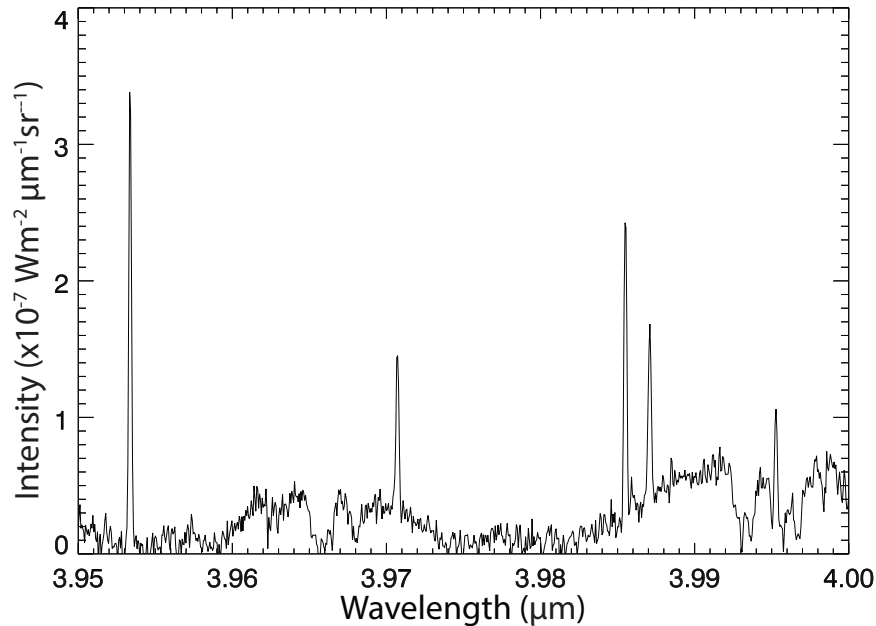


Figure 2.15: A flux calibrated profile of Saturn - This is the same as Figure 2.12, but is now corrected for the effects of atmospheric extinction. Note that the ratios between different lines of emission are now adjusted, failure to account for this would result in incorrect line ratios and thus higher errors in the derived properties listed in section 2.5.

2.4 Pixel registration

There are more adjustments that need to be made so that data from a target planet is meaningful and accurate. We need to assign latitudes or co-latitudes to each pixel and perform line-of-sight (LoS) corrections. LoS corrections are a standard practice in planetary data reduction. In this work, the greatest uncertainties in pixel registration are those introduced by atmospheric turbulence, known as seeing, defined as the full-width half-maximum (FWHM) of a point source such as a star, measured in arcseconds. Essentially, seeing is a metric of the extent to which light from a source is smeared.

It is preferable when studying the upper atmospheres of other planets to state atmospheric densities and emissions as column densities and column emissions. Column integrated properties such as these are useful because they allow a real comparison between different locations on the planet. At a given time, the pole-to-pole angular size for Jupiter and Saturn in the sky as seen from Earth is known. At the same time the target planet has a known pole-to-pole size in

2.4 Pixel registration

pixels on the CCD, so the assignment of a radial distance from the center of the planet and subsequently co-latitudes to each pixel on a CCD (known as pixel registration) is straightforward, as we can divide the number of pixels subtended by the physical size of the planet to give pixels per kilometre. First, the positions of the limbs (edges) of the planet must be found on the CCD. The peak reflected sunlight is associated with the hydrocarbon layer and is located close to the 1 bar surface of Saturn and Jupiter, so for the location of the 1 bar limb (see Figure 3.4 for illustration) we can use that as a proxy. Above the limb the intensity of reflected sunlight abruptly drops off, in other words, the largest intensity gradient is observed. For Saturn, an additional check of the position can be made by examining the reflected sunlight from the rings, which remain constantly bright on Saturn as a function of the wavelengths used in this study. This begins with fitting Gaussian distribution curves to Saturn's large, bright rings, in order to find a central ring position on the pole-to-pole cut of the planet and subsequently mapping poleward until the limbs are reached. The errors associated with pixel registration are less than 1 pixel for both Saturn and Jupiter; the similarity in pixel registration arising from the fact that the rings of Saturn provide a third data point to the two limbs and that Jupiter's angular size in the sky is twice that of Saturn's. The random error associated with seeing is responsible for adjacent pixels leaking (smearing) intensity into the well-constrained co-latitudes, and is on the order of 2 - 7 degrees latitude of smear for Saturn and 1 - 5 for Jupiter (discussed in more detail in Chapters 3 and 5). With the position of the limbs found, units of distance across the disk of the planet under study can be converted into co-latitudes, starting from 0° at the limb and reach 90° at the equator.

For the Saturn case (the Jupiter case is given in great detail in Chapter 5) we produce a model of two oblate spheroids (ellipses) of tilted at 8.2° relative to the observer on Earth. The inner ellipse perimeter at the 1 bar Saturn surface $1 R_S + 900$ km, and the outer one at $1 R_S + 2000$ km (the additions of 900 and 2000 km corresponding to the approximate range in which the bulk of the H_3^+ resides

(Moore et al., 2004; Mueller-Wodarg et al., 2012)). We can then easily find the planetocentric co-latitudes and the column depth through which we observe as a function of distance from the center of the planet in pixels or kilometres. The following equation is used to convert distances from the limb into co-latitudes:

$$\Theta = \arccos\left(\frac{R_{P,Sat} \times R_{Limb}}{R_{P,Sat}}\right) + \Theta_{SEL} \quad (2.7)$$

where Θ is co-latitude, $R_{P,Sat}$ is the polar radius of Saturn and R_{Limb} is the distance from the limb of the planet to a point within the planet's disk. The addition of the sub-Earth latitude (SEL) is also added at this stage for the planet in order to account for its axial tilt. The radius and distance can be in units of arc seconds, kilometres or pixel number. Due to viewing geometry, high latitudes and polar regions have a LoS column which is much deeper than that of low latitudes and equatorial regions. To correct for deeper columns, there must be a reduction factor applied to properties at different latitudes. This reduction will be greatest towards the limb where LoS brightening is at its largest. This simplified correction factor C is computed by equation 2.8 below

$$C = \sin(\Theta) \quad (2.8)$$

where C is the value that will multiply with the column density and total emission values, Θ is the co-latitude of the selected property as given by equation 2.7. Note that temperature is not reduced in this way because it does not change with latitude due to viewing geometry: we assume that we successfully measure the entire 900 - 2000 km altitude range in which H_3^+ exists. To elaborate further, if in the extreme case that this column is at the limb, then all of the measured H_3^+ would subtend less than 0.5 pixels. Finally, during a typical night of observations the telescope tracking means the planet will appear to move along the CCD chip.

This is corrected for by shifting the limb and rings in the spatial direction so that they are at a fixed point in each spectral image.

2.5 Extracting properties from H_3^+

Following all of the data reductions that have taken place, the spectrum of light emitted from the H_3^+ ion is now ready to have physical properties derived from its analysis. This section highlights how properties such as temperature, column density and total emission can be derived by using both the ratios of emissions of different spectral lines (line ratios) and the energies that are responsible for causing them.

2.5.1 H_3^+ transition line intensities

In a molecule or atom, a transition from a higher energy state to a lower energy state results in the emission of a photon in this work we are concerned only with the rotational-vibrational energy levels in the H_3^+ molecule, as discussed in Chapter 1. The loss of energy of H_3^+ is representative how much cooling has taken place (Miller et al., 2010). Assuming the conditions of local thermodynamic equilibrium, the intensity of a single spectral line (transition line) produced by a single H_3^+ molecule is given by (Stallard et al., 2002):

$$I(\omega_{if}, T) = g_f(2J_f + 1)hc\omega_{if}A_{if} \exp\left[\frac{-hcE_f/kT}{4\pi Q(T)}\right], \quad (2.9)$$

where subscript ‘i’ stands for initial (lower energy level) and ‘f’ for final (upper energy level), g is the nuclear spin degeneracy and J is the angular momentum. E is the energy measured at the detector whilst ω and A are the wavenumber and Einstein coefficients of the transition, $Q(T)$ is the partition function and k is Boltzmann’s constant. The factor ‘ hc ’ is used to convert wavenumber into SI

units. In this thesis, transition line intensities are found by using an in-house collection of routines that have been developed as part of the thesis work of Henrik Melin in 2006 (Melin, 2006). These routines measure multiple spectral lines simultaneously and fit them to theoretically modelled values to derive properties such as temperature, column density and total emission - which are described in detail below.

2.5.2 The partition function of H_3^+

The partition function $Q(T)$ describes the statistical properties of a system when the system is considered to be in local thermodynamic equilibrium (LTE). The partition function constants for the H_3^+ molecule used in this work are the latest (from 2010) and most accurate (by 2%) to date (Miller et al., 2010). This is an improvement on work by Neale and Tennyson (Neale and Tennyson, 1995). The new partition function of Miller et al. (2010), as used in this work, is shown in Equation 2.10 below

$$Q(T) = A_0 + A_1T + A_2T^2 + A_3T^3 + A_4T^4 + A_5T^5 + A_6T^6 \quad (2.10)$$

where $Q(T)$ is the partition function as a function of temperature and A_n are Einstein coefficients (constants). The Einstein A coefficients give the probability per unit time that an atom will spontaneously emit a photon, moving the atom to a lower energy state. For temperatures between 100 - 1800 K the coefficients are calculated *ab initio* to be:

$$A_0 = 1.11391 \text{ s}^{-1}$$

$$A_1 = 0.0581076 \text{ s}^{-1}$$

$$A_2 = 0.000302967 \text{ s}^{-1}$$

$$A_3 = 2.837240 \times 10^{-7} \text{ s}^{-1}$$

2.5 Extracting properties from H_3^+

$$A_4 = 2.31119 \times 10^{-10} \text{ s}^{-1}$$

$$A_5 = 7.158950 \times 10^{-14} \text{ s}^{-1}$$

$$A_6 = 1.00150 \times 10^{-17} \text{ s}^{-1}$$

Miller et al. (2010) state that the previous partition function constants by Neale and Tennyson (1995) underestimated the amount of heat that is radiated into space by H_3^+ . In Figure 2.16 we show that Neale et al derive a higher partition function for all temperatures. Temperatures derived by Miller et al are between 13 to 33 K warmer compared to Neale et al.

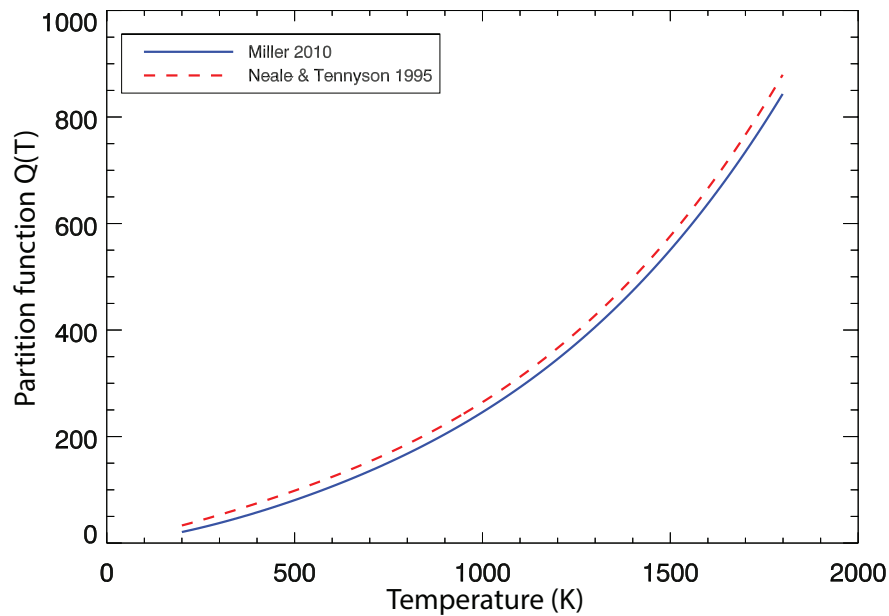


Figure 2.16: $Q(T)$ as a function temperature - This figure illustrates that different partition function ($Q(T)$) values lead to different derived temperatures. Miller et al. (2010) has a lower partition function at any given temperature.

2.5.3 H_3^+ temperature calculation

The H_3^+ molecule is considered to be in quasi-local thermodynamic equilibrium with its surroundings and therefore its temperature is representative of the region of atmosphere in which it measured (Miller et al., 1990b) (see Subsection 1.4.2). To calculate the effective ro-vibrational temperatures of H_3^+ , $T(\text{H}_3^+)$, the relative intensities between different transition lines calculated by Equation 2.9 must be found. First, the ratio of the intensities of two transition lines (subscript) ‘a’ and ‘b’ can be written as

$$\frac{I(\omega_a)}{I(\omega_b)} = \frac{g_a(2J_a + 1)hc\omega_a A_a \exp\left[\frac{-E_a}{kT}\right]}{g_b(2J_b + 1)hc\omega_b A_b \exp\left[\frac{-E_b}{kT}\right]} \quad (2.11)$$

where g is the nuclear spin degeneracy, J is the angular momentum, E is the energy measured at the detector, ω is the wavenumber which is multiplied by hc to obtain SI units for energy, k is Boltzmann’s constant and A is the Einstein coefficient of the transition. To simplify this equation, the constant gamma (γ) is introduced, which is defined as follows

$$\gamma = \frac{g_a(2J_a + 1)hc\omega_a A_a}{g_b(2J_b + 1)hc\omega_b A_b} \quad (2.12)$$

If we insert Equation 2.12 into Equation 2.11 we obtain

$$\frac{I(w_a)}{I(w_b)} = \gamma \exp\left[\frac{(E_b - E_a)}{kT}\right] \quad (2.13)$$

Which we can then solve for temperature T to produce a temperature which

2.5 Extracting properties from H_3^+

depends on the ratio between the intensity of two different spectral lines

$$T(H_3^+) = \frac{\frac{[E_b - E_a]}{k}}{\ln \gamma - \ln \left[\frac{I(w_b)}{I(w_a)} \right]} \quad (2.14)$$

Theoretical spectral lines as a function of temperature for H_3^+ originate from a database known as a ‘linelist’ in which the user may select a temperature and wavelength range in which to view the spectrum of H_3^+ . The linelist used in this thesis was developed in 1996 and contains over 3 million transitions of the H_3^+ molecular ion Neale et al. (1996a). In addition, this linelist (and many others) have been made freely available to download via the internet by University College London from <http://www.exomol.com/data/molecules/>. Figure 2.17 shows a plot of line ratio against temperature between 100 - 1300 K for two R-branch lines at 3.41277 μm and 3.45483 μm . The ratio displayed is found by fitting a Gaussian to each line to find the maximum intensity.

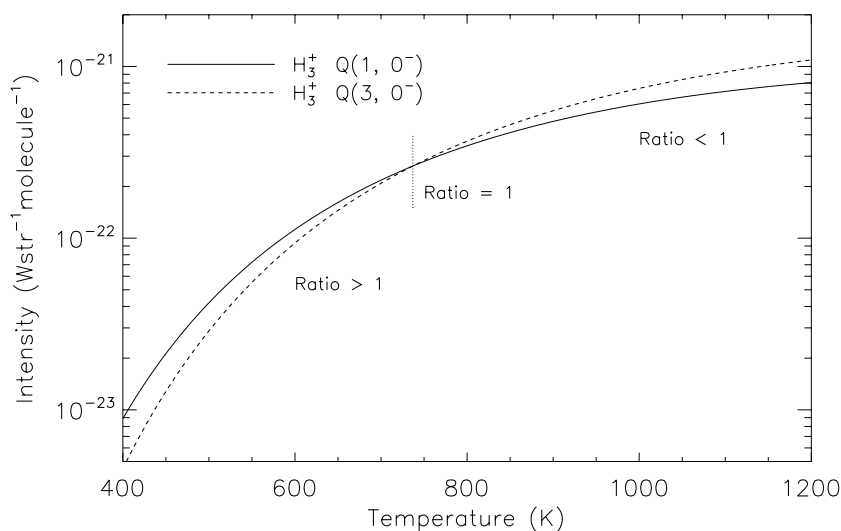


Figure 2.17: Line ratio example - This illustrates Equation 2.14 for a range of temperatures, showing how a simple ratio between two lines can obtain a temperature. These lines are located in the Q-branch as noted. Figure 1 from Melin et al. (2014).

Uncertainties in temperature fitting arise from the uncertainties in the fit of Gaussian distribution curves to the spectral lines used, an increase in the S/N

ratio will thus decrease uncertainties. The peak intensity is subject to errors as large as the fraction of background hydrocarbon reflection (noise) at the base of H_3^+ spectra divided by the measured peak intensity of the spectral line being measured. These errors can be very small for low background noise at the poles, but much larger as measurements proceed equatorward; eventually it is impossible to fit a Gaussian curve to a spectral line due to hydrocarbon noise having a higher intensity than that of H_3^+ . The routines developed in the thesis work of Henrik Melin (Melin, 2006) compute this error automatically.

2.5.4 H_3^+ column density calculation

The column density ($N(H_3^+)$) is the average density in units of molecules per metre squared (m^{-2}) of a given volume of material, in this case H_3^+ . The density of H_3^+ is linked to the ionisation rate, hence H_3^+ production, and thus shows where the H_3^+ aurorae are located. In order to calculate column density, the overall intensity must be compared with emissions from a single molecule. Due to the temperature of H_3^+ being intrinsically linked with the internal energy of the system, the previously derived temperature is used to calculate the molecular emission. As the intensity of the spectrum is already known, it is divided by the theoretical single-molecule emission to find the LoS column density $N(H_3^+)$ in units of m^{-2} as shown below

$$N(H_3^+) = \frac{I_{obs}}{I_{calc}(T)} \quad (2.15)$$

where I_{obs} is the observed intensity in units of $Wm^{-2}sr^{-1}$ of a given spectral line and I_{calc} is the calculated emission of that line as a function of temperature T in units of Wsr^{-1} . To calculate the total energy emitted by an H_3^+ molecule at a

2.5 Extracting properties from H_3^+

particular temperature the following equation is used (Miller et al., 2010):

$$\begin{aligned}
 E_{mol}(H_3^+, T) = & -6.11904 \times 10^{-21} + 4.96694 \times 10^{-23} T - 1.44360810^{-25} T^2 \\
 & + 1.6092610^{-28} T^3 - 3.87932 \times 10^{-32} T^4
 \end{aligned}
 \tag{2.16}$$

where $E_{mol}(H_3^+)$ is the total rate of emission by a single molecule of H_3^+ at temperature T and the constants are from *ab initio* computations. This equation covers temperatures in the range $T = 400 - 900$ K, which is an acceptable range of temperatures for Saturn (expected 400 - 700 K). However, for Jupiter the expected highest temperatures can be up to 1,100 K, in which case it is appropriate to use the following equation

$$\begin{aligned}
 E_{mol}(H_3^+, T) = & -8.24045 \times 10^{-21} + 3.54583 \times 10^{-23} T - 8.6629610^{-25} T^2 \\
 & + 9.7660810^{-29} T^3 - 1.61317 \times 10^{-32} T^4
 \end{aligned}
 \tag{2.17}$$

This is the same as Equation 2.16 but has new constant terms that are suitable for temperatures: $T = 900 - 3000$ K. In this work, the fitting routines check the temperature first and then select which constants to use. The associated errors in column densities arise from two factors; the accuracy of measurement of peak intensity for a given spectral line, and the accuracy of the derived temperature. The former is calculated in the same manner as discussed in Subsection 2.5.3 for temperature. Anti-correlations observed between H_3^+ temperature and density are often seen as a product of this fitting routine, and recent work by Melin et al. (2014) shows that such anti-correlation is a physical phenomenon provided that it is outside of the range of uncertainties involved, as opposed to a product of the least-squares fit. The uncertainties in column density and total emission are from Cramer's rule in-bedded within the H_3^+ fitting routine and they are an indicator

of the quality of the spectral fit (see Melin et al. (2014) and Melin (2006) and references therein for a more thorough discussion of the fitting routine).

2.5.5 H_3^+ total emission calculation

This parameter was introduced by Lam et al. (1997) for Jupiter, to be used as a separate parameter for studying the ionosphere, due to their observation of an anti-correlation between temperature and column density. $E(H_3^+)$ is a useful parameter as it reveals the amount of energy lost by the ionosphere via radiative cooling to space. The principle advantage of this term is that it provides a probe into the bulk energy of a given region of thermosphere. It is also useful because it has errors of typically less than 1%, and removes the effects of anti-correlation. $E(H_3^+)$ is the sum of emission across all transition lines and is multiplied by the column density to give the total emission (per steradian) of all molecules in a given LoS column of H_3^+ as defined below

$$E(H_3^+) = E_{mol}(H_3^+, T) \times N(H_3^+, T) \quad (2.18)$$

where $E_{mol}(H_3^+, T)$ is the total emission per molecule, $N(H_3^+, T)$ is the column density and T is the temperature. Note that the following parameters are for H_3^+ , e.g. by E we mean $E(H_3^+)$; this notation is dropped for readability. The uncertainties in total emission, E are given by the temperature and column density (and their respective uncertainties) using the general formula for error propagation,

$$\Delta E = \sqrt{\left[\frac{\delta E}{\delta N} \Delta N\right]^2 + \left[\frac{\delta E}{\delta T} \Delta T\right]^2}, \quad (2.19)$$

where ΔE , ΔT , ΔN are the errors in total emission, temperature and column density, respectively. Additionally, $\delta E/\delta N$ and $\delta E/\delta T$ are the partial derivative

2.5 Extracting properties from H_3^+

of total emission with respect to N and T , which can be given as

$$\frac{\delta E}{\delta N} = \frac{\delta}{\delta N}(NE) = E, \quad (2.20)$$

and

$$\frac{\delta E}{\delta T} = \frac{\delta}{\delta T}(NE) = N \frac{\delta E}{\delta T} = N(C_1 + 2C_2T + 3C_3T^2 + 4C_4T^3), \quad (2.21)$$

where C_n represent constants which depend on temperature from Equations 2.16 and 2.17. Which can then finally be re-arranged to form the total emission error

$$\Delta E = \sqrt{(E\Delta N)^2 + (N\Delta T(C_1 + 2C_2T + 3C_3T^2 + 4C_4T^3))^2}. \quad (2.22)$$

Chapter 3

Ring ‘rain’ on Saturn’s ionosphere

The work in this chapter represents one of the first direct studies of the low-latitude ionosphere of Saturn, and reveals the influence of Saturn’s rings on ionospheric chemistry. We discuss the discovery, interpretation and implications of Saturn’s ring ‘rain’ within the ionosphere (O’Donoghue et al., 2013).

Saturn’s ionosphere is produced when the otherwise neutral atmosphere is exposed to a flow of energetic charged particles or solar radiation (Stallard et al., 2012b). At low latitudes, the latter should result in a weak planet-wide glow in infrared (IR), corresponding to the planet’s uniform illumination by the Sun (Miller et al., 2010). However, in addition to the solar EUV ionisation, the low latitude ionosphere could also be affected by an exogenous water influx from the rings and moons (e.g. Enceladus water influx (Stallard et al., 2008)). A planet-ring magnetic connection has been previously suggested in which an influx of water from the rings could explain the lower than expected electron densities in Saturn’s atmosphere (Connerney and Waite, 1984; Connerney, 1986; Wilson and Waite, 1989). In this chapter, we discuss the detection of a pattern of features within the H_3^+ emission, extending across a broad latitude band from $\sim 25^\circ$ to 60°

3.1 Introduction to low-latitude H_3^+ at Saturn

in both hemispheres, that is superposed on the lower latitude background glow, with peaks in emission that map along the planet's magnetic field lines to gaps in Saturn's rings. This pattern implies the transfer of charged water products from the ring-plane along magnetic field lines to the ionosphere, revealing an influx on between 30 to 43% of the planet's upper-atmospheric surface. This ring 'rain' could play a fundamental role in modulating ionospheric emissions and suppressing electron densities.

3.1 Introduction to low-latitude H_3^+ at Saturn

Observations of Saturn's low-latitude ionosphere via the H_3^+ molecular ion began with a study by Stallard et al. (1999). The authors obtained and co-added 36-minutes of exposures using the NASA IRTF and facility echelle spectrometer (CSHELL) in October 1998. At the time, Saturn was in conditions of southern summer, with a Sub-Earth Latitude (SEL) of 19.2° , giving an extended view of the southern hemisphere. The resulting H_3^+ profile of intensity from pole-to-pole is shown in Figure 3.1 and is the first pole-to-pole profile of H_3^+ intensity. Clear from the profile is that the noise is high along the non-auroral component (the body of the planet), which has led to a jagged profile of dozens of peaks and troughs as opposed to a smooth drop-off in intensity from the auroral regions; Stallard et al. (1999) concluded that no emissions could be clearly identified given this low signal-to-noise (S/N) ratio profile.

More recent observations taken using the NASA IRTF and CSHELL instrument (Greene et al., 1993) in 2005, 2007 (Stallard, private communication) and 2010 (Stallard et al., 2012b), show H_3^+ intensity profiles with higher S/N ratios, owing to longer integration times of several hours of exposure each year. These profiles are shown in Figure 3.2. The background noise is greatly reduced in these recent observations, leading to a relatively smooth H_3^+ intensity from pole-to-pole, particularly in the bottom panel. However, a series of features such as peaks and

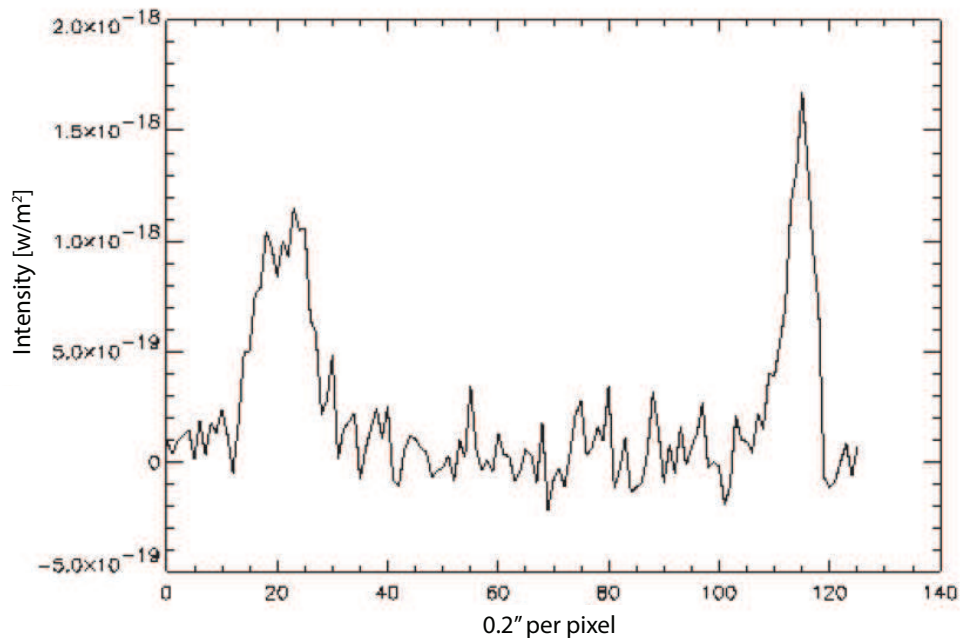


Figure 3.1: First low-latitude observations of H_3^+ - This figure is taken from Stallard et al. (1999) (figure 2). It derives from the fundamental spectral emission line of H_3^+ , the $\text{Q}(1,0^-)$ line. From left to right, the southern and northern hemispheres are shown - the high intensity at ~ 20 and ~ 115 pixels is associated with the main auroral ovals. The estimated ring position is between pixels 75 and 100 and the high intensity solar reflected sunlight from these locations has been removed for clarity.

3.1 Introduction to low-latitude H_3^+ at Saturn

troughs appear to be present, hinting that there may be some low-latitude structure at least some of the time. Important to note is that the larger slit widths allow significantly more light to hit the CCD (described in the figure), thus we see the largest low-latitude emissions in the lower panel.

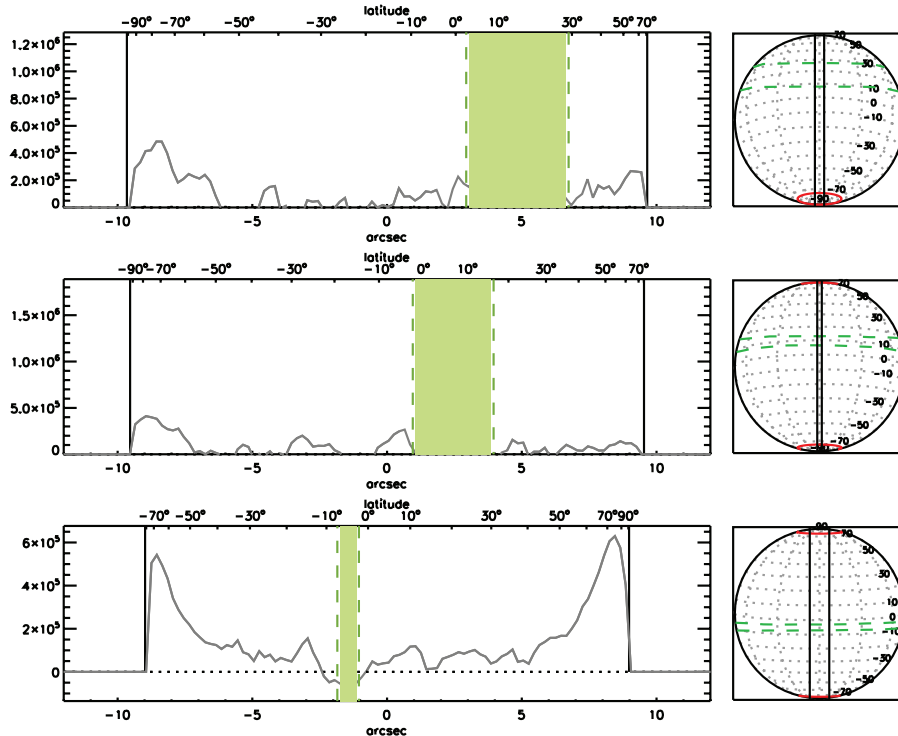


Figure 3.2: Recent low-latitude H_3^+ observations - These 3 panels derive from data obtained by the NASA IRTF in 2005, 2007 (Stallard, private communication) and 2010 (Stallard et al., 2012b) from top to bottom. Within each one, pole-to-pole H_3^+ intensity (arbitrary units, dark grey line) on the vertical axis as a function of latitude and arcseconds subtended in Earth's sky on the horizontal axes. Positive latitudes indicate northern hemisphere values. The emission has been line-of-sight (LoS) corrected. The rings are denoted by the green shaded area enclosed by dashed green lines. The panels to the right indicate the orientation of Saturn as viewed from Earth and show the location of the main auroral oval in red. The panels have spectral slit widths and spectral resolutions as follows, Top: $1.0''$ and $R = \lambda/\Delta\lambda \sim 21,500$; Middle: $0.5''$ and $R = \lambda/\Delta\lambda \sim 43,000$; Bottom: $2.0''$ and $R = \lambda/\Delta\lambda \sim 10,800$.

Equatorward of the auroral regions, Saturn was expected to exhibit a uniform brightness similar to that of Jupiter (Stallard et al., 2012b), corresponding to uniform illumination by the sun. In Figure 3.3 we show an example of an H_3^+ intensity profile of Jupiter from pole-to-pole. These data were obtained with the NASA IRTF in July 1996 by Rego et al. (2000), and using the IR instrument

3.2 Saturn-specific data acquisition

CSHELL (see Greene et al. (1993)), a spatial resolution of $0.2'' \text{ pixel}^{-1}$ was obtained, which is similar to that of the W.M. Keck telescope used here for Saturn. The integration time was ~ 15 minutes, during which time Jupiter rotated 9° , making it comparable to the observations of Saturn we will present in this chapter. The smoothly falling intensity of H_3^+ emission at sub-auroral latitudes at these particular longitude swaths illustrates the lack of variability from pole-to-pole. However, this is revisited in more detail in Chapter 5, where we find that longitudinal effects are important for Jupiter.

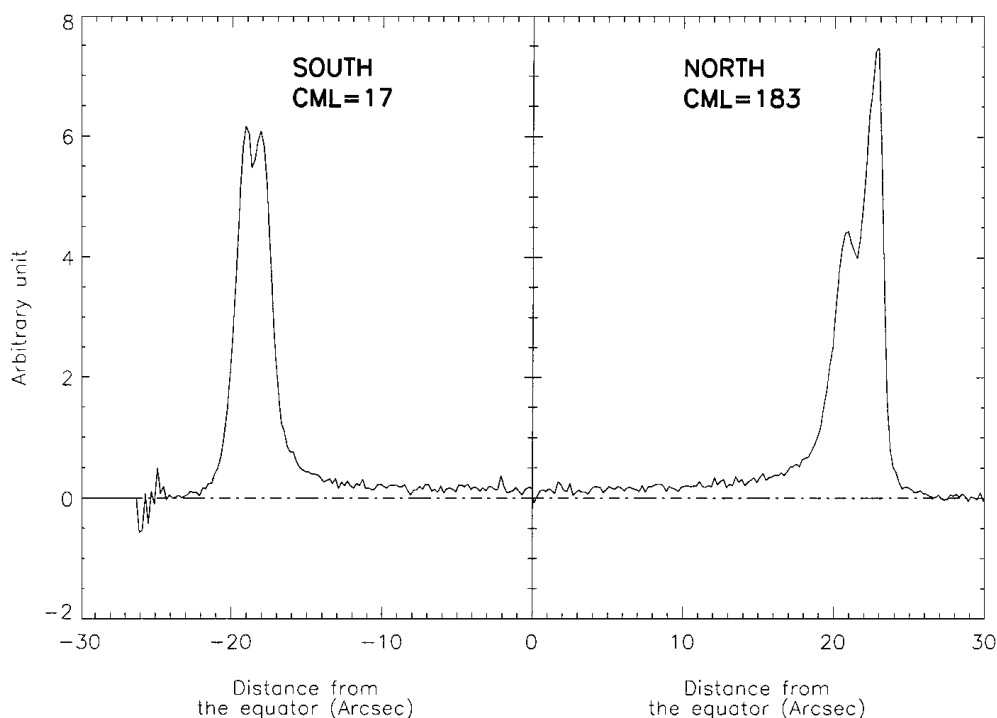


Figure 3.3: Simple Jupiter profile - The $Q(1,0^-) \text{H}_3^+$ emission line intensity for Jupiter plotted as a function of spatial scale. The southern hemisphere is to the left, the northern to the right. Central Meridian Longitudes (CML) indicated in the figure are given in the Jupiter System III coordinate system, where they correspond to the beginning of a 9° integration mentioned in the main text. This plot is Figure 2 from Rego et al. (2000).

3.2 Saturn-specific data acquisition

The following subsections outline the observing methods, conditions, instrumental settings and subsequent data selection relevant to this chapter.

3.2.1 Observational setup

This study examines ~ 2 hours of data obtained between 10:33:42 and 12:46:28 Universal Time (UT) on April 17 2011, using the 10-metre Keck telescope. The data were reduced using the standard astronomical data reduction techniques discussed in Chapter 2; in this chapter we thus only discuss the instrument settings, observational conditions and any unique methodology employed. On the night of these observations, Saturn's northern hemisphere was tilted towards Earth with a SEL of 8.2° , during conditions of Saturn early northern spring. The skies were clear of clouds, though thin cirrus may have passed by during the observations. The seeing was $\sim 0.4''$ and was calculated by the telescope's guide star system. The dataset was obtained using the NIRSPEC spectrometer (McLean et al., 1998) in high-resolution cross-dispersed mode (resolution of $R = \lambda/\Delta\lambda \sim 25,000$) as described in Subsection 2.1.2. The slit on the spectrometer was positioned along Saturn's noon meridian as shown in Figure 3.4 and the intensity of two bright H_3^+ ro-vibrational emission lines is visible almost completely from pole-to-pole, such that low-latitude emissions can be studied. The planet rotates beneath the slit, allowing the acquisition of spectral images at a fixed local time, but varying in Saturn longitude. In addition, note that the dipole axis of Saturn's magnetic field is almost exactly aligned (within 0.1°) to its axis of rotation (Burton et al., 2010).

The spectra taken consist of the co-addition of twelve 5-second integrations, creating exposures 60 seconds long. During one such exposure, Saturn rotates 0.57° CML in the Saturn longitude system III (SLS III) coordinate system (Kurth et al., 2008), a negligible amount given that the width of the slit covers $\sim 2.6^\circ$ CML. The H_3^+ emission emanating from Saturn is a LoS integrated column, so we see more than just the radially outward emissions from the planet's surface. In the ~ 2 hours of recorded data, 21% of longitude of the planet was observed - between $101 - 177^\circ$ longitude. The telescope movement during the observations has been corrected for by aligning each spectral image to the position of the main rings and

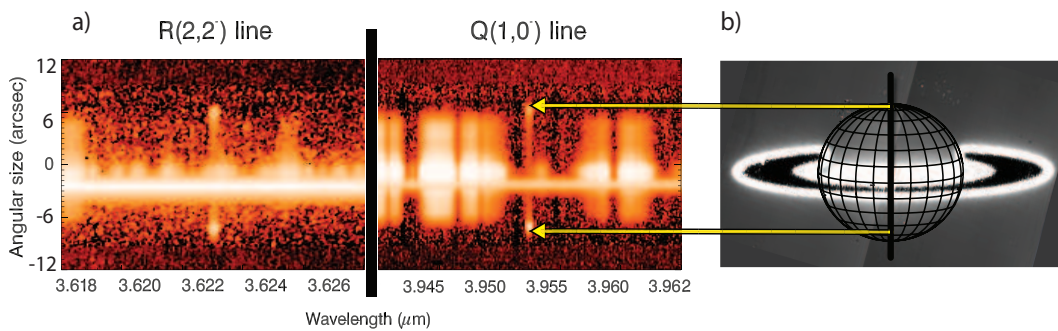


Figure 3.4: Observational set-up - The spectral images shown in a) are separated by a thick black line to indicate the different wavelength ranges. The horizontal and vertical axes in these ranges show wavelength and spatial position along the slit, respectively, whilst intensity ranges from low to high from black to orange to white. Two spectral lines, $Q(1,0^-)$ at $3.953 \mu\text{m}$ and $R(2,2^-)$ at $3.622 \mu\text{m}$, are centered in each wavelength range, and are from the Q- and R-branches of the H_3^+ emission spectrum. These spectra are obtained through the slit of the spectrometer seen in b), which was orientated in the north-south position on Saturn, aligned along the rotational axis. The bright IR emission measured at the -3 arc second position in a) across the entire wavelength range is the uniform reflection of sunlight by the rings, whilst the remaining bright white areas are due to hydrocarbon (e.g. methane) reflection on sunlight. This background methane reflection obscures the $R(2,2^-)$ line emission more than the $Q(1,0^-)$ line, leading to a lower signal-to-noise ratio.

in doing so the pixels were registered, i.e. assigned co-latitude values, as detailed in Subsection 2.4.

3.2.2 Data selection

The atmospheric seeing of $\sim 0.4''$ translates to an intensity ‘smearing’ on the planet of $\sim 2^\circ$ rising to $\sim 4^\circ$, between the range of 28° and 52° latitude. To provide an accurate latitudinal mapping of the $Q(1,0^-)$ line, we selected the data in which the rings were least broadened by seeing; this was done by fitting Gaussian curves to the intensity of the rings along the noon meridian in order to collect a FWHM in pixels of the rings for each of the 47 spectral images. Next, a median of all 47 spectral images was taken; if the ring width was smaller than the median ring width of all data it was selected for the study, whilst those that were of large width were not - this is shown clearly in Figure 3.5. This led to a total 38 minutes of exposures (19 images) for the $Q(1,0^-)$ line. This rather harsh selection criterion yields an excellent S/N as we shall soon see, but results in very little signal left if applied to the $R(2,2^-)$ line data. Only three images were removed from the $R(2,2^-)$ line and these were the images in which the rings were greater than 5 pixels in width. The drawback in only eliminating three images is that the latitudinal uncertainty increases because of the higher-seeing data.

For a seeing of $0.4''$, the pixel blurring (or smearing) is 2.8 pixels (as 1 pixel = $0.144''$). Due to viewing geometry, a single pixel may represent several degrees latitude at the poles and just ~ 2 near the equator, thus the effect of seeing changes as a function of latitude. In Figure 3.6 we have converted seeing in pixels to a corresponding latitudinal smearing to illustrate the effect that seeing has at different latitudes.

The $Q(1,0^-)$ and $R(2,2^-)$ spectral lines at $3.622 \mu\text{m}$ and $3.953 \mu\text{m}$ also had a spectral background subtraction performed to improve the signal, as shown in Figure 3.7. This was performed in order to eliminate any possible intensity variation in the spatial component of the CCD that would result in intensity

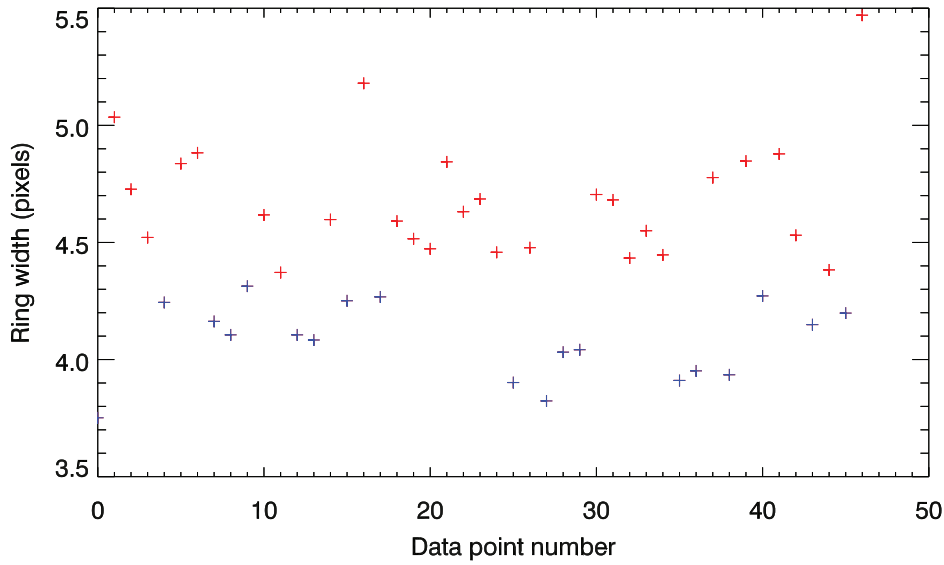


Figure 3.5: Saturn’s rings smeared by seeing - This illustrates the 47 data points (spectral images; x-axis) available for this study and their corresponding measured ring-width in pixels. The larger the seeing, the larger the width of the rings and so the worse the latitudinal resolution will be. As described in the text, the threshold for selection for the $Q(1,0^-)$ line was the median of all data points: the 19 blue symbols were those below the median (good seeing) and the 28 red were the ones above (bad seeing). Only the three data points above 5 were not selected for the $R(2,2^-)$ line.

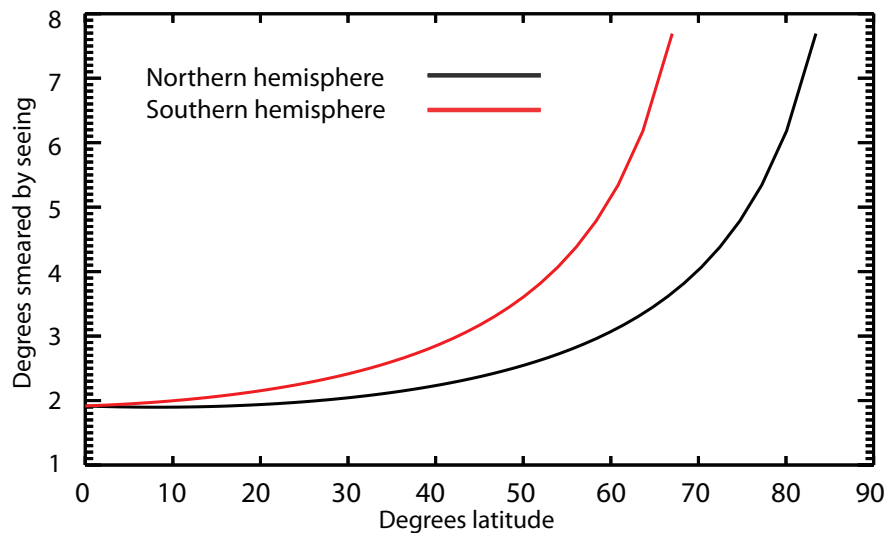


Figure 3.6: Latitudinal error as a function of latitude - Here, the x- and y-axes show latitude on Saturn and the corresponding error in latitude induced by the effect of atmospheric attenuation (seeing), respectively. The black and red lines indicate the northern and southern hemispheres. Note that the southern hemisphere is more susceptible to errors in seeing due to viewing geometry

3.2 Saturn-specific data acquisition

variations as a function of latitude in the H_3^+ emission. There are two likely candidates for a modulation such as this. The first is that bright lines have previously been seen overlain across the entire spectral image (on many telescopes and instruments); the cause for this is unknown and it is rarely seen, but could be the result of an unexpected heating of the CCD chip during the observations, even though spatial variations are unlikely to be instrumental because dark current by this point has been removed. The second is that little is known about hydrocarbon sunlight reflection as a function of latitude, and wavelengths near the discrete H_3^+ lines are modulated by unforeseen hydrocarbon intensity structure. Subtracting this region therefore ensures that the emissions in the blue box region shown in Figure 3.7 are representative of only H_3^+ emission. The signal strength of the subtracted box is less than 5% that of the $Q(1,0^-)$ line, the main line relevant for the work herein, so there is negligible contribution from this subtraction.

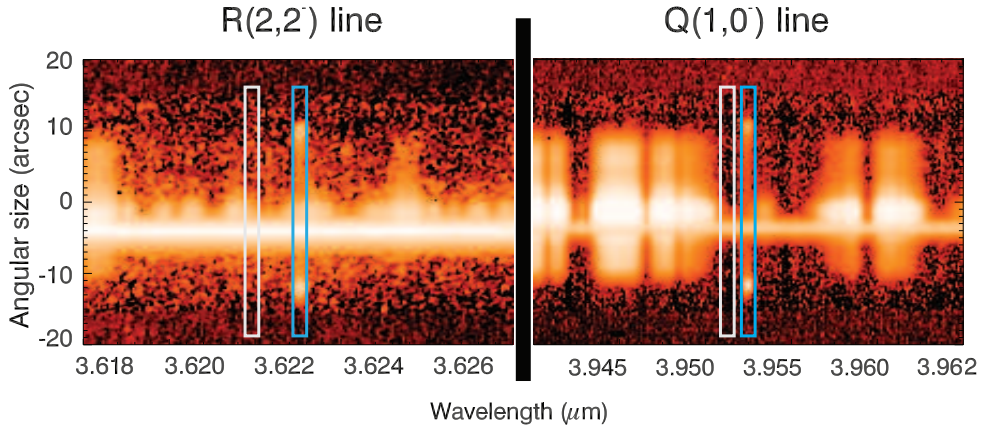


Figure 3.7: Background subtraction regions - The $Q(1,0^-)$ and $R(2,2^-)$ H_3^+ lines are shown within the highlighted blue regions, the spectral backgrounds that were smoothed and subtracted are shown as white boxes adjacent to these spectral lines. The $Q(1,0^-)$ line background region is directly adjacent (~ 10 pixels away) whereas the $R(2,2^-)$ background is taken from ~ 20 pixels away as explained in the main text.

To determine the background subtraction area we set two conditions. The first is that the box should be over 5 pixels away from the existing H_3^+ line - this is to avoid subtracting the H_3^+ from the line itself. The second condition is that the low latitude hydrocarbon and ring intensity (which is reflected sunlight) needs to be similar in terms of pattern and intensity to how it is near the H_3^+

3.2 Saturn-specific data acquisition

line. The former condition is trivial, but the latter is approximated empirically by studying the north-south profiles at multiple wavelengths. In Figure 3.8 we show an example background subtraction region in terms of intensity as a function of pixel position. Note that the background region was also smoothed by 5 pixels in order to avoid stochastic noise. The subtraction itself does not greatly change the overall profile in terms of peaks and troughs, however, it does reduce the intensity of the low latitude region. An improvement in methodology would be to fit Gaussian distribution curves to the spectral line, from pole-to-pole. However, the S/N ratio meant such fits failed at most latitudes.

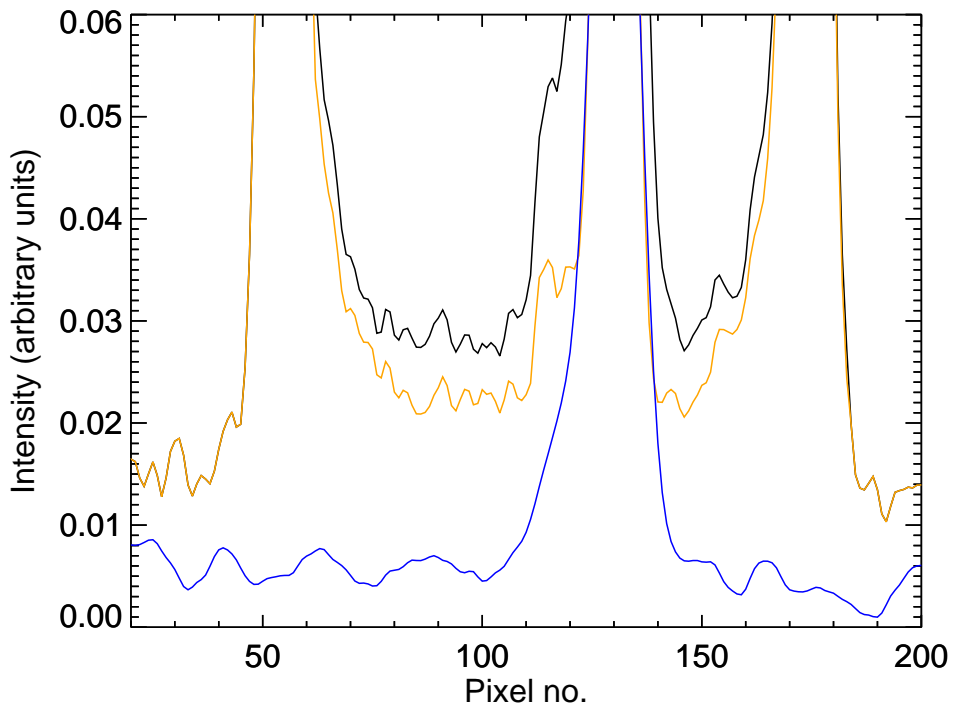


Figure 3.8: Background subtraction effect - H_3^+ $\text{Q}(1,0^-)$ line intensity (y-axis) as a function of pixel position (x-axis) is shown as black and orange corresponding to before and after a background subtraction, respectively. The blue line corresponds to the background intensity that was subtracted. This plot is similar to Figure 3.1 although in this case the north is the large peak in intensity centered at pixel 55 and the south at pixel 175. The peak in intensity at pixel number 130 is the reflection of the rings the right.

3.3 Low-latitude H_3^+ emission

Here we examine the intensity of H_3^+ emission in two spectral lines, as a function of latitude. We discuss the results of the aforementioned observations in the context of previous studies and expectations and describe the magnetic field mapping used.

3.3.1 Magnetic field model: Bunce et al., 2008

An axisymmetric magnetic field like Saturn's and the conservation of magnetic flux means that we can use a flux function which produces contours of magnetic flux around the planet, such that mapped locations can be found by setting $F_{ion} = F_{eq}$ (ionospheric flux equals equatorial flux) (Bunce et al., 2008b; Nichols and Cowley, 2004). Here we use the axisymmetric magnetic mapping model of Bunce et al. (2008b) based on Cassini data, with updated internal field coefficients from Burton et al. (2010). This field model contains the full order-3 internal field, ring current, oblateness of the planet and a choosable height in the ionosphere to map latitudes on the planet via magnetic field lines to the equatorial plane. The spherical harmonic coefficients used were $g_1 = 21,136$ nT, $g_2 = 1,526$ nT and $g_3 = 2,219$ nT and are associated with the dipole, quadrupole and octupole terms, respectively. A number of parameters within the model can be varied, leading to latitudes mapping from the planet to varying distances in the equatorial plane. The sub-solar magnetopause distance was set to 20 planetary radii from Saturn's center; this was not measured empirically but is a typical value derived from observations. Variations in this parameter lead only to marginal differences in mapping at the latitudes discussed in this chapter, e.g. magnetopause distances between 16 - 26 R_S (the full expected range) leads to a difference of just $\pm 0.5^\circ$ in latitude mapping for a given radial distance at $\sim 45^\circ$ latitude (Bunce et al., 2008b). The height of the ionosphere was set to 1,000 km above the 1 bar level at the equator, where the peak H_3^+ density is approximately located (Stallard et al.,

2012a). Adjusting this value by a few 100s of kilometres makes little difference in mapping. The 1 bar level is at 1 Saturn planetary radii, which itself was set to the IAU definition of 60,268 km.

It is worth noting that the magnetic field data from the Cassini spacecraft used by this magnetic field model is based on orbits through magnetic field lines mapping to outside of $2.1 R_S$, because the rings obstruct orbits inside of this radius. Because of this, there may be an increasing uncertainty in mapping from the equatorial plane planetward of $2.1 R_S$ which represents latitudes equatorward of 65° . This model was employed in the work herein because 1) it is the most recent available and 2) it is the only model based on multiple orbits worth of collected magnetic field data.

3.3.2 Observational result

The two bright H_3^+ ro-vibrational emission lines from Figure 3.4 are plotted as a function of latitude in Figure 3.9. In this figure, a portion of the midnight meridian is seen due to the 8.2° SEL; the limbs seen are therefore not at 90° . The $\text{Q}(1,0^-)$ line is of considerably higher intensity at all latitudes peaking in intensity at $\sim 0.3 \mu\text{Wm}^{-2}$, whilst the $\text{R}(2,2^-)$ line peaks at $\sim 0.15 \mu\text{Wm}^{-2}$, both in the southern hemisphere. These auroral regions near the limb are the subject of the Chapter 4.

Far from being featureless as we might expect by analogy to Jupiter (Stallard et al., 2012b), the mid- to low-latitude H_3^+ emissions show a number of peaks and troughs before increasing strongly towards the two polar auroral regions; a number of these peaks are observed in both spectral lines. The $\text{Q}(1,0^-)$ line shows more substantial peaks and troughs at mid- to low-latitudes than that of the $\text{R}(2,2^-)$ line; this is owing to the fact there is less contamination by reflected sunlight in neighbouring spectral pixels where methane is not absorbing this light effectively (see again Figure 3.4). The apparently symmetric peaks and troughs do not occur at the same latitudes either side of the equator. These features

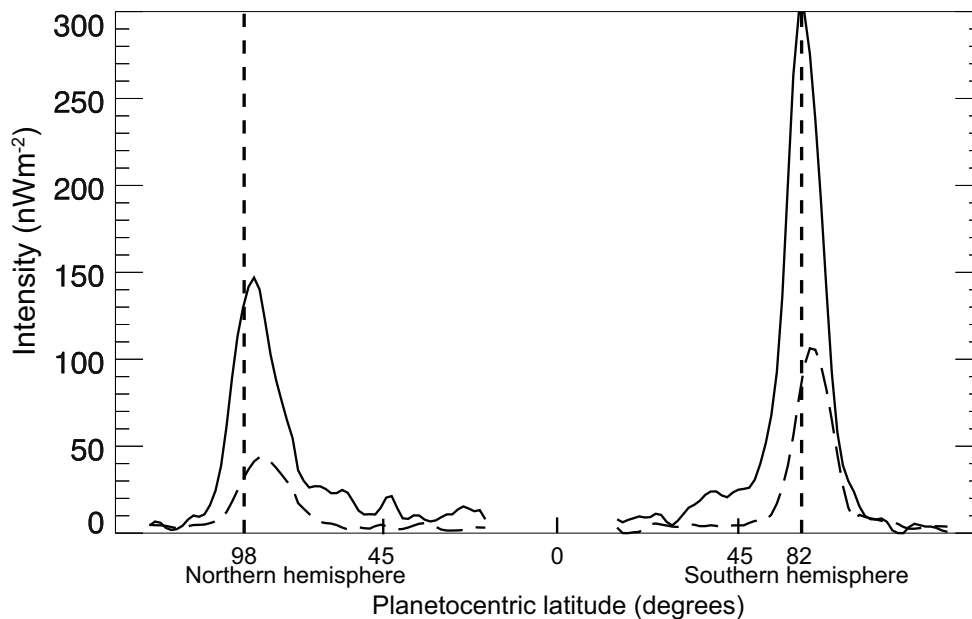


Figure 3.9: Saturn’s pole-to-pole H_3^+ IR emission - Here, a basic plot of the discrete $\text{Q}(1,0^-)$ and $\text{R}(2,2^-)$ spectral lines of H_3^+ are shown as a solid line and long-dashed line, respectively. The x-axis is planetocentric latitude in degrees whilst the y-axis is the intensity of the observed emission. Northern and southern hemispheres and the dashed lines which represent the planetary limbs (as observed) are indicated. The 98° marker represents the northern midnight sector. The data gap in the middle corresponds to ring emission that is removed.

occur at higher latitudes in the north than in the south. The lack of latitudinal symmetry along with the absence of a similar variability at Jupiter (Stallard et al., 2012b), suggests the phenomenon is unrelated to weather patterns or other processes produced in the neutral atmosphere. Instead, the peaks in emission are found to be mapped via planetary magnetic field lines to gaps in Saturn’s rings. In Figure 3.10, we zoom in to the mid-latitude regions of the ionosphere and we relate the intensity there to different features in the rings that are joined by magnetic field lines. The Cassini division is the largest gap within the rings and acts as the divider between the A and B rings at $\sim 2.1 R_S$. The latitudes to which this magnetically maps in both the northern and southern hemispheres have prominent peaks in H_3^+ intensity, particularly in the $\text{Q}(1,0^-)$ line. The Herschel, Laplace, Encke and Keeler gaps are significantly smaller in width and lie slightly further out in the ring plane: these magnetically map to latitudes (within $\sim 1^\circ$) of the Cassini division, so these will henceforth be included in our

definition of the Cassini division. The Colombo gap lies within the C ring at $\sim 1.29 R_S$ and also maps to prominent intensity peaks in Saturn's northern and southern ionospheres, though not as precisely as the other gaps. In addition, we define the 'instability region' as the region between two 'instability radii' located at $1.52 R_S$ and $1.62 R_S$. These are two regions in which the outward centrifugal forces on particles balance with the inward gravitational forces within the rings (Northrop and Hill, 1982, 1983). Within the instability at $1.62 R_S$ a ring particle or dust grain (henceforth particle) can follow magnetic field lines and enter Saturn if given a velocity component perpendicular to the ring plane, e.g. via collisions. Outside of this region a particle will instead oscillate in the ring plane (Northrop and Hill, 1982). The radius $1.52 R_S$ is associated with the breed of particles that has a non-zero gyroradius and magnetic moment, and this has the effect of stabilizing them. This stabilization moves the instability radius from $1.62 R_S$ to $1.52 R_S$ for this particular population (Northrop and Hill, 1982). We find that the majority of the emission peaks correspond to prominent gaps in the rings and the instability radii/region.

3.3.3 Temporal investigation

To investigate the temporal evolution of the observations, we divide the dataset into three ~ 1 hour bins which overlap each other, i.e. a 'rolling bins' method. In the rolling bins method we maximize S/N compared to a method that splits the data into three segments. Referring to Figure 3.11 one can see where the data come from as a function of ring width - a proxy for the extent of latitudinal smearing due to seeing. In this figure, the average ring width is calculated to be 4.42, 4.39 and 4.47 pixels for bins 1, 2 and 3, respectively. The resulting intensity against latitude profiles are displayed in Figures 3.12, 3.13 and 3.14: each bin representing 1 hour of the ~ 2 hour dataset - the first, middle and final hour. Correspondingly, the uncertainty in intensity is increased as indicated by the error shaded errors on the plots, following the reduction in S/N.

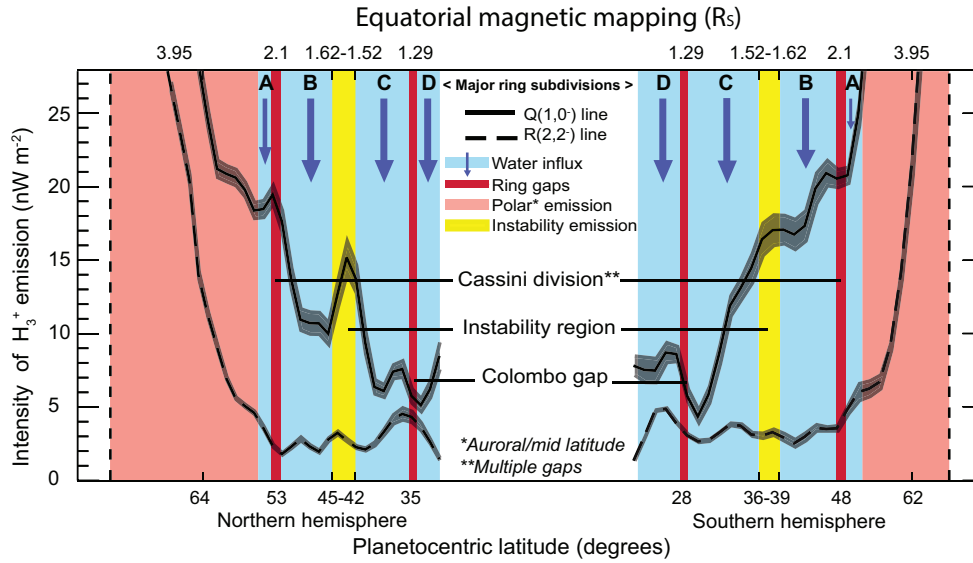


Figure 3.10: Intensity of H_3^+ IR emission along Saturn's noon meridian - The horizontal axes show a scale of planetocentric latitude at the bottom and the planetocentric equatorial distances which those latitudes magnetically map to at the top, where R_S is the 1 bar Saturn equatorial radius of 60,268 km. The y-axis shows the intensity of H_3^+ emission of the two spectral lines that are shown, Q(1,0⁻) at 3.953 μm (black line) and R(2,2⁻) at 3.622 μm (dashed black line) with a central gap where the observed emission is swamped by solar photon reflection from the planetary rings. Latitude bands mapping along planetary magnetic field lines to the main ring subdivisions in the equatorial plane are coloured blue, whilst dark red maps to the ring gaps, as labelled. The yellow shading is the instability region between the stability radii. High- to mid-latitude emission is shaded pink out to the limb of the planet (dashed black line). The 1-sigma error in intensity measurements are denoted by the grey shading. The errors in latitude are on average 3°, mainly caused by the Earth's atmospheric attenuation, i.e. seeing, of 0.4 seconds of arc.

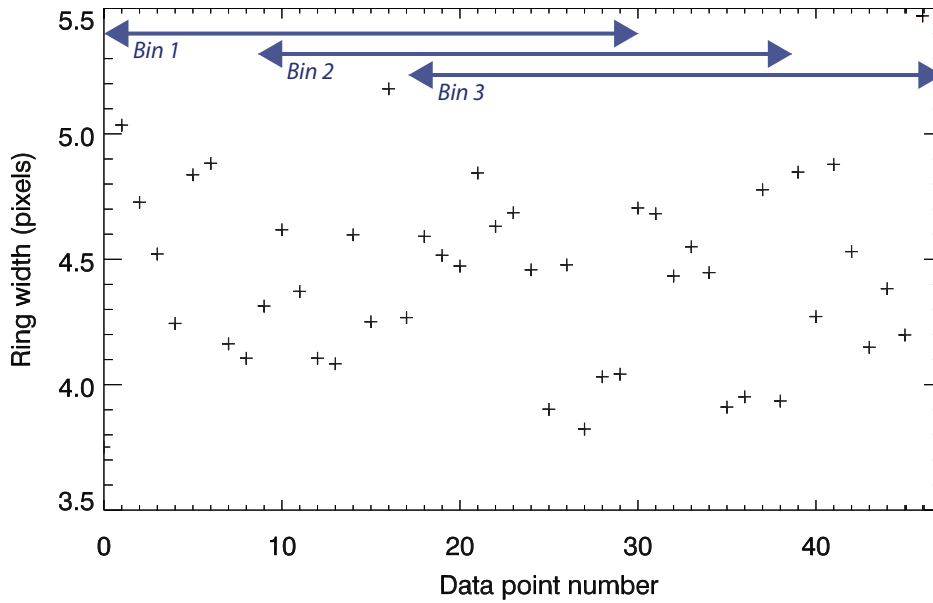


Figure 3.11: Saturn’s ring smearing distributed by temporal bins - This is the same as Figure 3.5 but this time the data are grouped into 3 temporal bins as indicated by the navy blue arrows and labels.

The pattern of peaks and troughs seen in Figure 3.10 appears to persist in each bin. The latitudinal profiles in intensity are similar in the first two bins, whilst the final bin looks to be broader and smoothed. The true atmospheric seeing value was only recorded at the start of the observations, however, so this cannot be empirically verified; the rings act as a good proxy but they are not a point source. We conclude from examining these shorter integration time bins that a combination of both a large quantity of exposures and excellent atmospheric conditions are needed to resolve the features seen in Figure 3.10 with high structural detail. If atmospheric seeing is too large, the small features seen will appear smeared in the spatial component. If an exposure is too short, the signal from the features will be too weak relative to the planets background reflection of sunlight (noise) to show any structure.

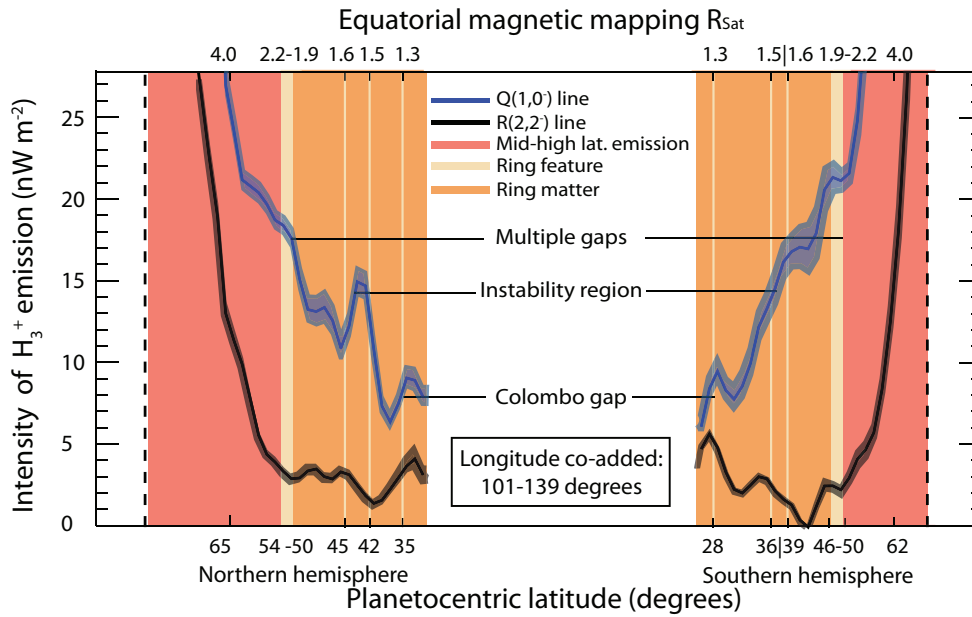


Figure 3.12: Temporal bin 1 - The first temporal binning of data from the dataset displayed in Figure 3.10, this represents approximately 1-hour of co-added data. Here, the $Q(1,0^-)$ (blue) and $R(2,2^-)$ (black) H_3^+ emission lines are plotted as intensity as a function of spatial position in both planetocentric latitude and equatorial mapping coordinates. Even with the reduction in total exposure time, most features can still be seen - the emission at low latitudes is not uniform.

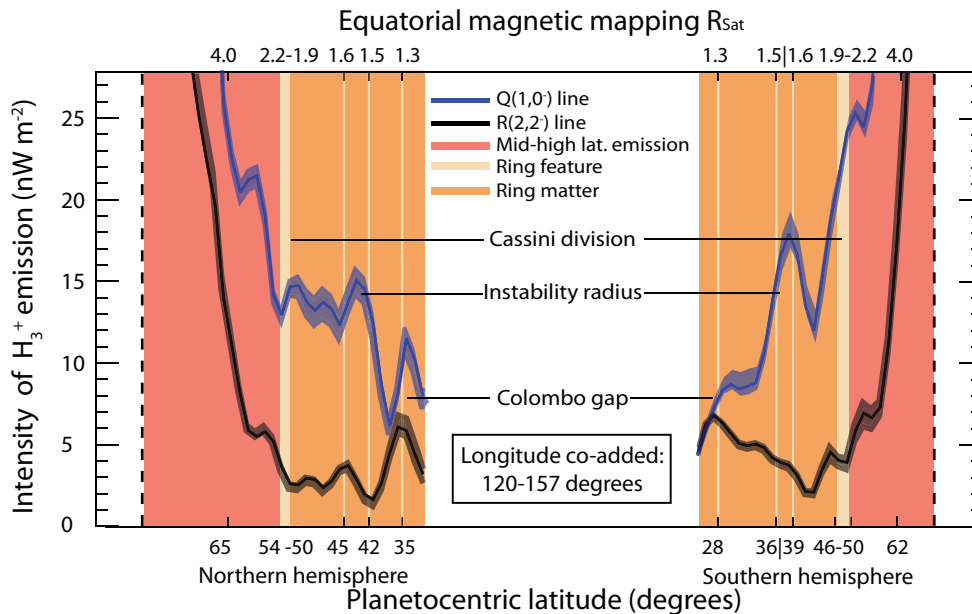


Figure 3.13: Temporal bin 2 - Same as Figure 3.12 but representing the co-addition of the central hour of the dataset, this overlaps the first and the third temporal bin. Again, most features can still be seen, although the relative strengths appear slightly shifted.

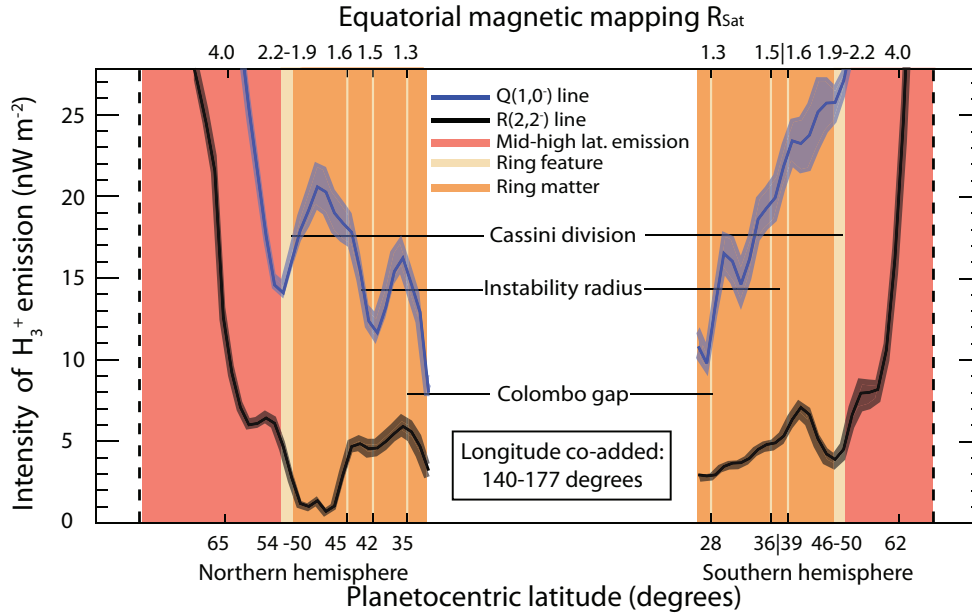


Figure 3.14: Temporal bin 3 - Same as Figure 3.12 but representing the co-addition of the final hour of the dataset. This plot is somewhat smeared in the spatial component, most likely due to an increase in atmospheric turbulence - i.e. seeing during the night of the observation, which acts to displace features in the north-south direction, thus causing the intensity peaks to become broad. The smeared plotting does however still display a large variation in the same pattern as the other bins, highlighting the non-uniformity of the low latitude region.

3.3.4 Alternative magnetic model: Connerney et al., 1982

To examine the effects of a different magnetic field model, we remodelled our magnetic mapping using the Z3 magnetic field model created by Connerney et al. (1982) which is based on the Voyager 1 and 2 spacecraft fly-bys. In the interest of making as fair a comparison as possible, we used identical parameters (such as the magnetopause stand-off distance), and the latest available coefficients for this model: $g_1 = 21,248$ nT, $g_2 = 1,613$, $g_3 = 2683$ from Dougherty et al. (2005). In Figure 3.15 we show our data mapped using the Z3 model. The two main differences are that the northern instability region is shifted more northward in the Z3 model and the mapping of the Colombo gap is improved in the southern hemisphere but less accurate in the north.

For a given radial distance from Saturn in the equatorial plane, the differences in the magnetically mapped latitudes are less than half that of the observational

3.4 Saturn's ring 'rain' interpretations

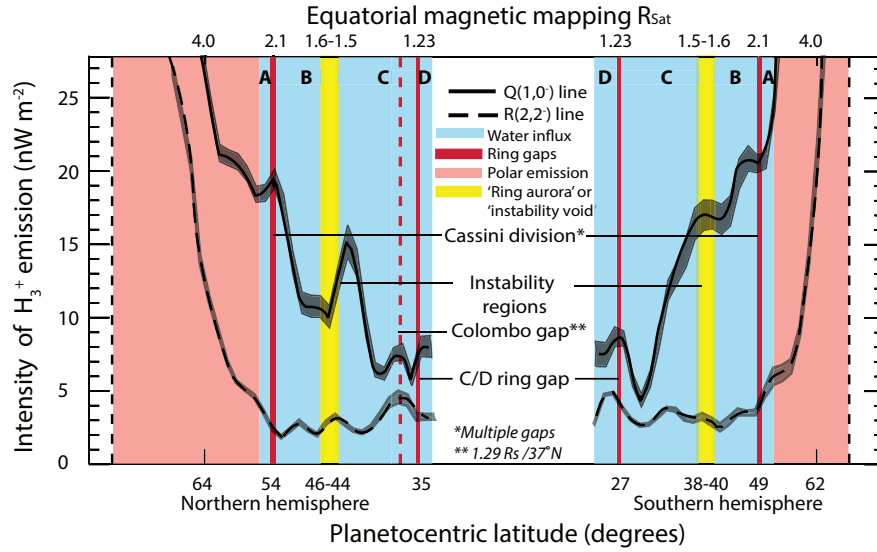


Figure 3.15: Figure 3.10 cast in the Z3 field model mapping - This plot is similar to that of Figure 3.10 but this time the coefficients of the Z3 model are used.

errors in latitude (see Figure 3.6) such that these observations are unable to decide which model is more accurate. We continue to our interpretation using the field model of Bunce et al. (2008b), given that it is the more modern and based on far more data. The instability region mapping is significant because the use of the Z3 model may have affected our interpretation of it, whereas the Colombo gap mapping is 'off' in both models in a similar manner for reasons presently unknown.

3.4 Saturn's ring 'rain' interpretations

Here we posit three interpretations to explain the observed H_3^+ profiles. The first is based on recent modelling using the Saturn Thermosphere Ionosphere Model (STIM), which is the most comprehensive Saturnian upper-atmosphere model available; the simulations were performed by Luke Moore and colleagues at Boston University in support of this work. This model shows that water ought to enhance H_3^+ intensity, and therefore that the gaps in the rings are a larger water source than the solid sub-divisions. The second interpretation is that water particles flow from the rings into the planetary ionosphere, causing the destruction of the

3.4 Saturn's ring 'rain' interpretations

H_3^+ ion, thus a reduction in brightness occurs at those locations; this was the original interpretation of these observations and is illustrated in Figure 3.16. The third and final interpretation involves a current system which links the planet to the rings; such a system is likely by analogy to auroral currents, but as yet no observational evidence exists in support of it, e.g. in-situ measurements of inner-magnetospheric currents. Whilst the first two hypotheses explain the results soundly, they directly contradict each other; the third hypothesis however, may operate simultaneously with either of the first two regimes.

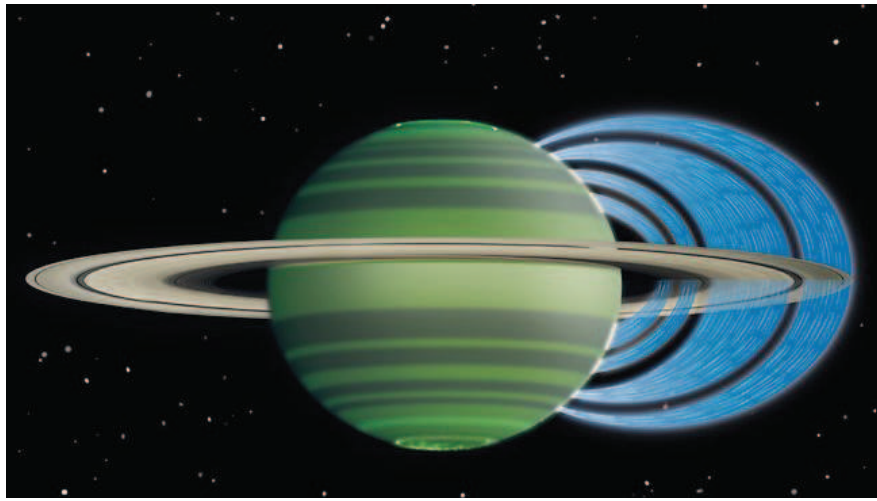


Figure 3.16: Saturn's ring rain - This artist's concept illustrates how charged water particles flow into the Saturnian atmosphere from the planet's rings, causing a reduction in atmospheric brightness. This image was produced for the press release associated with this work by the author. Additional image credits: NASA/JPL-Caltech/Space Science Institute/University of Leicester

It is appropriate that we first discuss the source of water in the rings and then what effects water has on ionospheric chemistry, before the interpretations are outlined.

3.4.1 The ring water source

As stated in Subsection 1.6.3, the rings have an ionosphere which we call the ionodisk. In Figure 3.17, Luhmann et al. (2006) modelled the distribution of O^+ and O_2^+ ions (in a 'test particle' model), one of the key results is that these ions appear able to precipitate into the ionosphere. The mechanism by which

3.4 Saturn's ring 'rain' interpretations

water is transferred to the low-latitude ionosphere is likely to be similar to that which occurs in the auroral regions, e.g. by pitch angle scattering and/or auroral-like acceleration due to magnetic field aligned potential differences (discussed in Section 1.6.2), though neither models or observational evidence is available to confirm this.

It is not just solitary molecules that make it into Saturn's atmosphere. Aggregates of molecules called icy grains can also leave the ring plane, provided they have a high charge to mass ratio, otherwise they will be too massive to move via e.g. collisions. Connerney (2013) state that one electron charge per 1000 water molecules can suffice. Further modelling suggests that the rate at which water

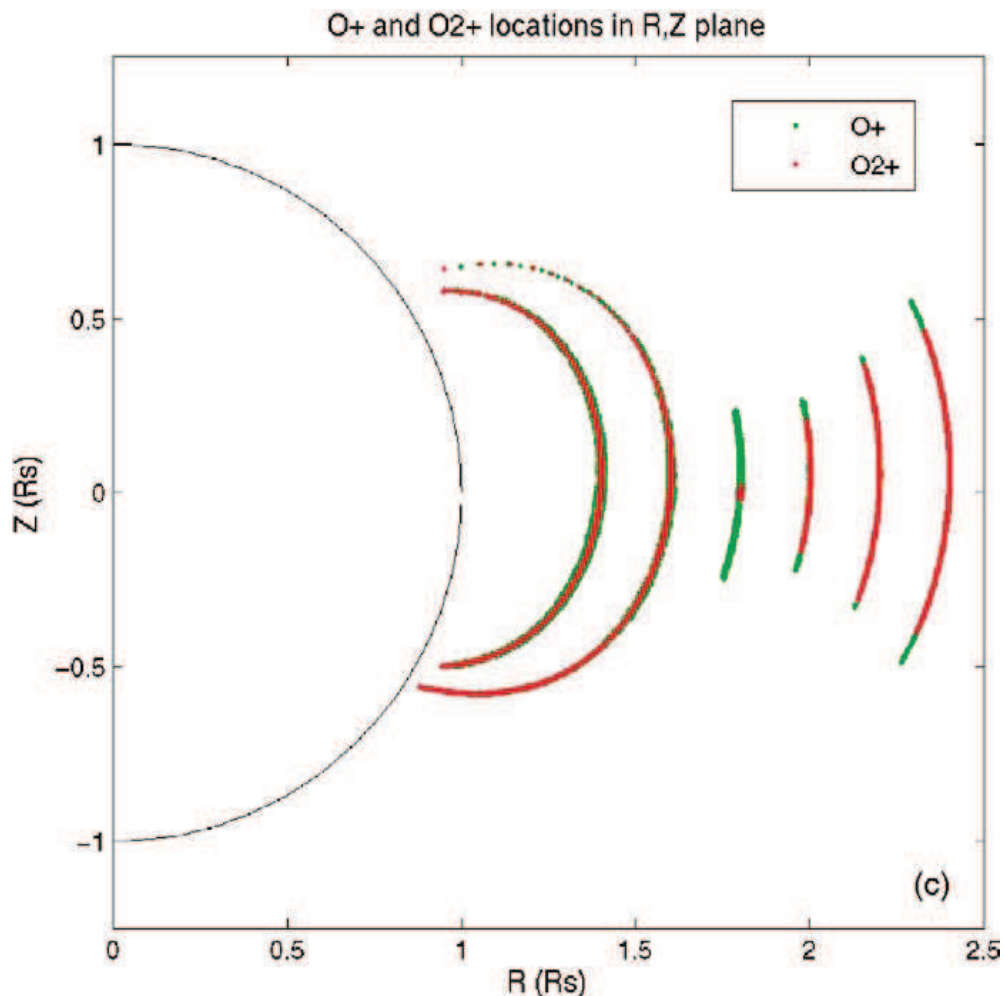


Figure 3.17: Modelled O^+ and O_2^+ - Here the trajectories of O^+ and O_2^+ ions are projected onto the X-Z plane taken from Figure 1c in (Luhmann et al., 2006).

products are ionized is positively correlated with the solar incident angle with

3.4 Saturn's ring 'rain' interpretations

respect to the ring plane. In other words, the production increases when the rings are more exposed to solar EUV ionization (Tseng et al., 2010). At equinox, the axial tilt of Saturn (and rings) is 0° , so the solar flux absorbed by the rings is at a minimum; at solstice, Saturn's axial tilt reaches 26.7° and therefore the rings capture far more solar radiation. Taking this into account, later ionodisk modelling by Tseng et al. (2013) clearly showed that the number of ions produced per second by photo-dissociation, the photolytic source rate, is two orders of magnitude larger for solstice rather than equinox as shown in Figure 3.18 for O_2^+ .

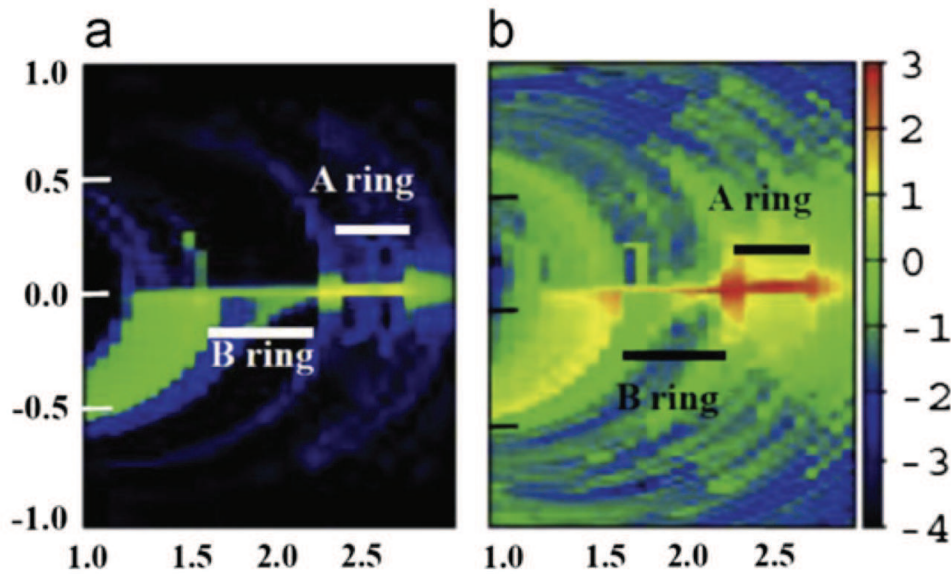


Figure 3.18: Seasonal effects on the ionodisk - Here the photolytic source rate of O_2^+ is shown for (a) Equinox phase and (b) SOI phase. In (a) the photolytic source rate is $2.0 \times 10^{25} \text{ s}^{-1}$ whilst in (b) it is 2 orders of magnitude greater at $2.0 \times 10^{27} \text{ s}^{-1}$. The ion density is colour-coded in the logarithmic scale indicated by the colour bar. The x- and y-axes show the radial and vertical distances, respectively, in R_S .)

3.4.2 Rain effects on ionospheric chemistry

We have focused on the idea of a water ion influx when describing the transfer of water molecules to Saturn's atmosphere. However, these incoming water ions dissociatively recombine with electrons several times faster than H_3^+ , so the ma-

3.4 Saturn's ring 'rain' interpretations

jority are expected to become neutral by the time they reach ionospheric peak altitudes - we show the relevant reaction rates from Table A2 of Moses and Bass (2000) in Table 3.1 to elaborate upon this. For example, the reaction $\text{H}_3\text{O}^+ + e \rightarrow \text{H}_2\text{O} + \text{H}$ has a reaction rate of $6.1 \times 10^{-6} \text{ T}^{-0.5} \text{ cm}^3 \text{ s}^{-1}$, which is ~ 6 times faster than the reaction $\text{H}_3^+ + e \rightarrow 3\text{H}$, which has a slower rate given by $9.7 \times 10^{-7} \text{ T}^{-0.5} \text{ cm}^3 \text{ s}^{-1}$. Note that these electron-ion dissociative recombination reactions are inversely dependant on the temperature (i.e. kinetic energy), due to the competition between the constituents' electrostatic attraction and their relative velocities.

Reaction		Rate constant*
H_3^+	$+ e \rightarrow 3\text{H}$	$9.7 \times 10^{-7} \text{ T}^{-0.5}$
H_3^+	$+ e \rightarrow \text{H}_2 + \text{H}$	$7.6 \times 10^{-7} \text{ T}^{-0.5}$
O^+	$+ e \rightarrow \text{O}$	$1.2 \times 10^{-10} \text{ T}^{-0.63}$
H^+	$+ e \rightarrow \text{H}$	$1.9 \times 10^{-10} \text{ T}^{-0.7}$
OH^+	$+ e \rightarrow \text{O} + \text{H}$	$6.5 \times 10^{-7} \text{ T}^{-0.5}$
H_3O^+	$+ e \rightarrow \text{H}_2\text{O} + \text{H}$	$6.1 \times 10^{-6} \text{ T}^{-0.5}$
H_2O^+	$+ e \rightarrow \text{O} + \text{H}_2$	$3.5 \times 10^{-6} \text{ T}^{-0.5}$
H_2O^+	$+ e \rightarrow \text{OH} + \text{H}$	$2.8 \times 10^{-6} \text{ T}^{-0.5}$
H_3O^+	$+ e \rightarrow \text{OH} + 2\text{H}$	$1.1 \times 10^{-5} \text{ T}^{-0.5}$
O_2^+	$+ e \rightarrow 2\text{O}$	$1.1 \times 10^{-5} \text{ T}^{-0.7}$

Table 3.1: Ion-electron reactions

*Two-body reaction rate constants in units of $\text{cm}^3 \text{ s}^{-1}$. Temperature T is in kelvins.
 Data excerpted from Table A2 of Moses and Bass (2000)

In addition, ion-neutral charge exchange reactions between ring water ions and atmospheric H_2 ultimately lead to H_3O^+ via the multiple pathways shown in Table 3.2, which has the fastest electron recombination reaction rate of all water group ions. With predominantly neutrals left from the interactions in both Tables 3.1 and 3.2, we can assume that ionized water group particles interact with the ionosphere effectively in the same fashion as neutral ones. For the aforementioned high charge-to-mass ratio icy grains (1 unit charge per $\sim 10 - >1000$ molecules), orders of magnitude more neutral molecules will be released by these single interactions.

3.4 Saturn's ring 'rain' interpretations

Reaction	Rate constant*
H + O ⁺ → H ⁺ + O	6.4 × 10 ⁻¹⁰
H ₂ + O ⁺ → H + OH ⁺	1.6 × 10 ⁻⁹
H ₂ + OH ⁺ → H + H ₂ O ⁺	9.7 × 10 ⁻¹⁰
H ₂ + H ₂ O ⁺ → H + H ₃ O ⁺	7.6 × 10 ⁻¹⁰

Table 3.2: Water ion reactions with H₂

*Two-body reaction rate constants in units of cm³ s⁻¹. Temperature T is in kelvins.
Data excerpted from Table A2 of Moses and Bass (2000)

The majority of charged ions present in Saturn's ionosphere are H⁺, H₂⁺ and H₃⁺. This material charge-exchanges with the neutral water present in the ionosphere and subsequently produces further water ions as well as neutral H and H₂; the relevant reaction rates are shown in Table 3.3 again from Moses and Bass (2000). The fastest reaction rates listed in this table result in the production of H₂O⁺ and H₃O⁺, which ultimately leads to production of more neutrals as per Table 3.1. Examining the myriad of possible reactions in all tables reveals that most reactions involving water involve the removal of hydrogen ions and molecules in the ionosphere, as well as reducing the number of electrons.

H₃⁺ is a special case; being a stable yet reactive molecule due to its high proton affinity (Oka, 2012), it reacts easily with other species. Where X is a charge-neutral molecule, the resulting ion, XH⁺, is much more likely to dissociatively recombine than it is to lead back to H₃⁺ through a chemical reaction chain (Moses and Bass, 2000). For the purposes of removing or enhancing H₃⁺ in the ionosphere, any type of water ion such as OH⁺ and H₂O⁺ etc influx is roughly equivalent, within a factor of 2 - 3 based on the different H₃⁺ charge-exchange reaction rates outlined in Table 3.3. Based on the evidence available it seems likely that there is a combination of both neutral and ionized water influxes present at Saturn Jurac and Richardson (e.g. 2007).

Only a fraction of the chemical reactions that can take place in the ionosphere are listed above, and already it is clear that computer modelling is needed to decipher what happens to the ionosphere when exposed to a water influx.

3.4 Saturn's ring 'rain' interpretations

Reaction	Rate constant*
$H^+ + O \longrightarrow O^+ + H$	3.8×10^{-10}
$H^+ + OH \longrightarrow OH^+ + H$	2.1×10^{-9}
$H^+ + H_2O \longrightarrow H_2O^+ + H$	8.2×10^{-9}
$H_2^+ + H \longrightarrow H^+ + H_2$	6.4×10^{-10}
$H_2^+ + O \longrightarrow OH^+ + H$	1.5×10^{-9}
$H_2^+ + H_2O \longrightarrow H_2O^+ + H_2$	3.9×10^{-9}
$H_2^+ + H_2O \longrightarrow H_3O^+ + H$	3.4×10^{-9}
$H_3^+ + O \longrightarrow OH^+ + H_2$	4.0×10^{-10}
$H_3^+ + O \longrightarrow H_2O^+ + H$	4.0×10^{-10}
$H_3^+ + OH \longrightarrow H_2O^+ + H_2$	1.3×10^{-9}
$H_3^+ + H_2O \longrightarrow H_3O^+ + H_2$	5.3×10^{-9}

Table 3.3: Water ion reactions with H₂

*Two-body reaction rate constants in units of cm³ s⁻¹. Temperature T is in kelvins.
Data excerpted from Table A2 of Moses and Bass (2000)

We now show preliminary atmospheric modelling results using STIM. At H₃⁺ relevant altitudes, Saturn's ionosphere is in photochemical equilibrium, meaning that chemical processes are dominant over transport (Moore et al., 2004), and we can consequently equate production and loss to find that

$$[H^+] = \frac{j_3[H_2]}{k_1q[H_2] + k_2[H_2O]} \quad (3.1)$$

where square-bracketed terms are number densities, j and k refer to relevant photoionization and charge-exchange rates given by Table 1 of Moore et al. (2004), respectively. The value q is the fraction of H₂ in the 4th or higher vibrational level, i.e. [H₂*]/[H₂] (see also Subsection 4.5.3). The q value has a different effect depending on the reaction: a higher q will speed up the reactions that produce H₃⁺, whilst at the same time will diminish the electron population. Each of the terms in the equation above correspond to either a production or loss of material in a steady state, for example $k_2[H_2O]$ is the number density of neutral water introduced into the system. A similar photochemical analysis for H₃⁺ yields a

3.4 Saturn's ring 'rain' interpretations

quadratic with a dependency on H^+

$$\alpha[H_3^+]^2 + \alpha[H^+] + \{k_4[H_2O][H_3^+]\} - j_2[H_2] = 0 \quad (3.2)$$

where α is the dissociative recombination coefficient of H_3^+ . The results of these equations are run using STIM and can be visualised in Figure 3.19. This demonstrates the response of H_3^+ to varying degrees of water influx and vibrational excitation of H_2 ; H_2O densities come from STIM neutral diffusion calculations (Moore and Mendillo, 2007). In the absence of a strong water influx, the dominant loss process for H_3^+ is dissociative recombination (Moore et al., 2010), therefore H_3^+ is also affected by any reactions that lead to a reduction in electron densities. There are two main aspects of Figure 3.19 to consider. First, a water influx can act to both increase and decrease H_3^+ densities through two competing mechanisms: an increase in H_3^+ density is the result of a reduction in electron density N_e , which represents a reduction in the dissociative recombination loss of H_3^+ , and this is in turn primarily due to $H^+ + H_2O \rightarrow H_2O^+ + H$ and subsequent reactions - for example, note that H_2O^+ recombines with electrons four orders of magnitude faster than H^+ , so more water ions result in lower N_e ; a decrease in H_3^+ density however, is due to H_3^+ charge exchanging with neutral molecules such as H_2O . Second, H_3^+ is relatively insensitive to changes in the fraction of H_2 that is in the 4th or higher vibrational level (q).

As highlighted by Subsection 1.6.3, the earliest models of ring rain suggested a water influx of $\sim 4 \times 10^7$ molecules $\text{cm}^{-2} \text{sec}^{-1}$ planet-wide and $\sim 2 \times 10^9$ molecules $\text{cm}^{-2} \text{sec}^{-1}$ at the instability radii specifically (Connerney and Waite, 1984); whilst later models suggest an influx of $\sim 1.5 \times 10^6$ molecules $\text{cm}^{-2} \text{sec}^{-1}$ (Feuchtgruber et al., 1997; Moses and Bass, 2000). Therefore, there is ambiguity in whether or not H_3^+ density (hence, emission) will decrease or increase as we can clearly see from Figure 3.19.

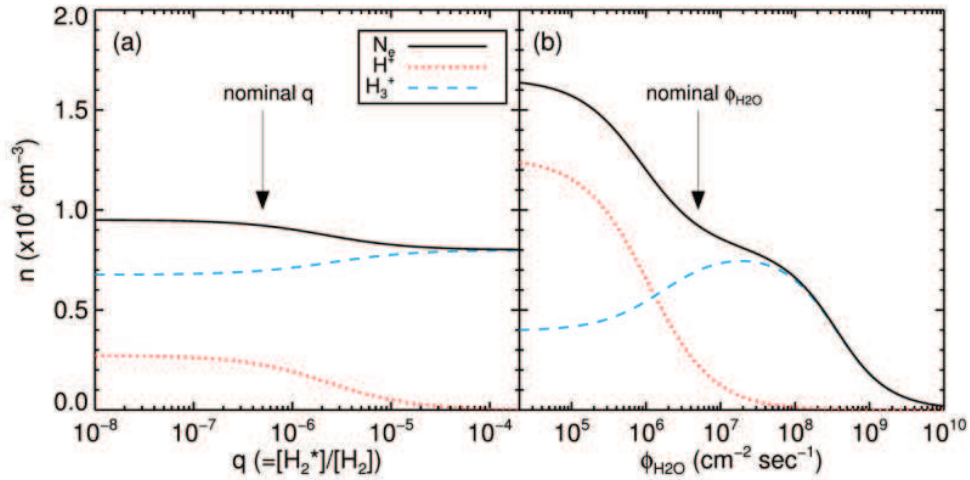


Figure 3.19: Saturn modelled ionosphere by STIM - (a) Effect of vibrationally excited H_2 on Saturn's ionosphere. (b) Effect of water influx on Saturn's ionosphere. Nominal q (a) and water influx (b) values are also indicated by arrows, based on Moore et al. (2010). Note that N_e is neglecting the contribution from water group ions in this demonstration (justified by their fast recombination rates) and that (b) uses nominal q from (a).

3.4.3 Interpretation 1 (main): Water influx enhancing H_3^+

This interpretation is derived from the latest models and observational evidence, i.e. that the water influx is approximately centered at $\sim 1.5 \times 10^6$ molecules $\text{cm}^{-2} \text{sec}^{-1}$ (Moses and Bass, 2000) and any variability lies near this value on the slope of H_3^+ density in Figure 3.19. In this range of water influx, we expect that higher water influxes result in higher densities of H_3^+ and therefore higher emissions. In explaining the pattern seen in Figure 3.10 under this regime, it is apparent that there must be an enhancement of water influx emanating from ring gap mapped latitudes, whilst latitudes mapped to solid (dense) subdivisions of the rings must be associated with a lesser influx. This seems counter-intuitive given that the water ice supply is far greater in the dense subdivisions of the rings, but it is supported by both measurements from Cassini when it flew through these gaps, and by subsequent modelling which followed, as seen in Figure 3.17. The peaks in the emission of H_3^+ , particularly in the $\text{Q}(1,0^-)$ line, appear to all be larger in the south than in the north, perhaps indicating a higher water influx there; indeed both Luhmann et al. (2006) and Tseng et al. (2010) predicted an enhancement

3.4 Saturn's ring 'rain' interpretations

in precipitation at southern latitudes as a result of the magnetic field strength asymmetry, in which the resulting lower southern field strength allows for particles to penetrate deeper.

The instability radii are now of particular importance because they are not simply a gap in the rings where there may or may not be water flow into the ionosphere, but are both a theoretically predicted source (Northrop and Hill, 1983) and have produced an observable effect at lower altitudes than the ionosphere (Connerney, 1986). The measurements herein show that between the instability radii (i.e. instability region) there is a peak in emission, and this is supportive of the argument that H_3^+ density is being enhanced in this region by an impinging flow of water. The caveat with this is the observed instability region peak enhancement should be formed of two separated peaks rather than one large one, such that for this interpretation of Saturn's ring rain to be valid, one or more of the following must be true:

- a) The latitudinal resolution at low-latitudes is insufficient to pick out such detail.
- b) The water isn't falling precisely at those latitudes due to the large gyroradii of the particles along field lines.
- c) That the H_3^+ signature of the water influx is mixed by at least $\sim 2^\circ$ meridionally within the atmosphere.
- d) There may be water falling from both the instability region and radii.

3.4.4 Interpretation 2: Water influx quenching H_3^+

The initial assumption for the cause of variable H_3^+ emission was that charged material, which ought to be more dense around the solid portions of the rings, is responsible only for the destruction of the H_3^+ molecule and the intensity it would otherwise have emitted. Water ions flowing from the rings along magnetic field lines into the ionosphere cause the electron density to be reduced through

3.4 Saturn's ring 'rain' interpretations

rapid chemical recombination (quenching) (Connerney, 1986). Water products are known to deplete H_3^+ because it protonates (charge-exchanges) quickly with molecules heavier than H and He (Miller et al., 2006), hence a drop in H_3^+ density and thus intensity at latitudes where the most water is delivered to the planet ought to be expected. However, for this to be in accordance with Figure 3.19, the required water influx must be greater than 1×10^8 molecules $\text{cm}^{-2} \text{sec}^{-1}$ for latitudes mapped to the subdivisions of the rings, and $\sim 5 \times 10^7$ molecules $\text{cm}^{-2} \text{sec}^{-1}$ for gap-mapped latitudes (see Figure 3.19). The former influx however, is 2 orders of magnitude greater than that based on ISO observations of Feuchtgruber et al. (1997).

In this scenario, the peaks in emission that are mapped to gaps in the rings are peaks in intensity only by virtue of having severely reduced water influx associated with them. Thus, these peaks are not really 'peaks' at all, but regions in which the ionosphere is quenched less by water compared to latitudes either side of them. The Cassini division, for example, which maps on average to $\sim 2.1 R_S$ in Figure 3.10, occurs at latitudes where an increase in the emission of H_3^+ is clearly visible. Water influx from the A and B ring quenches the ionosphere at locations on either side of these latitudes, leading to the prominent peak seen between.

In Figure 3.10, the instability radii appear to be on the slope of the peak in-between. If we consider an exogenous water influx as something that decreases the density of H_3^+ , there must be both an enhanced water influx from the instability radii and a reduced influx for the instability region. In the ring plane, this corresponds to a reduced water source in the instability region, which in turn could be the result of the instability radii consuming the local supply at either side of the instability region, effectively cutting off the supply.

3.4.5 Interpretation 3: Ring-ionosphere coupling currents

An alternative interpretation for the observations is that the peaks in intensity correspond to temperature increases in H_3^+ , whilst the troughs correspond to the natural background levels of H_3^+ emission produced by solar EUV ionisation. These temperature increases would be the result of Joule heating via the flow of charged particles (current), which requires that the resultant rise in H_3^+ intensity is large enough to overcome any quenching of H_3^+ density that may take place as outlined above. Detailed modelling of the effects of ring rain are required to establish what the background H_3^+ emission intensity in these latitudes should be (based on solar EUV ionisation), and whether or not the peaks in emission found here are equal to or higher than this level. In Figure 3.20, we show a simple sketch that may explain the observed emissions from this current system perspective.

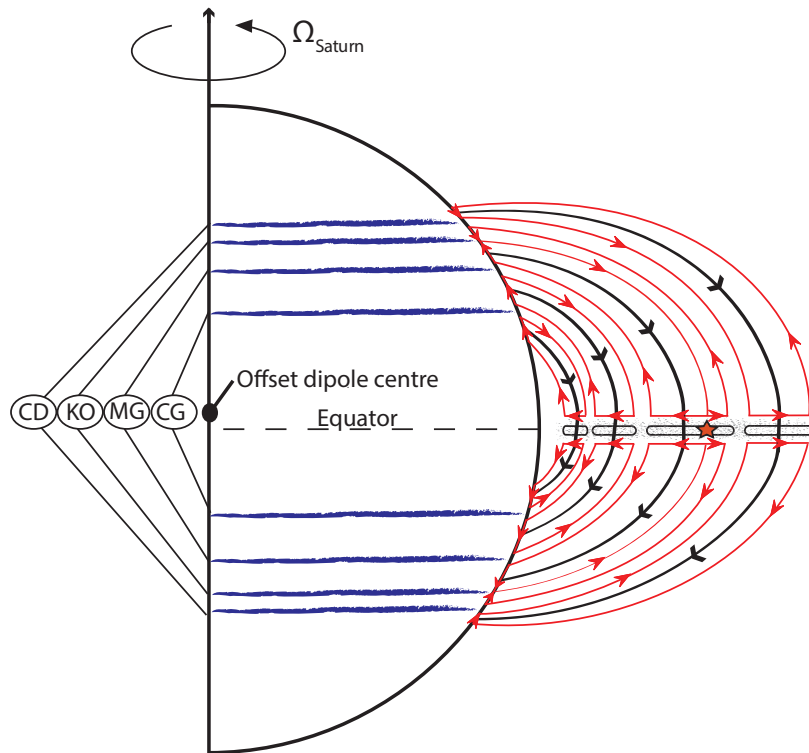


Figure 3.20: Low-latitude current system - Sketch showing current circuits that couple angular momentum between the planetary ionosphere and the ionodisk. The planetary magnetic field is shown by the black arrowed lines and the large-scale current system is shown by the arrowed red lines. Kronostationary orbit is denoted by the star symbol.

The existence of these coupling currents is implied by the formation of an ionodisk in the equatorial magnetosphere. In the absence of a planetary magnetic field, the charged particles in Saturn's ionosphere and the ionodisk would rotate with their respective neutral gases, at the Kepler speed in the rings and with the planetary rotation speed in the ionosphere (Ω_{Saturn}). However, the planetary field threads these regions, and so enforces an angular velocity on the ions relative to the two neutral gases. Collisions between the ions and the rotating neutrals then produce oppositely-directed drag forces in the ionosphere and ionodisk. The large-scale currents transfer this angular momentum from the ionosphere to the ionodisk outside kronostationary orbit and vice versa inside of kronostationary orbit. The directions of the ionospheric currents thus reverse about this orbital distance, from radially outward to radially inward in the ring ionosphere, and from equatorward to poleward in the planetary ionosphere. Field-aligned currents complete the ring-modulated circuits, and latitudes in which upward and downward currents are present in the ionosphere are potentially associated with the observed enhancements of H_3^+ emission. It is these currents that could drive Joule heating that may enforce increased emission mapping to the ring boundaries.

3.5 Future work

The work presented herein is only a single measurement of an extraordinary phenomenon and as such may be the tip of a rather large iceberg; had we only one observation of the Earth's aurorae we might have been subjected to great pains to explain how they work.

3.5.1 Future investigation

In future, if two distinct peaks in emission were observed in H_3^+ intensity that corresponded to the instability radii, then interpretation 1 is certainly the most favourable in explaining the observations. A measure of H_3^+ density as a function of latitude is also required; with this, we can see whether or not H_3^+ is produced or reduced at a given latitude. In addition, higher latitudinal resolution observations are needed to constrain the finer structures related to the instability region. Having a temperature profile from pole-to-pole on Saturn rather than just an intensity profile, we may be able to deduce whether or not a current system exists through the analogy that the auroral regions are hotter due to the stronger current flow. The Cassini spacecraft ends its mission in 2016 and is due to pass through the inner-edge of the D-ring, so in-situ measurements of the inner-magnetosphere (i.e. low-latitude mapped field lines) are likely to be taken (Sarah Badman, private communication). In principle, the first two interpretations of the result should be playing a role simultaneously with the third, though the present lack of evidence of the above current system means we must postpone a comprehensive analysis of it. An additional concern is that of the shadow cast by the rings onto the ionosphere; in the past, through modelling, it has been found to create significant variations in the ion density with latitude (Mendillo et al., 2005). However, this is unable to explain the features seen here as the shadow always falls behind the rings in ground-based geometry (see Figure 3.4) and the reflection of sunlight by the rings obscures this region entirely.

3.5.2 Future observations

Ground-based observations in the years to come are likely to be technically similar to those executed here, in that Saturn will be observed by a large-class (at or above 8-metre diameter) telescope such as Keck, when Saturn is at opposition.

The observations in this study were advantaged by the fact that both hemispheres could be viewed simultaneously, allowing ring rain to be confirmed as a symmetric phenomenon (about the magnetic equator). Future observations will lose this benefit but gain from superior spatial resolution in the north itself, as the planet approaches solstice and the northern regions are tilted increasingly towards Earth. This heightened resolution will reduce the smearing of nearby latitude elements, allowing a more detailed analysis of the data. In addition, Saturn's rings also significantly block low-latitude regions from view owing to their high sunlight reflectivity - the distance between this interference and the equator increases throughout the planned observations, allowing us to probe to lower and lower latitudes. Figure 3.21 highlights the geometric advantages of future observations compared to the data used in this work.

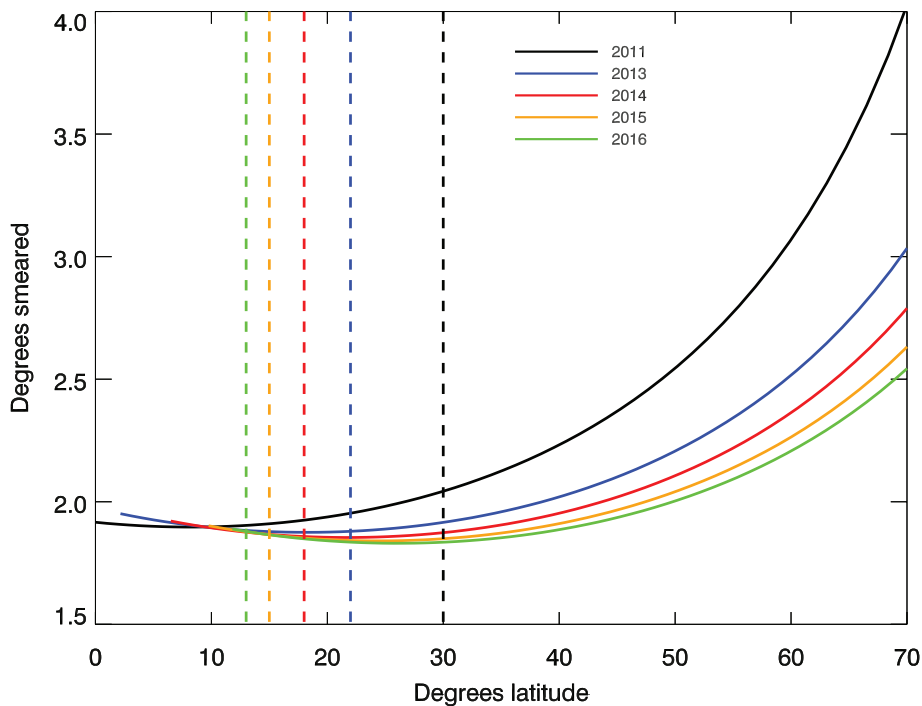


Figure 3.21: Spatial smearing of pixels - Solid lines show the extent of latitude smearing due to decreases in latitudinal resolution in the northern hemisphere for past (2011) and future observations. Dashed horizontal lines show the estimated latitudinal range that is not affected by solar reflection from the rings (and hence, where H_3^+ parameters can be derived), while vertical lines show the limiting latitudes. E.g., during 2015 we can expect to observe down to $\sim 15^\circ$ latitude (as opposed to $\sim 30^\circ$ during 2011).

Longer periods of observation are essential; with 20 hours of data we can

achieve a factor of three higher S/N over the previous observations (a S/N of ~ 15 and ~ 45 for the R(2,2⁻) and Q(1,0⁻) lines, respectively). The latitudinal precision of peaks and troughs will be correspondingly improved, as with more data we can afford to be more rigorous with the data selection - i.e. selecting only those images least perturbed by atmospheric turbulence, which can reduce latitude resolution by as much as $\sim 2.5^\circ$. Observing 2-or-more spectral lines other than Q1(1,0⁻) simultaneously yields the ability to calculate H₃⁺ temperature and density as outlined in Chapter 2. In addition, contemporary estimates of the ring lifetime range from 4.4 million (Northrop and Connerney, 1987) to 100 million (Salmon et al., 2010) to 4.5 billion years (Canup, 2010), a massive uncertainty. Combining modelling of Saturn's ionosphere with the H₃⁺ densities resulting from the proposed work, we will be able to derive the rate of water influx into Saturn's atmosphere as a function of latitude; this will allow us to address the origin and evolution of Saturn's rings, a problem with important implications for Solar System formation.

Chapter 4

Conjugate observations of Saturn's aurorae

This chapter details the first conjugate study of Saturn's northern and southern auroral regions in terms of H_3^+ temperature, density and total emission. Saturn's main auroral ovals were observed at local noon using the same ~ 2 hour dataset used in the previous chapter. Previous ground-based work has derived only an average temperature for an entire auroral region, by summing an entire night of observations. We significantly increase temporal resolution here by analysing 10 H_3^+ auroral spectra within a single night. Each provides H_3^+ temperature, column density and total emission in both the northern and southern auroral regions simultaneously, improving on past results in temporal cadence and simultaneity. We find that: 1) the average thermospheric temperatures are 527 ± 18 K in northern Spring and 583 ± 13 K in southern Autumn, respectively; 2) this asymmetry in temperature is likely to be the result of an inversely proportional relationship between the total thermospheric heating rate (Joule heating and ion drag) and magnetic field strength - i.e. the larger northern field strength leads to reduced total heating rate and a reduced temperature, irrespective of season, and 3) this implies that magnetic effects outweigh seasonal effects in this case.

4.1 Introduction

4.1.1 Previous work

Prior to the findings of this study, measurements of auroral thermosphere temperatures have been limited to time-averaged values as Saturn's auroral H_3^+ emissions in the infrared are relatively weak: they are less than a hundredth the intensity of those at Jupiter when observed from Earth owing to Jupiter's higher ionospheric temperature (~ 1000 K, Lam et al., 1997). This rising temperature causes an almost exponential increase in H_3^+ emission (see Neale et al., 1996b, Figure 2). Melin et al. (2007) performed the most recent ground-based study of auroral thermospheric temperatures at Saturn, combining results from the 3.8-metre UKIRT telescope and CGS4 spectrograph obtained in 1999 and 2004, with exposure times of 210 and 26 mins, to derive a temperature of 450 ± 50 K for the southern spring/summer auroral thermosphere. More recently, data from the Visual and Infrared Mapping Spectrometer (VIMS) on board the Cassini Saturn orbiter (Brown et al., 2004), analysed by Stallard et al. (2012b) and Melin et al. (2011), showed temperatures in the southern auroral region range between 560 - 620 (± 30) K over a 24-hour period in June 2007, and 440 ± 50 K in measurements in September 2008, respectively. These temperatures are far warmer, by hundreds of Kelvin, than predicted by models using only the Sun as an energy input (Bagenal et al., Chapter 9). This discrepancy in temperature is known as the energy crisis. It and other motivations are more broadly discussed in Subsection 1.6.1.

4.1.2 Context

Heating in the auroral region has been shown, through modelling, to be dominated by Joule heating and ion drag via ionospheric Pedersen currents (Cowley et al., 2004; Smith et al., 2005; Galand et al., 2011; Mueller-Wodarg et al., 2012). The sum of these two heating mechanisms we call the total (polar) heating rate,

although it is actually responsible for approximately 98% of the energy input into the thermosphere, with the remainder being due to particle precipitation (Cowley et al., 2004). Only through a greater understanding of the mechanisms and conditions that control physical parameters such as temperature, column density, and the total energy emitted from H_3^+ over all wavelengths (henceforth, total emission), can we start to add constraints to models and theories of the ionosphere. However, whilst individual temperature measurements have been made over long time scales, a study in both hemispheres simultaneously has not yet been performed. Short term variability and conjugate auroral studies are needed in order to understand how persistent these temperatures are. Here, we present and discuss the new results of observations taken in April, 2011. We study the main auroral oval H_3^+ temperature, column density and total emission in the northern and southern hemispheres of Saturn at the same time with a temporal resolution of 15 minutes, and explore the implications of these measurements.

4.2 Data acquisition

These observations were taken on 17 April 2011 in conditions of Saturn's northern spring; the observational set-up is as shown in Section 3.2 and as such the data were reduced using the standard data reduction techniques in Chapter 2; here we discuss the methods employed in the data reduction and analysis that are unique to this chapter. The wavelength range here is between 3.95 and 4.0 μm , covering the Q-Branch ($\Delta J = 0$) ro-vibrational transition lines of H_3^+ . The NIRSPEC (McLean et al., 1998) instrument operating at $R = \lambda/\Delta\lambda \sim 25,000$, provides minimum resolution in this wavelength range of $\delta\lambda \approx 0.16$ nm (at 3.975 μm). An example of a typical reduced exposure in our wavelength range is shown in Figure 4.1. The auroral regions are ~ 100 times brighter (see the Figure 3.10) than the low-latitude regions of the previous chapter, so we have dissected our reduced spectral images into co-added 15 minute segments. During one such seg-

ment, Saturn rotates through 8.5° of longitude. This dataset represents a unique opportunity because both hemispheres are now no longer able to be observed from the ground simultaneously until ~ 2023 .

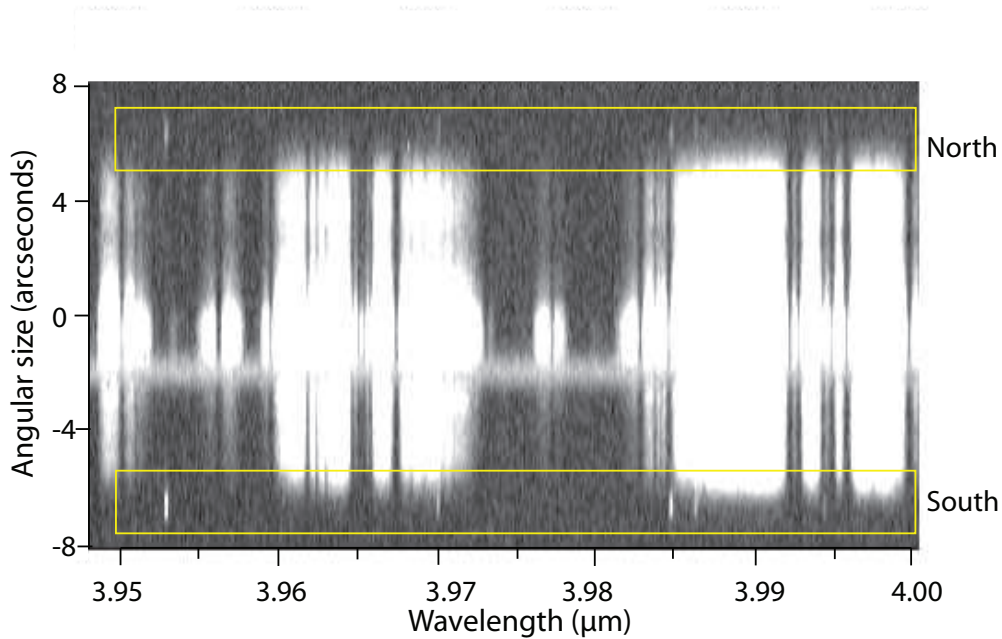


Figure 4.1: Observational set-up - A typical sky-subtracted (A-B) spectral image of Saturn taken at Saturn local noon of exposure length 60 seconds. The wavelength range is shown on the horizontal axis and the angular size in the sky is shown on the vertical axis. The north and south discrete H_3^+ emission lines are the regions of interest in this chapter and are highlighted by the yellow rectangles; the emissions are the white vertical lines within these boxes. Hydrocarbon absorption of solar radiation appears as black between these regions, and the white bar of emission at $-2''$ is the continuum reflection of sunlight from the rings. The remaining white pixels are due to reflected sunlight.

We collated data between $\sim 10^\circ$ and $\sim 22^\circ$ co-latitude in the northern and southern hemispheres, observing the northern and southern main auroral ovals. The error in assigning pixels to co-latitudes (pixel registration) was ± 1 pixel, which is negligible because the error introduced by atmospheric seeing is ~ 3 pixels. Standard sky subtraction and flux calibration (using the star HR6035) techniques were applied to the data, accounting for the Earth's atmosphere, and correlating CCD count to physical photon flux. The hydrocarbons (such as methane) present in Saturn's upper atmosphere below approximately 1000 km

altitude (Moore et al., 2009) act to both reflect and absorb solar radiation, depending on the wavelength of light. For instance, in Figure 4.1, sunlight is seen to reflect strongly at wavelengths centered at approximately $3.95 \mu\text{m}$ and $3.99 \mu\text{m}$, but methane (CH_4) acts to absorb light at the remaining wavelengths. Due to the increased column depth of CH_4 towards the limb, sunlight is absorbed enough to see auroral H_3^+ emission with a high S/N ratio. However, reflected sunlight increases equatorward until it eventually swamps the signal from discrete H_3^+ emission lines. Reflected sunlight is removed from the auroral emission by measuring the spectrum of light received near the equator and subtracting it from the auroral spectrum. The intensity of the hydrocarbon spectrum is itself reduced or increased by-eye until a pure auroral spectrum is visible, as shown in Figure 4.2. An underlying assumption is that the hydrocarbon layer reflection is invariant with latitude in terms of the wavelengths it emits at; this is a valid assumption given that neutral chemistry at low altitudes in the polar cap should be approximately the same as the rest of the planet (Moses and Bass, 2000). This ‘reduction function’ is deemed to be an accurate means of removing noise from spectra, and a failure to account for this noise at all results in fits with larger errors. With this subtraction, the only significant spectral signature that remains is the auroral H_3^+ emission.

As detailed in Chapter 2, for a given temperature H_3^+ produces a unique spectrum, such that there is a fixed temperature-dependent ratio between emission lines at different wavelengths. Transition-line intensities for a given temperature (also described by Melin et al. (2013)) give the H_3^+ temperature, $T(\text{H}_3^+)$. The spectral function of H_3^+ is varied until the line ratios match the least-squares-fit to the observed data, this is shown for a typical 15 minute-integrated spectrum in Figure 4.3. The line-of-sight (LoS) corrected column density, $N(\text{H}_3^+)$, accounts for the differing observed path-lengths through the atmosphere across the disk of the planet (see Subsection 2.4). Saturn’s sub-Earth latitude was 8.2° , by the addition of this angle to the observed latitude we correctly locate the position of

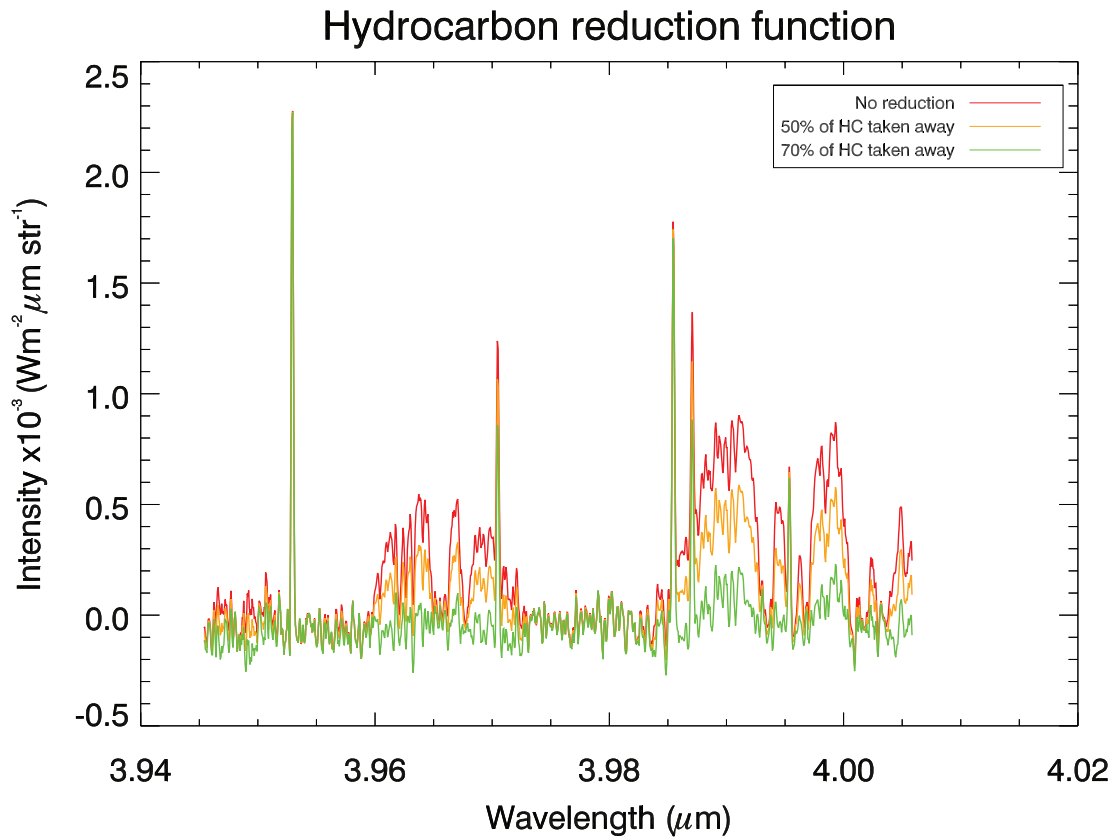


Figure 4.2: A hydrocarbon subtracted spectrum of Saturn - This shows different levels of hydrocarbon (HC) subtraction expressed as a percentage of hydrocarbon emission taken away. Note that the height of reduction in some H_3^+ lines in green is approximately equal to the height of the noise (hydrocarbon emission) in that region in red, meaning that the assumption of a linearly decaying quantity of hydrocarbon emission heading towards the limb is valid.

pixels. A measure of wavelength-integrated total emission from a LoS corrected column of H_3^+ , $E(\text{H}_3^+)$ can then be calculated by multiplying the total emission per molecule for the calculated $T(\text{H}_3^+)$ by $N(\text{H}_3^+)$ (see Subsection 2.5.5).

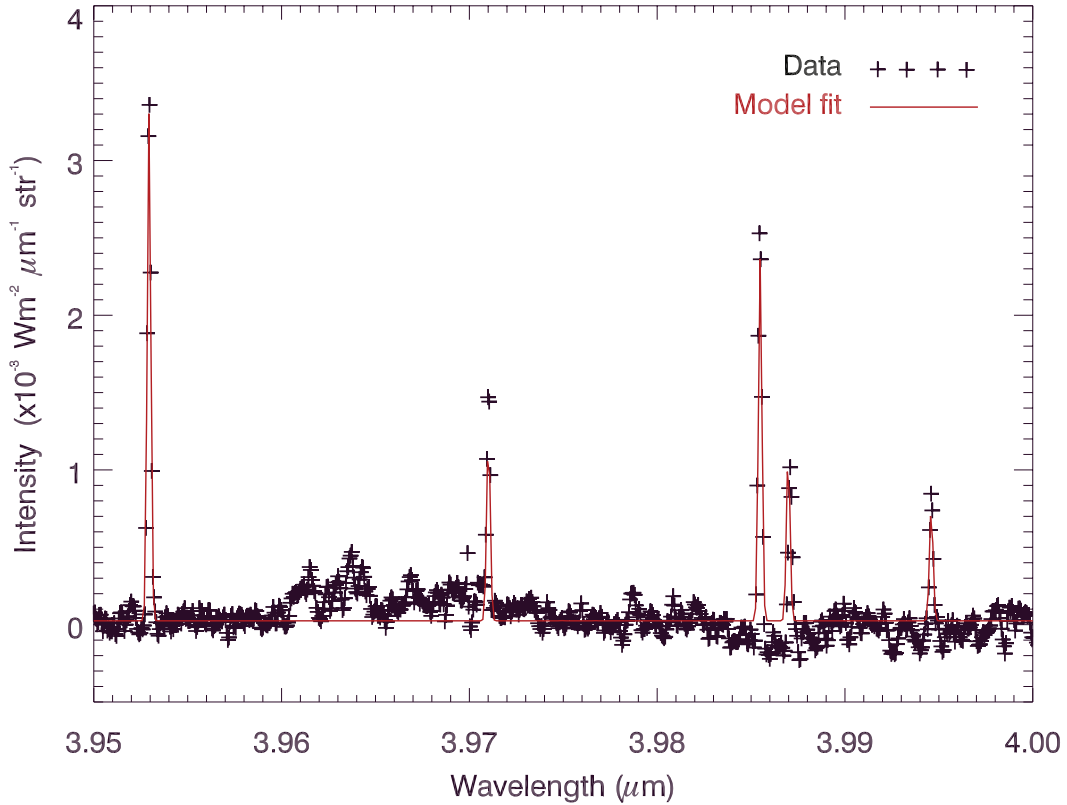


Figure 4.3: Model fit to data - An example model fit to the data. H_3^+ emission is shown as a function of wavelength (black crosses), fitted to a model of the expected emission (red) for a given temperature. The data in this figure are from a $0.144''$ (height) by $0.432''$ (width) area of the planet, which corresponds to an area of approximately $3320 \text{ km} \times 2700 \text{ km}$ at 19° co-latitude. From this fit we obtained a temperature of $523 \pm 13 \text{ K}$. The S/N ratio is up to 20 in this typical spectral profile. Low levels of solar reflection from hydrocarbons is visible over all wavelengths, though these levels are much reduced from their original values by the empirically calculated solar reflection subtraction.

4.3 Results

In Figure 4.4 we present simultaneous measurements of Saturn's H_3^+ temperature, column density, and total emission in the northern and southern auroral regions at local noon as a function of time. We view the auroral ovals as they rotate

past the spectrometer slit and so variability is a combination of temporal changes occurring at local noon and longitudinal variations rotating into view. The relationships between these parameters and between hemispheres are investigated. A summary of the results is given in Table 4.1. The northern thermospheric temperature is on average 527 ± 18 K, while the southern is 583 ± 13 K. The column density averages for the north and south aurorae are $1.56 \pm 0.32 \times 10^{15} \text{ m}^{-2}$ and $1.16 \pm 0.14 \times 10^{15} \text{ m}^{-2}$, respectively. An anti-correlation between H_3^+ temperature and column density is observed in our data. The total emission is ~ 1.5 times higher in the south, $0.98 \pm 0.02 \text{ Wm}^{-2}\text{sr}^{-1}$, compared with $0.65 \pm 0.03 \text{ Wm}^{-2}\text{sr}^{-1}$ in the north. This result is similar to previous work based on Cassini VIMS observations which examined IR wavelengths associated with H_3^+ emission at $\sim 3.6 \mu\text{m}$, showing that the pre-equinox southern main oval is on average ~ 1.3 times more intense than the northern main oval (Badman et al., 2011). The higher levels of emission cause the S/N ratio to be higher in the south so that the errors in all parameters are lower there relative to the north.

Start Time (UT)	E(North,H ₃ ⁺) ($\times 10^{-5}$ Wm ⁻² sr ⁻¹)	T(North,H ₃ ⁺) (Kelvin)	N(North,H ₃ ⁺) ($\times 10^{15}$ m ⁻²)	E(South,H ₃ ⁺) ($\times 10^{-5}$ Wm ⁻² sr ⁻¹)	T(South,H ₃ ⁺) (Kelvin)	N(South,H ₃ ⁺) ($\times 10^{15}$ m ⁻²)
10 : 33	0.81 \pm 0.03	528 \pm 17	1.85 \pm 0.34	0.92 \pm 0.02	592 \pm 13	0.96 \pm 0.11
10 : 49	0.69 \pm 0.02	529 \pm 17	1.59 \pm 0.30	0.90 \pm 0.02	580 \pm 14	1.10 \pm 0.14
11 : 02	0.64 \pm 0.02	539 \pm 18	1.33 \pm 0.25	0.89 \pm 0.02	575 \pm 14	1.16 \pm 0.15
11 : 19	0.66 \pm 0.03	544 \pm 19	1.29 \pm 0.25	0.96 \pm 0.02	588 \pm 14	1.07 \pm 0.13
11 : 36	0.64 \pm 0.03	537 \pm 19	1.41 \pm 0.28	1.00 \pm 0.02	586 \pm 13	1.15 \pm 0.13
11 : 49	0.61 \pm 0.03	528 \pm 20	1.49 \pm 0.33	1.06 \pm 0.02	585 \pm 13	1.22 \pm 0.14
12 : 04	0.57 \pm 0.03	513 \pm 20	1.66 \pm 0.39	1.06 \pm 0.02	580 \pm 12	1.30 \pm 0.20
12 : 17	0.60 \pm 0.03	521 \pm 20	1.51 \pm 0.35	1.02 \pm 0.02	579 \pm 13	1.25 \pm 0.14
12 : 32	0.62 \pm 0.02	517 \pm 18	1.66 \pm 0.34	0.99 \pm 0.02	580 \pm 13	1.19 \pm 0.14
12 : 46	0.65 \pm 0.02	515 \pm 15	1.77 \pm 0.32	0.97 \pm 0.02	579 \pm 12	1.20 \pm 0.13

Table 4.1: Saturn's main auroral oval properties as a function of time for 17th April 2011

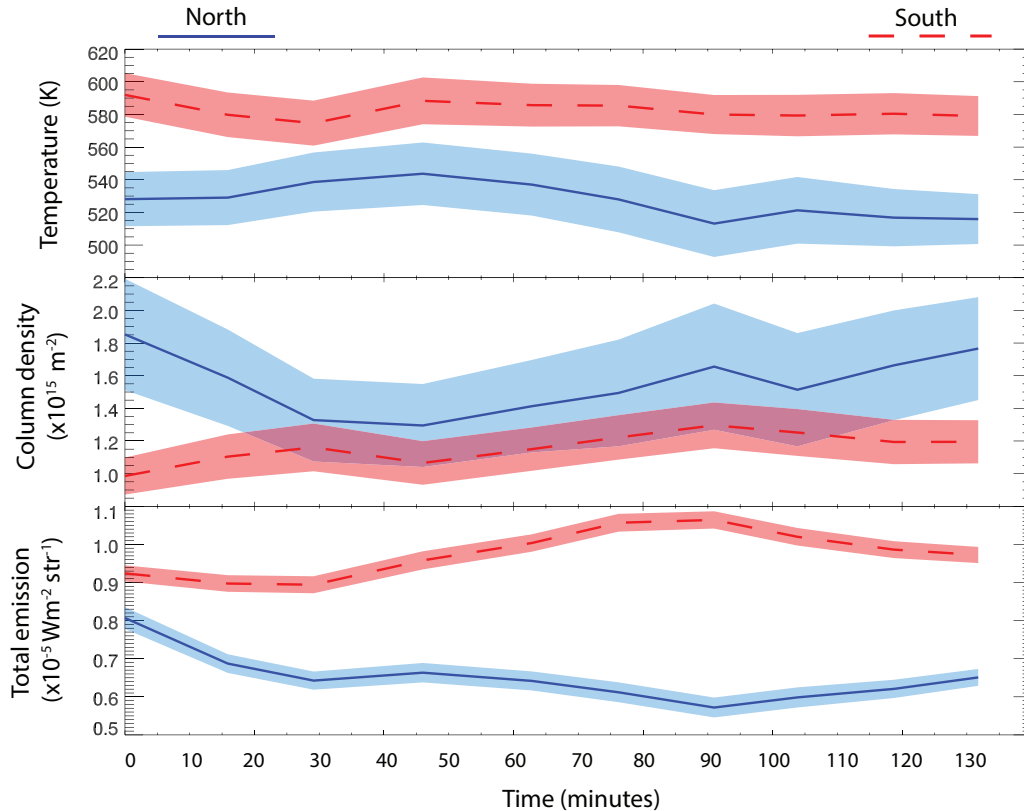


Figure 4.4: Saturn’s auroral parameters as a function of time - Temperature, H_3^+ column density and total emission of Saturn’s main oval auroral emission for each hemisphere integrated over $10 - 22^\circ$ latitude (y-axis), plotted as a function of time (x-axis). Northern data are shown in blue, and southern data in red. The thin dark coloured lines show data values, while the light coloured shading shows their corresponding uncertainty ranges. The time at 0 minutes is 10:34 UT on 17th April 2011.

4.4 General discussion

Here we discuss the measurements of Saturn’s auroral regions both combined and individually so as to compare with previous datasets.

4.4.1 Seasonal temperature differences

The average auroral thermospheric temperature in the south, ~ 583 K, is within the 560 - 620 K range found by Stallard et al. (2012b) using Cassini VIMS data from June 2007. However, this is substantially higher than the ground-based 1999/2004 UKIRT result of 400 ± 50 K found by Melin et al. (2007) and the

Cassini VIMS September 2008 result of 440 ± 50 K by Melin et al. (2011). These differences suggest that while temperatures are stable on the short time scales observed here, they vary significantly over longer time scales. The relatively higher temperatures here, stable over the timescale of the observations in both hemispheres, may indicate that Saturn is in the midst of a slow ‘heating event’ on time scales greater than hours. For instance, the temperatures herein versus those of Melin et al. (2011) are about 100 K different in three years. Only through further observations taken of the same latitudes can we identify the true nature of such long-term trends.

4.4.2 Correlations between parameters

The northern auroral thermosphere exhibits an anti-correlation between temperature and column density of $r = -0.72$ with a probability that these values are uncorrelated of $p = 0.02$. This is less pronounced in the south, with a correlation coefficient of $r = -0.52$ and $p = 0.12$. These anti-correlations are based on small variations in these parameters - small because they remain within the error bars of neighbouring values, such that variability is within the uncertainty, particularly for temperatures. If the anti-correlation here is real and not a product of the least-squares fitting routines discussed in Chapter 2, the physical ramification may be that increases in the density of H_3^+ lead to decreases in temperature, i.e. H_3^+ may be acting as a ‘thermostat’ to cool the planet in a small way as it does on Jupiter and Uranus (Miller et al., 2006) (although recent work by Mueller-Wodarg et al. (2012) shows such cooling plays a minor role at Saturn). In the north, there is a positive correlation coefficient of $r = 0.54$ ($p = 0.11$) between temperature and total emission whilst the correlation coefficient between total emission and column density is significantly weaker at $r = 0.13$ ($p = 0.74$), suggesting that it is changes in temperature that modulate changes in total emission. In the south, the H_3^+ column density and total emission are instead correlated strongly,

with a coefficient of $r = 0.76$ ($p = 0.01$), contrasting with the north. For both hemispheres, either new regions of the main oval are passing by the spectrograph slit or there are large changes in the particle precipitation at local noon during this period. Both such effects have been observed in the H_3^+ aurora using Cassini VIMS data by Badman et al. (2012a,b). Due to the observational techniques employed here (observing only Saturn local noon), it is difficult to distinguish between these processes.

4.5 Saturn's conjugate aurorae

Here we compare and contrast the northern and southern main auroral ovals.

4.5.1 Interhemispheric energy asymmetry

The most striking result shown in Figure 4.4 is that the southern auroral thermosphere is significantly hotter and more emissive than the north over the ~ 2 hour duration of these observations. Although the observations represent a 'snapshot' of the possible conditions in Saturn's ionosphere, the following discussions and conclusions assume this represents conditions that are typical on Saturn at that time in its season. Additional observations are required over time scales of weeks and months, to validate that this asymmetry is not due to short term (hours or days) effects. To investigate the reasons for this unexpected temperature difference, we consider the combined Joule and ion drag heating rate per unit area of the ionosphere (also described in Subsection 1.6.2), in particular the effect of the hemispheric difference in ionospheric magnetic field strength, where the northern polar field is a factor ~ 1.2 times the strength of the southern polar field (both integrated between $\sim 10^\circ - 22^\circ$) due to the quadrupole term in the planet's internal field. This is illustrated in Figure 4.5, where we plot the field strength in the Pedersen layer versus co-latitude from the respective poles for the northern (solid line) and southern (dashed) hemispheres, respectively. Here we have used

4.5 Saturn's conjugate aurorae

the latest internal field model based on Cassini data by Burton et al. (2010), consisting of axial dipole, quadrupole and octupole terms, evaluated at an altitude of 1000 km above the IAU 1 bar reference spheroid. The latter 1 bar surface has equatorial and polar radii of 60,268 and 54,364 km, respectively, with the Pedersen layer located ~ 1000 km above this surface (e.g., Burton et al., 2010).

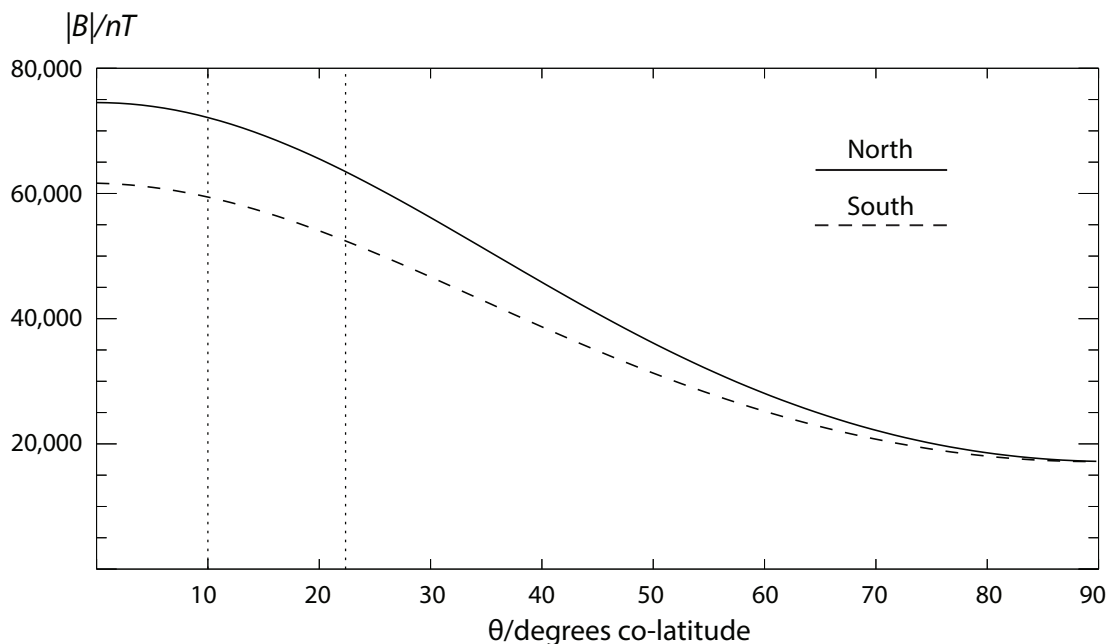


Figure 4.5: Saturn's magnetic field strength versus co-latitude - Saturn's internal magnetic field strength $|B|$ in the ionospheric Pedersen layer, shown plotted as a function of planetocentric co-latitude in degrees from the corresponding pole for the northern (solid) and southern (dashed) hemispheres, respectively. The Pedersen layer is taken to lie 1000 km above the IAU 1 bar pressure reference spheroid. The vertical lines (dotted) indicate the auroral region co-latitudes.

Joule heating is formally defined as heating associated with electron collisions with ions, whereas ion drag pertains to collisions between ions and neutrals. In recent literature in this field the term Joule heating is better defined as the dissipation of heat due to the mechanical collisions between plasma and neutrals, i.e. not the electromagnetic dissipation of heat (Vasyliunas and Song, 2005). The combined Joule heating and ion drag thermospheric heating rate per unit area in the northern (N) and southern (S) hemispheres is given by (e.g., Smith et al.

(2005); Cowley et al. (2005a))

$$q_{N,S} = \Sigma_{P_{N,S}}^* \mathbf{E}_{eqN,S}^2 , \quad (4.1)$$

where $\Sigma_{P_{N,S}}^*$ is the effective height-integrated Pedersen conductivity of the ionosphere, modified from the true value $\Sigma_{P_{N,S}}$ due to drag-induced atmospheric sub-corotation, and $E_{eqN,S}$ is the equatorward-directed ionospheric electric field ($\mathbf{E} = -\mathbf{v} \times \mathbf{B}$) in the rest frame of the planet at a given co-latitude with respect to the rotation/magnetic axis. The latter is given by

$$\mathbf{E}_{eqN,S} = \rho_{iN,S}(\Omega_{Sat} - \omega)\mathbf{B}_{iN,S} , \quad (4.2)$$

where $\rho_{iN,S}$ is the perpendicular distance of the Pedersen conducting layer from the axis, Ω_{Sat} is the angular velocity of Saturn defining the planetary ‘rest frame’ of rigid corotation, ω is the magnetospheric plasma angular velocity on the field line passing through the ionosphere at that co-latitude, and $\mathbf{B}_{iN,S}$ is the corresponding ionospheric magnetic field strength. The field is taken to be uniform and perpendicular to the polar ionosphere to a sufficient approximation, the latter peaking in Pedersen conductivity at an altitude of ~ 1000 km in the auroral region (Galand et al., 2011). The effective Pedersen conductivity is given by

$$\Sigma_{P_{N,S}}^* = (1 - k)\Sigma_{P_{N,S}} , \quad (4.3)$$

where k is the ratio between the neutral atmospheric velocity and the plasma angular velocity in the planet’s frame

$$(\Omega_{Sat} - \Omega_{Sat}^*) = k(\Omega_{Sat} - \omega) , \quad (4.4)$$

where Ω_{Sat}^* is the angular velocity of the neutral atmosphere. Atmospheric modelling results indicate that $k \sim 0.5$ at Saturn (Galand et al., 2011). Combining

Equations 4.1 and 4.2 we obtain

$$q_{N,S} = \Sigma_{PN,S}^* \rho_{iN,S}^2 (\Omega_{Sat} - \omega)^2 \mathbf{B}_{iN,S}^2 . \quad (4.5)$$

Now the magnetic flux threading the whole ionosphere between the pole and radial distance $\rho_{iN,S}$ from the pole is given by

$$\Phi_i = \pi \rho_{iN,S}^2 \mathbf{B}_{iN,S} , \quad (4.6)$$

such that we can write Equation 4.5 as

$$q_{N,S} = \frac{1}{\pi} \Sigma_{PN,S}^* (\Omega_{Sat} - \omega)^2 \Phi_i \mathbf{B}_{iN,S} . \quad (4.7)$$

We now consider conjugate points in the northern and southern hemispheres that share the same field line, thus contain equal magnetic flux Φ_i and have equal plasma angular velocities ω (under steady state conditions). It can be seen that the relative heating rates per unit area north and south (for conjugate locations) then depend only on the product of the effective height-integrated Pedersen conductivity, $\Sigma_{PN,S}^*$, and the field strength in the ionosphere, $\mathbf{B}_{iN,S}$. However, when assuming approximately equal ionospheric Pedersen layer number densities north and south (we validate this assumption in Subsection 4.5.4), the Pedersen conductivity is expected to vary approximately inversely as the ionospheric field strength i.e. $\Sigma_{PN,S}^* \propto \frac{1}{\mathbf{B}_{iN,S}}$, as reported by Galand et al. (2011) for near-equinoctial conditions. In these circumstances the thermospheric heating rates per unit area will be equal in the two hemispheres at conjugate points, independent of the magnetic field strength, because the $\mathbf{B}_{iN,S}$ terms cancel. This result does not, therefore, give immediate reason to expect the southern thermosphere to be hotter than the northern, unless the northern ionospheric conductivity is lower than that in the south by an unexpectedly large factor. The above result does, however, imply that the total heat input to the thermosphere from Joule heating and ion drag

integrated over the whole polar region will be larger in the south than in the north as we will now show, because the area of heating is larger in the south than in the north due to the lower field strength. If we consider conjugate circular ionospheric strips north and south with equal magnetic flux $d\Phi_i = 2\pi\mathbf{B}_{iN,S} \rho_{iN,S} d\rho_{iN,S}$, then the total heating north and south in the strips is given by

$$dQ_{N,S} = 2\pi q_{N,S} \rho_{iN,S} d\rho_{iN,S} = \frac{1}{\pi} \Sigma_{PN,S}^* (\Omega_{Sat} - \omega)^2 \Phi_i d\Phi_i . \quad (4.8)$$

Thus the total heating rate, obtained by integrating over all the flux strips from the pole to the point where rigid corotation is attained, is then proportional only to $\Sigma_{PN,S}^*$, such that if the latter varies approximately inversely with the field strength as indicated above, the total power dissipated to heat in the polar thermosphere will be larger in the southern hemisphere than in the northern. The local heating rates are the same in the thermosphere but the total heating is greater in the south. The removal of the $\mathbf{B}_{iN,S}$ term from Equation 4.7 by working in the reference frame of magnetic flux Φ_i , which is the same here in both hemispheres and therefore already accounts for the effects of $\mathbf{B}_{iN,S}$: this actually implies that the heated area is in fact larger in the south due to the weaker magnetic field strength. It remains to be investigated by modelling whether such an effect could produce the temperature differences measured here. If not, then some other heating mechanism, such as hemispheric differences in wave driving from below, must be implicated.

4.5.2 Comparison to previous studies

The work herein is not the only conjugate study of both of the northern and southern auroral ovals. However, whilst such studies have been done (and we compare them here), they have not been advantaged by measurements of the ionospheric temperature. A comparison with recent modelling work by Galand et al. (2011) agrees with the interpretation above in that an asymmetry is present

(during equinox) in which the Pedersen and Hall conductivities were 1.2 and 1.3 times higher, respectively, in the southern hemisphere than in the northern. Previous observations by Cassini VIMS analysed by Badman et al. (2011) also found the same trend in intensity - and likely therefore in temperature - in their pre-equinox 2006 - 2009 data. The fact that this asymmetry persists post-equinox in our data suggests that the magnitude of the magnetic field is the dominant effect on Pedersen conductivity rather than the solar-EUV ionization, at least in northern spring. In other words, magnetic field strength may dominate over seasonal effects in determining inter-hemispheric auroral thermosphere temperatures, though further observations and modelling are required to test this - in particular whether or not it persists into the northern summer season.

In the UV, simultaneous observations of the conjugate northern and southern aurora taken by the HST in 2009 have been analysed by Nichols et al. (2009) and Meredith et al. (2013). The former showed, from the data acquired over a period of just ~ 1 month pre-equinox, that the northern auroral region had on average $\sim 17\%$ higher emitted power than the south, the opposite to the IR case presented here. The latter study found transient eastward-propagating patches of UV emission in the dawn-to-noon sector for 70% of the 32 visits using the HST, which are similar to the small-scale features found by Grodent (2011). In this chapter, such small-scale features are therefore very likely to be passing by the spectrograph slit, and could lead to small-scale variations in the column density of H_3^+ . However, UV emissions are a prompt emission in which hydrogen is excited by particle precipitation and immediately releases the newly acquired energy to space via the emission of UV photons. Hydrogen that emits in the UV is not therefore in thermal equilibrium with the surrounding thermosphere. By contrast, H_3^+ emission is, to a good approximation, thermalised with the thermosphere (Miller et al., 2006); also, H_3^+ is largely driven by temperature changes due to Joule heating and ion drag, so its temperature represents changes

in those. As a consequence of the differing IR and UV emission production mechanisms, direct comparison is difficult. Given that Joule heating and ion drag is ~ 50 times greater in power than auroral particle precipitation (Cowley et al., 2004) (responsible for UV emission), it is understandable in the above UV studies that a stronger northern UV emission or the appearance of small-scale structures/patches need not necessarily correspond to higher temperatures or IR emission. We were unable to resolve small-scale features here with small uncertainties, so we cannot compare individual features. In addition, it should be noted that the above UV observations took place over two years earlier than those herein.

4.5.3 Modelled versus observed H_3^+ density

The ratio between the average column integrated densities in the north and south auroral regions is 1.35. The cause for this asymmetry could be an increase in the northern H_2 ionization rate, which itself arises from the larger incident solar photon flux in the north owing to Saturn's 9.1° sub-solar latitude. An increase in the quantity of ionized H_2 then leads to a greater production of H_3^+ , although this is overlain atop the dominating particle precipitation auroral mechanism. This was also demonstrated using a 1-D model, the Saturn Thermosphere Ionosphere Model (STIM), which found a range of north-south H_3^+ density ratios between 1.2 - 3.0 based on solar EUV influx alone (between 10° - 22° co-latitude): this is shown for a nominal value of 'q' which is the ratio of H_2 in the fourth or higher vibrational state to ground-state H_2 , i.e. H_2^*/H_2 . The nominal value of q is 10^{-6} in Figure 4.6 and for multiple values of q in figure 4.7 (the latter to illustrate the large range of ratios due to q).

Despite having lower column densities, the average total emission is ~ 1.5 times higher in the south; this is due to the higher temperature there. The previous section concerned itself with an inverse relationship between Pedersen conductivity and field strength, with the caveat being that the number density of the

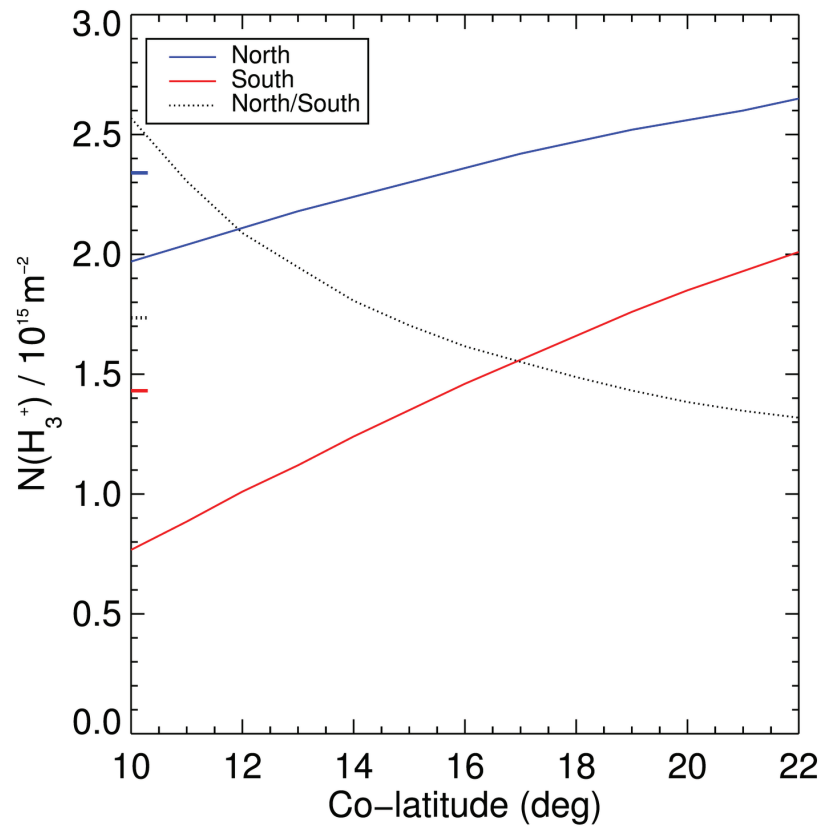


Figure 4.6: Modelled EUV modulated H_3^+ density for nominal q - STIM modelled values of H_3^+ density based on solar EUV ionization alone for the northern and southern hemispheres for $q = 10^{-6}$. The x- and y-axes show planetocentric co-latitude and H_3^+ density, respectively.

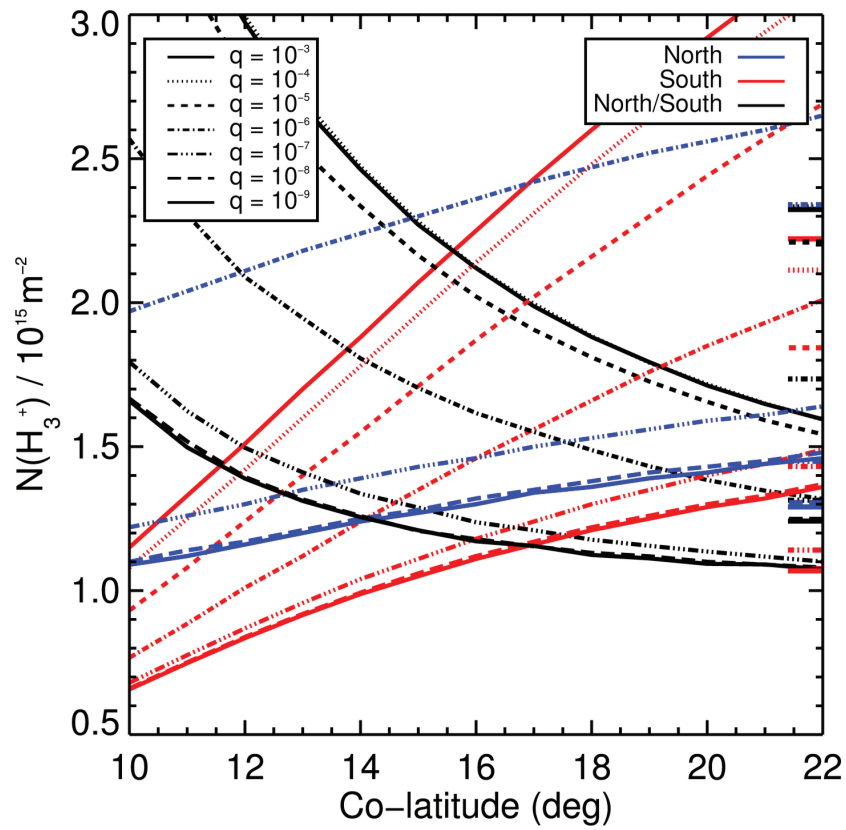


Figure 4.7: Modelled EUV modulated H_3^+ density for multiple values of q - As Figure 4.6 but this time for multiple values of q .

Pedersen layer is the same for both hemispheres. In Figure 4.4, it appears at first glance that the contrary is true because H_3^+ density is higher in the north, which would imply our previous argument is incomplete. However, H_3^+ density which peaks at an altitude of 1155 km (Stallard et al., 2012b) is not wholly representative of the Pedersen layer number density which itself peaks at an altitude of 1000 km (Moore et al., 2010; Galand et al., 2011). The ions (and their companion electrons) that create the Pedersen layer are largely hydrocarbon ions, which are dominant below ~ 1000 km (Mueller-Wodarg et al., 2012), and so the H_3^+ density does not have direct implication for the previous derivation. Following from the above, the H_3^+ temperature must differ from the Pedersen layer temperature because it is higher in altitude in a region of positive temperature gradients. However, an increase in temperature at 1000 km will lead to an increase in temperature at altitudes above it, due to the vertical conduction of heat.

4.5.4 Particle precipitation

One might assume that a higher H_3^+ density and lower temperature (as in the northern auroral thermosphere) could indicate that the column of H_3^+ sampled was deeper in the atmosphere: an inverse relationship like this exists at Jupiter (Lystrup et al., 2008). As previously stated, the H_3^+ densities presented herein are column integrated and LoS corrected, such that altitudinal information is averaged for the observed atmospheric column. If the H_3^+ densities were higher in the northern hemisphere relative to the south because of the inverse relationship above, it implies that electrons must penetrate deeper in the north, thus leading to enhancements in H_3^+ production (density) in a colder region. For this to occur, the electron precipitation energy must be relatively higher in the northern auroral region, since higher energy electrons penetrate to lower altitudes than lower energy electrons (Tao et al., 2011a). To test this, we employed the magnetosphere-ionosphere coupling model known as the ‘CBO’ model, created

by Cowley and Bunce (2003), and used updated parameters derived from Cassini spacecraft measurements (Cowley et al., 2008). As field-aligned currents depend on conductivity, which in turn depends on field strength, it is appropriate to reduce the northern conductivity from 4 mho in Cowley et al. (2008) by a factor of 1.215 corresponding to the field asymmetry already mentioned, such that it is fixed at 3.3 mho whilst the south remains at 4 mho. Following this, we find that the average electron precipitation energy in both hemispheres is approximately the same at ~ 11.4 keV. Therefore, we have no reason to expect that there be a difference in the altitude at which auroral electrons are deposited in either hemisphere. In addition, because of the similarity in the precipitation population at the conjugate points in each hemisphere, we assume that contributions due to precipitation-induced enhancements of the Pedersen conductivity are negligible. This interpretation is based on electrons accelerated planet-ward along closed field lines that require accelerating voltages of ~ 10 kV to enter the planet. Poleward of this, currents along open field lines can be carried by cool dense magnetosheath plasma that requires accelerating voltages of $\sim 0.1 - 1$ kV (Bunce et al., 2008a), hence the majority of auroral emission is associated with particle precipitation along closed field lines.

4.6 Conclusions

Ground-based Keck NIRSPEC observations of auroral H_3^+ emission from Saturn have been analyzed. During the ~ 2 hours of data obtained here, temperatures remained effectively constant within the error range achieved. At the same time, column density and total emission vary greatly, by up to a factor of 2, particularly in the north. This may be caused by temporal or spatial variation in the aurora, likely due to varying particle precipitation, leading to the small variations seen in all H_3^+ parameters. The main oval in the south is significantly warmer and

more emissive than its northern counterpart. This asymmetry is attributed to an inversely proportional relationship between ionospheric Joule and ion drag heating and magnetic field strength. This effect outweighs the increased heating produced by seasonal enhancements in conductivity, meaning that the southern autumn auroral oval is 50 K warmer than that in the northern spring hemisphere. This is consistent with model predictions of a higher Pedersen conductivity in the south than the north (Galand et al., 2011) and an intensity asymmetry observed by Cassini VIMS pre-equinox (Badman et al., 2011). A number of correlations exist between parameters that may be significant and we highlight possible causes for them, such as a possible anti-correlation between temperature and column density. A dedicated observing campaign of Saturn's aurora is required to verify these relationships and assess the long-term behaviour of Saturn in response to seasonal variations. Although the southern auroral oval is unfortunately no longer viewable until at least 2023 from Earth-based telescopes, the changing viewing geometry will allow for more comprehensive studies of the northern aurora for several years.

Chapter 5

Jupiter: comparative aeronomy

Jupiter is the planet in our solar system that is the most similar to Saturn for a host of reasons, including size, composition and in the production of bright auroral H_3^+ emissions at the poles of the planet. They are both associated with the aforementioned ‘energy crisis’ and both subjected to continuous material influx by moons, and in Saturn’s case also the rings. We are thus interested in comparing the low latitudes of Jupiter investigated in this chapter to those of Chapter 3 (Saturn’s ring rain) to examine the aeronomy of a planet in the absence of a significant ring system. In this chapter we shall compare newly produced global maps of Jovian H_3^+ parameters based on observations taken in 2012, to the those of similar maps which were produced by Lam et al. (1997) in 1993, and with our observations of Saturn presented in this thesis.

5.1 Jupiter-specific data acquisition

5.1.1 Observations

The observations of Jupiter described herein span four nights between 4 - 8 December 2012 (UT). They were taken using the 3-metre NASA IRTF and SpeX instrument (Rayner et al., 2003) and the standard astronomical data reduction techniques outlined in Chapter 2 were employed. The additional and unique

5.1 Jupiter-specific data acquisition

methodology, observing conditions, and specifics for these observations are discussed here. Jupiter was at a sub-Earth latitude (SEL) of 3° during these observations, with the northern hemisphere slightly inclined towards Earth; given this small tilt we define the prevailing conditions as equinoctial rather than northern spring and southern autumn, in comparison with Saturn which was in spring. We aligned the spectrometer’s slit from pole-to-pole at Jovian local noon and the planet rotated as we took spectral images. The weather and seeing varied throughout the observations, leading to different quantities of spectral images per night: a summary of the observations is given in Table 5.1.

Date	Time range (UT)	Cloud cover	Seeing	No. spectra
Dec 4 th	06:45 - 15:30	Clear	0.8''	137
Dec 5 th	04:15 - 13:45	Cloudy, clear spells	1.0''	15
Dec 7 th	04:15 - 10:00	Clear, passing Cirrus	1.1''	23
Dec 8 th	04:30 - 15:00	Clear	0.8''	93

Table 5.1: Summary of Jupiter observation times and conditions

In total, over the four nights, we obtained 268 spectral images; the vast majority of these were on the first and final night. The spectra taken consist of the co-addition of two 30-second integrations, creating exposures 60 seconds long. In simultaneity with these, we were able to take images of Jupiter through the slit-viewing camera on the SpeX instrument - these were 2-second exposures that were taken throughout the observations each night. An example guider image that shows the observational set up is shown in Figure 5.1.

During the observations the telescope was stable, due to the telescope being able to off-axis guide on a nearby star, meaning that the slit was well centered at local Jovian noon. However, at times guiding was lost due to clouds obscuring the guiding camera (which were seen in the guider images) and thus dozens of spectral images were excluded from this study. A complete summary of the central meridian longitudes (CML) obtained (in Jovian system III coordinates) over the 4 nights is shown in Figure 5.2. Within, note that the data gap between 170° to 200° happens to be in the longitudes in which Jupiter’s main oval drapes

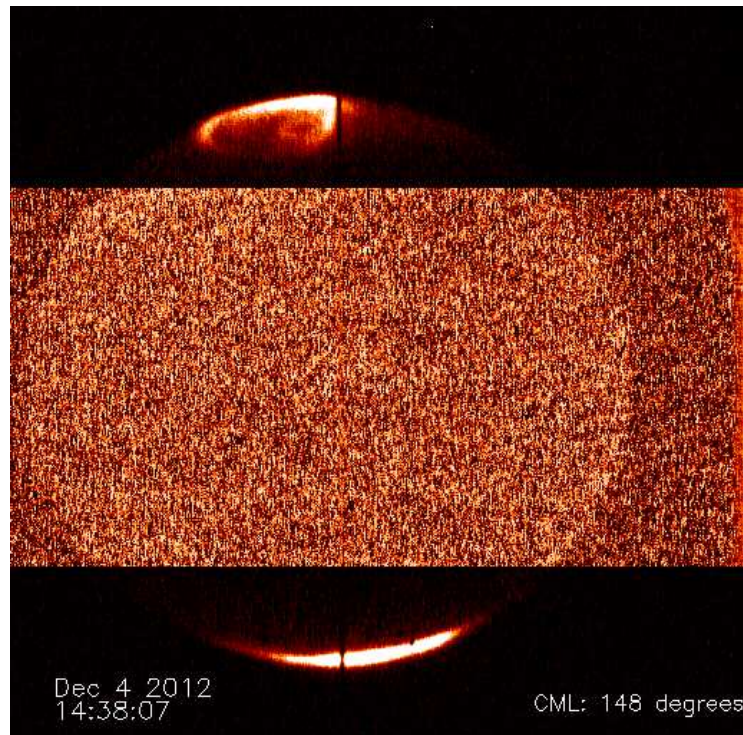


Figure 5.1: IR image of Jupiter - This image shows IR radiation of Jupiter at $\sim 3.4 \mu\text{m}$; the majority of this emission is from the discrete emission lines of H_3^+ . This IR image of Jupiter was taken with the slit-viewing camera on SpeX, it is a co-addition of five 2-second integrations. The spectral slit passes through the local noon meridian and Jupiter's main oval is seen to drape down the planet. The body (non-auroral) component of the planet is made brighter by thresholding as it is otherwise too dark to see.

5.1 Jupiter-specific data acquisition

down the planet, which means we are not afforded an clearer view of Jupiter’s main auroral oval in the spectral images which are taken at local noon (this is highlighted again later).

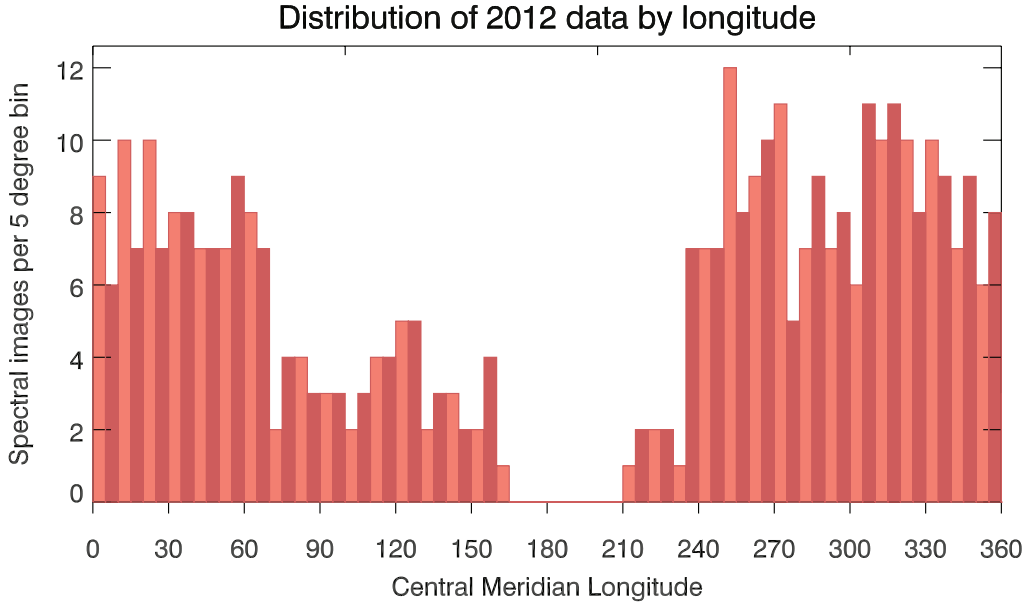


Figure 5.2: Jovian longitudes observed - This histogram shows the distribution of longitudes in terms of central meridian longitude (CML) in the Jupiter system III coordinate system. The dates encompasses are given in Table 5.1 and the spectral image counts are shown in 5° bins.

5.1.2 Spectral map construction

To construct maps of H_3^+ parameters, an empty 360° (longitude) by 180° (latitude) by 450 (wavelength pixels) grid was created. It was populated as follows: the rows in a spectral image are latitudes (-90° to +90°); the longitudes (0 - 359° CML) are found by the spectral image exposure time and the wavelength domain is the horizontal component of the spectral image - varying in intensity as a function of 450 elements of wavelength. Together, these elements represent a three dimensional data cube of H_3^+ intensity as a function of wavelength, longitude and latitude. From this, one may select longitude and latitude ranges and derive H_3^+ parameter maps.

Although it is a trivial process to assign latitudes and longitudes to pixels on an image, there are first some corrections to be made. A pixel subtends a range of

5.1 Jupiter-specific data acquisition

longitudes and latitudes, and this changes depending on where they are located on the planet. The width of the slit is two pixels and subtends $0.3''$; the minimum longitude is the right part of the slit and the maximum longitude is the left of the slit (CML increases as the planet rotates). Jupiter rotates 0.605° during the 60 second exposure, this is accounted for by adding 0.605° to the left side of the slit. The longitudinal area covered by the slit increases and so a correction must be made. The pixel height represents an increasing range of latitudes towards the poles, so this too must be corrected. The latitude, θ , of a pixel is given by

$$\theta = \arcsin\left(\frac{R_{Jp} - (0.15 \times n)}{R_{Jp}}\right) + \Theta_{SEL} \quad (5.1)$$

where R_{Jp} is the Jovian polar radius ($22.6''$), $0.15''$ is the size of 1 pixel and n is the pixel number from pole-to-pole (Jupiter subtends 302 pixels from pole-to-pole; the limbs of the planet were found as outlined in Subsection 2.4). The Θ_{SEL} for these observations was 3.0° . The top and bottom of each pixel in terms of latitude is calculated by finding the half-way point to the adjacent pixels, the extent that the pixels smear latitudinally is shown by Figure 5.3.

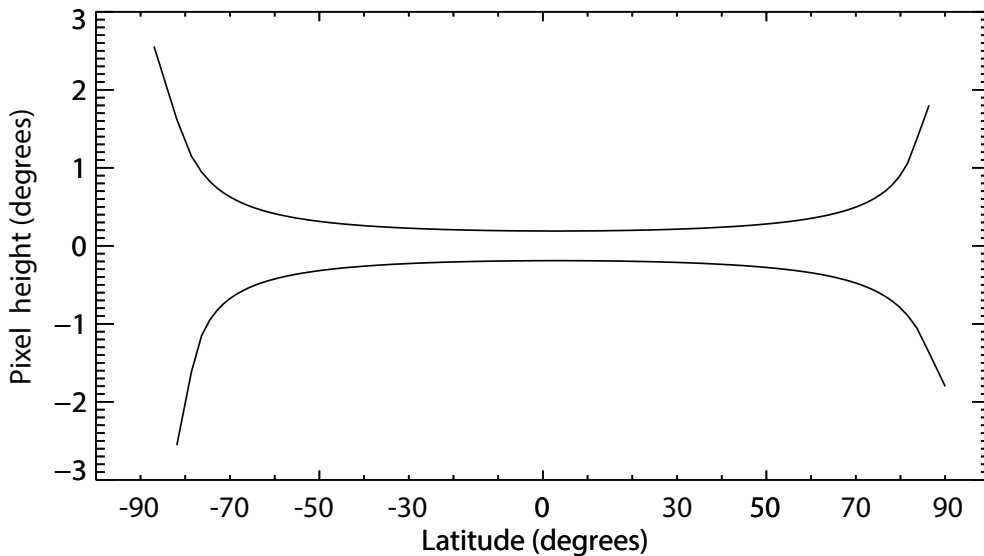


Figure 5.3: Latitudinal broadening of pixels - The latitudinal size of a pixel begins to increase towards the polar regions due to viewing geometry. This figure illustrates that a pixel located near the pole represents a larger range of latitudes than those pixels near the equator.

5.1 Jupiter-specific data acquisition

The diameter of the planet depends on these latitudes and is given by D_θ ; the longitudes of the slit edges are then calculated by

$$\begin{aligned}
 D_\theta &= D_{eq} \times \cos(\theta) \\
 Slit_{right} &= \arcsin\left(\frac{0.15''}{D_\theta/2}\right) \\
 Slit_{left} &= \arcsin\left(\frac{0.15''}{D_\theta/2}\right) + 0.605^\circ
 \end{aligned} \tag{5.2}$$

where D_{eq} is Jupiter's equatorial diameter, $0.15''$ is half the slit width, note that 0.605° was added to the left side of the slit in the direction of increasing longitude as the planet rotates. Using this process we produce Figure 5.4, which shows the longitude coverage of the slit as a function of latitude. In the polar regions the

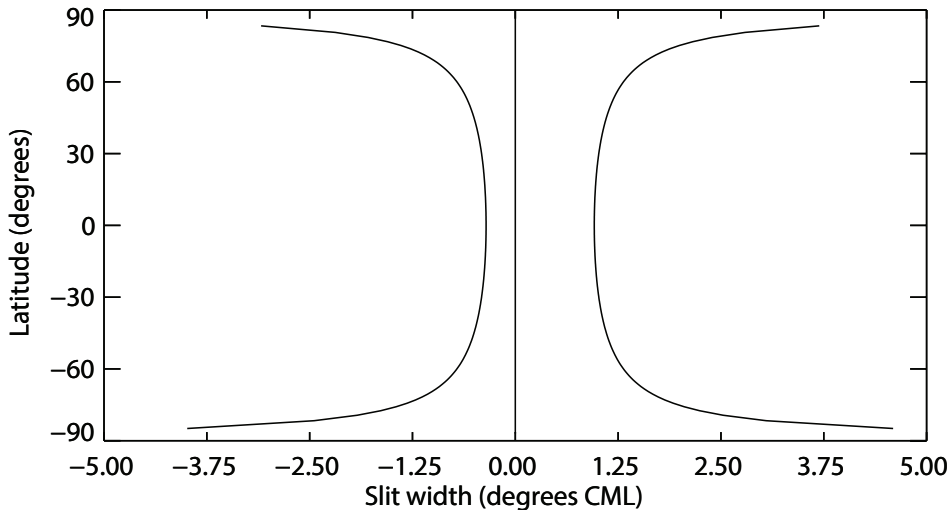


Figure 5.4: Longitudinal broadening of data - The slit width is a fixed value on the SpeX instrument, but represents a differing value of longitudes on the curved surface of Jupiter. The polar regions are significantly stretched due to viewing geometry, more so on the right because of planetary rotation.

latitudes that a given pixel cover are large, the consequence of this is twofold: first, there are fewer data points per degree of latitude at the poles compared to lower latitudes; second, each pixel covers a larger surface area at the poles, so there is considerably more overlap as the data are stretched to adjacent pixels. Once a map has been produced, an overlap is accounted for by dividing it by the number of times the region has been observed. In addition, overlaps also take

place when multiple days are coadded and are dealt with in the same way.

5.1.3 Uncertainty limited spectral fitting

From these maps of spectra versus longitude and latitude, we can select varying bin sizes for the data to be fitted; the details of the fitting routine used are outlined in Chapter 2. We derived the properties of H_3^+ temperature, column density, total emission for the range of latitude and longitude spatial bin sizes below (format: latitude \times longitude)

- | | | |
|-------------------------------|-------------------------------|--------------------------------|
| 1. $2^\circ \times 4^\circ$ | 4. $15^\circ \times 30^\circ$ | 7. $45^\circ \times 90^\circ$ |
| 2. $5^\circ \times 10^\circ$ | 5. $20^\circ \times 40^\circ$ | 8. $60^\circ \times 120^\circ$ |
| 3. $10^\circ \times 20^\circ$ | 6. $30^\circ \times 60^\circ$ | 9. $90^\circ \times 180^\circ$ |

Each parameter in a spatial bin has an uncertainty that depends on the quality of the fit; a lower uncertainty corresponds to a higher S/N ratio (Melin et al., 2014). As a result, the uncertainties are greatest where the H_3^+ emission is weak, such as the equator, and least in the much more intense auroral regions; consequently, selecting larger bin sizes will produce smaller uncertainties, but in using a larger bin size we clearly lose spatial resolution as we are averaging emission over a larger area. The discovery that there are lower latitudinal variations in H_3^+ at Saturn, as shown in Chapter 3, coupled with the polar to mid latitude intensity gradient, has prompted us to use longitudinal bins that were twice as large as the latitude bins.

The construction of a map of temperatures (for instance) is then produced by choosing an uncertainty limit; with this limit, a program is tasked with searching through the bins in order of size from smallest to largest. For instance, a whole 360° by 180° grid is populated first by $2^\circ \times 4^\circ$ elements that are below the uncertainty threshold (which comes from the spectral fitting routine discussed in

5.1 Jupiter-specific data acquisition

Chapter 2), leading to many gaps in the map, the data gaps are then filled by the next bin size; $5^\circ \times 10^\circ$. This process is repeated until the map is completely filled with temperature data that are below 11% uncertainty. An example of a completed map for temperature, in terms of which bins are ultimately selected, is shown in Figure 5.5. In this figure it is clear that lower uncertainties reside in the auroral region where the S/N is highest, because the smallest bin sizes are able to fully populate it, whereas in the equatorial region, bin sizes are forced to become larger to accommodate the uncertainty limit.

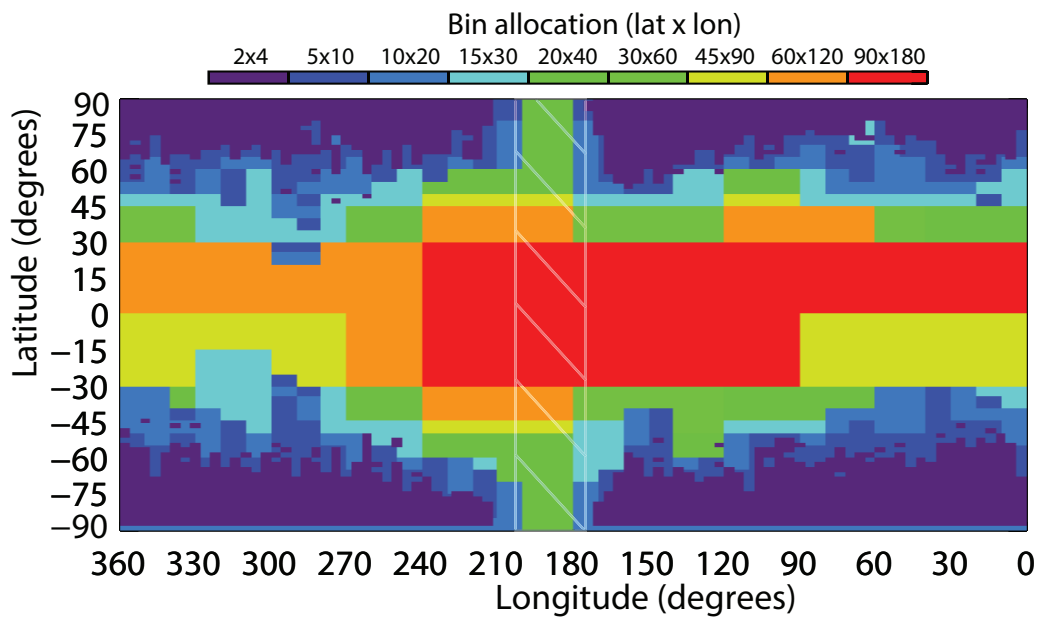


Figure 5.5: Bin allocation visualisation - A map of spatial bin sizes as a function of longitude and latitude (Jupiter system III planetocentric coordinates) as described in the main text. The grey diagonal lines in the centre indicate the interpolation of data from adjacent longitudes.

5.2 Comparison with previous studies

5.2.1 Observational differences

The first global maps of temperature and other parameters of H_3^+ were published in 1997 by Lam et al. (1997). Later that year Miller et al. (1997) performed a similar analysis, with focus on the origins of Jovian sub-auroral emissions. We now compare these observations to our own. Lam et al's data were based on observations using the 3.8-metre United Kingdom IR Telescope (UKIRT) in 1993 and the Cooled Grating Spectrometer 4 (CGS4). An overview of the differences are shown in Table 5.2, note that although the telescope size in this work is 0.8 metres smaller, we achieve a spatial resolution ~ 37 times finer on the planet due to the limits of the respective spectrometers.

	Lam et al. (1997)	This work
Year observed	1993	2012
Seeing during observations	1.5''	1-1.5''
Jupiter sub-Earth latitude	-3°	+3°
Telescope & size	UKIRT, 3.8-metre	NASA IRTF, 3-metre
Telescope diffraction limit	0.23''	0.29''
Spectrometer & resolving power	CGS4, $R = \lambda/\Delta\lambda \sim 1700$	SpeX, $R = \lambda/\Delta\lambda \sim 2500$
Spectral resolution at 3.5 micron	2.92 nm	1.40 nm
Instrument angular resolution	3.08'' pixel ⁻¹	0.15'' pixel ⁻¹
Instrument spatial resolution	9800 km pixel ⁻¹	475 km pixel ⁻¹
Exposure time & degrees rotated	10 minutes, 6°	1 minute, 0.6°

Table 5.2: Observational differences between Lam et al and this work

Lam et al's observational set up was essentially the same as that in our study, with the spectrograph slit aligned along the Jovian noon meridian. An example 10 minute spectral image obtained by Lam et al. (1997) is shown in Figure 5.6, and a 10 minute co-add (10 images) from this work is shown in Figure 5.7. The major differences highlighted in Table 5.2 are illustrated by these figures, and of particular importance is the improvement in spatial resolution using SpeX compared to CGS4, which leads to both a better spatial resolution and a higher

5.2 Comparison with previous studies

signal-to-noise ratio. A further improvement in our data is the increase in spectral resolution, allowing for a higher S/N ratio, thus giving a lower uncertainty in the H_3^+ fitting routines outlined in Chapter 2.

In the subsequent figures is the magnetic mapping of satellite ‘footprints’ and the main oval location, Lam et al. (1997) used an older magnetic model published in 1993 (Connerney, 1993), whereas we used one published in 1998 (Connerney et al., 1998). In each figure, the locations of the main oval and footprints of magnetically linked large Jovian satellites are shown as white lines (as are indicated in the figure legends). These locations are found using the Voyager Io Pioneer 4 (VIP4) magnetic model, which uses both in-situ spacecraft data from Pioneer and Voyager and observations of the location of the Io footprint in Jupiter’s ionosphere (Connerney et al., 1998). The main oval location maps to the breakdown in corotation of plasma in the equatorial plane at 20 - 30 R_J in the equatorial plane, whereas Europa’s footprint maps to 9.4 R_J , Io to 5.9 R_J and finally Amalthea to 2.54 R_J .

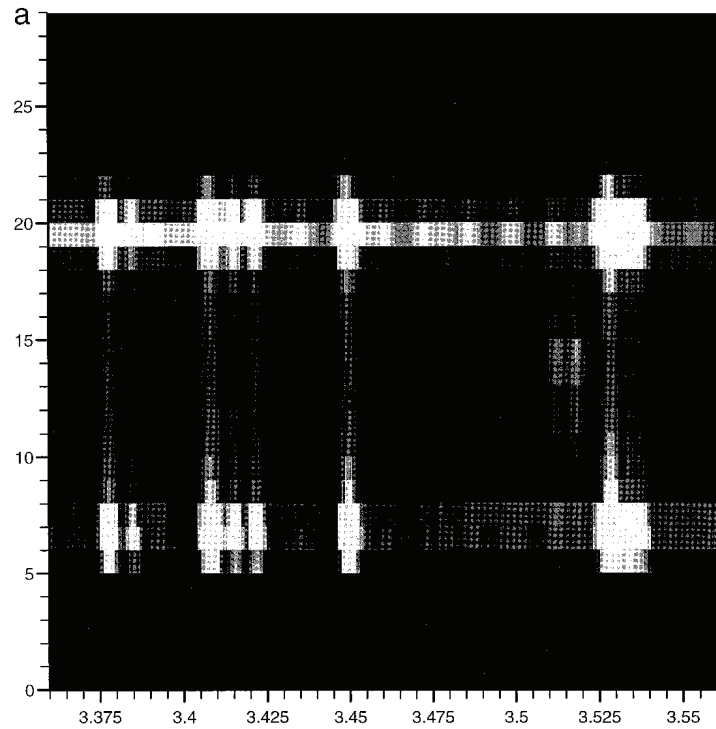


Figure 5.6: Lam et al Jovian spectra - A spectral image obtained with CGS4 on UKIRT. X- and y-axes show wavelength in microns and pixel position (pole-to-pole; 1 pixel is ~ 3.08 arcseconds). Figure 1 from Lam et al. (1997)

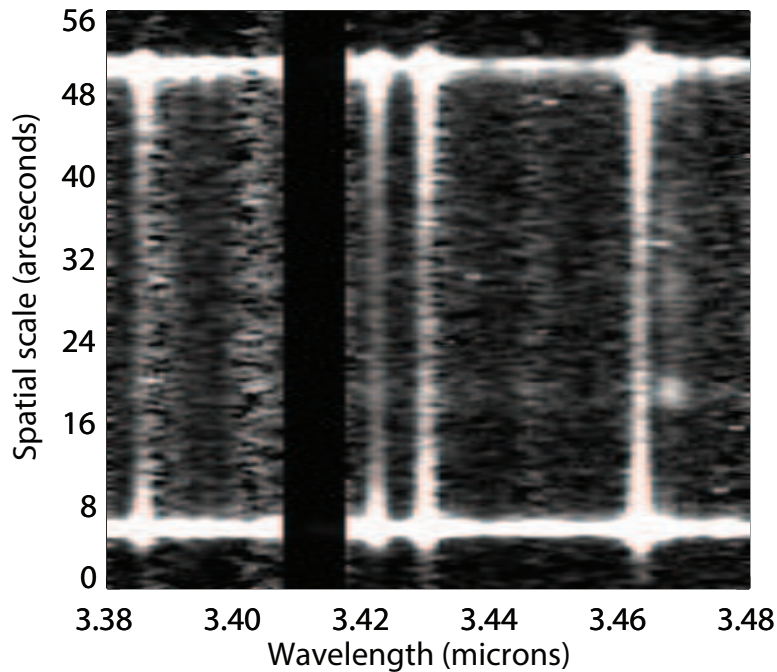


Figure 5.7: Jovian spectra; this work - This is an example co-add of 10 spectral images (10 minute total exposure) taken with SpeX on the IRTF. X- and y-axes show wavelength and spatial position in arcseconds. The sharp cut out in intensity at $3.41 \mu\text{m}$ was to exclude a spectral region of high attenuation by the Earth's atmosphere.

5.2.2 H_3^+ temperature comparison to Lam et al

The resulting temperature map by Lam et al. (1997) is shown in Figure 5.8. The authors chose a contoured map to display their data, the benefit of which is that adjacent elements can be smoothly linked, which is certainly easier on the eye, but if anomalously high or low values exist in individual pixels, they will go on to artificially modify neighbouring pixels.

To perform a fair comparison between Lam et al. (1997) and our work, it is necessary to reduce our spatial resolution. Given that Lam et al's resolution was approximately 10° per pixel in latitude, we have chosen only the spectral bins equal to and greater than $10^\circ \times 20^\circ$ (bins 3 to 9 in Subsection 5.1.3). We present our data as a contour map which is smoothed by 10 degrees of longitude and latitude in Figure 5.9, which is uncertainty limited to 12%. This value and others are chosen because they are similar to the uncertainties of previous studies, e.g. see Chapter 3.

Morphologically the two figures are similar, with hotter auroral regions compared to the majority of the mid- and low-latitudes. The differences in viewing geometries are apparent as Lam et al appear to have resolved the southern auroral region far away from the limb. Perhaps the largest differences at the poles stem from the fact that our pixels have been stretched as outlined in Subsection 5.1.2, such that viewing geometry is fully accounted for in both the longitude and latitude dimensions.

There are multiple regions in which the temperature structure for both datasets appears to be similar. One example is the apparently cold (~ 700 K) region at around 60° longitude and latitude, and there also appears to be large elongated 'blobs' of hot H_3^+ across the planet.

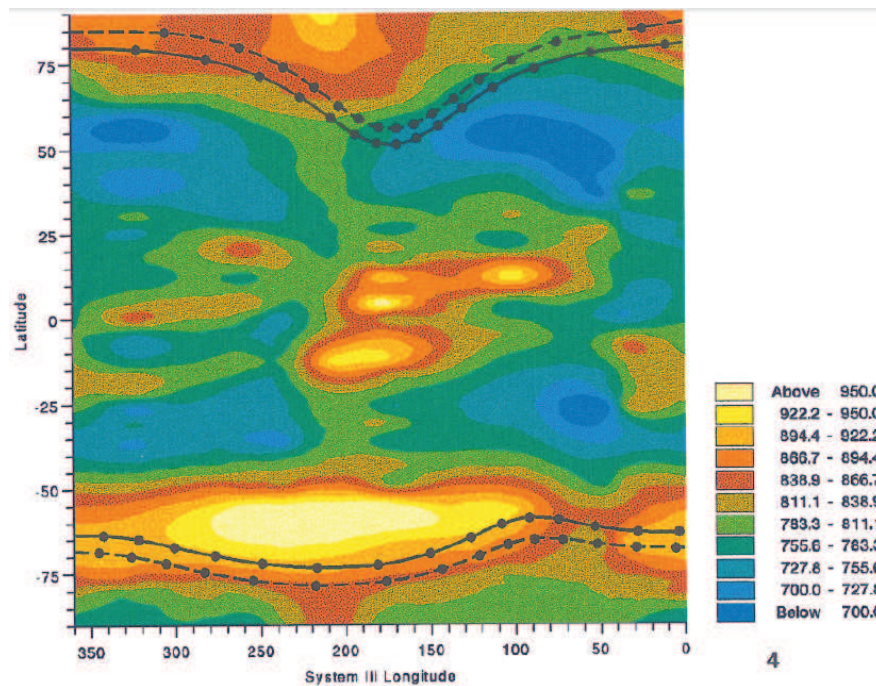


Figure 5.8: Map of Jovian H_3^+ column density by Lam et al. (1997) - The first global ionospheric temperature map based on analysis of H_3^+ spectra (Jupiter system III planetocentric coordinates). The temperature colour scale is given on the right and is in Kelvins. The over-plotted black lines show the magnetic footprints as indicated. Figure 4 from Lam et al. (1997).

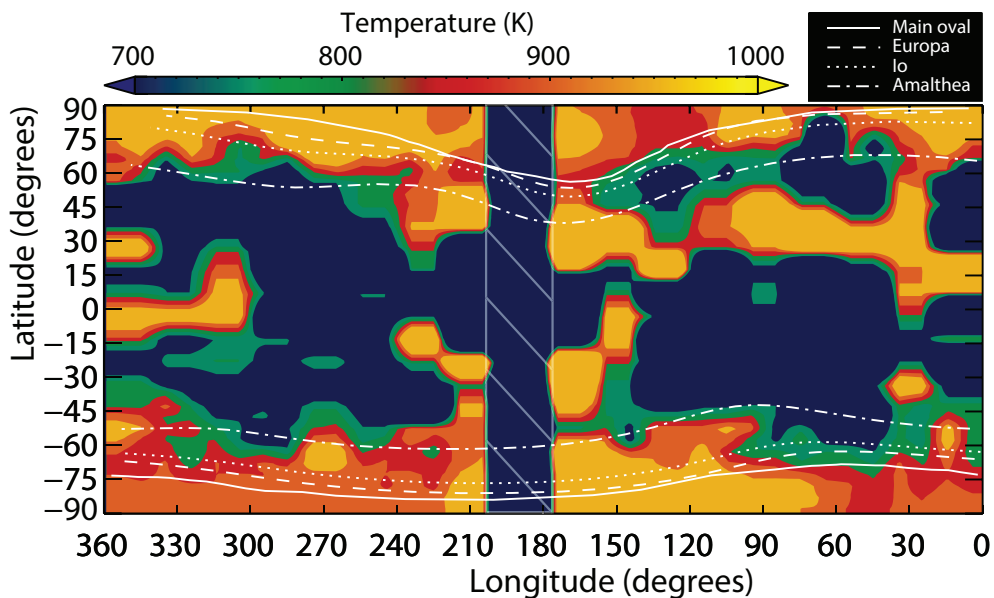


Figure 5.9: Comparative map of Jovian H_3^+ temperatures - A comparison between Lam et al and the data herein, described in the main text (Jupiter system III planetocentric coordinates). The temperature colour scale is given on the right and is in Kelvins. The over-plotted white lines show the magnetic footprints of satellites and the main oval, as indicated. The grey diagonal lines in the centre indicate the interpolation of data in longitude.

5.2.3 H_3^+ column density comparison to Lam et al

The H_3^+ column density of Lam et al. (1997) is shown in Figure 5.10, whilst the comparison based on our data is shown in Figure 5.11 and has an uncertainty limit of 35%. The latter map also corrects for line-of-sight (LoS) effects (see Chapter 2). (Lam et al. (1997) also corrected for LoS effects). The column densities in both Figures are scaled to the same range. We find that the auroral regions match well between the two in both morphology and in H_3^+ density. The body of the planet however, appears to be significantly different: Figure 5.11 shows considerably higher and more structured densities as opposed to a smooth transition from pole to equator, with a number of high and low density regions also corresponding to low and high temperature regions, respectively, in Figure 5.9. Lam et al do not see a similar anti-correlation between these parameters near the equator.

Given that column density uncertainties are generally a minimum of $\sim 30\%$, it is unclear as to how well both of these figures can be trusted. However, the higher spectral resolution herein must lead to a more reliable spectral profile of H_3^+ , hence a more accurate H_3^+ column density, owing to the reduction in unwanted emissions at nearby wavelengths.

5.2 Comparison with previous studies

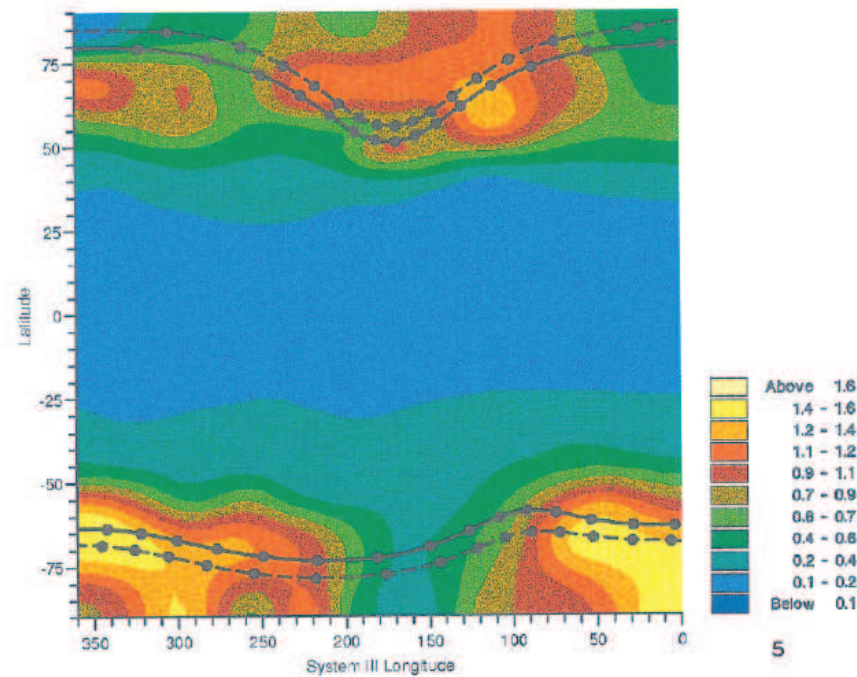


Figure 5.10: Map of Jovian H_3^+ column density by Lam et al. (1997) - As Figure 5.8 but for column density in units of $\times 10^{12} \text{cm}^{-2}$. Figure 5 from Lam et al. (1997).

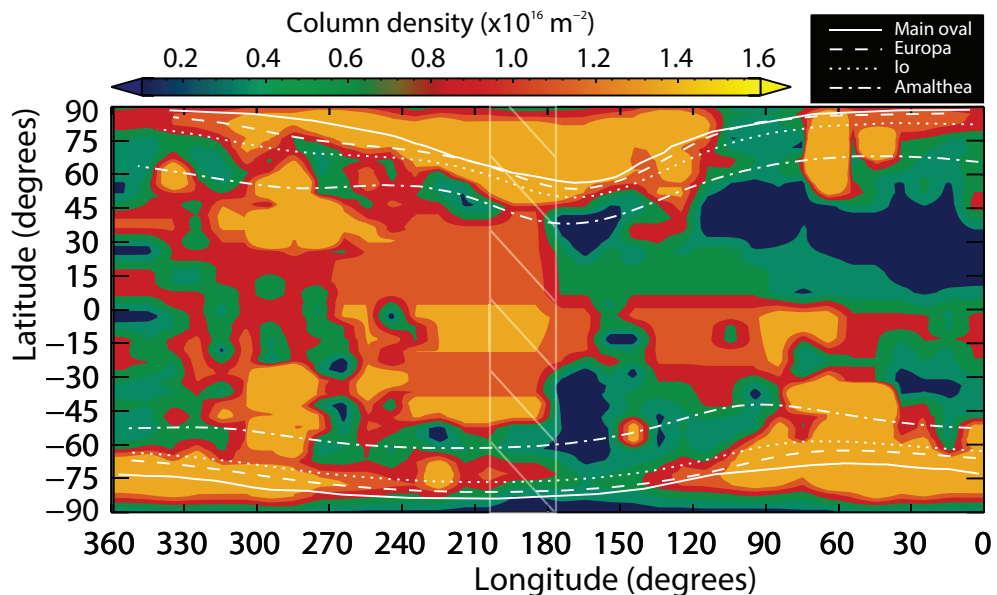


Figure 5.11: Comparative map of Jovian H_3^+ column density - As Figure 5.9 but for column densities.

5.2.4 H_3^+ total emission comparison to Lam et al

Figure 5.12 shows the Lam et al. (1997) total emission map and Figure 5.13 shows the new map which is uncertainty limited to 5%. (Both maps are corrected for line-of-sight (LoS) effects). Immediately clear is the similarity between both figures, despite the slight difference in the way they are scaled (the newer figure was scaled to a lower value to bring out lower intensity features). The uncertainty in total emission is typically on the order of a few percent for both datasets, the least of all three parameters of H_3^+ , thus by far the most reliable.

The mid- to low-latitudes are, surprisingly, virtually identical in their morphology and values. The majority of large high and low total emissions are coincident in both figures. Drawing conclusions about the smaller pockets of high or low emission in one individual dataset (e.g. the low located at 270° longitude at the equator) would have been difficult to justify, but this comparison shows that such features may be real and even persistent for nearly two decades.

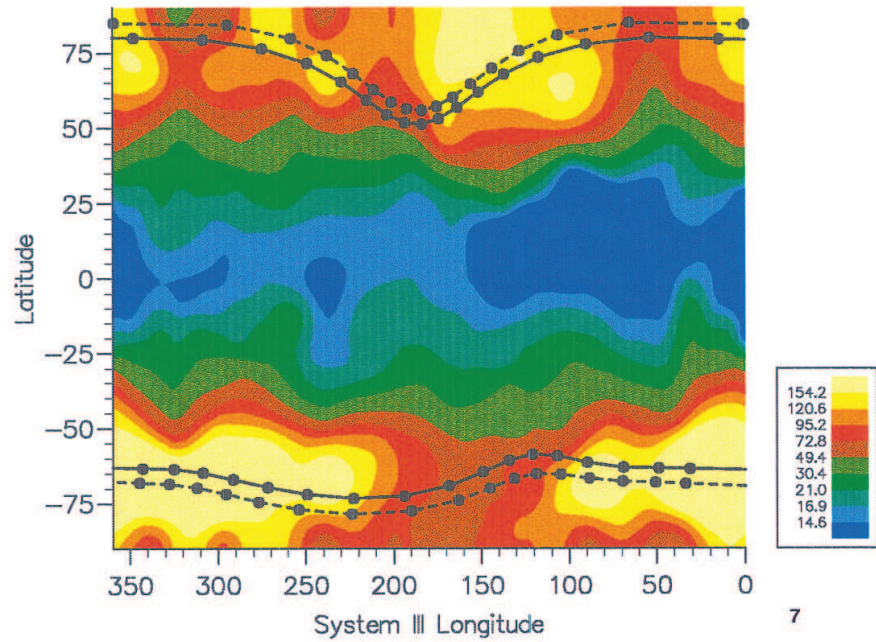


Figure 5.12: Map of Jovian H_3^+ total emission - As Figure 5.8 but for total emission in units of $\text{ergs} \times 10^{-3} \text{s}^{-1} \text{cm}^{-2} \text{sr}^{-1}$. Figure 6 from Lam et al. (1997).

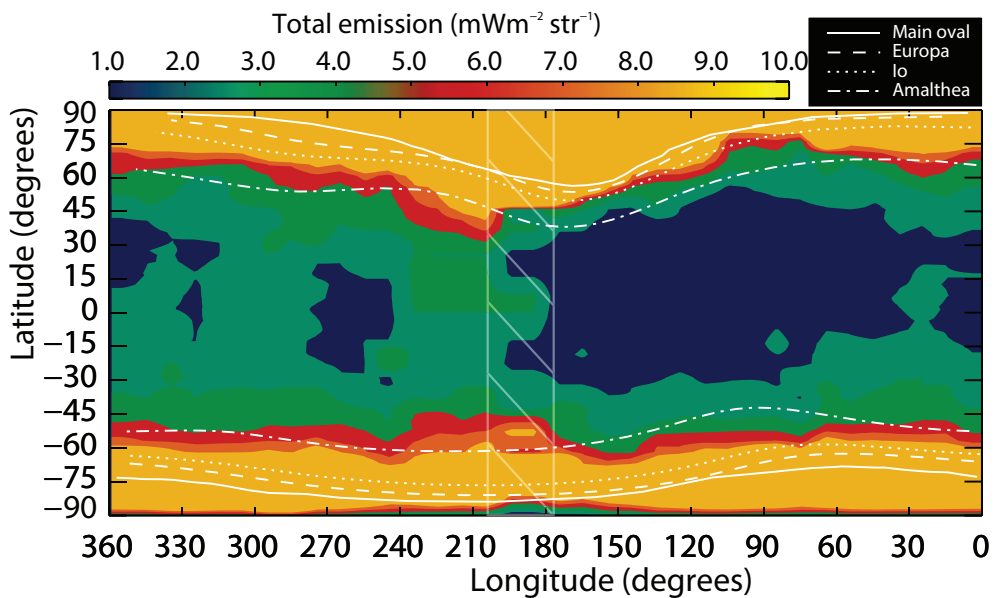


Figure 5.13: Comparative map of Jovian H_3^+ total emission - As Figure 5.9 but for total emission.

5.2.5 Validation of dataset

The uncertainties between datasets are low enough (less than 12%) in the temperature and total emission of both datasets to validate that our methodology is accurate. This is particularly evidenced by the Jovian total emission maps, in which the mid- to low-latitude regions are virtually the same. The column density differences can be explained by the higher spectral resolution (the spectral resolution was not scaled to Lam *et al*'s). With the values obtained (reassuringly) showing similarity to past results, we can confidently compare the results of these observations with the Saturn observations in Chapters 3 and 4.

5.3 Comparison to Saturn

Here we will compare the Jovian mid- and low-latitude region to that of Saturn, in an effort to fully explore whether or not the ‘ring rain’ phenomenon is unique to Saturn in Chapter 3. High resolution maps are needed to perform a valid study, as we are looking for differences in H_3^+ parameters on spatial scales of the order of a few degrees of latitude. Instead of contouring as before, the following maps are simply raw data points that are smoothed only by 2° latitude and longitude at the end of their construction, with the exception of the missing longitudes (as indicated in Figure 5.2), which are interpolated in longitude. In the case for Saturn, a simple line intensity from pole-to-pole was used; here, however, we are able to be more thorough, because Jupiter is approximately twice the size of Saturn in the sky and we have obtained a broader range of longitudes.

The uncertainties were set as low as possible such that the map could be fully populated with no missing data, e.g. a 20% uncertainty-limited column density map results in a map only one-third populated with data, whereas at beyond 70% uncertainty the features on the map no longer make any physical sense. The uncertainty limits empirically chosen here for the parameters of H_3^+ were: temperature = 11%, column density = 30% and total emission = 5% and the

resultant maps are shown in Figure's 5.14, 5.15 and 5.16, respectively. The latter two maps are corrected for line-of-sight (LoS) effects (see Chapter 2).

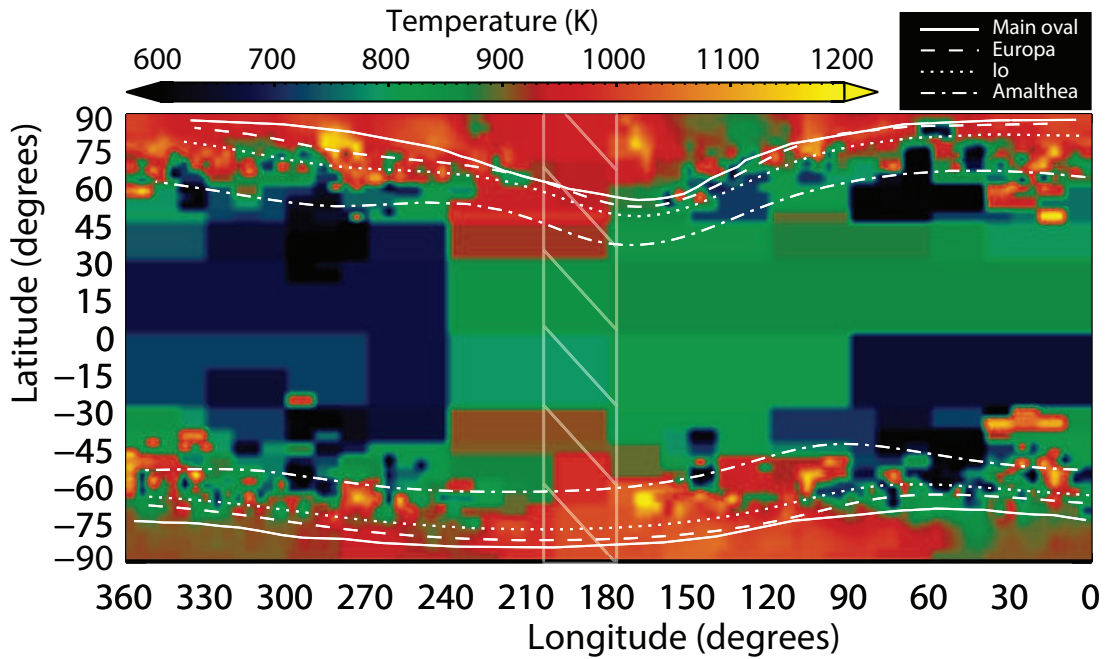


Figure 5.14: Map of Jovian H_3^+ temperatures - A map of H_3^+ temperatures as a function of longitude and latitude for varying bin sizes as described in the main text (Jupiter system III planetocentric coordinates). All temperatures are below 11% uncertainty. Values are limited between 600 and 1200 K in order to preserve colour contrast. The grey diagonal lines in the centre indicate the interpolation of data. The over-plotted white lines show the magnetic footprints of satellites and the main oval, as indicated. The grey diagonal lines in the centre indicate the interpolation of data.

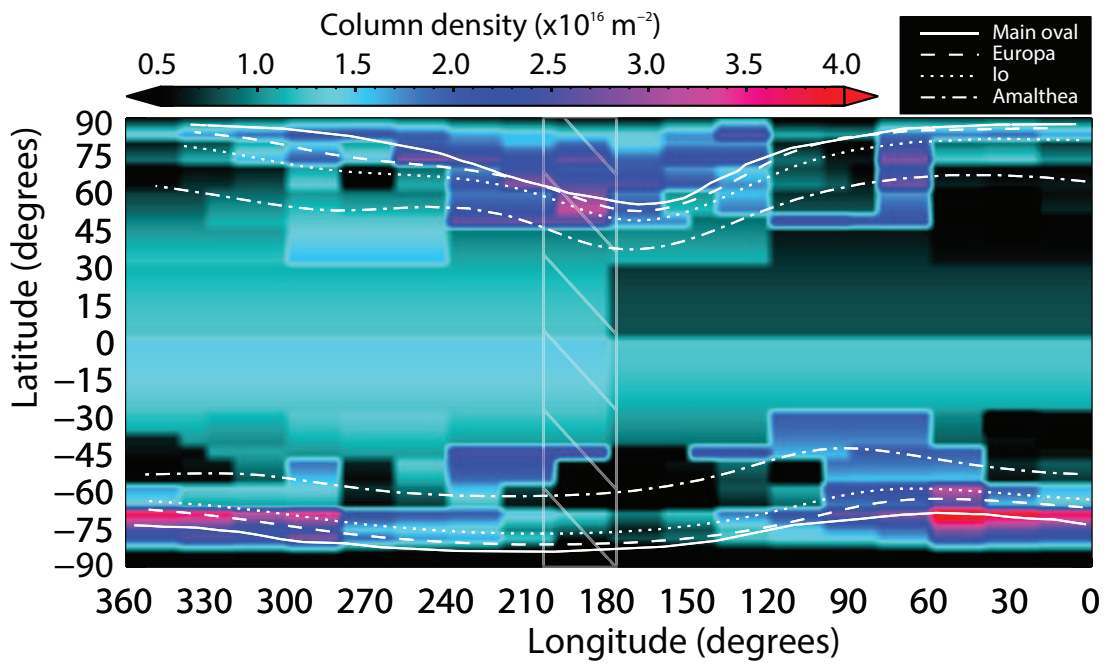


Figure 5.15: Map of Jovian H_3^+ column densities - As Figure 5.14 but for H_3^+ column density. All uncertainties are less than 30%.

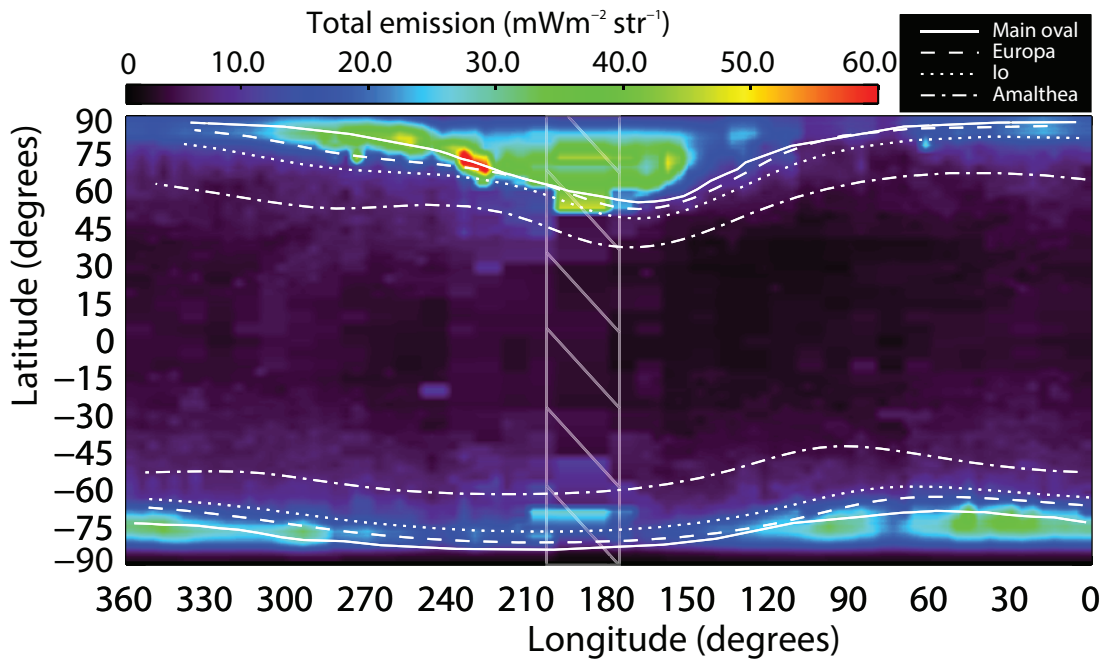


Figure 5.16: Map of Jovian H_3^+ total emission - As Figure 5.14 but for H_3^+ total emission. All uncertainties are less than 5%.

5.3.1 Mid-to-low latitudes

In this study, we define the Jovian mid-to-low latitudes as those at and equatorward of the Europa magnetic footprint. Although the overall temperatures in this region are lower than those found in the auroral region. Due to the far weaker total emission in the mid-to-low latitudes it is now useful to investigate the low levels of emission in Figure 5.16 via thresholding; limiting the maximum value to $10 \text{ mWm}^{-2}\text{sr}^{-1}$ we obtain Figure 5.17. The total emission in this figure exhibits significant variability in both latitude and longitude; it is broadly similar structure to that seen in Section 5.2, and Miller et al. (1997) have reproduced a similar structure in their work, but here we have now revealed the finer detail of the variability. The latitudinal variability however, does not obviously show a structure similar to that found at Saturn, i.e. magnetically conjugate peaks and troughs of intensity, although the data would need to be integrated in longitude for a fair comparison. The rings of Jupiter are relatively rarefied, and so it is unsurprising that the variability seen at Saturn is not repeated here, but the lack of latitudinal banding is further confirmation that the results of Chapter 3 are a direct result of the interaction between Saturn and its rings. The total emission

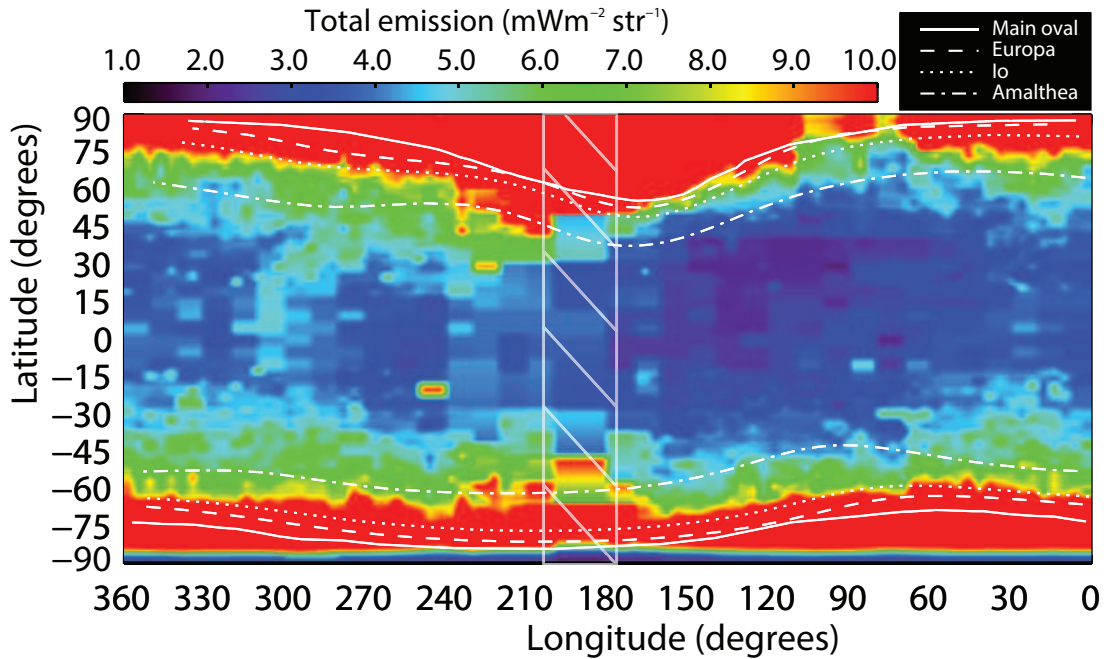


Figure 5.17: Thresholded map of Jovian H_3^+ total emission - As Figure 5.16 but here the map has been limited to $10 \text{ mWm}^{-2} \text{sr}^{-1}$.

is a measure of H_3^+ cooling, so the relatively high total emission indicates that H_3^+ is radiatively cooling down the planet more than in areas of relatively lower total emission. This global phenomenon appears in both hemispheres between approximately 180° to 70° longitude, and appears magnetically aligned with e.g. the Amalthea footprint (at $2.54 R_J$) projection as opposed to geographic lines of latitude, possibly indicating this phenomenon to be magnetospheric in origin. Miller et al. (1997) also discovered these global patterns and proposed a number of possible mechanisms. Due to the low spatial resolution of their results, which is the same as that shown in Figure 5.12, their conclusions were only weakly supported. Here, with higher spatial resolution and the benefit of recent work, we revisit two of the mechanisms suggested by Miller et al. (1997):

1. **Meridional transport** In Chapter 1 it was discussed that a possible solution to the energy crisis was the equatorward transport of heat from the polar regions to the equator. Smith et al. (2007) showed using 2D model simulations of Saturn that the sub-corotating ionosphere, which is associated with Saturn's auroral oval, undergoes a reduction in the centrifugal

component due to ion drag - thus the ionosphere down-wells. As it sinks, the lower altitudes become compressed and therefore heated, and this results in the expansion of the entire altitude column. The down-welling gases introduce a pressure gradient which in turn leads to poleward winds. At the top of this column, the gases adiabatically cool and because of the divergence in flow, these high altitude gases flow equatorward, leading to a net cooling effect at all low latitudes. This pattern of transport was also modelled by Yates et al. (2012) specifically for the case of Jupiter. The maps in this work may support the hypothesis that meridional winds flow equatorward, provided that dense waves of H_3^+ or H^+ are capable of propagating to latitudes of $\sim \pm 30^\circ$.

2. **Satellite and ring precipitation** Jupiter's magnetospheric field lines sweep through the equatorial plane as it rotates, on passing over Io they become magnetically linked to the plasma it produces. Connerney et al. (1993) examined images of H_3^+ centered at $3.4 \mu\text{m}$ and found that the ionospheric planetary footprint of this magnetic flux tube is more intense than the background in which it was situated; at the time of observation it was located 8° equatorward of the southern main auroral oval and between 15° to 20° system III longitude. The Io footprint was later seen in H and H_2 UV emissions using HST, indicating charged particle precipitation (Clarke et al., 2002). The bright IR footprint in H_3^+ images is likely then to be associated with an increase in H_3^+ density, not temperature; and although this cannot be ruled out without direct measurements, an increase in density tends to lead to an anti-correlating lower temperature. We predict therefore that this footprint should be associated with cold temperatures, high densities and high emissions of H_3^+ . During day 1 of the observations, Io was located on field lines mapping to 160° longitude, but while we were able to detect some variation in temperature, the scale of this variation was not significant compared with variations seen at other similar locations away from the Io

spot mapping. The footprints for the satellites Europa and Ganymede were also found in UV by Clarke et al. (2002), but these are too close to the main oval to be resolvable here due to the constraints introduced by seeing.

The plasma tori, which are associated with the out-gassing of Io and Europa in the equatorial plane, could represent the source of charged particles through which field lines sweep and collect material. The mechanism may be similar to the pick up of the charged material around Saturn's rings as in Chapter 3. However, Io's plasma torus has only been measured as far in as $4.5 R_J$ (Bagenal and Sullivan, 1981), and so magnetically maps to latitudes near the auroral region - too high to be considered a source for the raised total emission.

In Figure 5.18 an illustration of Jupiter's inner rings, (small) moons and 'halo' is shown. This halo extends from 1.29 to $1.71 R_J$ in the equatorial plane and is up to $0.18 R_J$ full-width at half-maximum in thickness (Ockert-Bell et al., 1999). From this location until $1.8 R_J$ the main rings are present. The main ring is mostly composed of micron-sized grains, whereas the halo is composed of even finer sub-micron particles (Burns et al., 1984). The particles are thought to be created by micro-meteoroid bombardment of small bodies in the main rings, and are removed by orbital decay (e.g. atmospheric drag and collisions resulting in a planetward trajectory) (Meier et al., 1999). In the absence of a creation mechanism, the lifetime of the rings and halo is on the order of 100's to 1000's of years, so in order to exist they must be being continuously replenished (Burns et al., 1984). The Jovian ring/halo system is clearly far better constrained than Saturn's ring system in terms of lifetime; the Galileo spacecraft had multiple orbits through it, which is not possible at Saturn due to the icy environment (Ockert-Bell et al., 1999), and it is observable from Earth using e.g. Keck (Meier et al., 1999).

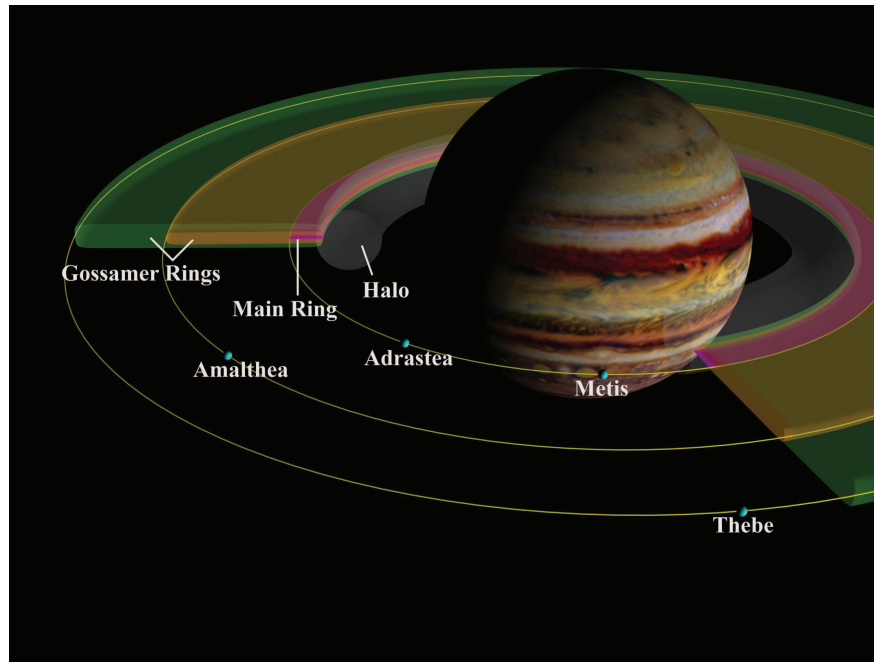


Figure 5.18: Jovian rings and small moons - An artists impression of Jupiter's ring and moons. Figure 8 from Ockert-Bell et al. (1999)

Solar EUV ionisation and collisions may ionise a significant portion of this material, thus creating a source of charged material over a large range of radial distances. Though a more complex magnetic field model would need to be employed to be more specific, the latitude mapping to the planet from this region is essentially everything below the Amalthean footprint. By analogy with the discovery of Saturn's ring rain, it is possible that these charged particles travel along magnetic field lines and collide with the planet. On impact, they would increase H_3^+ density (see Chapter 3, Figure 3.19), which leads to more efficient cooling through radiative emission - hence a lower temperature. The longitudinal variation seen can be explained by the asymmetry in Jupiter's magnetic field strength. The latest available magnetic field models are shown in Figure 5.19; comparing this figure and Figure 5.17, there appears to be an inverse relationship between field strength and total emission in certain areas, particularly at around 130° longitude and 45° latitude, where the field strength is high and the total emission is lowest. This apparent relationship must be assessed by a more quantitative values

in future work in order to be valid, but if true it is suggestive that the emissions could be related to pitch angle scattering. Particles contained within a magnetic field line mirror between ionospheric footprints on the planet due to the magnetic field gradient becoming larger towards the planet (i.e. a magnetic bottle, described in more detail in Chapter 1). Due to the higher field strength between 90° and 180° , particles may be unable to penetrate as deep into the atmosphere compared to other longitudes, and this could result in a reduced H_3^+ production there. If a background temperature of ~ 850 K is assumed, which corresponds to $\sim 120^\circ$ longitude, where magnetic field strength is strongest, then the Jovian ionosphere may be being cooled by hundreds of Kelvin due to the precipitation elsewhere. The implication for the equatorial plasma associated with the halo and main ring is that Jupiter periodically collects material as it rotates. This suggests that a similar magnetic link exists between Jupiter and Saturn's ionosphere and their rings, but the resultant variability within the ionosphere's of these planets is significantly different, largely as a result of the relative strength and alignment of the planetary magnetic field, and the density and perhaps the composition of the rings.

5.3.2 Auroral/polar regions

It is difficult to directly apply the calculations of auroral heating used for Saturn (as given in Chapter 4) to the Jovian auroral ovals, as the magnetic field is tilted ~ 10 degrees from the rotational axis for Jupiter, compared with being almost exactly aligned at Saturn. In addition, we have already seen that magnetic field strengths vary greatly between the northern and southern aurorae at Jupiter, as a function of both longitude and latitude, such that the Pederson conductance also varies drastically. For this subsection we will thus mostly discuss the phenomena unique to Jupiter that we were unable to resolve for Saturn.

The auroral/polar regions will here be referred to as the areas at and poleward of

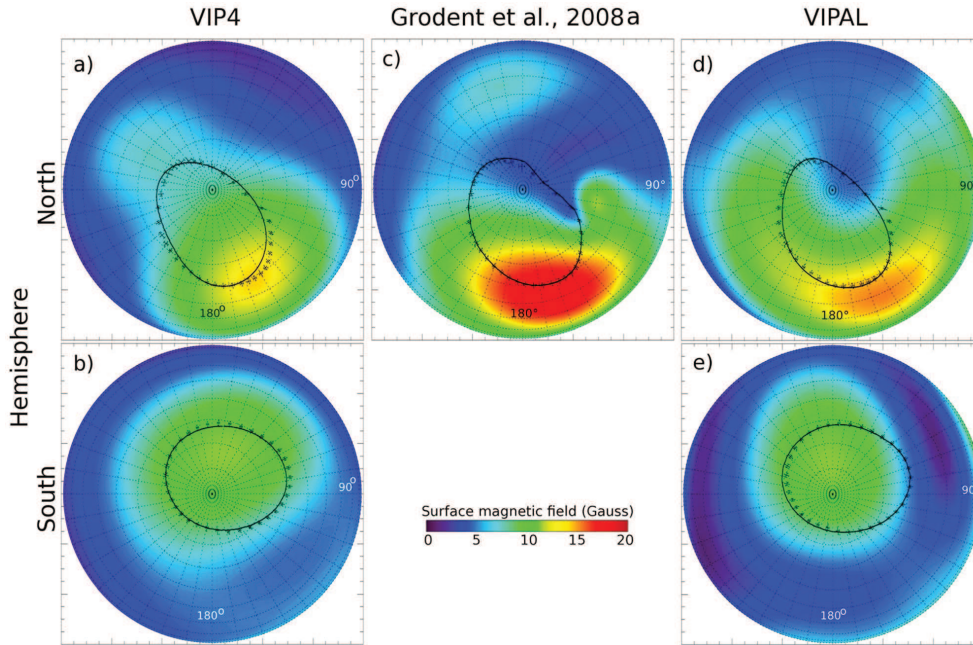


Figure 5.19: Surface magnetic field strength of Jupiter - Jupiter's magnetic field strength is shown in 3 different field models. The modelled Ionian footprint is indicated by the solid line, whereas the observed Ionian UV footprint is shown as crosses. The following field models are used: (a & b) VIP4 model (Connerney et al., 1998); (c) Grodent et al. (2008) model; (d & e) VIP Anomaly Longitude (VIPAL) model (Hess et al., 2011). This is Figure 2 from the latter model.

the main auroral oval. Although the majority of the main auroral oval was not observed in this work, due to a combination of Jupiter's 3° sub-Earth latitude and the longitudes measured, a greater portion of the northern main oval closest to the pole was observed throughout. Total emissions, temperatures and column densities are all highest in the polar regions, particularly along the main oval. The main oval appears to be a location in which Joule heating is continuously replenishing the lost radiated heat, whereas as we have seen, the remainder of the planet exhibits an apparent by-eye temperature versus density anti-correlation. Temperatures are on average ~ 1000 K, with large areas that appear to rise to 1200 K and beyond, over 500 K hotter than at Saturn. These temperatures are in agreement with work by Raynaud et al. (2004); Stallard et al. (2002); Lystrup et al. (2008) in which the authors found auroral temperatures of typically ~ 1100 K. Raynaud et al. (2004) also found a so-called auroral 'hot spot' between 150° - 170° longitude, in which temperatures were 250 K hotter than nearby regions.

A possible explanation - the authors suggest - is that the homopause is elevated there, which leads to the vertical mixing of hydrocarbons. The cause for this is attributed to strong particle precipitation, which leads to localised heating and the expansion of the homopause to higher altitudes (Livengood et al., 1990); indeed, this is modelled to be the case for Earth via solar effects at the equator (Snieder and Fels, 1988). Such vertical mixing will destroy the lower part of the H_3^+ altitudinal column, and because models assign temperatures of 800 K at 500 km altitude - rising to over 1200 K by 1300 km (Lystrup et al., 2008) - the observed H_3^+ emission is representative of a higher temperature region. Figure 5.14 neither confirms nor denies the existence of the 'hot spot' at 150 - 170°, but it is clear that there are an array of large hot and cold spots elsewhere that are $\sim \pm 200$ K compared to the background.

Column densities appear to be anti-correlated with temperature away from the main oval line, and as H_3^+ is an efficient coolant in the ionosphere, this should result in cooler ionospheric temperatures there (Miller et al., 2006). Understanding this process will likely involve comprehensive 3D modelling - or - close spacecraft observations that are able to produce H_3^+ altitudinal profiles. The total emission, which is a direct measure of H_3^+ cooling, appears to follow the main oval; this is particularly noticeable at 180° where the shape of the oval is clearly discernible.

5.4 Conclusion

The observations of Jupiter's global H_3^+ distribution herein is a vast improvement on previous work. The main reasons for these improvements are advances in telescopic and instrumental technologies, which have allowed the ability to probe at spatial resolutions over 30 times finer than before (9800 km by Lam et al. (1997) versus 475 km here), as well as achieving a 1.4 nm minimum wavelength resolution as opposed to 2.92 nm (at 3.5 μm). The new observations in this chapter

were scaled down in spatial resolution to match the work of Lam et al, and similar results were found - particularly in the total emission of H_3^+ , where both datasets were virtually identical at mid- to low-latitudes. Following this validation of the methods used, we restored our data to high spatial resolution in order to compare it with Saturn. The mid- and low-latitudes of Jupiter were revealed as never before, showing that there are departures from expectations in both longitude and latitude in terms of temperatures, column densities and total emissions of H_3^+ . At mid- to low-latitudes, Jupiter appears to have significant longitudinal asymmetry. We postulated two main reasons as to why this could be so and we here conclude that there is greater evidence for a Jovian ring-planet coupling as in the Saturn case, as opposed to meridional transport. Jupiter's magnetic field strength is highest in a region of low total emission, indicating inhibited diffuse particle precipitation, which then leads to higher H_3^+ density and a colder ionosphere. It is difficult to envisage a scenario in which magnetic field strength plays a major role in inhibiting a transport mechanism, especially one which has not been shown to exist through either observations or modelling. Jupiter's ring-planet coupling thus may be revealed herein through its longitudinal origins, rather than latitudinal ones as on Saturn. Far from helping to explain the high temperature 'energy crisis' at Jupiter, this cooling mechanism gives reason for it to be more severe, for in the absence of this cooling mechanism the ionosphere would be far hotter. Jupiter's auroral regions are difficult to compare conjugately as was done for Saturn, this is primarily because Jupiter's magnetic field is not aligned with its spin axis. Instead, common features were examined between the aurorae. There was unusual variability in H_3^+ temperature, with hot spots and cold spots that span from \sim few to several degrees in longitude and latitude. It is the conclusion of this work that they are likely to be driven by strong variations in particle precipitation, for example in an area of strong precipitating flux, the homopause is thought to expand due to heating, subsequently releasing hydrocarbons to higher altitude. Once there, these hydrocarbons destroy the cooler H_3^+ at low altitudes,

leading to the observed column to be weighted towards the hotter H_3^+ material at high altitudes.

Chapter 6

Conclusion

Ground-based observations of H_3^+ emission from Saturn and Jupiter have been analysed. The observations were taken using the Keck II telescope and NIRSPEC instrument for Saturn, and the NASA IRTF and SpeX instrument for Jupiter. Both sets of observations have greatly improved on previous work because of the advances in telescopic and instrumental technology, which have allowed the H_3^+ ionospheres of the gas giants to be probed at high spatial and spectral resolution. Previous literature, particularly for Jupiter, suggested that Saturn's lower latitudes should fall off in H_3^+ intensity towards the equator, corresponding to the transition from the high levels of emission in the auroral regions produced by particle precipitation, to the low background glow elsewhere produced by solar EUV ionisation (Miller et al., 2010; Stallard et al., 1999). However, by obtaining a pole-to-pole profile of H_3^+ intensity along Saturn's noon meridian, a pattern of peaks and troughs in intensity was seen. This pattern of features was found to be symmetric in either hemisphere about Saturn's magnetic equator, located northward of the solid-body centre of the planet. Through the use of a magnetic model (Burton et al., 2010), the peaks in intensity were mapped to gaps in Saturn's rings, whereas the troughs were mapped to the solid sections. We presented three interpretations for this result, two of which state that ring-derived water ions are transported via magnetic mirroring along field lines and enter the

planetary ionosphere; the third interpretation was that a current system exists between the planet and rings. In the former two regimes, either H_3^+ is created or destroyed by this influx, whereas in the third H_3^+ is simply Joule-heated by the current system. By comparing this work to models of Saturn's ionosphere, the strongest evidence appears to support the first interpretation; the largest flow of water entering the ionosphere stems from the ring gaps, which ultimately leads to the creation of additional H_3^+ and therefore, more emission associated with the ring gaps.

Within this same Saturn dataset, which was ~ 2 hours worth of exposures, the auroral ovals were also studied; the fact that Saturn's magnetic field is aligned almost completely with its axis of rotation was exploited. During this time both auroral oval H_3^+ temperatures remained effectively constant, whilst at the same time the H_3^+ column density and total emission varied greatly, particularly in the north. The main oval in the south was found to be significantly warmer than its northern counterpart, having temperatures of 583 and 527 K, respectively; the south also had 1.5 times more H_3^+ total emission than the north. This asymmetry was attributed to an inverse relationship between ionospheric Joule and ion drag heating with magnetic field strength. This was found to be consistent with model predictions of a higher Pedersen conductivity at the southern pole compared with the north (Galand et al., 2011) and an asymmetry in intensity measured pre-equinox by Cassini VIMS (Badman et al., 2011).

Saturn's lower latitude emissions were too faint to derive parameters for H_3^+ , such as temperature, in this work, so the interpretations herein were limited to simply a spectral emission line intensity. It is useful therefore to observe Jupiter, which has H_3^+ emissions intense enough and close enough to derive parameters for; it is also a planet in the absence of a significant ring system and as such serves as a useful comparison. The previous low-latitude Jupiter work was in the form of low spatial resolution global maps of H_3^+ parameters (Lam et al., 1997), so the new observations of Jupiter taken in this thesis had to be scaled down in spatial

resolution (i.e. from 1 pixel ~ 475 km to $\sim 10,000$ km) in order to first validate our methodology. Similar results were found - particularly in the total emission of H_3^+ , which for both datasets was virtually identical at mid- to low-latitudes. Increasing the spatial resolution of our observations, this the mid- and low-latitudes of Jupiter were revealed as never before, showing that at mid- to low-latitudes, Jupiter appears to have significant longitudinal asymmetry. We concluded that there is a greater body of evidence in support of a Jovian ring-planet coupling as was found for Saturn; Jupiter's magnetic field strength is high in a region of low total emission, indicating a possible inhibition of particle precipitation - this leads to higher H_3^+ density and a colder ionosphere.

The fact that H_3^+ appears to be inextricably linked to the magnetosphere at Jupiter as opposed to geographical structures is reassuring for the methodology employed in Chapter 3, in which H_3^+ maps to ring-plane features magnetically. A Jovian ring-planet coupling thus may have been unveiled here through its longitudinal origins, rather than latitudinal ones as on Saturn. Far from helping to explain the high temperature 'energy crisis' at Jupiter, this cooling mechanism gives reason for it to be more severe, for in the absence of this cooling mechanism the ionosphere would be far hotter. If a material influx into the Jovian ionosphere is occurring, it could be sulphur- or water-based ion influx. It could be the case that Saturn also receives a similar modulation in its H_3^+ parameters in response to an influx of ions from space, such as a lowering of temperature, although the chemistry of the influx should be determined before drawing that inference.

The principle aim of this thesis was to study the response of gas giant ionospheres to external forcing by their local space environments. We have found that the magnetic fields that protect the gas giant ionospheres from space-weathering are not a perfect shield; the planetary ionospheres of Saturn and Jupiter are globally subjected to space environment forcing. Whilst such forcing was well established for the auroral regions, we have here discovered that particle precipitation interactions across the entire planet.

References

- S. V. Badman, S. W. H. Cowley, J.-C. Gérard, and D. Grodent. A statistical analysis of the location and width of Saturn's southern auroras. *Annales Geophysicae*, 24:3533–3545, December 2006. doi: 10.5194/angeo-24-3533-2006. 32
- S. V. Badman, C. Tao, A. Grocott, S. Kasahara, H. Melin, R. H. Brown, K. H. Baines, M. Fujimoto, and T. Stallard. Cassini VIMS observations of latitudinal and hemispheric variations in Saturn's infrared auroral intensity. *Icarus*, 216: 367–375, December 2011. doi: 10.1016/j.icarus.2011.09.031. 115, 124, 130, 162
- S. V. Badman, N. Achilleos, C. S. Arridge, K. H. Baines, R. H. Brown, E. J. Bunce, A. J. Coates, S. W. H. Cowley, M. K. Dougherty, M. Fujimoto, G. Hospodarsky, S. Kasahara, T. Kimura, H. Melin, D. G. Mitchell, T. Stallard, and C. Tao. Cassini observations of ion and electron beams at Saturn and their relationship to infrared auroral arcs. *J. Geophys. Res.*, 117:A01211, January 2012a. doi: 10.1029/2011JA017222. 119
- S. V. Badman, D. J. Andrews, S. W. H. Cowley, L. Lamy, G. Provan, C. Tao, S. Kasahara, T. Kimura, M. Fujimoto, H. Melin, T. Stallard, R. H. Brown, and K. H. Baines. Rotational modulation and local time dependence of Saturn's infrared H_3^+ auroral intensity. *J. Geophys. Res.*, 117:A09228, September 2012b. doi: 10.1029/2012JA017990. 32, 119
- F. Bagenal and J. D. Sullivan. Direct plasma measurements in the Io torus and inner magnetosphere of Jupiter. *J. Geophys. Res.*, 86:8447–8466, September 1981. doi: 10.1029/JA086iA10p08447. 154

- F. Bagenal, T. E. Dowling, and W. B. McKinnon. *Jupiter. The Planet, Satellites and Magnetosphere*. 28, 31, 40, 41, 42, 43, 109
- C N Banwell. *Fundamentals of molecular spectroscopy (4th edition)*. European Chemistry Series. McGraw-Hill, London, 1994. ISBN 9780074620250. 13, 17, 21
- W. Baumjohann and R. A. Treumann. *Basic space plasma physics*. 1996. 2, 3, 4, 6, 8, 9
- D. E. Blackwell, S. K. Leggett, A. D. Petford, C. M. Mountain, and M. J. Selby. Absolute calibration of the infrared flux from VEGA at 1.24, 2.20, 3.76 and 4.6 microns by comparison with a standard furnace. *Monthly notices of the Royal Astronomical Society*, 205:897–905, December 1983. 57
- R. H. Brown, K. H. Baines, G. Bellucci, J.-P. Bibring, B. J. Buratti, F. Capaccioni, P. Cerroni, R. N. Clark, A. Coradini, D. P. Cruikshank, P. Drossart, V. Formisano, R. Jaumann, Y. Langevin, D. L. Matson, T. B. McCord, V. Mennella, E. Miller, R. M. Nelson, P. D. Nicholson, B. Sicardy, and C. Sotin. The Cassini Visual And Infrared Mapping Spectrometer (Vims) Investigation. *Space Science Reviews*, 115:111–168, December 2004. doi: 10.1007/s11214-004-1453-x. 30, 109
- E. J. Bunce, C. S. Arridge, J. T. Clarke, A. J. Coates, S. W. H. Cowley, M. K. Dougherty, J.-C. Gérard, D. Grodent, K. C. Hansen, J. D. Nichols, D. J. Southwood, and D. L. Talboys. Origin of Saturn’s aurora: Simultaneous observations by Cassini and the Hubble Space Telescope. *J. Geophys. Res. (Space Physics)*, 113:A09209, September 2008a. doi: 10.1029/2008JA013257. 129
- E. J. Bunce, C. S. Arridge, S. W. H. Cowley, and M. K. Dougherty. Magnetic field structure of Saturn’s dayside magnetosphere and its mapping to the ionosphere: Results from ring current modeling. *J. Geophys. Res. (Space Physics)*, 113:A02207, February 2008b. doi: 10.1029/2007JA012538. 84, 92

- J. A. Burns, M. R. Showalter, and G. E. Morfill. The ethereal rings of Jupiter and Saturn. In R. Greenberg and A. Brahic, editors, *IAU Colloq. 75: Planetary Rings*, pages 200–272, 1984. 154
- M. E. Burton, M. K. Dougherty, and C. T. Russell. Saturn’s internal planetary magnetic field. *J. Geophys. Res.*, 37:L24105, December 2010. doi: 10.1029/2010GL045148. 28, 78, 84, 120, 161
- R. M. Canup. Origin of Saturn’s rings and inner moons by mass removal from a lost Titan-sized satellite. *Nature*, 468:943–946, December 2010. doi: 10.1038/nature09661. 35, 107
- J. T. Clarke, J. Ajello, G. Ballester, L. Ben Jaffel, J. Connerney, J.-C. Gérard, G. R. Gladstone, D. Grodent, W. Pryor, J. Trauger, and J. H. Waite. Ultra-violet emissions from the magnetic footprints of Io, Ganymede and Europa on Jupiter. *Nature*, 415:997–1000, February 2002. 153, 154
- A. J. Coates, H. J. McAndrews, A. M. Rymer, D. T. Young, F. J. Crary, S. Maurice, R. E. Johnson, R. A. Baragiola, R. L. Tokar, E. C. Sittler, and G. R. Lewis. Plasma electrons above Saturn’s main rings: CAPS observations. *Geophys. Res. Lett.*, 32:L14S09, June 2005. doi: 10.1029/2005GL022694. 36
- J. Connerney. Solar system: Saturn’s ring rain. *Nature*, 496:178–179, April 2013. doi: 10.1038/496178a. 94
- J. E. P. Connerney. Magnetic connection for Saturn’s rings and atmosphere. *Geophys. Res. Lett.*, 13:773–776, August 1986. doi: 10.1029/GL013i008p00773. 36, 38, 73, 101, 102
- J. E. P. Connerney. Magnetic fields of the outer planets. *J. Geophys. Res.*, 98: 18659, October 1993. doi: 10.1029/93JE00980. 140
- J. E. P. Connerney and J. H. Waite. New model of Saturn’s ionosphere with

- an influx of water from the rings. *Nature*, 312:136–138, November 1984. doi: 10.1038/312136a0. 36, 73, 99
- J. E. P. Connerney, N. F. Ness, and M. H. Acuna. Zonal harmonic model of Saturn’s magnetic field from Voyager 1 and 2 observations. *Nature*, 298:44–46, July 1982. doi: 10.1038/298044a0. 91
- J. E. P. Connerney, R. Baron, T. Satoh, and T. Owen. Images of Excited H_3^+ at the Foot of the Io Flux Tube in Jupiter’s Atmosphere. *Science*, 262:1035–1038, November 1993. doi: 10.1126/science.262.5136.1035. 153
- J. E. P. Connerney, M. H. Acuña, N. F. Ness, and T. Satoh. New models of Jupiter’s magnetic field constrained by the Io flux tube footprint. *J. Geophys. Res.*, 103:11929–11940, June 1998. doi: 10.1029/97JA03726. 140, 157
- S. W. H. Cowley and E. J. Bunce. Origin of the main auroral oval in Jupiter’s coupled magnetosphere-ionosphere system. *Planetary and Space Science*, 49: 1067–1088, August 2001. doi: 10.1016/S0032-0633(00)00167-7. 43, 44
- S. W. H. Cowley and E. J. Bunce. Corotation-driven magnetosphere-ionosphere coupling currents in Saturn’s magnetosphere and their relation to the auroras. *Annales Geophysicae*, 21:1691–1707, August 2003. doi: 10.5194/angeo-21-1691-2003. 32, 33, 129
- S. W. H. Cowley, E. J. Bunce, and J. M. O’Rourke. A simple quantitative model of plasma flows and currents in Saturn’s polar ionosphere. *J. Geophys. Res.*, 109:A05212, May 2004. doi: 10.1029/2003JA010375. 1, 31, 32, 33, 34, 109, 110, 125
- S. W. H. Cowley, I. I. Alexeev, E. S. Belenkaya, E. J. Bunce, C. E. Cottis, V. V. Kalegaev, J. D. Nichols, R. Prangé, and F. J. Wilson. A simple axisymmetric model of magnetosphere-ionosphere coupling currents in Jupiter’s polar ionosphere. *J. Geophys. Res.*, 110:A11209, November 2005a. doi: 10.1029/2005JA011237. 121

- S. W. H. Cowley, I. I. Alexeev, E. S. Belenkaya, E. J. Bunce, C. E. Cottis, V. V. Kalegaev, J. D. Nichols, R. Prangé, and F. J. Wilson. A simple axisymmetric model of magnetosphere-ionosphere coupling currents in Jupiter's polar ionosphere. *J. of Geophys. Res.*, 110:A11209, November 2005b. doi: 10.1029/2005JA011237. 1, 41, 43
- S. W. H. Cowley, C. S. Arridge, E. J. Bunce, J. T. Clarke, A. J. Coates, M. K. Dougherty, J.-C. Gérard, D. Grodent, J. D. Nichols, and D. L. Talboys. Auroral current systems in Saturn's magnetosphere: comparison of theoretical models with Cassini and HST observations. *Annales Geophysicae*, 26:2613–2630, September 2008. doi: 10.5194/angeo-26-2613-2008. 33, 129
- M. K. Dougherty, N. Achilleos, N. Andre, C. S. Arridge, A. Balogh, C. Bertucci, M. E. Burton, S. W. H. Cowley, G. Erdos, G. Giampieri, K.-H. Glassmeier, K. K. Khurana, J. Leisner, F. M. Neubauer, C. T. Russell, E. J. Smith, D. J. Southwood, and B. T. Tsurutani. Cassini Magnetometer Observations During Saturn Orbit Insertion. *Science*, 307:1266–1270, February 2005. doi: 10.1126/science.1106098. 91
- P. Drossart, J.-P. Maillard, J. Caldwell, S. J. Kim, J. K. G. Watson, W. A. Majewski, J. Tennyson, S. Miller, S. K. Atreya, J. T. Clarke, J. H. Waite, and R. Wagoner. Detection of H_3^+ on Jupiter. *Nature*, 340:539–541, August 1989a. doi: 10.1038/340539a0. 19
- P. Drossart, J.-P. Maillard, J. Caldwell, S. J. Kim, J. K. G. Watson, W. A. Majewski, J. Tennyson, S. Miller, S. K. Atreya, J. T. Clarke, J. H. Waite, and R. Wagoner. Detection of H_3^+ on Jupiter. *Nature (ISSN 0028-0836)*, 340: 539–541, August 1989b. doi: 10.1038/340539a0. 40
- J. W. Dungey. Interplanetary Magnetic Field and the Auroral Zones. *Physical Review Letters*, 6:47–48, January 1961. doi: 10.1103/PhysRevLett.6.47. 33
- U. A. Dyudina, A. P. Ingersoll, S. P. Ewald, C. C. Porco, M. M. Hedman, J. A.

- Burns, and C. Sebastien. Visible Aurora on Saturn and the Vertically Extended E-ring Observed in Cassini ISS Night Side Images. In *AAS/Division for Planetary Sciences Meeting Abstracts*, volume 41 of *Bulletin of the American Astronomical Society*, page 562, January 2009. 32
- H. Feuchtgruber, E. Lellouch, T. de Graauw, B. Bézard, T. Encrenaz, and M. Griffin. External supply of oxygen to the atmospheres of the giant planets. *Nature*, 389:159–162, September 1997. doi: 10.1038/38236. 36, 99, 102
- M. Galand, L. Moore, I. Mueller-Wodarg, M. Mendillo, and S. Miller. Response of Saturn’s auroral ionosphere to electron precipitation: Electron density, electron temperature, and electrical conductivity. *J. Geophys. Res. (Space Physics)*, 116:A09306, September 2011. doi: 10.1029/2010JA016412. 109, 121, 122, 123, 128, 130, 162
- D. M. Gates and W. J. Harrop. Infrared transmission of the atmosphere to solar radiation. *Applied Optics*, 2:887–898, September 1963. 54
- T. R. Geballe, M.-F. Jagod, and T. Oka. Detection of H_3^+ infrared emission lines in Saturn. *Astrophysical Journal*, 408:L109–L112, May 1993. doi: 10.1086/186843. 19, 29
- T. P. Greene, A. T. Tokunaga, D. W. Toomey, and J. B. Carr. CSHELL: a high spectral resolution 1-5 um cryogenic echelle spectrograph for the IRTF. In A. M. Fowler, editor, *Infrared Detectors and Instrumentation*, volume 1946 of *Society of Photo-Optical Instrumentation Engineers (SPIE) Conference Series*, pages 313–324, October 1993. 74, 77
- D. Grodent. UV and visible planetary auroral emissions: Jupiter and Saturn. In *EPSC-DPS Joint Meeting 2011*, page 241, October 2011. 124
- D. Grodent, B. Bonfond, J.-C. Gérard, A. Radioti, J. Gustin, J. T. Clarke, J. Nichols, and J. E. P. Connerney. Auroral evidence of a localized mag-

- netic anomaly in Jupiter's northern hemisphere. *J. Geophys. Res.*, 113:A09201, September 2008. doi: 10.1029/2008JA013185. 157
- D. A. Gurnett, W. S. Kurth, G. B. Hospodarsky, A. M. Persoon, T. F. Averkamp, B. Cecconi, A. Lecacheux, P. Zarka, P. Canu, N. Cornilleau-Wehrlin, P. Galopeau, A. Roux, C. Harvey, P. Louarn, R. Bostrom, G. Gustafsson, J.-E. Wahlund, M. D. Desch, W. M. Farrell, M. L. Kaiser, K. Goetz, P. J. Kellogg, G. Fischer, H.-P. Ladreiter, H. Rucker, H. Alleyne, and A. Pedersen. Radio and Plasma Wave Observations at Saturn from Cassini's Approach and First Orbit. *Science*, 307:1255–1259, February 2005. doi: 10.1126/science.1105356. 32
- J. Gustin, J.-C. Gérard, D. Grodent, S. W. H. Cowley, J. T. Clarke, and A. Grard. Energy-flux relationship in the FUV Jovian aurora deduced from HST-STIS spectral observations. *J. Geophys. Res.*, 109:A10205, October 2004. doi: 10.1029/2003JA010365. 44
- S. L. G. Hess, B. Bonfond, P. Zarka, and D. Grodent. Model of the Jovian magnetic field topology constrained by the Io auroral emissions. *J. Geophys. Res.*, 116:A05217, May 2011. doi: 10.1029/2010JA016262. 157
- M. P. Hickey, R. L. Walterscheid, and G. Schubert. Gravity Wave Heating and Cooling in Jupiter's Thermosphere. *Icarus*, 148:266–281, November 2000. doi: 10.1006/icar.2000.6472. 1, 42
- T. W. Hill. Inertial limit on corotation. *J. Geophys. Res.*, 84:6554–6558, November 1979. doi: 10.1029/JA084iA11p06554. 43
- W. L. Jolly. *Modern Inorganic Chemistry (2nd edition)*. New York: McGraw-Hill, 1991. ISBN 0-07-032768-8. 20
- D. L. Judge, F.-M. Wu, and R. W. Carlson. Ultraviolet photometer observations of the Saturnian system. *Science*, 207:431–434, January 1980. doi: 10.1126/science.207.4429.431. 31

- S. Jurac and J. D. Richardson. Neutral cloud interaction with Saturn's main rings. *Geophys. Res. Lett.*, 34:L08102, April 2007. doi: 10.1029/2007GL029567. 97
- M. G. Kivelson and C. T. Russell. *Introduction to Space Physics*. April 1995. 2, 5, 6
- W. S. Kurth, T. F. Averkamp, D. A. Gurnett, J. B. Groene, and A. Lecacheux. An update to a Saturnian longitude system based on kilometric radio emissions. *J. Geophys. Res. (Space Physics)*, 113:A05222, May 2008. doi: 10.1029/2007JA012861. 78
- H. A. Lam, N. Achilleos, S. Miller, J. Tennyson, L. M. Trafton, T. R. Geballe, and G. E. Ballester. A Baseline Spectroscopic Study of the Infrared Auroras of Jupiter. *Icarus*, 127:379–393, June 1997. doi: 10.1006/icar.1997.5698. xiv, 41, 42, 71, 109, 131, 139, 140, 141, 142, 143, 144, 145, 146, 147, 158, 162
- A. L. Lane, C. W. Hord, R. A. West, L. W. Esposito, D. L. Coffeen, M. Sato, K. E. Simmons, R. B. Pomphrey, and R. B. Morris. Photopolarimetry from Voyager 2 - Preliminary results on Saturn, Titan, and the rings. *Science*, 215: 537–543, January 1982. doi: 10.1126/science.215.4532.537. 39
- C. F. Lillie, C. W. Hord, K. Pang, D. L. Coffeen, and J. E. Hansen. The Voyager mission photopolarimeter experiment. *Space Sci. Rev.*, 21:159–181, November 1977. doi: 10.1007/BF00200849. 39
- T. A. Livengood, D. F. Strobel, and H. W. Moos. Long-term study of longitudinal dependence in primary particle precipitation in the north Jovian aurora. *J. Geophys. Res.*, 95:10375–10388, July 1990. doi: 10.1029/JA095iA07p10375. 158
- J. G. Luhmann, R. E. Johnson, R. L. Tokar, S. A. Ledvina, and T. E. Cravens. A model of the ionosphere of Saturn's rings and its implications. *Icarus*, 181: 465–474, April 2006. doi: 10.1016/j.icarus.2005.11.022. 36, 93, 94, 100

- M. B. Lystrup, S. Miller, N. Dello Russo, R. J. Vervack, Jr., and T. Stallard. First Vertical Ion Density Profile in Jupiter's Auroral Atmosphere: Direct Observations using the Keck II Telescope. *The Astrophysical Journal*, 677:790–797, April 2008. doi: 10.1086/529509. 128, 157, 158
- W. M. MacDonald and M. Walt. Distribution function of magnetically confined electrons in a scattering atmosphere. *Annals of Physics*, 15:44–62, July 1961. doi: 10.1016/0003-4916(61)90165-8. 6
- I. S. McLean, E. E. Becklin, O. Bendiksen, G. Brims, J. Canfield, D. F. Figer, J. R. Graham, J. Hare, F. Lacayanga, J. E. Larkin, S. B. Larson, N. Levenson, N. Magnone, H. Teplitz, and W. Wong. Design and development of NIRSPEC: a near-infrared echelle spectrograph for the Keck II telescope. In A. M. Fowler, editor, *Society of Photo-Optical Instrumentation Engineers (SPIE) Conference Series*, volume 3354 of *Society of Photo-Optical Instrumentation Engineers (SPIE) Conference Series*, pages 566–578, August 1998. 47, 49, 78, 110
- R. Meier, B. A. Smith, T. C. Owen, E. E. Becklin, and R. J. Terrile. Near Infrared Photometry of the Jovian Ring and Adrastea. *Icarus*, 141:253–262, October 1999. doi: 10.1006/icar.1999.6172. 154
- H. Melin. Comparative Aeronomy of the Upper Atmospheres of the Giant Planets. *University College London*, 2006. 21, 59, 65, 69, 71
- H. Melin, S. Miller, T. Stallard, and D. Grodent. Non-LTE effects on H₃⁺ emission in the jovian upper atmosphere. *Icarus*, 178:97–103, November 2005. doi: 10.1016/j.icarus.2005.04.016. 21
- H. Melin, S. Miller, T. Stallard, L. M. Trafton, and T. R. Geballe. Variability in the H₃⁺ emission of Saturn: Consequences for ionisation rates and temperature. *Icarus*, 186:234–241, January 2007. doi: 10.1016/j.icarus.2006.08.014. 30, 109, 117

- H. Melin, T. Stallard, S. Miller, J. Gustin, M. Galand, S. V. Badman, W. R. Pryor, J. O'Donoghue, R. H. Brown, and K. H. Baines. Simultaneous Cassini VIMS and UVIS observations of Saturn's southern aurora: Comparing emissions from H, H₂ and H₃⁺ at a high spatial resolution. *Geophys. Res. Lett.*, 38: L15203, August 2011. doi: 10.1029/2011GL048457. 20, 32, 109, 118
- H. Melin, T. S. Stallard, J. O'Donoghue, S. V. Badman, S. Miller, and J. S. D. Blake. On the anticorrelation between H₃⁺ temperature and density in giant planet ionospheres. *Mon. Not. R. Astron. Soc.*, 438:1611–1617, February 2014. doi: 10.1093/mnras/stt2299. 32, 68, 70, 71, 137
- Henrik Melin, Tom. S. Stallard, Steve Miller, Thomas R. Geballe, Laurence M. Trafton, and James O'Donoghue. Post-equinoctial observations of the ionosphere of uranus. *Icarus*, 223(2):741 – 748, 2013. ISSN 0019-1035. doi: 10.1016/j.icarus.2013.01.012. URL <http://www.sciencedirect.com/science/article/pii/S0019103513000274>. 112
- M. Mendillo, L. Moore, J. Clarke, I. Mueller-Wodarg, W. S. Kurth, and M. L. Kaiser. Effects of ring shadowing on the detection of electrostatic discharges at Saturn. *Geophys. Res. Lett.*, 32:L05107, March 2005. doi: 10.1029/2004GL021934. 105
- C. Meredith, S. W. H. Cowley, K. C. Hansen, J. D. Nichols, and T. K. Yeoman. Simultaneous conjugate observations of small-scale structures in Saturn's day-side ultraviolet auroras - implications for physical origins. *J. Geophys. Res. (Submitted)*, 2013. 32, 124
- S. Miller, R. D. Joseph, and J. Tennyson. Infrared emissions of H₃(+) in the atmosphere of Jupiter in the 2.1 and 4.0 micron region. *Astrophys. J.*, 360: L55–L58, September 1990a. doi: 10.1086/185811. 21

REFERENCES

- S. Miller, R. D. Joseph, and J. Tennyson. Infrared emissions of H_3^+ in the atmosphere of Jupiter in the 2.1 and 4.0 micron region. *The Astrophysical Journal*, 360:L55–L58, September 1990b. doi: 10.1086/185811. 67
- S. Miller, N. Achilleos, G. E. Ballester, H. A. Lam, J. Tennyson, T. R. Geballe, and L. M. Trafton. Mid-to-Low Latitude H_3^+ Emission from Jupiter. *Icarus*, 130:57–67, November 1997. doi: 10.1006/icar.1997.5813. 139, 151, 152
- S. Miller, A. Aylward, and G. Millward. Giant Planet Ionospheres and Thermospheres: The Importance of Ion-Neutral Coupling. *Space Sciences Series of ISSI*, 116:319–343, January 2005. doi: 10.1007/s11214-005-1960-4. 1, 31
- S. Miller, T. Stallard, C. Smith, and et al. H_3^+ : the driver of giant planet atmospheres. *Phil. Trans. Roy. Soc. London.*, 364:3121–3137, November 2006. doi: 10.1098/rsta.2006.1877. 32, 102, 118, 124, 158
- S. Miller, T. Stallard, H. Melin, and J. Tennyson. H_3^+ cooling in planetary atmospheres. *Faraday Discussions*, 147:283, 2010. doi: 10.1039/c004152c. 64, 65, 66, 70, 73, 161
- L. Moore and M. Mendillo. Are plasma depletions in Saturn’s ionosphere a signature of time-dependent water input? *Geophys. Res. Lett.*, 34:L12202, June 2007. doi: 10.1029/2007GL029381. 99
- L. Moore, M. Galand, I. Mueller-Wodarg, R. Yelle, and M. Mendillo. Plasma temperatures in Saturn’s ionosphere. *J. Geophys. Res. (Space Physics)*, 113:A10306, October 2008. doi: 10.1029/2008JA013373. 21, 29
- L. Moore, M. Galand, I. Mueller-Wodarg, and M. Mendillo. Response of Saturn’s ionosphere to solar radiation: Testing parameterizations for thermal electron heating and secondary ionization processes. *Planetary and Space Science*, 57:1699–1705, December 2009. doi: 10.1016/j.pss.2009.05.001. 30, 41, 112

- L. Moore, I. Mueller-Wodarg, M. Galand, A. Kliore, and M. Mendillo. Latitudinal variations in Saturn's ionosphere: Cassini measurements and model comparisons. *J. Geophys. Res.*, 115:A11317, November 2010. doi: 10.1029/2010JA015692. 99, 100, 128
- L. E. Moore, M. Mendillo, I. C. F. Müller-Wodarg, and D. L. Murr. Modeling of global variations and ring shadowing in Saturn's ionosphere. *Icarus*, 172: 503–520, December 2004. doi: 10.1016/j.icarus.2004.07.007. 63, 98
- J. I. Moses and S. F. Bass. The effects of external material on the chemistry and structure of Saturn's ionosphere. *J. Geophys. Res.*, 105:7013–7052, March 2000. doi: 10.1029/1999JE001172. 30, 36, 96, 97, 98, 99, 100, 112
- I. C. F. Mueller-Wodarg, L. Moore, M. Galand, S. Miller, and M. Mendillo. Magnetosphere-atmosphere coupling at Saturn: 1 - Response of thermosphere and ionosphere to steady state polar forcing. *Icarus*, 221:481–494, November 2012. doi: 10.1016/j.icarus.2012.08.034. 1, 21, 29, 31, 63, 109, 118, 128
- L. Neale and J. Tennyson. A High-Temperature Partition Function for H_3^+ . *The Astrophysical Journal*, 454:L169, December 1995. doi: 10.1086/309789. 65, 66
- L. Neale, S. Miller, and J. Tennyson. Spectroscopic Properties of the H_3^+ Molecule: A New Calculated Line List. *The Astrophysical Journal*, 464:516, June 1996a. doi: 10.1086/177341. 68
- L. Neale, S. Miller, and J. Tennyson. Spectroscopic Properties of the H_3^+ Molecule: A New Calculated Line List. *Astrophysical Journal*, 464:516, June 1996b. doi: 10.1086/177341. 22, 109
- J. Nichols and S. Cowley. Magnetosphere-ionosphere coupling currents in Jupiter's middle magnetosphere: effect of precipitation-induced enhancement of the ionospheric Pedersen conductivity. *Annales Geophysicae*, 22:1799–1827, May 2004. doi: 10.5194/angeo-22-1799-2004. 43, 84

- J. D. Nichols, S. V. Badman, E. J. Bunce, J. T. Clarke, S. W. H. Cowley, F. J. Crary, M. K. Dougherty, J.-C. Gérard, D. Grodent, K. C. Hansen, W. S. Kurth, D. G. Mitchell, W. R. Pryor, T. S. Stallard, D. L. Talboys, and S. Wanawichian. Saturn's equinoctial auroras. *Geophysical Research Letters*, 36: L24102, December 2009. doi: 10.1029/2009GL041491. 32, 124
- T. G. Northrop and J. E. P. Connerney. A micrometeorite erosion model and the age of Saturn's rings. *Icarus*, 70:124–137, April 1987. doi: 10.1016/0019-1035(87)90079-0. 35, 107
- T. G. Northrop and J. R. Hill. Stability of negatively charged dust grains in Saturn's ring plane. *J. Geophys. Res.*, 87:6045–6051, August 1982. doi: 10.1029/JA087iA08p06045. 87
- T. G. Northrop and J. R. Hill. The inner edge of Saturn's B ring. *J. Geophys. Res.*, 88:6102–6108, August 1983. doi: 10.1029/JA088iA08p06102. 87, 101
- M. E. Ockert-Bell, J. A. Burns, I. J. Daubar, P. C. Thomas, J. Veverka, M. J. S. Belton, and K. P. Klaasen. The Structure of Jupiter's Ring System as Revealed by the Galileo Imaging Experiment. *Icarus*, 138:188–213, April 1999. doi: 10.1006/icar.1998.6072. 154, 155
- J. O'Donoghue, T. S. Stallard, H. Melin, G. H. Jones, S. W. H. Cowley, S. Miller, K. H. Baines, and J. S. D. Blake. The domination of Saturn's low-latitude ionosphere by ring 'rain'. *Nature*, 496:193–195, April 2013. doi: 10.1038/nature12049. 73
- T. Oka. Observation of the infrared spectrum of H_3^+/H_3 . *Physical Review Letters*, 45:531–534, August 1980. doi: 10.1103/PhysRevLett.45.531. 19
- T. Oka. Interstellar Chemistry Special Feature: Interstellar H_3^+ . *Proceedings of the National Academy of Science*, 103:12235–12242, August 2006. doi: 10.1073/pnas.0601242103. 19, 20

- T. Oka. Chemistry, astronomy and physics of H_3^+ . *Royal Society of London Philosophical Transactions Series A*, 370:4991–5000, November 2012. doi: 10.1098/rsta.2012.0243. 20, 22, 97
- Christopher Palmer and Erwin Loewen. *Diffraction Gratings Handbook (6th Edition)*. Newport Corporation, 2005. 51
- E. Raynaud, E. Lellouch, J.-P. Maillard, G. R. Gladstone, J. H. Waite, B. Bézard, P. Drossart, and T. Fouchet. Spectro-imaging observations of Jupiter’s 2- μ m auroral emission. I. H_3^+ distribution and temperature. *Icarus*, 171:133–152, September 2004. doi: 10.1016/j.icarus.2004.04.020. 157
- J. T. Rayner, D. W. Toomey, P. M. Onaka, A. J. Denault, W. E. Stahlberger, W. D. Vacca, M. C. Cushing, and S. Wang. SpeX: A Medium-Resolution 0.8-5.5 Micron Spectrograph and Imager for the NASA Infrared Telescope Facility. *Astronomical Society of the Pacific*, 115:362–382, March 2003. doi: 10.1086/367745. 46, 49, 131
- D. Rego, S. Miller, N. Achilleos, R. Prangé, and R. D. Joseph. Latitudinal Profiles of the Jovian IR Emissions of H_3^+ at 4 μ m with the NASA Infrared Telescope Facility: Energy Inputs and Thermal Balance. *Icarus*, 147:366–385, October 2000. doi: 10.1006/icar.2000.6444. 1, 41, 76, 77
- C. S. Roberts. Pitch-angle diffusion of electrons in the magnetosphere. *Reviews of Geophysics and Space Physics*, 7:305–337, 1969. doi: 10.1029/RG007i001p00305. 5, 6
- J. Salmon, S. Charnoz, A. Crida, and A. Brahic. Long-term and large-scale viscous evolution of dense planetary rings. *Icarus*, 209:771–785, October 2010. doi: 10.1016/j.icarus.2010.05.030. 35, 107
- D. E. Shemansky and J. M. Ajello. The Saturn spectrum in the EUV - Electron excited hydrogen. *J. Geophys. Res.*, 88:459–464, January 1983. doi: 10.1029/JA088iA01p00459. 32

- D. E. Shemansky and X. Liu. Saturn upper atmospheric structure from Cassini EUV and FUV occultations¹¹This article is part of a Special Issue that honours the work of Dr. Donald M. Hunten FRSC who passed away in December 2010 after a very illustrious career. *Canadian Journal of Physics*, 90:817–831, August 2012. doi: 10.1139/p2012-036. 31
- C. G. A. Smith, S. Miller, and A. D. Aylward. Magnetospheric energy inputs into the upper atmospheres of the giant planets. *Annales Geophysicae*, 23:1943–1947, July 2005. doi: 10.5194/angeo-23-1943-2005. 109, 120
- C. G. A. Smith, A. D. Aylward, G. H. Millward, S. Miller, and L. E. Moore. An unexpected cooling effect in Saturn’s upper atmosphere. *Nature*, 445:399–401, January 2007. doi: 10.1038/nature05518. 1, 31, 42, 152
- R. K. Snieder and S. B. Fels. The flywheel effect in the middle atmosphere. *J. Atmos. Sci.*, 45:3996–4004, December 1988. doi: 10.1175/1520-0469(1988)045<3996:TFEITM>2.0.CO;2. 158
- D. J. Southwood and M. G. Kivelson. Magnetospheric interchange motions. *J. Geophys. Res.*, 94:299–308, January 1989. doi: 10.1029/JA094iA01p00299. 43
- T. Stallard. Dynamical Studies of the Jovian Ionosphere. *University College London*, 2001. 32
- T. Stallard, S. Miller, G. E. Ballester, D. Rego, R. D. Joseph, and L. M. Trafton. The H_3^+ Latitudinal Profile of Saturn. *The Astrophysical Journal*, 521:L149–L152, August 1999. doi: 10.1086/312189. 74, 75, 161
- T. Stallard, S. Miller, G. Millward, and R. D. Joseph. On the Dynamics of the Jovian Ionosphere and Thermosphere. II. The Measurement of H_3^+ Vibrational Temperature, Column Density, and Total Emission. *Icarus*, 156:498–514, April 2002. doi: 10.1006/icar.2001.6793. 64, 157

- T. Stallard, S. Miller, H. Melin, M. Lystrup, S. W. H. Cowley, E. J. Bunce, N. Achilleos, and M. Dougherty. Jovian-like aurorae on Saturn. *Nature*, 453: 1083–1085, June 2008. doi: 10.1038/nature07077. 73
- T. S. Stallard, H. Melin, S. Miller, S. V. Badman, R. H. Brown, and K. H. Baines. Peak emission altitude of Saturn’s H_3^+ aurora. *Geophys. Res. Lett.*, 39:L15103, August 2012a. doi: 10.1029/2012GL052806. 30, 84
- T. S. Stallard, H. Melin, S. Miller, J. O’ Donoghue, S. W. H. Cowley, S.V. Badman, A. Adriani, R. H. Brown, and K. H. Baines. Temperature changes and energy inputs in giant planet atmospheres: what we are learning from H_3^+ . *Phil. Trans. Roy. Soc.*, 370:5213–5224, October 2012b. doi: 10.1098/rsta.2012.0028. 31, 73, 74, 76, 85, 86, 109, 117, 128
- C. Tao, S. V. Badman, and M. Fujimoto. UV and IR auroral emission model for the outer planets: Jupiter and Saturn comparison. *Icarus*, 213:581–592, June 2011a. doi: 10.1016/j.icarus.2011.04.001. 128
- C. Tao, S. V. Badman, and M. Fujimoto. UV and IR auroral emission model for the outer planets: Jupiter and Saturn comparison. *Icarus*, 213:581–592, June 2011b. doi: 10.1016/j.icarus.2011.04.001. 41, 42
- J. Tennyson and S. Miller. Spectroscopy of H_3^+ and its impact on astrophysics. *Spectrochimica Acta*, 57:661–667, March 2001. 16
- L. M. Trafton, T. R. Geballe, S. Miller, J. Tennyson, and G. E. Ballester. The Detection of H_3^+ in Uranus’ Atmosphere. In *AAS/Division for Planetary Sciences Meeting Abstracts #24*, volume 24 of *Bulletin of the American Astronomical Society*, page 989, June 1992. 19
- W.-L. Tseng, W.-H. Ip, R. E. Johnson, T. A. Cassidy, and M. K. Elrod. The structure and time variability of the ring atmosphere and ionosphere. *Icarus*, 206:382–389, April 2010. doi: 10.1016/j.icarus.2009.05.019. 95, 100

REFERENCES

- W.-L. Tseng, R. E. Johnson, and M. K. Elrod. Modeling the seasonal variability of the plasma environment in Saturn's magnetosphere between main rings and Mimas. *Planetary and Space Science*, 77:126–135, March 2013. doi: 10.1016/j.pss.2012.05.001. 95
- V. M. Vasyliunas. *Plasma distribution and flow*, pages 395–453. 1983. 33
- V. M. Vasyliunas and P. Song. Meaning of ionospheric Joule heating. *J. Geophys. Res. (Space Physics)*, 110:A02301, February 2005. doi: 10.1029/2004JA010615. 120
- G. R. Wilson and J. H. Waite, Jr. Kinetic modeling of the Saturn ring-ionosphere plasma environment. *J Geophys. Res.*, 94:17287–17298, December 1989. doi: 10.1029/JA094iA12p17287. 73
- J. N. Yates, N. Achilleos, and P. Guio. Influence of upstream solar wind on thermospheric flows at Jupiter. *Planetary Space Science*, 61:15–31, February 2012. doi: 10.1016/j.pss.2011.08.007. 153